PFG

# Photogrammetrie Fernerkundung Geoinformation

Journal for Photogrammetry, Remote Sensing
and Geoinformation Science

Organ der Deutschen Gesellschaft für Photogrammetrie,
Fernerkundung und Geoinformation (DGPF) e. V.

Jahrgang 2014, Heft 5




E. Schweizerbart'sche Verlagsbuchhandlung
(Nägele u. Obermiller) Stuttgart 2014

Deutsche Gesellschaft für Photogrammetrie, Fernerkundung
und Geoinformation (DGPF) e.V.
Gegründet 1909

Die *Deutsche Gesellschaft für Photogrammetrie, Fernerkundung und Geoinformation* (DGPF) e.V. unterstützt als Mitglieds- bzw. Trägergesellschaft die folgenden Dachverbände:

International Society
for Photogrammetry
and Remote Sensing

**DAGM**

Deutsche Arbeits-
gemeinschaft für
Mustererkennung e.V.

GeoUnion
Alfred-Wegener-Stiftung

Herausgeber:

Präsident: Prof. Dr. Thomas Kolbe, Technische Universität München, Institut für Geodäsie, GIS und Landmanagement, Lehrstuhl für Geoinformatik, Arcisstraße 21, 80333 München, Germany, Tel. +49-89-289-23888
Geschäftsstelle: Tanja Nyc, c/o Technische Universität München, Institut für Geodäsie, GIS und Landmanagement, Lehrstuhl für Geoinformatik, Arcisstraße 21, 80333 München, Germany, Tel.: +49-89-289-22578, e-mail: geschaeftsstelle@dgpf.de, Gläubiger-Identifikationsnummer DE54 ZZZ0 0000 8351 37
Published by: E. Schweizerbart'sche Verlagsbuchhandlung (Nägele u. Obermiller), Johannesstraße 3A, 70176 Stuttgart, Germany, Tel.: +49-711 351456-0, Fax: +49-711 351456-99, e-mail: mail@schweizerbart.de
Internet: http://www.schweizerbart.de
♾ Gedruckt auf alterungsbeständigem Papier nach ISO 9706-1994

ISSN 1432-8364
Science Citation Index Expanded (also known as SciSearch®) Journal Citation Reports/Science Edition

Erscheinungsweise: 6 Hefte pro Jahrgang.
Bezugspreis im Abonnement: € 239,– pro Jahrgang. Mitglieder der DGPF erhalten die Zeitschrift kostenlos. Der Online-Zugang ist im regulären Subskriptionspreis enthalten.
Anzeigenverwaltung: E. Schweizerbart'sche Verlagsbuchhandlung (Nägele u. Obermiller), Johannesstraße 3A, 70176 Stuttgart, Germany, Tel.: +49-711 351456-0; Fax: +49-711 351456-99.
e-mail: mail@schweizerbart.de, Internet: http://www.schweizerbart.de
Bernhard Harzer Verlag GmbH, Westmarkstraße 59/59a, 76227 Karlsruhe, Germany, Tel.: +49-721 944020, Fax: +49-721 9440230, e-mail: Info@harzer.de, Internet: www.harzer.de
Printed in Germany by Tutte Druckerei & Verlagsservice GmbH, 94121 Salzweg, Germany.

# PFG – Jahrgang 2014, Heft 5
# Inhaltsverzeichnis

## Editorial



## Originalbeiträge



## Mitteilungen

Zusammenfassungen der „Originalbeiträge“ und der „Beiträge aus Wissenschaft und Praxis“ (deutsch und englisch) sind auch verfügbar unter www.dgpf.de/neu/pfg/ausgaben.htm

PFG 2014 / 5, 0309–0311
Stuttgart, October 2014

Editorial

# Special Issue on Geodata Processing at the Institute of Surveying, Remote Sensing and Land Information at BOKU in Vienna

The Institute of Surveying, Remote Sensing and Land Information (IVFL) is part of the Department of Landscape, Spatial and Infrastructure Sciences (RaLI) at the University of Natural Resources and Life Sciences (BOKU) in Vienna, Austria. The institute is mentioned first in 1875 and has nowadays about twenty scientific and technical staff.

IVFL is involved in a number of Bachelor and Master study programs at BOKU such as Forest Sciences, Landscape Architecture and Landscape Planning, Environment and Bio-Resources Management and Environmental Engineering. The main topics taught are in surveying, GIS, remote sensing and photogrammetry. Additional courses are provided in Land Administration.

The work published in this issue of PFG is intended to give a concise overview of our current research activities. These are centred on the acquisition, processing, analysis, interpretation and visualization of geodata. In Tab. 1, the ten papers presented in this special issue are categorized in terms of (main) instruments and scale of application, along with the main methodologies applied.

As demonstrated by the paper contributions presented in this special issue, we conduct research in a wide range of topics such as:

- Measurement of soil roughness
- Forest height and yield class estimation
- Mud structure mapping
- Forest vitality assessment
- Modelling of crop water requirements
- Detection of illicit crops
- Wide-area land cover mapping
- Land surface phenology characterization
- Optimization of spectroradiometric measurements
- Wildlife migration modelling

In the work of Grims et al. (2014), low-cost cameras are used in a field-setting for deriving soil surface roughness indicators using photogrammetric methods. We demonstrate the potential of this simple and low-cost method for assessing soil roughness, which itself is an important input to model soil erosion.

Photogrammetric methods are also used in the work of Windisch et al. (2014) where the potential of digital aerial images is analysed for deriving forest height and yield classes. Through comparison with airborne laser scanning techniques (ALS) we show that important information about the forest structure can be derived from this source of information.

Three-dimensional information is also derived in the work of Heine et al. (2014). In contrast to the previous work, however, we use acoustic instruments (sonar) mounted on boats and sounding the lake bed. In this way it is possible not only to measure water depth but also to characterize the lake's mud layer.

Immitzer & Atzberger (2014) use pattern recognition techniques such as random forest (RF) to detect bark beetle infestations in Norway spruce. We demonstrate that using 8-band very high resolution WorldView-2 imagery it is possible to detect infestations in an early stage of development, which has important implications for an efficient disease control.

Multi-temporal and multi-spectral images from medium-resolution (DEIMOS-1) satellites are used in Neugebauer & Vuolo (2014) to map bio-physical land surface characteristics such as leaf area index (LAI) and albedo. Together with local agrometeorological data, we use this information to infer crop water consumption for agriculture.

Using data with similar spatial resolution (Landsat-5 and ETM+) but acquired at a higher temporal frequency, Mattiuzzi et al. (2014) monitor and detect illicit crops (based on time series of vegetation greenness – NDVI). The study enables us to optimize the acquisition window for relatively expensive (commercial) very high resolution (VHR) satellites.


www.schweizerbart.de
DOI: 10.1127/1432-8364/2014/0225
1432-8364/14/0225 $ 0.75

**Tab. 1:** Coarse categorization of manuscripts presented in this issue and prepared by members of the Institute of Surveying, Remote Sensing and Land Information (IVFL) in Vienna, Austria.

| **Instrument** | **Spatial resolution** | **Wavelength range** | **Scale** | | | |
|---|---|---|---|---|---|---|
| | | | In situ | Sub-regional | Regional | Continental |
| Low-cost digital cameras | $mm^2$ | VIS | Photogrammetry (Grims et al.) | | | |
| Digital, aerial cameras | $cm^2$ | VIS-NIR | | Photogrammetry (Windisch et al. 2014) | | |
| Very high resolution satellites | $m^2$ | VIS-NIR | | Pattern recognition (Immitzer & Atzberger 2014) | | |
| Medium resolution satellites | ha | VIS-NIR-SWIR | | Pattern recognition (Neugebauer & Vuolo 2014) | Pattern recognition (Mattiuzzi et al. 2014) | |
| Coarse resolution satellites | $km^2$ | VIS-NIR | | | | Time series analysis (Vuolo & Atzberger 2014, Klisch & Atzberger 2014) |
| Spectro-radio-meter | $cm^2$ | VIS-NIR-SWIR | Spectro-radiometry (Einzmann et al. 2014) | | | |
| Sonar instruments | $m^2$ | Acoustic | | Acoustic echo sounding (Heine et al. 2014) | | |
| GIS | n.a. | n.a. | | | GIS modelling (Suppan & Frey-Roos 2014) | |

Again using time series analysis combined with pattern recognition techniques, Vuolo & Atzberger (2014) map major land cover classes across Europe at 250 m spatial resolution. We demonstrate that our land cover map outperforms (globally available) alternative products by using training data derived from Google Earth and NDVI time series from MODIS.

In Klisch & Atzberger (2014), MODIS-derived NDVI time series are used to map and monitor the start of season (SOS) across Europe. Through comparison with other published work and plausibility checks, we are able to demonstrate the feasibility and reliability of such an approach for mapping land surface phenology.

In the work of Einzmann et al. (2014), we assess different measurement protocols for using portable field spectrometers for collecting needle spectra in the field/laboratory. The collection of reference samples is for example necessary when using airborne imaging spectroscopy for mapping forest vitality.

GIS techniques are used in Suppan & Frey-Roos (2014) to model the movement of large mammals (deer). The necessary resistance maps are derived from remotely-sensed land use and land cover maps as well as expert knowledge regarding the animals' migration behaviour with respect to favourable and unfavourable conditions.

Together these ten technical and research papers provide an overview of our ongoing research activities. The reader will recognize the broad area of covered topics, as well as instrumentation and methodology. For the future, we strive to further integrate the different research topics and make better use of existing synergies between various sensors and approaches. Whenever possible, we try to integrate our research findings in teaching and education activities.

## References


Einzmann, K., Ng, W.T., Immitzer, M., Bachmann, M., Pinnel, N. & Atzberger, C., 2014: Method Analysis for Collecting and Processing in-situ hyperspectral Needle Reflectance Data for Monitoring Norway Spruce. – PFG – Photogrammetrie, Fernerkundung, Geoinformation **2014** (5): 423–434.

Grims, M., Atzberger, C., Bauer, T., Strauss, P. & Mansberger, R., 2014: Low-cost Terrestrial Photogrammetry as a Tool for a Sample-Based Assessment of Soil Roughness. – PFG – Photogrammetrie, Fernerkundung, Geoinformation **2014** (5): 313–323.

Heine, E., Kogelbauer, I., Prokoph, A. & Loiskandl, W., 2014: Hydrographic Surveying of the Steppe Lake Neusiedl – Mapping the Lake Bed Topography and the Mud Layer. – PFG – Photogrammetrie, Fernerkundung, Geoinformation **2014** (5): 339–350.

Immitzer, M. & Atzberger, C., 2014: Early Detection of Bark Beetle Infestation in Norway Spruce (Picea abies, L.) using WorldView-2 Data. – PFG – Photogrammetrie, Fernerkundung, Geoinformation **2014** (5): 351–367.

Klisch, A. & Atzberger, C., 2014: Evaluating Phenological Metrics derived from the MODIS Time Series over the European Continent. – PFG – Photogrammetrie, Fernerkundung, Geoinformation **2014** (5): 409–421.

Mattiuzzi, M., Bussink, C. & Bauer, T., 2014: Analysing Phenological Characteristics Extracted from Landsat NDVI Time Series to Identify Suitable Image Acquisition Dates for Cannabis in Afghanistan. – PFG – Photogrammetrie, Fernerkundung, Geoinformation **2014** (5): 383–392.

Neugebauer, N. & Vuolo, F., 2014: Crop Water Requirements on Regional Level using Remote Sensing Data – A Case Study in the Marchfeld Region. – PFG – Photogrammetrie, Fernerkundung, Geoinformation **2014** (5): 369–381.

Suppan, F. & Frey-Roos, F., 2014: Generating Resistance Surfaces for Wildlife Corridor Extraction. – PFG – Photogrammetrie, Fernerkundung, Geoinformation **2014** (5): 435–450.

Vuolo, F. & Atzberger, C., 2014: Improving Land Cover Maps in Areas of Disagreement of Existing Products using NDVI Time Series of MODIS - Example for Europe. – PFG – Photogrammetrie, Fernerkundung, Geoinformation **2014** (5): 393–407.

Windisch, K., Bronner, G., Mansberger, R. & Koukal, T., 2014: Derivation of Dominant Height and Yield Class of Forest Stands by Means of Airborne Remote Sensing Methods. – PFG – Photogrammetrie, Fernerkundung, Geoinformation **2014** (5): 325–338.


Clement Atzberger, Vienna, Austria

PFG 2014 / 5, 0313–0323
Stuttgart, October 2014

Article

# Low-cost Terrestrial Photogrammetry as a Tool for a Sample-Based Assessment of Soil Roughness

Michael Grims, Clement Atzberger, Thomas Bauer, Peter Strauss & Reinfried Mansberger, Wien/Petzenkirchen, Österreich

**Keywords:** soil roughness, digital surface model, low-cost photogrammetry, soil microtopography

**Summary:** In cooperation with soil experts, a simple and reliable photogrammetric system was developed to acquire three-dimensional data of soil surfaces in sample areas sized 1 m². The work and data flow incorporates the automatic derivation of several soil roughness parameters. The procedure is usable for the in situ quantitative assessment of changes of soil volumes across weather and site conditions. The time- and cost-effective approach is based on terrestrial photogrammetry and meets all performance and accuracy requirements formulated by soil scientists of the Austrian Federal Institute of Land and Water Management Research.

**Zusammenfassung:** *Preiswerte terrestrische Photogrammetrie als Werkzeug zur Bestimmung der Rauigkeit von Böden.* In Zusammenarbeit mit Bodenfachleuten wurde ein einfaches und zuverlässiges photogrammetrisches Verfahren zur dreidimensionalen Erfassung von Bodenoberflächen mit Hilfe von Probeflächen mit einer Größe von jeweils 1 m² entwickelt. Zusätzlich werden automatisiert geeignete Bodenrauigkeits-Parameter abgeleitet. Das wetter- und ortsunabhängige Verfahren ist auch zur quantitativen Erfassung von Bodenabträgen einsetzbar. Die zeit- und kosteneffektive Methode basiert auf Verfahren der terrestrischen Photogrammetrie und erfüllt alle von Forschern des Österreichischen Instituts für Kulturtechnik und Bodenwasserhaushalt formulierten Genauigkeits- und Performance-Anforderungen.

## 1 Introduction

Soil erosion is a serious problem in many parts of the world. It decreases the agricultural productivity of soils due to relocation of soil-material (Wegmann et al. 2001, Moritani et al. 2010). Furthermore, the transportation of material into rivers pollutes them with agricultural chemicals and leads to siltation. Therefore, it is a main goal of soil scientists to get knowledge on how to minimize soil erosion.

To investigate the erosion processes, researchers focus their activities by developing proper models. These models, like the revised universal soil loss equation (RUSLE) (Renard et al. 1997) enable the estimation of the amount and the location of soil erosion. Soil erosion models are based on parameters such as soil surface roughness indices, which are also important for other environmental applications (Marzahn et al. 2012).

A broad range of indices were defined for describing the roughness of soil surfaces, e.g. the roughness indices by Taconet & Ciarletti (2007), Planchon et al. (2002), Allmaras et al. (1966) or Linden & Van Doren (1986). Such indices are needed for the calculation of soil erosion with erosion models (Renard et al. 1997). To calculate those indices, three-dimensional data of the soil surfaces is needed. Additionally, the dynamic of soil surfaces (changes) has to be assessed. It is a big challenge for soil scientists to get significant information on all kinds of soils and their development due to the diversity of soils on local level


www.schweizerbart.de
DOI: 10.1127/1432-8364/2014/0226
1432-8364/14/0226 $ 2.75

(within fields) as well as on regional level (in different areas).

The Austrian Federal Institute of Land and Water Management Research (BAW) has a long tradition and expertise on soil erosion. Based on different datasets, a number of soil erosion models have been developed suitable for multiple spatial scales.

The main objective of this study was to develop and design a method for assessing 3D-data of soil surfaces. Moreover, from the acquired 3D-data, suitable soil roughness parameters were to be derived.

The presented photogrammetric method is a missing link for the characterization of the surface roughness variability (and its changes over time) at field and catchment scale. Necessary is a low-cost photogrammetric method with a high level of automation to enable the complete assessment of soil surfaces and soil roughness parameters in areas sized 1 m² within 15 minutes. In this way, soil characteristics over whole fields and/or whole regions can be assessed by applying the 3D-measurements following a suitable (statistical) sample design.

## 2 Background and Related Work

Many methods have been developed for the detailed assessment of (micro-)soil surfaces and soil roughness. They can be divided in methods of measurement which have contact to soil (roller chain, pin-meter) and in methods without touching the soil surface (photogrammetry, laser scanning).

The roller chain method, as described by Saleh (1993), is a simple, fast, and inexpensive technique for the quantification of soil roughness. A chain with a known length is placed on a soil. The horizontal distance covered by the chain is a measure for the level of roughness.

Jester & Klik (2005) used pins with a diameter of 1 mm and a spacing of 5 mm to each other. Those pins were mounted on an aluminium frame with the possibility to shift the pins down to the surface of the soil. The final position was registered. This method enabled the measurement of surface profiles of the soil.

According to Mirzaei et al. (2012), high spatial resolution (vertically between ± 0.1 mm and ± 0.5 mm and horizontally between ± 0.1 mm and ± 2.0 mm) can be achieved by laser scanning applications. Haubrock et al. (2009) achieved height accuracies within a grid of 1 mm with an average error of ± 0.19 mm, by mounting the scanning-device on a tripod at a distance of 1.5 m to 2.5 m to the assessed soil surface. However, laser scanner instruments are quite unhandy for in situ measurements and need considerable power supply. Furthermore, they are fragile (Mirzaei et al. 2012) and no laser scanners for the accuracy requirements are provided in the commercial low-price sector (Abd Elbasit et al. 2009).

The increasing performance and usability of digital photogrammetry were the main drivers for the renaissance of image-based methods for soil surface assessment.

Marzahn et al. (2012) describes a photogrammetric soil assessing procedure using a Canon EOS 5D camera in combination with a Canon EF 2/35 mm lens. The dimension of the test sites was 1 m x 2.5 m. Mirzaei et al. (2012) mounted two cameras on a frame to enable stereoscopic measurements in a distance from 1 m to 4 m to the soil surface. Aguilar et al. (2009) also worked with a system of two cameras. The photogrammetric software PhotoModeler Pro 5 was used for camera calibration and OrthoEngine V9.1 for DSM generation to assess an area of 1.2 m x 0.8 m. Gessesse et al. (2010) developed a photogrammetric method to acquire micro-topographic soil surface changes caused by erosion. They also investigated the sediment transport and rill erosion development in the inter-rill areas at storm scale. The method is based on a frame with a movable bar, where two cameras were mounted to assess test site areas with approximately 4 m x 15 m with vertical accuracies between ± 2.8 mm and ± 5.3 mm.

Schneeberger & Willneff (2003), finally, assessed the roughness of soils by using a solid frame as reference for photogrammetric measurements in a local system.

## 3 Methodology

### 3.1 *Objectives and Tasks*

The requirements defined by soil scientists of the Austrian Federal Institute of Land and Water Management Research are the following:

- test area of approximately 1 m$^2$,
- local Cartesian coordinate reference system with height coordinates (z) and plane coordinates (x and y) (the x/y-plane has to be levelled horizontally and the x-axis points to cultivation direction),
- acquisition of a digital soil surface model with a ground resolution less than 1 cm,
- sub-centimetre accuracy (± 3 mm – 5 mm in plane and height),
- time-effective data assessment and post processing,
- low costs,
- equipment easy to handle in the field (one person).

As part of the task, a workflow-integrated derivation of soil roughness indices should be developed with the input of the photogrammetrically assessed 3D point cloud. The BAW predefined the specific indices and the formulas for the calculation of the roughness parameters.

### 3.2 *Photogrammetry*

The proposed method needs a calibrated camera, i.e. with known interior orientation, and a reference frame, which has to be placed horizontally above a soil surface. For reaching good accuracy of the exterior orientation and for deriving a reliable digital surface model (DSM), photographs have to be taken in oblique and vertical directions. The requirements for this task are low costs for the whole system (camera, software, acquisition time) and a high level of automation.

#### Camera and interior orientation

To keep the costs low, consumer-level cameras were used instead of high-precision photogrammetric cameras. It is known, that DSM-generation with consumer-level cameras can achieve high accuracy (Marzahn et al. 2012).

The following consumer-level cameras covering different price segments and different qualities were investigated:

- Canon EOS 1100D
- Nikon Coolpix P5000
- Olympus SP-590UZ
- Panasonic Lumix DMC-FS10
- Sony SteadyShot DSC-W380

The above listed cameras are equipped with zoom and autofocus lenses and thus in principle not suited for the type of photogrammetric software that assumes a fixed focus. However, in view of the photoscale of 1:100 or larger and the comparatively low accuracy requirements the slightly changing focal length caused by the autofocus process had no significant influence on the quality of the results. On the other hand, sharp images were important for a reliable identification of the ring codes and sufficient dense point clouds.

The determination of the parameters of the interior orientation of the cameras (focal length, coordinates of principle point, and coefficients of distortion polygon) was performed with the software module 'Camera Calibration Project' of the PhotoModeler Scanner (PMS, EOS Systems Inc.). Photographs of a so called calibration grid (Fig. 1) were taken from four different view angles, each with three different camera rotations (in total 12 photographs).

The coded ring patterns generated as pdf-files by the PhotoModeler Scanner (software)

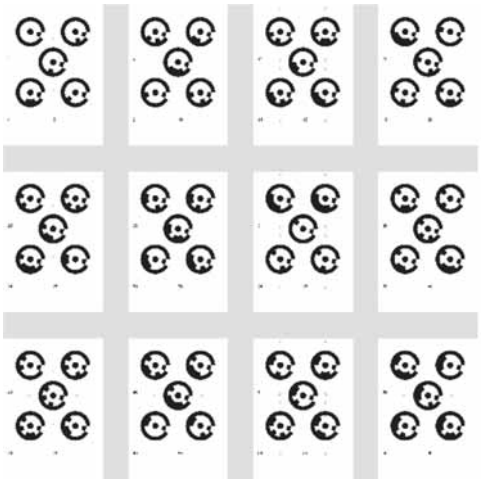

**Fig. 1:** Calibration grid used to determine the parameters of the interior orientation.

and printed enable an automatic computation of the parameters of the interior orientation. Additionally, the software calculates accuracy measures describing the quality of the camera geometry. The repetition of the interior orientation assessment allowed the estimation of the stability of the investigated cameras.

Regarding the photographic quality of the cameras, photographs from soil samples with different characteristics (roughness, wetness, composition) were visually assessed.

### Exterior orientation and reference frame

Control points are used for the calculation of the parameters of the exterior orientation, i.e. position and attitude of the projection centre in a superior coordinate system. The coordinate reference system of the exterior orientation is horizontal realized by a levelled frame.

To support the automated workflow, coded control point marks (RADs – ring automatically detected) are used. The RADs are mounted on a movable frame in a balanced distribution over the test soil area to guarantee accuracies as high as possible. Additionally the reference frame has to fulfil the following requirements:

- easy to transport,
- high stability,
- sufficient size in order to obtain DSMs of an area of 0.9 m x 0.9 m according to Taconet & Ciarletti (2007),
- vertically adjustable up to slopes of 30%,
- enabling an easy mounting of targets.

In an iterative process the frame was developed. The constructed reference frame has a format of 1 m x 1 m. The horizontal alignment is realized by three vertically adjustable piles and by two spirit levels mounted on the frame (Fig. 2).

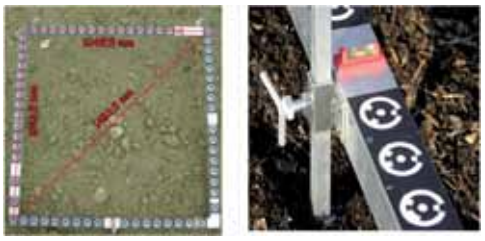

**Fig. 2:** Reference frame and levelling facility.

The material of the reference frame is aluminium and has a width of 5 cm. This dimension meets the requirements of being stable and to be handled by only one person. The width also has to be optimized to the size of the mounted control point targets (RADs). Control points have to be detected automatically and this requirement is dependent on the size and colour of the targets, on the quality of the camera, on the photogrammetric set-up, and on the weather conditions during the image acquisition. In a series of tests with various target characteristics (size and colour), with different cameras (Canon EOS 1100D and Nikon Coolpix P5000), and under different weather conditions (bright sky and cloudy), the minimal target size for automatic detection was determined. The size of 5 cm × 5 cm can be seen as a compromise between easy target-detection and handiness of the aluminium frame. Based on these findings further investigations with the developed reference frame were outlined to proof the accuracy of the exterior orientation for specific set-up configurations and for extreme weather conditions.

65 control points (targets) are mounted on the frame. The local coordinates of the control points were determined by conventional geodetic surveying with an achieved accuracy of ± 0.3 mm. As the frame is not perfectly right-angled and the targets are not placed exactly, the axis of the coordinate system fitting best to the frame were determined by adjustment methods.

### Photogrammetric set-up

Within this study, investigations were undertaken to optimize the (hand-held) camera positions for both, calculation of the exterior orientation and of the DSM generation, and for minimizing the total number of photographs for each test site and thus the costs. The position of the cameras has to be optimized to enable good geometry for the calculation of the exterior orientation as well as for the generation of the DSM. Photographs with near vertical view directions and high coverage facilitate better results of matching algorithms and thus better surface models. On the other hand, oblique view directions provide better accuracy of the exterior orientation.

Several photographs were taken for several test sites. By varying numbers of photographs and camera positions, the optimal assessment set-up was determined.

#### Generation of point cloud

The PhotoModeler Scanner software (PMS) generates automatically a point cloud of the surfaces. As the soil assessment system has to be simple as being used not only by photogrammetric experts and the soil conditions can vary within a broad spectrum, e.g. dry to wet, smooth to rough, coarse grained to fine grained, the point cloud extraction in the workflow is proposed to be done with predefined standard parameters, e.g. mean distance of surface grid: 1 mm, chosen pairs of photos have b/h-ratio between 0.1 and 0.6, coordinate reference system attached to targets in the same way for each DSM.

### 3.3 *Derivation of Soil Surface Parameters*

The PMS software provides an automatic workflow from photographs to point clouds by using RADs. In a post-processing process, a DSM based on the point cloud is calculated. Finally, the average inclinations (in the cultivation direction and rectangular to it), the maximal inclination, and the various roughness parameters of the soil surface are determined. All formulas for the calculation of the DSM were implemented in the software Matlab (MathWorks Inc.).

#### Grid generation

As a first step, a regular grid has to be calculated. The resolution of the point cloud (close to one point per one mm$^2$) enables the calculation of the regular grid with a grid size of 1 mm x 1 mm. The reference frame with a dimension of 1 m x 1 m enables the derivation of an area of 0.9 x 0.9 m$^2$ of the soil surface, which is suitable for soil roughness calculations (Taconet & Ciarletti 2007).

The quality assessment for the digital surface model was performed in two different ways:

- Firstly, the reliability of the method was assessed by analysing photogrammetric time series of the same soil sample.
- Secondly, an accuracy assessment of volume calculations was performed. Soil material with a known volume was deposited on one test site with a photogrammetrically assessed surface. The new surface was determined. The volume of the difference between the new model and the previous one was calculated and compared to the added soil mass.

#### Inclination

The average inclinations in the cultivation direction and rectangular to it, as well as the maximum inclinations have to be calculated. In a first step, the plane of best fit is calculated for the whole sample by the least-squares method. As the reference frame and its coordinate reference system are placed parallel to the cultivation directions, the adjusted plane provides the desired inclinations in cultivation direction and across.

The maximal inclination ($Inc_{max}$) is derived from the inclinations in x- ($Inc_x$) and y-direction ($Inc_y$) with (1):

$$Inc_{\max} = \sqrt{Inc_x^2 + Inc_y^2} \quad (1)$$

#### Roughness indices

The roughness indices calculated in the current study are listed in Tab. 1:

- Random roughness index (RRA) as described in Allmaras et al. (1966). In the calculation of RRA a log transformation is applied followed by a removal of the highest 10 % and lowest 10 % of the values. The height-values are smoothed as proposed in Helming (1992). The RRA is the standard deviation of these values.
- Random roughness (RR) index as described in Planchon et al. (2002).
- RC (roughness overall) index, the RCY (oriented roughness y-axis) and the RCX (oriented roughness x-axis) as described in Taconet & Ciarletti (2007) following Currence & Lovely (1970).

**Tab. 1:** Calculated roughness indices.

| Index abbreviation | Authors | Modification | Basics |
|---|---|---|---|
| RRA | Allmaras et al. 1966 | Helming 1992a | standard deviation |
| RR | Planchon et al. 2002 | | standard deviation |
| RC, RCY, RCX | Currence & Lovely 1970 | Taconet & Cialetti 2007 | standard deviation |
| LD, LS | Linden & Van Doren 1986 | | spatial variance analysis |
| TB | Helming et al. 1992b | | total surface area to map area |

- Indices based on spatial variability. LD and LS are indices described in Linden & Van Doren (1986).
- The tortuosity-index (TB) is defined as the ratio of the total surface area to the map area (Helming et al. 1992).

The calculation of all above outlined indices was implemented in Matlab software with the input of the DSM. The full data flow from the PhotoModeler Scanner to Matlab is realized.

### 3.4 *Case Study Application*

Tests of the handling of the photogrammetric method and of the roughness parameter calculations were executed on three different field sites. Field management was done on one field with a cultivator and on two fields with different types of mouldboard ploughs. To calculate mean absolute roughness values per field, replicate measurements were performed on several sample sites (10 replicates for each type of cultivator and 19 replicates for mouldboard plough). In addition, soil texture and organic carbon content were analysed on the field sites.

## 4 Results and Discussion

### 4.1 *Selection of a Proper Camera*

Five consumer-level cameras were investigated on their fitness for the outlined task. The applicability of a camera for photogrammetric measurements is given by the pixel resolution, by the geometric accuracy, and by the radiometric quality.

The quality of the camera geometry was evaluated using the calibration results for determining the interior orientation of the PhotoModeler Scanner. In Tab. 2 the 'Total Error' as well as 'Point Marking Residuals' of five tested cameras are listed.

Repetitions of the camera calibration were performed to verify the stability of the cam-

**Tab. 2:** Results of camera calibration (PhotoModeler Scanner) based on calibration set-up with 12 photographs and 60 reference points per photograph.

| Camera | Image format (MPixel) | Total image unit-weight RMSE | Point marking residuals overall RMSE (in pixels) |
|---|---|---|---|
| Canon EOS 1100D | 12.2 | 2.91 | ± 0.35 |
| Nikon Coolpix P5000 | 10.0 | 2.29 | ± 0.28 |
| Olympus SP-590UZ | 11.1 | 14.98 | ± 1.76 |
| Panasonic Lumix DMC-FS10 | 12.0 | 3.12 | ± 0.39 |
| Sony SteadyShot DSC-W380 | 14.0 | 24.11 | ± 3.08 |

eras. As the dimension of the errors is similar to the results outlined in (Tab. 2), all examined cameras can be assumed to be stable.

Based on the calibration results it was decided to continue the investigations with the Nikon Coolpix P5000 and Canon EOS 1100D cameras. These two cameras yield the lowest total error and overall point marking residuals. The total error with below ± 3 pixels as well as the RMSE of the calibration points with less than ± 0.5 pixels is acceptable for zoom and autofocus lenses.

After the camera calibrations, the photographic (radiometric) quality of the two selected cameras was judged visually and by interpreting the results of repeated photogrammetric measurements for different soil conditions and weather conditions (see Fig. 3). The investigations gave satisfactory results independent of the soil characteristics and weather.

## 4.2 *Configuration of Camera Stations*

To minimize the number of photographs and to optimize the positions of the camera stations several tests were run by varying numbers and configurations of camera stations with a maximum of 12 photographs (8 near-vertical, 4 oblique) as a reference. Fig. 4 outlines the results. The DSM with a grid size of 1 mm derived from all images served as a reference. Good results were obtained using 4 near-vertical and 4 oblique photos. Using this configuration the error was only ± 1.4 mm and hence almost as good as using six near-vertical and 4 oblique directions.

For the practical work a photogrammetric set-up with in total eight photographs was recommended. Four photographs have to be taken in near vertical direction (low angle) with


**Fig. 3:** Soil samples used for analysing the photographic quality.

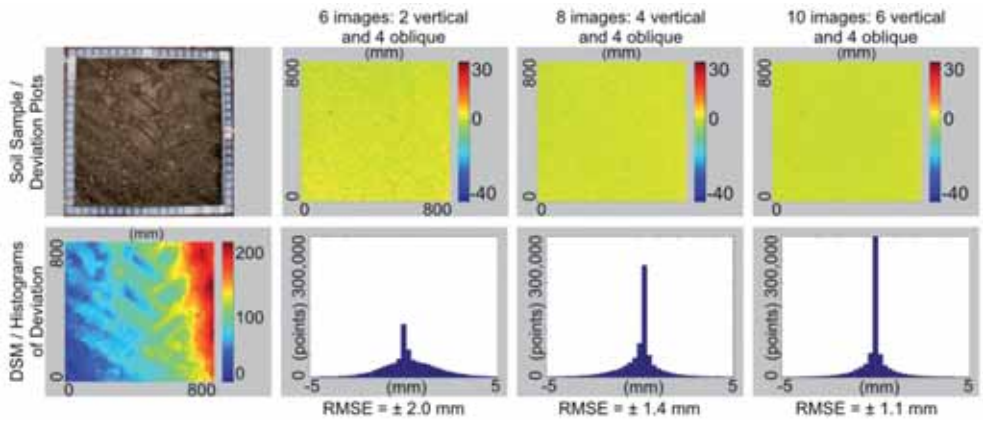


**Fig. 4:** Accuracies of different configurations of photo stations (same sample plot).

a high overlap (base-to-height ratio between 0.1 and 0.6). These images are important for the point cloud generation. Due to constraints of the PhotoModeler Scanner (PMS) software, only images with near vertical view can be successfully analyzed. The other four photographs have to be taken in oblique direction (angle of approximately 60 degrees to the soil plane and approximately 90 degrees between principal axes) to enable a reliable calculation of exterior orientation parameters.

The outlined RMSE of the exterior orientation lies between ± 0.5 and ± 2.0 pixels (Canon EOS 1100D, 17.8 mm focal length, 5.3 µm pixel size). Assuming an average photo distance from the camera to the frame position of 2 m this measures are equivalent to ± 0.35 mm and ± 1.4 mm in the local coordinate reference system.

## 4.3 *Accuracy Assessment of DSM*

### Comparing DSMs

For seven soil types photogrammetric measurements were performed. For each of the test sites eight photographs (4 near-vertical, 4 oblique) were taken handheld. The measurements were repeated for each test site with similar – albeit not identical – camera stations and with the same position of the reference frame.

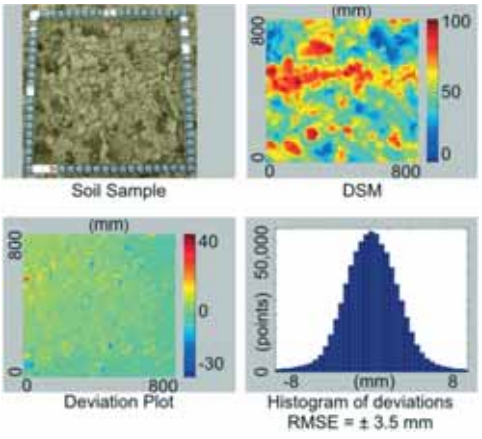


**Fig. 5:** Results of DSM Analysis of a soil with a high roughness.

The orientation and the generation of point clouds were calculated separately for each of the measurements (7 sites, two set-ups per site) using the PMS software. A Matlab script was used to interpolate a regular grid of all soil surfaces with a grid size of 1 mm x 1 mm based on the generated point cloud. Deviations between the DSMs generated from the same test site were calculated and analysed. Fig. 5 shows the results of one soil sample.

Generally, the investigations pointed out RMSE between ± 2 mm and ± 4 mm between the corresponding surface models. The analysis of the results made obvious, that the biggest errors occur increasingly in soil surfaces with a high roughness and that they are mainly caused by interpolation effects close to sharp edges and steep areas.

### Volume determination

One application of the method is to measure the change of volume of a soil during an erosion event such as heavy rainfall. In an experiment, various soil materials (quartz sand) of known volume were added to a soil several times and each time the difference of volume was assessed using the proposed photogrammetric method. This allowed comparing the photogrammetrically measured volume changes against the added volumes.

Seven DSMs with four different volumes were analysed with cross correlation methods. The resulting differences have a mean of 0.4 $dm^3$, a standard deviation of ± 0.3 $dm^3$ and a confidence interval ($\alpha = 0.05$) of 0.1 $dm^3$.

In a second experiment, volumes were removed. Again, the true value – determined by a vessel with a scale – was compared with the one measured photogrammetrically. The results of ten comparisons were surprisingly similar to the one of the first experiment with a mean of 0.4 $dm^3$ and a standard deviation of ± 0.3 $dm^3$.

## 4.4 *Field Observations (Case Study)*

Mean values and standard deviations of various roughness indices (RRA, RR, RC, LD, LS, and TB) for three different field sites are reported in Tab. 3. Additional information

about soil conditions and tillage tools for each site is given.

For our test sites, ploughing results in rough and heterogeneous surface conditions were assessed, whereas the use of a cultivator leads to smoother and more homogenous surfaces. During cultivation soil is broken into small and uniform aggregates whereas ploughing turns the soil and results in heterogeneous furrow slices. This is well reflected by all tested roughness indices (Tab. 3). Given the limited number of test sites and the lack of an absolute reference, it was not possible to rank the usefulness of the tested roughness indices. In addition, not all indices are being accepted as relevant for purposes of soil roughness or soil erosion research (Currence & Lovely 1970, Helming 1992, Taconet & Ciarletti 2007).

## 5 Summary and Conclusions

A method was developed to obtain digital surface models (DSM) and roughness indices from soil surfaces easily, cheaply, quickly and with sufficient accuracy. The proposed method has several characteristics making it appealing for further development:

- The method can be applied easily in the field as only limited equipment is necessary not requiring any sophisticated power supply.
- The use of consumer-level cameras makes the method affordable.
- Merely 15 minutes are necessary in order to get the raw data for about 1 m² of soil surface.
- The height accuracy of the soil surface is better than ± 3 mm.
- The processing of the raw data from the PhotoModeler Scanner (PMS) software could be realised quickly and in an uncomplicated way, using scripts from Matlab.

Several other authors, such as Marzahn et al. (2012) or Mirzaei et al. (2012) already worked with similar methods for soil surface assessment. The method developed in this study combines several aspects, resulting in a new approach:

- Only one camera is used, which makes the method cheaper while keeping a sufficient accuracy.
- Only one photogrammetric software program is used for the whole photogrammetric workflow (PhotoModeler Scanner), which also makes the method cheaper and furthermore saves time to convert and transfer the data from the calibration into another program.

**Tab. 3:** Field site description (texture, humus content and tillage tool), received roughness values and standard deviations for various roughness parameters (RRA, RR, RC, LD, LS, TB).

| | Site | Cultivator | Fine mouldboard plough | Rough mouldboard plough |
|---|---|---|---|---|
| soil and management | management tool | Regent – Tukan FSC | Kuhn – MultiMaster | Vogel&Noot – XM |
| | (number of samples) | 10 | 19 | 19 |
| | sand (%) | 48.2 | 16.4 | 7.0 |
| | silt (%) | 35.9 | 64.0 | 62.5 |
| | clay (%) | 15.9 | 19.6 | 30.5 |
| | humus (%) | 2.3 | 1.7 | 1.9 |
| roughness indices | RRA (mm) | 7±2 | 15±3 | 20±6 |
| | RR (mm) | 11±2 | 35±5 | 40±9 |
| | RC (mm) | 20±5 | 42±5 | 50±11 |
| | LD (mm) | 17±3 | 37±3 | 41±6 |
| | LS (mm) | 1.1±0.5 | 1.8±0.4 | 1.9±0.4 |
| | TB (%) | 1.5±0.5 | 3.8±0.8 | 2.6±0.5 |

- The reference frame is vertically adjustable which allows an easy application of a coordinate system with a horizontally aligned x/y-plane.
- Taking the photos hand-held instead of using a fixed system makes the method faster and much more applicable in the field. Obviously, a fixed system has the advantage of eliminating the risk of blurred images. However, the tests did not reveal this aspect as a problem.

## Acknowledgements

The authors would like to express their thanks to the useful contributions of the reviewers, which helped to improve the manuscript relevantly.

## References

Abd Elbasit, M.A.M., Anyoji, H., Yasuda, H. & Yamamoto, S., 2009: Potential of low cost close-range photogrammetry system in soil microtopography quantification. – Hydrological Processes **23** (10): 1408–1417.

Aguilar, M.A., Aguilar, F.J. & Negreiros, J., 2009: Off-the-shelf laser scanning and close-range digital photogrammetry for measuring agricultural soils microrelief. – Biosystems Engineering **103** (4): 504–517.

Allmaras, R.R., Burwell, R.E., Larson, W.E., Holt, R.F. & Nelson, W.W., 1966: Total porosity and random roughness of the interrow zone as influenced by tillage. – Conservation research report **7:** 22 p., U.S. Department of Agriculture (USDA), Agricultural Research Service, Washington DC, USA.

Currence, H.D. & Lovely, W.G., 1970: The analysis of soil surface roughness. – Transactions of the ASABE **13** (6): 710–714.

Eos Systems Inc: Photomodeler Scanner, Version 2012.0.0.586. – http://www.photomodeler.com/index.html (5.7.2014).

Gessesse, G.D., Fuchs, H., Mansberger, R., Klik, A. & Rieke-Zapp, D.H., 2010: Assessment of erosion, deposition and rill development on irregular soil surfaces using close range digital photogrammetry. – The Photogrammetric Record **25** (131): 299–318.

Haubrock, S.-N., Kuhnert, M., Chabrillat, S., Güntner, A. & Kaufmann, H., 2009: Spatiotemporal variations of soil surface roughness from in-situ laser scanning. – Catena **79** (2): 128–139.

Helming, K., 1992: Die Bedeutung des Mikroreliefs für die Regentropfenerosion. – Bork, H.-R., Alaily, M.R.F., Roth, C. & Wessolek, G. (eds.): Bodenökologie und Bodengenese (7), Berlin, p. 153.

Helming, K., Jeschke, W. & Storl, J., 1992: Surface Reconstruction and Change Detection For Agricultural Purposes By Close Range Photogrammetry. – Fritz, W.L. & Lucas, J.R. (eds.): 17th ISPRS congress, International archives for photogrammetry and remote sensing **29** (B5): 610–617, Washington DC, USA.

Jester, W. & Klik, A., 2005: Soil surface roughness measurement – methods, applicability, and surface representation. – Catena **64** (2–3): 174–192.

Linden, D.R. & Van Doren, D.M., 1986: Parameters for characterizing tillage-induced soil surface roughness. – Soil Science Society of America **50** (6): 1560–1565.

Marzahn, P., Rieke-Zapp, D.H. & Ludwig, R., 2012: Assessment of soil surface roughness statistics for microwave remote sensing applications using a simple photogrammetric acquisition system. – ISPRS Journal of Photogrammetry and Remote Sensing **72:** 80–89.

Mirzaei, M.R., Ruy, S., Ziarati, T. & Salehi, A., 2012: Monitoring of soilroughness caused by rainfall using stereo-photogrammetry. – International Research Journal of Applied and Basic Sciences **3** (2): 322–338.

Moritani, S., Yamamoto, T., Andry, H., Inoue, M. & Kaneuchi, T., 2010: Using digital photogrammetry to monitor soil erosion under conditions of simulated rainfall and wind. – Australian Journal of Soil Research **48** (1): 36–42.

Planchon, O., Esteves, M., Silvera, N. & Lapetite, J.-M., 2002: Microrelief induced by tillage: measurement and modelling of Surface Storage Capacity. – Catena **46** (2–3): 141–157.

Renard, K.G., Foster, G.R., Weesies, G.A., McCool, D.K. & Yoder, D.C., 1997: Predicting soil erosion by water. A guide to conservation planning with the revised universal soil loss equation (RUSLE). – Agriculture handbook 703, Washington DC, USA.

Saleh, A., 1993: Soil roughness measurement: chain method. – Journal of Soil and Water Conservation **48** (6): 527–529.

Schneeberger, K. & Willneff, J., 2003: Digital surface models for the estimation of hydraulic properties of soils. – El-Hakim, S.F., Gruen, A. & Walton, J.S. (eds.): Videometrics VII. – IS&T and SPIE **2003:** 209–216, Santa Clara, CA, USA.

Taconet, O. & Ciarletti, V., 2007: Estimating soil roughness indices on a ridge-and-furrow surface

using stereo photogrammetry. – Soil and Tillage Research **93** (1): 64–76.

Wegmann, H., Rieke-Zapp, D.H. & Santel, F., 2001: Digitale Nahbereichsphotogrammetrie zur Erstellung von Oberflächenmodellen für Bodenerosionsversuche. – Deutsche Gesellschaft für Photogrammetrie, Fernerkundung und Geoinformation (DGPF), Tagungsband **9:** 165–173.

Addresses of the Authors:

Dipl.-Ing. Michael Grims, Univ. Prof. Dr. Clement Atzberger & Dipl.-Ing. Dr. Reinfried Mansberger, University of Natural Resources and Life Sciences, Vienna (BOKU), Institute of Surveying, Remote Sensing and Land Information, Peter-Jordan-Straße 82, A-1190 Vienna, e-mail: michael.grims@gmx.at, {clement.atzberger} {reinfried.mansberger}@boku.ac.at

Dipl.-Ing. Dr. Peter Strauss & Mag. Thomas Bauer, Austrian Federal Agency of Water Management, Institute for Land and Water Management Research, Pollnbergstraße 1, A-3252 Petzenkirchen, Austria. e-mail: {peter.strauss}{thomas.bauer}@baw.at

Manuskript eingereicht: März 2014
Angenommen: Juni 2014

PFG 2014 / 5, 0325–0338
Stuttgart, October 2014

Article

# Derivation of Dominant Height and Yield Class of Forest Stands by Means of Airborne Remote Sensing Methods

Katrin Windisch, Günther Bronner, Reinfried Mansberger & Tatjana Koukal, Vienna, Austria

**Keywords:** digital photogrammetry, image matching, digital surface model, canopy height model, forestry

**Summary:** In forest management and planning there is a permanent need of up-to-date information on forest areas. Digital photogrammetry and airborne laser scanning (ALS) can provide 3-D information on the forest canopy over large areas. In particular, canopy height models (CHM) derived by subtracting the digital terrain model (DTM) from the digital surface model (DSM) provide promising possibilities to determine forest attributes, including tree/stand height and timber volume. In the current study, an ALS-based and a photogrammetric CHM (normalized using an ALS-DTM) were used to estimate forest growth between 2006 and 2011. It was investigated if the CHM can be used to derive dominant height and to estimate the yield power in terms of the yield class of a forest stand. Two approaches were tested. The first approach relies on the conventional input that is also used in the field, i.e. dominant height and stand age, with the tree height obtained from remote sensing data and the age of the stand by field measurement. In the second approach, the yield class was derived from dominant height and height growth, both obtained from remote sensing data. While with the first approach satisfying results could be achieved, the second approach was not successful. Yield class estimation is very sensitive to the input variable height growth, which could not be derived with sufficient accuracy from the CHMs used in the study. It is expected that in the future the estimation of yield class will be more accurate due to longer observation periods, e.g. 10 years, and due to the availability of CHM time series with more than two points in time.

**Zusammenfassung:** *Ermittlung der Oberhöhe und der Ertragsklasse von Waldstandorten mit Hilfe flugzeuggestützter Fernerkundungsmethoden.* Für die Bewirtschaftung forstlicher Ressourcen und eine vorausschauende Planung werden regelmäßig aktuelle Informationen über die zu bewirtschaftenden Flächen benötigt. Die digitale Photogrammetrie und Airborne Laserscanning (ALS) können räumliche Informationen über ausgedehnte Waldflächen liefern. Insbesondere bieten Kronenhöhen-Modelle (CHM) – berechnet aus der Differenz zwischen Oberflächen- (DSM) und Geländemodell (DTM) – vielversprechende Möglichkeiten zur Herleitung forstlicher Größen, wie z.B. Baum- oder Bestandeshöhe und Holzvorrat. In der vorliegenden Studie wurde ein ALS-basiertes und ein photogrammetrisch erzeugtes Kronenhöhenmodell (normalisiert mit einem ALS-basierten DTM) verwendet, um das Baumwachstum im Zeitraum 2006 bis 2011 zu ermitteln. Es wurde getestet, ob mit Hilfe des CHMs die Bestandesoberhöhe und die Ertragsleistung von Beständen in Form der Ertragsklasse ermittelt werden können. Dazu wurden zwei verschiedene Ansätze getestet. Im ersten Ansatz wurden die herkömmlichen Eingangsgrößen, wie sie auch bei der terrestrischen Aufnahme verwendet werden, herangezogen, nämlich Oberhöhe (fernerkundlich bestimmt) und Alter des Bestands (durch Stammbohrung bestimmt). Bei der zweiten rein fernerkundungsbasierten Methode wurde die Ertragsklasse aus Oberhöhe und Höhenzuwachs ermittelt. Während mit der ersten Methode zufriedenstellende Ergebnisse erzielt werden konnten, erwies sich die zweite Methode als nicht geeignet. Die Ermittlung der Ertragsklasse reagiert sehr sensitiv auf die Eingangsgröße Höhenzuwachs, welche aus den in der Studie verwendeten CHMs nur mit unzureichender Genauigkeit abgeleitet werden konnte. Es ist zu erwarten, dass künftig durch längere Beobachtungszeiträume, z.B. 10 Jahre, und bei Verwendung von Zeitreihen mit mehr als zwei Zeitpunkten eine Schätzung der Ertragsklasse mit höherer Genauigkeit möglich sein wird.


www.schweizerbart.de
DOI: 10.1127/1432-8364/2014/0227
1432-8364/14/0227 $ 3.50

## 1 Introduction

Forest management and forest planning require constantly updated information of forest areas. As the collection of data in the field for large areas is time-consuming and costly, methods of remote sensing have a long tradition in providing forest enterprises with relevant data (Gillis & Leckie 1996). During the last decades, new remote sensing sensors were developed with improved geometric, spectral, radiometric and temporal resolution. These new technologies, such as airborne laser scanning (ALS), digital airborne imaging, and high-resolution satellite-borne imaging, enable in combination with advanced software for data processing improved results in terms of thematic accuracy and level of detail.

Actual volume of growing stock and annual yield are the key figures in forest management. While the actual growing stock is important for short- and mid-term planning, annual yield figures are required for long-term strategies, like the determination of the sustainable annual cut rates. In central Europe, yield tables are usually used for this purpose. Yield tables show the expected increase of timber volume in even-aged stands, where a yield class figure and the age of the stand serve as input parameters. As output parameters, yield tables provide tree height, number of stems, basal area, standing volume per unit area, and the diameter at breast height (DBH) (Marschall 1992, Skovsgaard & Vanclay 2008). In reverse, the yield class (describing productivity) can be derived from the stand age and the height of dominant trees. The required input is usually collected in periodic field inventories. However, the measurement of tree height in the field is not very accurate. Errors of the order of up to ± 2 m are quite common (Jablko & Perlwitz 1997) due to the limited visibility of tree tops in dense forest stands. The stand age is usually determined by drilling the stems, which is very time-consuming.

In recent years, the possibility to obtain continuous 3-D information in space and time on the forest canopy has become more and more important for forest applications. In particular, canopy height models (CHM) derived by subtracting the digital terrain model (DTM) from the digital surface model (DSM) provide promising possibilities to determine forest attributes, including tree height and volume of growing stock. In addition, time series of CHMs allow monitoring changes of the forest canopy, i.e. height growth and loss of trees by harvesting and natural disturbances, over large areas. The DTM, particularly in forested areas, is usually obtained from airborne laser scanning (ALS) data. The DSM can be derived either from ALS data or from point clouds generated from aerial images by using matching algorithms.

Recently, the image-based approach has attracted increasing interest for several reasons. The availability of up-to-date digital airborne imagery is usually better than of ALS data, because in many countries there is a periodical nationwide update. At present, the costs of airborne imagery are significantly lower than the costs of ALS data. In addition, digital airborne imagery provides not only geometric but also spectral information, which, in contrast to ALS data, allow the derivation of additional forest information, such as information on tree species and the state of health.

The extraction of 3-D information from airborne imagery has been substantially pushed by the emergence of digital aerial cameras that are able to acquire images with higher overlaps than analogue cameras. This improvement reduces the problem of occlusions in general (Leberl et al. 2010) and makes it easier to capture gaps in the forest canopy. Furthermore, computing capacity is continuously increasing, paving the way for CPU-intensive image matching algorithms. As a consequence, existing algorithms are constantly improving and new algorithms have been developed as well as implemented in standard photogrammetry software.

### 1.1 *Objectives*

The goal of the current study is to assess the usability of canopy height models (CHMs) derived by photogrammetry and ALS to determine

- stand height,
- height growth, and
- yield class

of individual forest stands.

The yield class, i.e. the productive capacity, of a forest stand is usually determined in the field based on dominant height and stand age. In this study two alternative approaches for the determination of yield class are tested:

- The first approach relies on the conventional input, i.e. dominant height and stand age, with the tree height obtained from remote sensing data (hybrid field-/remote sensing based approach).
- In the second approach, the yield class is derived from dominant height and height growth, both obtained from remote sensing data (approach purely based on remote sensing). For this approach, the conventional yield tables used in Austria (Marschall 1992) were adapted. Usually the height growth can be estimated for a known yield class using yield tables. In the current study the height growth served as an input to determine the yield class.

The following steps were carried out:

- Generation of digital surface models (DSM) using three different photogrammetric software products.
- Calculation of canopy height models (CHM) based on the photogrammetrically generated DSMs and the ALS-derived DTM.
- Quality assessment of DSMs and CHMs.
- Spatial adjustment of field data and remote sensing data.
- Derivation of yield class using the approaches mentioned above.

## 1.2 *Related Work*

Digital surface models are widely used to model the forest canopy. Studies that compared DSMs derived by image matching with ALS-derived DSMs have demonstrated the potential of image matching techniques for modelling the surface of forest canopies (Baltsavias et al. 2008, Straub & Seitz 2011). However, some characteristic differences between ALS-based and image-based DSMs were found, such as discrepancies at edges of forest and forest stands as well as in inhomogenous stands (Schardt et al. 2004). White et al. (2013) provide a detailed review on the key properties of image-based point clouds in comparison with ALS in forested areas. Hobi & Ginzler (2012) examined DSMs obtained from aerial images and from satellite images. For reference, terrain control points, stereoscopic measurements and ALS-data were used. For forest, that was the most challenging land cover type for surface modelling, they report a median deviation from stereo measurements of -1.1 m (ADS 80) and -1.9 m (WorldView-2).

DSMs normalized by a DTM (usually obtained from ALS data) are widely used for estimating forest attributes, like mean tree height, dominant height, mean diameter, stem number, and growing stock. Compared to the number of ALS-based studies (e.g. Hyyppä et al. 2008, Hollaus et al. 2009, Straub et al. 2010), there are only few studies that investigated the use of image-based DSMs for this purpose so far. Bohlin et al. (2012), for example, used image-based point cloud data to estimate height, stem volume, and basal area by multiple linear regression with percentiles, canopy density measures and texture measures as independent variables. They achieved satisfying accuracies and conclude that photogrammetric matching of digital aerial images has significant potential for operational use in forestry. Straub et al. (2013) combined height information and spectral data, both obtained from stereo images, to estimate timber volume and basal area at the plot level in a mixed forest in Germany.

Some studies directly compared ALS-based and image-based CHMs for estimating forest attributes. However, it is difficult to draw general conclusions from them because the capability to extract forest attributes is dependent on numerous technical parameters, such as point density, flight altitude, image overlap, as well as on properties of the forest canopy itself, such as vertical and horizontal structure, tree species. Järnstedt et al. (2012), for example, found out that the results achieved with the ALS-based features data were more accurate than with the features based on the photogrammetric data. The stand dominant height was the variable that could be estimated most accurately and showed the smallest difference between the ALS and photogrammetric CHMs. Nurminen et al. (2013) also evaluated the feasibility of image matching and ALS for

forest variable estimation. They conclude that both methods provide similar performance.

Studies that adress the mapping of the productivity of forests by means of CHM time series are very rare. To the authors' knowledge there is only the study by Véga & St-Onge (2009) that deals with this subject. They tested if the site index (corresponding to the yield class used in Europe) and the age of jack pine stands can be mapped based on known age-height curves and height data extracted from time series of historical image- and ALS-based CHMs over a period of 58 years. They conclude that their method can be used to produce quasi-continuous maps of site index and age as well as to estimate productivity in a spatially explicit way.

## 2 Material and Methods

### 2.1 *Test Site*

The test site is located in the north-western part of Lower Austria (15°00' East, 49°00' North), close to the town of Litschau and to the border with Czech Republic (Fig. 1). The forest area with an extension of 4000 ha is part of the forest enterprise Seilern-Aspang.

The altitude of the area is about 500 m above sea level with an average rainfall per year of approximately 700 mm (average of the years 1961 to 1990) and a mean temperature of 7° Celsius (ZAMG 2013). The area is located in the forest growth area 9.2 (Kilian et al. 1994), the so-called Waldviertel, which is characterized by a rawer climate and a shorter growing season compared to areas of similar altitude. According to the forest inventory of 2011/12, the main tree species are spruce (*Picea abies*) with 69%, pine (*Pinus sylvestris*) with 21%, beech (*Fagus sylvatica*) with 4%, and larch (*Larix decidua*) with 1.7% of the area.

### 2.2 *Datasets*

#### 2.2.1 Permanent sample plots

In the study area, 23 permanent sample plots were installed by the Institute of Forest Growth (WAFO) at the University of Natural Ressources and Life Sciences (BOKU Wien) in 1977. The size of the sample plots, mainly in spruce-pine mixed forest, varies between 400 $m^2$ and 2000 $m^2$. On these plots, the tree species, the tree height, and the diameter at breast height (1.3 m) of all trees are assessed and documented every five years. The most recent inventory was carried out in 2012. The rough coordinates of the corner of each sample plot are known in the Austrian national grid. The location of each registered tree was measured relatively to the plot corner. In total, 13 permanent sample plots are located in the area, where also the DSMs were available (see section 2.3.1). These sample plots were considered in the current study.

#### 2.2.2 Non-permanent sample-based inventory

In the study area, a non-permanent sample-based inventory was carried out between 2011

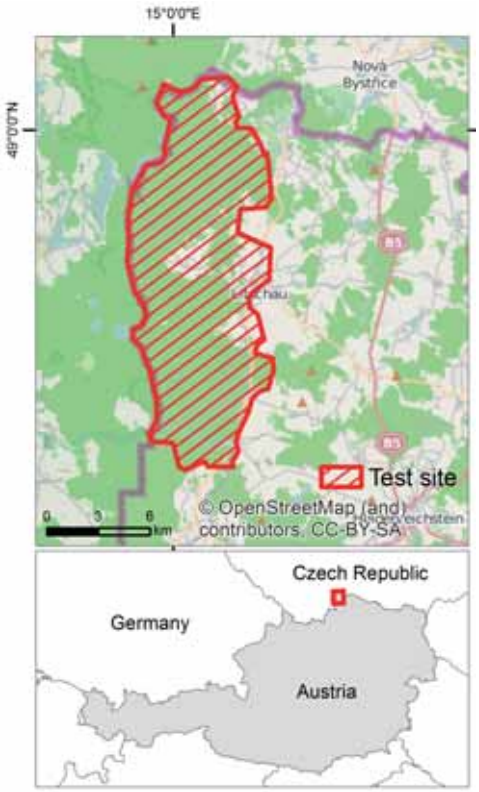


**Fig. 1:** Location of the test site in Austria.

and 2012. In total 759 sample plots were assessed (435 in 2011 and 324 in 2012) by means of the so-called angle-count-sampling (Bitterlich method; Winkelzählprobe), which is a common method for determining the basal area per ha at a height of 1.3 m above ground (Bestandesgrundfläche) and timber volume of a forest stand. The centre of each sample plot was measured using GNSS methods. For each sampled tree, several attributes were assessed, such as tree species, tree height, diameter at breast height, age, ten-years increment of the diameter. For the study, 63 sample plots were selected fulfilling the following criteria: homogenous stands; pole stage, timber stage or old growth; no harvesting since 2006; inventory carried out in 2012 corresponding to the acquisition year of the permanent sample plots.

#### 2.2.3 Airborne laser scanning data (ALS)

In 2006, airborne laser scanning data were acquired. The original ALS point density was about four points per $m^2$. For the current study, the EVN GeoInfo GmbH delivered a digital terrain model (DTM) and a digital surface model (DSM) with an interpolated grid of 1 m x 1 m. Based on these datasets, a normalized DSM (nDSM) corresponding to the canopy height model (CHM) in forest areas was derived.

#### 2.2.4 Digital aerial photos and orthophotos

On August 26th, 2011, the study area was covered by a photo flight with a forward lap of 70% and a side lap of 40%. The images were taken with a Vexcel UltraCam-Xp (image format: 11310 x 17310 pixels, physical pixel size: 6 µm, focal length: 100.5 mm, average ground resolution: 0.25 m). In total, the Austrian Federal Office of Surveying and Metrology (BEV) provided 146 digital images (four spectral bands, i.e. blue, green, red, and near infrared), orientation data as well as orthophotos with a ground resolution of 0.25 m.

### 2.3 *Methods*

#### 2.3.1 Generation of digital surface models (DSM)

Digital surface models were produced using the aerial images of 2011 and the exterior orientation parameters provided by the Austrian Federal Office of Surveying and Metrology. Three software products were tested:

- ERDAS LPS (Intergraph 2013): The authors prepared DSMs (LPS-DSM) with a grid size of 0.2 m for selected areas (in total 1000 ha) with LPS-eATE software (enhanced automatic terrain extraction).
- INPHO MatchT (Trimble 2014): The Austrian Federal Research and Training Centre for Forests, Natural Hazards and Landscape (BFW) generated a DSM (MatchT-DSM) with a grid size of 0.5 m for the entire study area.
- RSG Remote Sensing Software Package Graz (Joanneum Research Digital 2014): For approximately 1000 ha of the study area, a DSM with a grid size of 0.2 m was generated by Joanneum Research Graz using in-house software (RSG DSM).

The software-specific parameters for the DSM generation were optimized for forest surfaces. All datasets were produced with dense pixel-level resolution.

*Comparison of DSMs*

The original DSMs (LPS-DSM, MatchT-DSM, RSG-DSM) were converted to a common raster grid with a grid size of 0.5 m. Differences between the DSMs (including the ALS-DSM) were calculated pixel by pixel.

*Comparison of DSM-based profiles*

On selected sites, profiles were taken to examine the capability of the matching software to reproduce important features such as forest roads and gaps and to analyse the level of detail for stands of different age. Additionally, objects were considered that have definitively not changed within the five-year observation period such as buildings, roads or other open area objects. The profiles were compared qualitatively (visually) and quantitatively.

### 2.3.2 Generation of canopy height models (CHM)

The canopy height models were produced by calculating the difference between each DSM and the ALS-DTM. It can be assumed that in the test area the terrain did not change between the ALS-flight (2006) and the photo flight (2011). Therefore, the ALS-DTM could be used not only for the calculation of the canopy height model of 2006 (ALS-CHM, difference between ALS-DSM and ALS-DTM) but also for the canopy height models of 2011 (difference between photogrammetrically generated DSMs and ALS-DTM) that were produced using the MatchT-DSM (MatchT-CHM, for the whole area), the LPS-DSM (LPS-CHM, for selected areas), and the RSG-DSM (RSG-CHM, for selected areas).

*Examination of the ALS-DTM*

The correspondence between the ALS-DTM, which was used for the generation of the CHMs, and the image-based height models were checked by a sample of stereoscopic point measurements. All over the study area, points were selected that did not change in terms of height between 2006 (ALS flight) and 2011 (photo flight). The bias between these two datasets was used to adjust tree (or canopy) height derived by means of photogrammetry.

*Evaluation of CHMs*

The accuracy of the CHMs was estimated on the basis of tree height measured in the field (permanent sample plots) and with photogrammetric methods (stereoscopic measurements). As the bare ground was not visible, only the tree tops were measured stereoscopically and the height of the ground was extracted from the ALS-DTM. Errors in the co-registration of the field data and the remote sensing data were adjusted manually using tree patterns identified in both data sources by visual inspection.

### 2.3.3 Estimation of dominant height

In forestry, growing stock and yield class are estimated by means of yield tables using the dominant height and the age of a forest stand. There are several ways to determine dominant height based on field data (diameter at breast height, tree height), such as the dominant height by Assmann (1961) or by Weise (1880). In this study, a simplified approach recommended by Marschall (1992) was applied. The dominant height based on field data (reference) was determined by the mean height of the dominant trees, i.e. the trees with the largest height. Two options for the percentage of considered trees were tested (20% and 33% of all trees of a plot).

For estimating dominant height from the CHM, it was tested, which statistical measure (height percentiles: 75$^{th}$, 90$^{th}$, 93$^{th}$, 95$^{th}$, 98$^{th}$, 99$^{th}$, 100$^{th}$) derived from the CHM is correlating best with the field-based dominant height. To take into account a possible bias between the CHM-derived tree height and the tree height measured in the field, e.g. due to smoothing effects in the DSM, the CHM-derived tree height was adjusted by linear regression using the dominant height based on field data as a reference (Nuske & Nieschulze 2004). For the calculation of the regression parameters, the permanent plots were used. We did a global regression instead of individual regressions for each development class, because the number of permanent sample plots per development class was not sufficient to get reliable class-specific estimates for the regression parameters. By means of the resulting regression parameters, the 'dominant height' could be derived from the CHM.

### 2.3.4 Estimation of yield class

The yield class was estimated based on the yield table 'Fichte Hochgebirge' (Fig. 2) for 63 sample plots of the non-permanent inventory. Two approaches were used:

*Yield class derived from dominant height and age*

The yield class was estimated based on the CHM-derived dominant height and the age of the median basal area tree of the inventory. The results were compared with those derived from the field data.

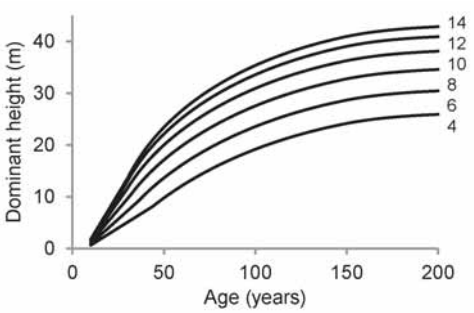


**Fig. 2:** Yield table 'Fichte Hochgebirge' shown as age-height curves for the yield classes 4 to 14 (MARSCHALL 1992).

*Yield class derived from dominant height and height growth*

The difference model calculated from the image-based CHM (2011) and the ALS-CHM (2006) represents the five-year growth of the forest stands. The mean height growth and the CHM-derived dominant height (2011) were used as input for estimating the yield class.

## 3 Results and Discussion

### 3.1 *Visual Evaluation of the Digital Surface Models*

The DSMs obtained from the image-based point clouds (LPS-DSM, MatchT-DSM, RSG-DSM) show a smoothed surface compared to the ALS-based DSM. Although the spatial resolution is the same for all grids, the crowns of individual trees are easier to identify in the ALS-DSM than in the image-based DSMs. Discontinuities, for example at stand borders, are captured more accurately in the ALS-DSM as well.

Differential images between the ALS-DSM and the photogrammetric DSMs (Fig. 3) show that in the image-based DSMs trees at the border or trees in areas with low stand density are often reduced in height or that they are even missing (highlighted in red). In most cases, these differences between the ALS-DSM (2006) and the image-based DSMs (2011) could not be explained by harvesting or any other change. According to the orthophoto (Fig. 3a), most of the missing trees

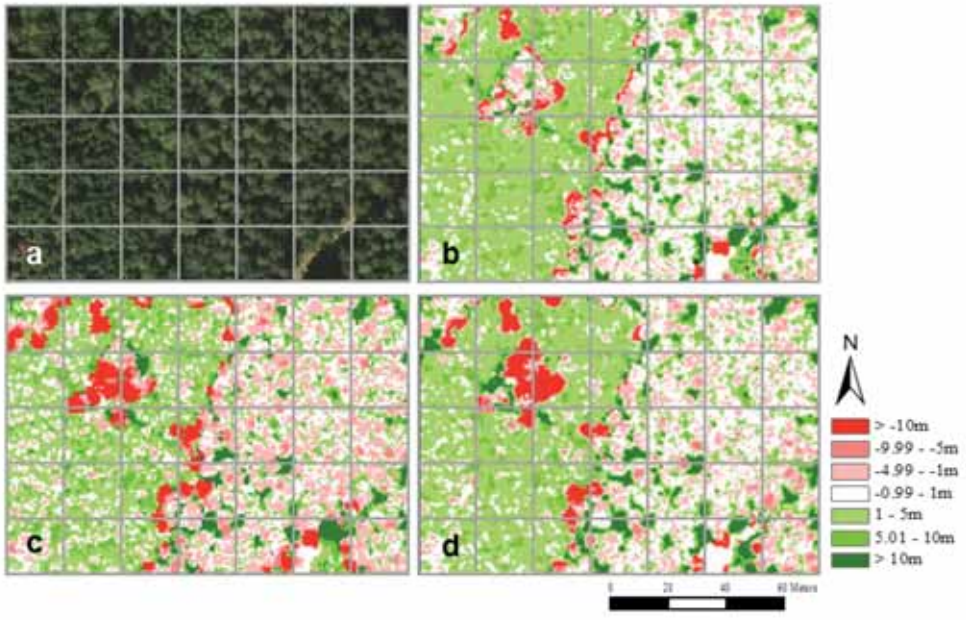


**Fig. 3:** Comparison of ALS-DSM (2006) and image-based DSMs (2011). (a) Orthophoto, (b) RSG-DSM minus ALS-DSM, (c) LPS-DSM minus ALS-DSM, (d) MatchT-DSM minus ALS-DSM.

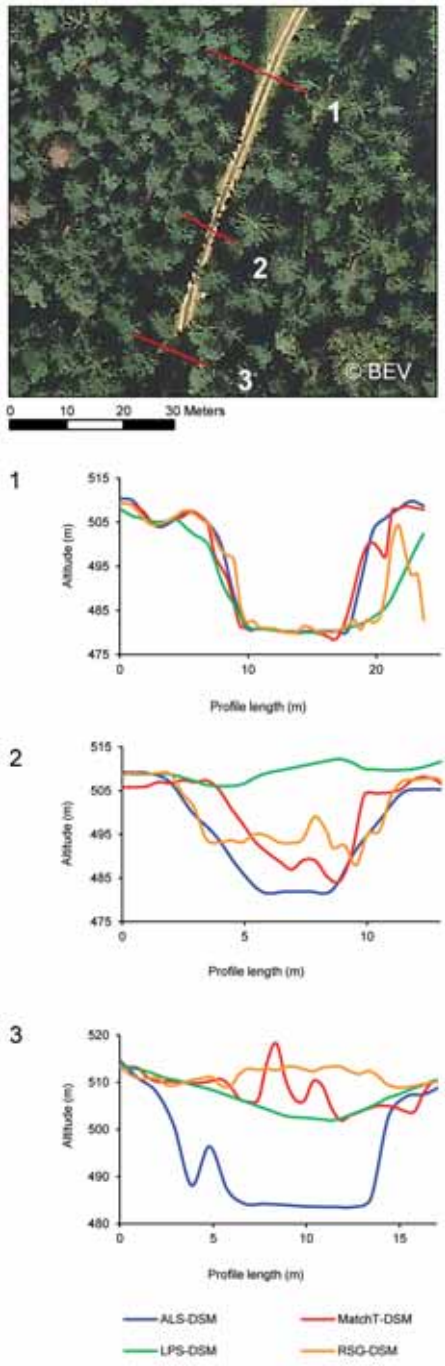


**Fig. 4:** DSM-based profiles at three positions along a forest road.

were still there in 2011. Pixels highlighted in light green, as prevailing in the left part of the shown area, indicate areas with moderate increase in tree height between 2006 and 2011. This area is dominated by a young stand, where tree growth is naturally stronger than in mature stands (right part of the shown area). In the right part, the tree height is partly a bit lower in the image-based DSMs than in the ALS-DSM (highlighted in light red). It shows that the tree tops are more smoothed in the image-based DSMs than in the ALS-DSM. This artifact is most evident in the LPS-DSM (Fig. 3c). Gaps are captured better in the ALS-DSM than in the image-based DSMs (highlighted in dark green).

The capability of the image-based DSMs to capture gaps depends on the size of the gap and on shadow effects in the images. Profiles at three positions along a forest road (Fig. 4) revealed that the discontinuities caused by the road are reproduced most accurately at position 1, where the area without canopy cover is wide. At position 2 and 3, where the canopy closure is higher and the image is severly affected by shadows, none of the image matching algorithms was able to model the cutting satisfyingly.

Occlusions and shadows caused by discontinuities in the forest canopy are the most limiting factors when deriving DSMs by image matching. While the risk of occlusions can be reduced (but not eliminated) by higher image overlaps, the problems caused by shadows can be controlled to a certain degree only by choosing the time of image acquisition properly. ALS, on the other hand is insensitive to shadows. Besides, it is less affected by occlusions, because data are acquired with only small off-nadir angles and just a single measurement suffices to measure surface height whereas for reconstructing surface height by means of photogrammetry, the surface element has to be captured at least twice. Problems with ALS-derived DSMs of forest canopies can arise due to unknown penetration depth of the emitted pulse that can lead to systematic underestimation of canopy height (Gaveau & Hill 2003, Yu et al. 2004). This effect, however, could not be examined in the current study due to the lack of synchronized reference data.

### 3.2 *Evaluation of CHM-derived Tree Height*

At first, the agreement between the ALS-based height and the image-based height was checked using 52 control points on the ground spread over the whole study area. The stereoscopically measured height was on average 0.5 m lower than the ALS-based height (RMSE = ± 0.7 m; paired t-test: p = 1.89e-10). The deviations did not show any regional pattern. Thus, a systematic shift between the ALS-data and the airborne images was assumed. To avoid systematic underestimation of tree height if calculated by combining both data sources, the tree height derived by ALS-normalized stereoscopic measurements and the tree height from image-based CHMs were adjusted.

For assessing the accuracy of CHM-derived tree height, 53 trees, which had been measured in the field in 2012 (permanent sample plot) and could be identified in the CHMs of 2011, were measured manually with photogrammetric methods. We found that the stereoscopically measured, shift-adjusted tree height was on average by 0.9 m lower than the height measured in the field (RMSE = ± 3.3 m; paired t-test: p = 0.05). This deviation is clearly larger than the expected growth in height within a 1-year period, suggesting some uncertainties in the field-measured tree height. In Tab. 1 the deviation between the stereoscopically measured and the CHM-derived tree height is documented. The MatchT-CHM showed the best agreement with the stereoscopic measurements and was therefore chosen for yield class estimation (section 3.4 and 3.5).

**Tab. 1:** Deviation of CHM-derived tree height from stereoscopic measurements.

| | **Bias (m)** *Stereo – CHM* | **RMSE (m)** |
|---|---|---|
| ERDAS LPS | 2.1 | ±3.1 |
| INPHO MatchT | 1.1 | ±1.9 |
| RSG | 2.0 | ±2.4 |

### 3.3 *Evaluation of CHM-derived Height Growth*

The ALS-CHM (2006) and the image-based CHMs (2011) were used to estimate the height growth during the corresponding period of five years. For accuracy assessment, once again the 53 individual trees, which were measured in the field (permanent sample plot) and could be identified in the CHMs, were used. The difference between tree height based on stereo measurements (2011) and the ALS-based height (2006) came to 2.3 m. According to MatchT, the height growth amounted to 1.0 m on average. The tree height derived by LPS and RSG was on average about 0.3 m lower in 2011 than in 2006, which can be explained by smoothing effects.

In addition to measurements at individual trees, we selected six stands per development stage (pole stage, timber stage, old growth) and draw a profile line with a length of approximately 50 m across each stand. Fig. 5 shows a representative example for the development stages ‘Pole stage’ and ‘Old growth’. The distance between the blue line (ALS-DSM) and the other lines (LPS-DSM, MatchT-DSM, and RSG-DSM) illustrates the height growth from 2006 to 2011. The growth in height was most notable in the youngest development stage (Fig. 5a), which is in agreement with the well known fact that the growth in height is most significant at a young age. The histograms of the differences between image-based height (2011) and ALS-based height (2006) summarize the results of all profiles per development stage. The histograms for the pole stage (Fig. 5a) show a clear prevalence of positive values indicating tree height growth with a maximum at a difference of about 0.5 m to 1.0 m. On the contrary, the histograms for the old growth stage (Fig. 5b) show the maximum around 0. In addition, there is a larger number of entries at higher values. These entries mainly correspond to gaps that were not reproduced satisfyingly by the image-based DSMs. These discrepancies are also evident in the profiles, e.g. at length of 7 m, 28 m, and 38 m.

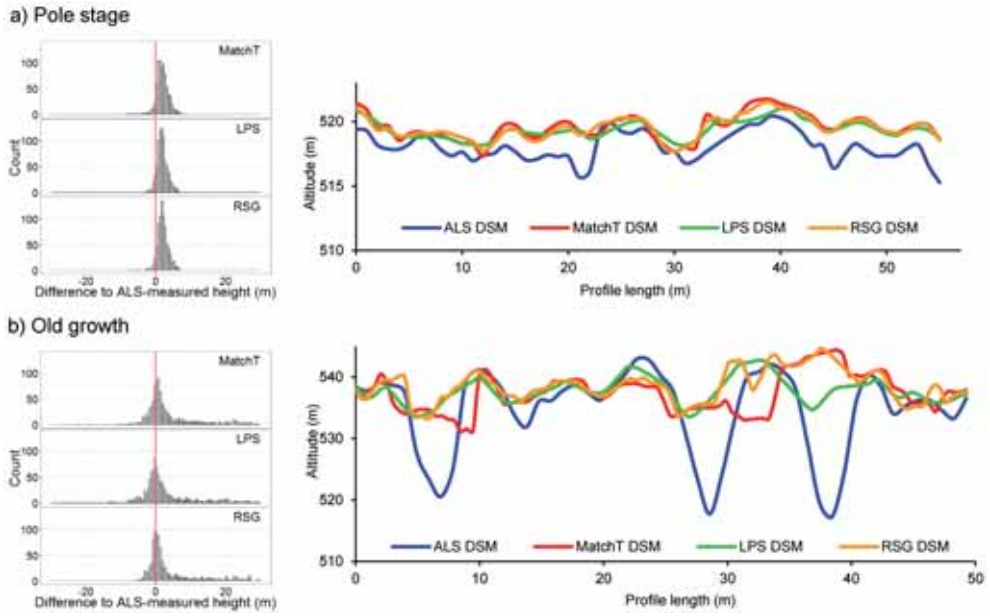


**Fig. 5:** Representative profiles through the MatchT-DSM, the LPS-DSM, the RSG-DSM, and the ALS-DSM a) for a young and b) for an old forest stand. The histograms summarize the differences between image-based height (2011) and ALS-based height (2006). For the histograms, six profiles per development stage were considered.

### 3.4 *Estimation of Dominant Height from CHM Data*

For the estimation of dominant height, the 95$^{th}$ percentile of the ALS-CHM and the MatchT-CHM provided the best results for the regression (ALS-CHM 2006/ground reference 2007: $R^2(75^{th}) = 0.92$, $R^2(90^{th}) = 0.93$, $R^2(95^{th}) = 0.94$; MatchT-CHM 2011/ground reference 2012: $R^2(75^{th}) = 0.91$, $R^2(90^{th}) = 0.94$, $R^2(95^{th}) = 0.95$). Using the mean height of 20% of the highest trees of the sample plot, the coefficients of determination were 0.94 (between ALS-CHM 2006 and the ground reference 2007; RMSE = ± 1.2 m) and 0.95 (between MatchT-CHM 2011 and the ground reference 2012; RMSE = ± 1.0 m). The option with the mean height of 33% of the highest trees revealed slightly better results (ALS-CHM 2006 / ground reference 2007: $R^2$ = 0.94, RMSE = ± 1.1 m; MatchT-CHM 2011/ground reference 2012: $R^2$ = 0.95, RMSE = ± 0.9 m, see Fig. 6), and were used during the further procedure.

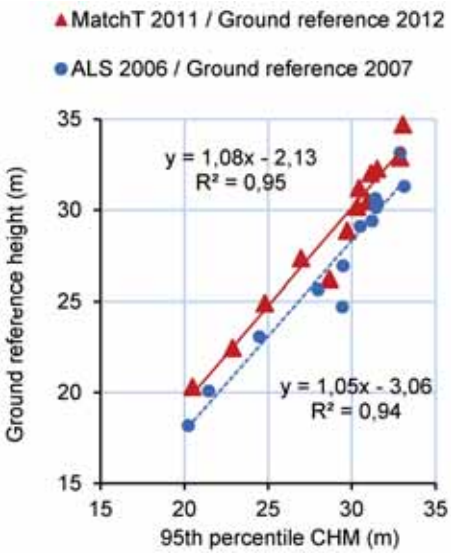


**Fig. 6:** Linear regression of 95$^{th}$ percentile (CHM) and mean height of the 33% highest ground-measured trees.

In other studies, different percentile values were used to correct tree respectively stand height. For example, Næsset (2002) used the 75th percentile to correct a DSM, and Nuske & Nieschulze (2004) used the 90th percentile for linear regressions to determine mean stand height.

For plausibility checks, 30 stands representing the development stages pole stage, timber stage, and old growth were selected. For these stands the height growth was estimated using the CHM-derived dominant height calculated by linear regression for 2006 (ALS-CHM) and 2011 (MatchT-CHM). The results are summarized in Tab. 2.

The estimates of tree height growth averaged per development stage are plausible for a period of five years. Field measurements in a recently thinned pole stand were in line with the figures outlined in Tab. 2. For 36 trees (27 cut trees, 9 remaining trees) the height growth corresponding to the last five years was measured. The resulting mean height growth was 2.9 m (CHM-derived height growth: 3.5 m).

## 3.5 *Derivation of Yield Class*

*Yield class derived from dominant height and age*

For 63 non-permanent sample plots, the yield class was estimated from age and CHM-derived dominant height (approach 1). The result was compared with the yield class based on age and field-measured height (reference) (Fig. 7). The yield class estimated from the CHM-derived dominant height was on average by 0.6 below the reference. The RSME was ± 0.8.

**Tab. 2:** Results of tree height growth estimation.

| | Pole stage | Timber stage | Old growth |
|---|---|---|---|
| Number of stands | 12 | 9 | 9 |
| Mean area of stands (ha) | 1.1 | 1.7 | 1.8 |
| Mean height growth (m) | 3.5 | 1.5 | 0.9 |
| Standard deviation (m) | ± 0.7 | ± 0.4 | ± 0.7 |

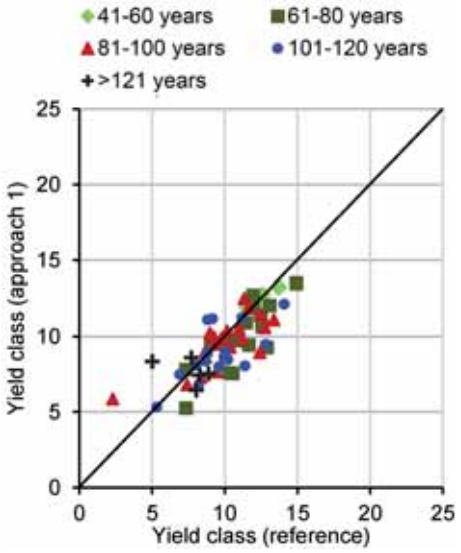


**Fig. 7:** Result of yield class estimation based on CHM-derived dominant height and age.

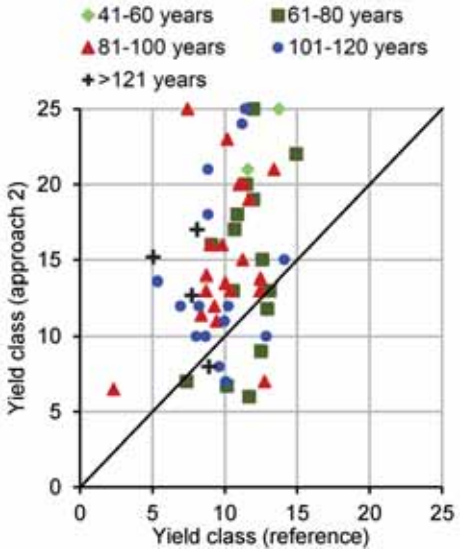


**Fig. 8:** Result of yield class estimation based on CHM-derived dominant height and height growth.

*Yield class derived from dominant height and height growth*

For 63 non-permanent sample plots, the yield class was obtained from the CHM-derived dominant height and the average height growth between 2006 and 2011 (approach 2). In Fig. 8 the results are plotted against the reference. The yield class estimated from the CHM-derived dominant height was on average by 5.2 higher than the reference. The RMSE was ± 7.9.

The results of the first approach corresponded to the terrestrial yield class estimates quite well. The results of the second approach were not satisfying. This can be explained by two reasons: First, the yearly tree height growth (depending on climate and other external influences) shows a high variability. Therefore, mean values of a five-year tree height growth are uncertain. Second, the estimation of tree height growth by means of photogrammetry showed uncertainties as well. In any case, the yield class estimation by means of yield tables is very sensitive on the parameter height growth due to the shape of the height curves (Fig. 2). Thus, a small uncertainty in height growth causes disproportional errors in the resulting yield class. Additionally, ambiguities can occur for specific combinations of dominant height and height growth. The error in estimating yield classes based on height growth may also be increased by the problem that the commonly used yield tables date back to the beginning of the 20th century and underestimate the height growth of today's forest stands (Bösch 2002).

## 4 Conclusions and Outlook

Based on ALS data acquired in 2006 and on digital aerial images taken in 2011, canopy height models (CHMs) were calculated. From the CHMs, the dominant height as well as the height growth of forest stands was derived, and it was tested if these parameters are suitable for the estimation of the yield class. The DSMs were generated photogrammetrically by means of image matching with three different software products. The resulting DSMs were evaluated with respect to their quality to characterise forest surfaces. For all investigations, ground reference data were available in form of forest inventory data and permanent sample plots.

The use of ALS data acquired some years ago for normalizing up-to-date DSMs was feasible, as the terrain relief below forest canopies can be assumed as constant for a longer period. However, multi-temporal CHMs from different data sources, e.g. ALS-based DTM and photogrammetrically generated DSM, essentially need to be co-registered accurately. Besides, a possible bias in height between the ALS data and the image data, e.g. determined by stereoscopic measurements, has to be considered.

The comparison of ALS-based and image-based DSMs revealed that photogrammetric methods have problems in representing small gaps, the surface of areas close to stand boundaries, and the surface of areas affected by shadows. All photogrammetric DSMs showed the tendency to smooth the surface of the forest canopy in general and to underestimate tree height of individual trees in particular. This systematic difference between the ALS-based and the image-based height affects the estimation of height growth based on these data sources.

The 95th percentile of the CHM proved to be a proper approximation of the dominant height. The estimation of yield class by means of CHM-derived dominant height and age provided satisfying results. The estimation of yield class from CHM-derived dominant height and height growth, however, revealed unsatisfactory results, caused by uncertainties in the determination of height growth and by limitations regarding the suitability of the available yield tables. It is expected that more accurate yield class estimates can be achieved if the observation period is longer, e.g. 10 years, and if CHM time series with more than two points in time are available.

The presented method will benefit from several technical improvements that are expected for the future. The systems for in-flight logging will provide more accurate results of the exterior orientation and consequently the geometric accuracy of the information derived from the images will be higher. The radiometric, spectral and geometric resolution of dig-

ital cameras are continuously improving and will contribute – in combination with image matching algorithms that are being constantly enhanced – to more detailed and more accurate surface models. Besides, in the future the CHM time series will be consistent in terms of sensor technology and systematic differences of DOMs caused by the diversity of the acquisition systems will be avoided.

The current study revealed that there are still some issues that need improvement, both in terms of data basis and data processing. However, it can be stated that remote sensing is able to substantially supplement conventional field-based methods as it provides information about forests and their development over large areas very efficiently and it is able to map important forest attributes in a spatially explicit and continuous way.

In general, the use of yield tables and the derivation of yield classes can be put into question due to the fact that small changes of input parameters result in a high variability of output parameters. Yield tables are mainly used to estimate future growth rates, and with no other methods available, yield tables may serve as a makeshift for this purpose. In a different and more promising approach, future growth rates should be derived by novel growth functions directly derived from multi temporal canopy height models.

## Acknowledgements

The authors would like to express their thanks to the Institute of Forest Growth (University of Natural Resources and Life Sciences – BOKU Vienna) and the forest enterprise Seilern-Aspang for providing inventory data free of charge. Special thanks are devoted to Dipl.-Ing. Christoph Bauerhansl from the Austrian Federal Research and Training Center of Forests, Natural Hazards and Landscape (BFW) and the research unit DIGITAL – Remote Sensing and Geoinformation (Joanneum Research) for generating digital surface models for this study. We thank the Austrian Federal Office of Surveying and Metrology (BEV) for providing digital images and orthophotos free of charge. We thank Dipl.-Ing. Boris Jawecki (Umweltdata GmbH) for his support in GIS data analysis. Finally, we acknowledge the useful comments of the reviewers, which contributed to relevant improvements of the manuscript.

## References

Assmann, E., 1961: Waldertragskunde – organische Produktion, Struktur, Zuwachs und Ertrag von Waldbeständen. – 490 S., BLV, München.

Baltsavias, E., Gruen, A., Eisenbeiss, H., Zhang, L. & Waser, L.T., 2008: High-Quality Image Matching and Automated Generation of 3D Tree Models. – International Journal of Remote Sensing **29** (5): 1243–1259.

Bösch, B., 2002: Neue Bonitierungs- und Zuwachshilfen. – Wissenstransfer in Praxis und Gesellschaft, FVA-Forschungstage 2001, Freiburger Forstliche Forschung **18:** 266–276.

Bohlin, J., Wallerman, J. & Fransson, J.E.S., 2012: Forest Variable Estimation Using Photogrammetric Matching of Digital Aerial Images in Combination with a High-Resolution DEM. – Scandinavian Journal of Forest Research **27** (7): 692–699.

Gaveau, D.L.A. & Hill, R.A., 2003: Quantifying canopy height underestimation by laser pulse penetration in small-footprint airborne laser scanning data. – Canadian Journal of Remote Sensing **29** (5): 650–657.

Gillis, M.D. & Leckie, D.G., 1996: Forest Inventory Update in Canada. – Forestry Chronicle **72** (2): 138–156.

Hobi, M.L. & Ginzler, C., 2012: Accuracy Assessment of Digital Surface Models Based on WorldView-2 and ADS80 Stereo Remote Sensing Data. – Sensors **12** (12): 6347–6368.

Hyyppä, J., Hyyppä, H., Leckie, D., Gougeon, F., Yu, X. & Maltamo, M., 2008: Review of methods of small-footprint airborne laser scanning for extracting forest inventory data in boreal forests. – International Journal of Remote Sensing **29** (5): 1339–1366.

Hollaus, M., Wagner, W., Schadauer, K., Maier, B. & Gabler, K., 2009: Growing Stock Estimation for Alpine Forests in Austria: a Robust Lidar-based Approach. – Canadian Journal of Forest Research **39** (7): 1387–1400.

Intergraph, 2013: ERDAS IMAGINE 2013, User Guide. – 1990–2013 Intergraph Corporation.

Jablko, P. & Perlwitz, W., 1997: Baumhöhenmeßgeräte im Vergleich. – AFZ / Der Wald **15:** 815–817.

Järnstedt, J., Pekkarinen, A., Tuominen, S., Ginzler, C., Holopainen, M. & Viitala, R.,

2012: Forest Variable Estimation Using a High-Resolution Digital Surface Model. – ISPRS Journal of Photogrammetry and Remote Sensing **74:** 78–84.

Joanneum Research Digital, 2014: http://dib.joanneum.at/rsg/ (24. 2. 2014).

Kilian, W., Müller, F. & Starlinger, F., 1994: Die forstlichen Wuchsgebiete Österreichs – Eine Naturraumgliederung nach waldökologischen Gesichtspunkten. – FBVA-Berichte 82, Forstliche Bundesversuchsanstalt, Wien, Österreich.

Leberl, F., Irschara, A., Pock, T., Meixner, P., Gruber, M., Scholz, S. & Wiechert, A., 2010: Point Clouds: Lidar versus 3 D Vision. – Photogrammetric Engineering and Remote Sensing **76** (10): 1123–1134.

Marschall, J., 1992: Hilfstafeln für die Forsteinrichtung. – 5th Ed., Österreichischer Agrarverlag, Wien, Österreich.

Næsset, E., 2002: Determination of Mean Tree Height of Forest Stands by Digital Photogrammetry. – Scandinavian Journal of Forest Research **17** (5): 446–459.

Nurminen, K., Karjalainen, M., Yu, X., Hyyppä, J. & Honkavaara, E., 2013: Performance of dense digital surface models based on image matching in the estimation of plot-level forest variables. – ISPRS Journal of Photogrammetry and Remote Sensing **83** (2013): 104–115.

Nuske, R. & Nieschulze, J., 2004: Die Vegetationshöhe als Werkzeug zur Ermittlung von Bestandeshöhen: Eine Anwendung automatisierter digitaler Photogrammetrie in der Forstwissenschaft. – Allgemeine Forst- und Jagdzeitung **175:** 13–21.

Schardt, M., Hruby, W., Hirschmugl, M., Wack, R. & Franke, M., 2004: Comparison of Aerial Photographs and Laser-Scanning Data as Methods for Obtaining 3D Forest Stand Parameters. – International Archives of the Photogrammetry, Remote Sensing and Spatial Information Sciences **XXXVI-8/W2:** 272–276.

Skovsgaard, J.P. & Vanclay, J.K., 2008: Forest Site Productivity: A Review of the Evolution of Dendrometric Concepts for Even-aged Stands. – Forestry **81** (1): 13–31.

Straub, C., Weinacker, H. & Koch, B., 2010: A Comparison of Different Methods for Forest Resource Estimation using Information from Airborne Laserscanning and CIR Orthophotos. – European Journal of Forest Resource (2010) **129:** 1069–1080.

Straub, C. & Seitz, R., 2011: Möglichkeiten der automatisierten Generierung von Oberflächenmodellen in Waldgebieten aus digitalen Luftbildern. – Seyfert, E. (ed.): 31. Wissenschaftlich-Technische Jahrestagung der DGPF (Deutsche Gesellschaft für Photogrammetrie, Fernerkundung und Geoinformation) **20:** 153–162.

Straub, C., Stepper, C., Seitz, R. & Waser, L.T., 2013: Potential of UltraCamX Stereo Images for Estimating Timber Volume and Basal Area at the Plot Level in Mixed European Forests. – Canadian Journal of Forest Research **43** (8): 731–741.

Trimble, 2014: http://www.trimble.com/imaging/inpho.aspx (24.2.2014).

Véga, C. & St-Onge, B., 2009: Mapping Site Index and Age by Linking a Time Series of Canopy Height Models with Growth Curves. – Forest Ecology and Management **257** (3): 951–959.

Weise, W., 1880: Ertragstafeln für die Kiefer. – Springer, Berlin.

White, J., Wulder, M., Vastaranta, M., Coops, N., Pitt, D. & Woods, M., 2013: The Utility of Image-Based Point Clouds for Forest Inventory: A Comparison with Airborne Laser Scanning. – Forests **4** (3): 518–536.

Yu, X., Hyyppä, J., Hyyppä, H. & Maltamo, M., 2004: Effects of Flight Altitude on Tree Height Estimation Using Airborne Laser Scanning. – International Archives of the Photogrammetry, Remote Sensing and Spatial Information Sciences **XXXVI** (Part 8/W2): 96–101.

Zamg, 2013: http://www.zamg.ac.at/cms/de/klima/klimauebersichten/klimamittel-1971-2000 (15.7.2013).

Addresses of the Authors:

Dipl.-Ing. Katrin Windisch, Dipl.-Ing. Dr. Tatjana Koukal & Dipl.-Ing. Dr. Reinfried Mansberger, University of Natural Resources and Life Sciences, Vienna (BOKU), Institute of Surveying, Remote Sensing and Land Information, Peter-Jordan-Straße 82, A-1190 Vienna, e-mail: katrin_windisch@gmx.net, {tatjana.koukal} {reinfried.mansberger}@boku.ac.at

Dipl.-Ing. Günther Bronner, Umweltdata GmbH, Bahnhofsplatz 1a, A-2340 Mödling, Austria, e-mail: g.bronner@umweltdata.at

Manuskript eingereicht: März 2014
Angenommen: Juli 2014

PFG 2014 / 5, 0339–0350
Stuttgart, October 2014

Article

# Hydrographic Surveying of the Steppe Lake Neusiedl – Mapping the Lake Bed Topography and the Mud Layer

Erwin Heine, Ilse Kogelbauer, Vienna, Austria, Andreas Prokoph, Hamburg & Willi Loiskandl, Vienna, Austria

**Keywords:** hydrographic surveying, sub-bottom-profiling, side scan sonar, Lake Neusiedl, mud layer

**Summary:** To ensure the various functions of the Lake Neusiedl, commercial as well as ecological, in the future a sound management of the water, the mud and the reed belt is required. Management needs concise data to assess the risks and vulnerability. In order to build on previous investigations, to observe changes, and to create a high resolution digital terrain model (DTM) of the lake bed, a comprehensive survey of the lake bottom and the mud layer was initiated. Hydrographic surveying methods based on acoustic echo sounding techniques provide the back bone of topographic data generation of the lake bottom and the mud layer. The acoustic echo sounding system consists of side scan sonars, single beam sounders and a sediment profiler. Shallow lakes with a composition of thick mud layers compared to the water depth are a challenge for these systems. Transects were measured in a regular grid by boat. To verify the echo sounding measurements, to obtain data in areas with a water depth lower than 50 cm (where echo sounding is not applicable), and to provide data for the transition zone between the water body and the reed belt, a combination of soil physical sensors in a measuring system was introduced. The single-point measurement system consists of a capacitive sensor and a cone penetrometer. At selected points soil cores were taken as an additional reference. A global navigation satellite system (GNSS) for real-time kinematic (RTK) positioning of dynamic, precise vertical point-measurements was utilized for the exact positioning of all measurements.
Cross-correlation of the dataset enabled the identification of outliers and systematic errors, hence the provision of the dataset with high quality. This spatial data is now available with an overall accuracy of better than ± 10 cm to generate DTMs of the lake bottom and the mud layer.

**Zusammenfassung:** *Hydrographie des Steppensees Neusiedler See – Vermessung des Seebodens und der Schlammschicht.* Damit der Neusiedler See als besonders schützenswertes Ökosystem sowohl in seiner ökologischen Funktionsfähigkeit aber auch in seiner ökonomischen Funktion erhalten bleibt, ist eine genaue Kenntnis der Wasserfläche, des Schlammkörpers und des angrenzenden Schilfgürtels von Nutzen. Daher wurde eine topografische Aufnahme des Seebodens und der Verteilung und Mächtigkeit des darin abgesetzten Schlamms initiiert. Durch den Vergleich mit vorangegangen Vermessungen können so auch Veränderungen aufgezeigt werden. Die hydrographische Vermessung basierend auf Echolotmessungen mit Einzelstrahl-Echolot, Sub-Bottom-Profiler und Seitensichtsonar stellt die Basis für die Generierung von Seeboden und Schlammoberflächenmodellen dar. Zur Validierung der Echolot-Schallausbreitungswerte für Schlamm und zur Erfassung der Seichtwasserflächen im Uferbereich (Übergang von der Wasserfläche zum Schilfgürtel) wurden zusätzlich Einzelpunktmessungen mit einem adaptierten bodenphysikalischen Messsystem durchgeführt. Dieses Messsystem basiert auf zwei gebräuchlichen Sensoren, einem kapazitiven Sensor und einem Penetrometer, welche mit einem RTK-GNSS georeferenzierte Vertikalprofile von der Wasser-Schlamm Seebodensedimentschichtung liefern. Die Referenzmessungen dienen zur Eliminierung von Ausreißern und systematischen Fehlern der Echolotmessungen. Damit wurde als Ergebnis ein hochwertiger Datensatz mit einer Genauigkeit von besser als ± 10 cm zur Generierung Digitaler Geländemodelle (DGM) der Schlammoberfläche und des Seebodens und somit zur Bestimmung der Schlammverteilung erstellt.


www.schweizerbart.de
DOI: 10.1127/1432-8364/2014/0228
1432-8364/14/0228 $ 3.00

## 1 Introduction

Shallow endorheic lakes, like Lake Neusiedl (Hungarian: Fertö), are particularly vulnerable to changes in climate parameters. An increase of the air temperature because of global climate change would have a considerable impact on the water balance of Lake Neusiedl. Extreme water levels will cause significant changes in the expanse of the water surface, causing multiple consequences for the lake's eco-system, agriculture and local tourism (Soja et al. 2013, EuLakes vol. 2 2013: 44ff.).

Another important factor for a reduction of water volume of the lake is the accumulation of unconsolidated sediments (mud) in the lake basin. It is enhancing due to a shift of wind-driven sediments, which are accumulated in the surrounding reed belt (Bácsatyai et al. 1997).

To carry out investigations on present vulnerabilities and risk assessment, and for the improvement of lake water management issues it is necessary to develop realistic water level scenarios (Schönerklee et al. 2006: 45ff.). In 2011 a cooperative project between Hungary and Austria was initiated in order to provide a homogeneous topographic data base of the Lake Neusiedl basin and the Hanság-Channel also including the investigation of the huge, stratified mud body of the lake (GeNeSee 2011).

Hydrographic surveying methods based on acoustic echo sounding techniques were chosen to provide the topographic data of the lake bottom and of the mud layer, particularly with regard to generate high resolution digital terrain models (DTMs) of the lake bed.

Applying acoustic echo sounding techniques for detecting the acquisition of mud in shallow waters, like lakes and estuaries, is highly demanding due to the presence of unconsolidated material suspended in the water column. The distortion of the acoustic signals in unconsolidated fine grained sediments (mud) may result in an erroneous detection of the lake bed sediment structure (Buchanan 2005, Schrottke et al. 2006, Missiaen et al. 2008). To deal with those misleading acoustic parameters at Lake Neusiedl with a stratified mud body of up to 2 m, additional tools for the provision of density information are required.

The aim of this paper is to describe the acquisition of highly accurate lake bed data for generating DTMs of Lake Neusiedl with special regard to the distortion of acoustic signals in the mud body. The aim is reached by the application of a high frequency echo sounder, a parametric sub-bottom profiler, side scan sonars, and measurements with soil physical sensors for the detailed interpretation of the sediment structure.

## 2 Site Description

Lake Neusiedl is the westernmost steppe lake in Europe located in the western part of the Little Hungarian Plain (Fig. 1). The lake basin covers a total area of 321 km² at the boundary line of 116.50 m above sea level, of which 233 km² are on the Austrian and 88 km² on the Hungarian territory (Bácsatyai et al. 1997). The open water body of Lake Neusiedl has a total area of about 143 km² and is surrounded by an extensive reed belt of about 178 km² (Schmidt & Csaplovics 2011), which is the second largest connected reed belt in Europe. The lake is quite shallow with a huge stratified mud body consisting mainly of fine sediments. On the Austrian territory the mud volume has almost doubled during the period from 1963 – 1988, from 75 Mio. m³ to 150 Mio. m³ (Csaplovics 1998: 58, Bácsatyai et al. 1997: 41). These values provide only an order of magnitude of the increase, because the data acquisition methods and the amount of surveyed data in the years 1963 and 1988 are not directly comparable.

The water balance of the lake is dominated by precipitation and evaporation, and just minor inflow of the river Wulka and even less inflow (~ 2%) origins from ground water springs. 80% of the water gain originate from precipitation and 90% of the water loss is due to evaporation, which is the predominant factor concerning the water balance. Groundwater level changes due to extensive agriculture have no significant impact on the lake water level. Indirect connection is given by the climate, which affects both water bodies in a significant way (Schönerklee et al. 2006: 54 ff.). Variations in sunshine duration, mean air temperature, precipitation and other meteorologi-

cal components cause significant changes in evaporation. The change of air temperature of +0.7 °C in the period of 1991 – 2004 compared to 1961 – 1990 induced a rise in evaporation of nearly 10%. Since 1740, the lake has dried out four times. The last vanishing was from 1864 to 1870 (Nationalpark Neusiedler See – Seewinkel 2012, Loiskandl et al. 2012). The Lake Neusiedl has no natural outflow. At the end of the 19th century, an artificial channel for excess water drainage was constructed. A weir at the main regulation channel Hanság regulates nowadays the lake water level according to operation rules and supervised by an Austro-Hungarian committee for water bodies. The weir can only prevent flooding, drainage of excess water, but not raise the lake water level, thus the lake water level is predominated by precipitation and evaporation (Eitzinger et al. 2009).

## 3 Methodology

The core of the applied hydrographic measurement system is based on different acoustic sensors for depth measurement and image acquisition of the lake bed (3.2, 3.3 & 3.4), combined GNSS/IMU components to determine ships position and attitude and a hydrographic data acquisition, navigation and processing software package to plan, manage and synchronize all different sensor measurements (3.1). Fig. 1 gives an overview of the system of the survey vessel.

Subsequently, the application of a soil physical sensor system delivers precise height information of the mud layer and the sediment structure at 61 individual reference points, thus enabling the determination of proper sound velocity parameter for processing the sub-bottom echo soundings of the entire lake.

### 3.1 *Positioning and Navigation Data*

Positioning and navigational data are needed for determining the correct geographic coordinates of the depth measurements (depth soundings) and for navigational purposes of the survey boat.

The geographical situation of the lake in an open plain and the nearly constant appearance of wind causes waves on the lake surface, and a water level rise at one lake side and a drop at the other, with a period of minutes or even hours, called a *wind tide* or a *seiche.* In March 2013, strong north-westerly winds sustaining over many hours caused a water level difference between Breitenbrunn (NW-end) and Apetlon (SE) up to 90 cm (Geschnatter 2013).

As waves cause heavy motions of the survey vessel in all six parameters (fore-aft, lateral, vertical, roll, pitch, and yaw), the accurate determination of position and attitude parameters are crucial for the quality of the final lake bed coordinates, i.e. for the vertical component.

This could be achieved with the integration of satellite based positioning (GNSS) and high quality inertial measurement system (IMS) based on fibre optic gyroscope.

A RTK-GNSS system was used to provide real-time 3D-position data with an accuracy of ± 3 cm and a data rate of 10 Hz. Permanent GNSS base stations distributed on three places around the lake delivered the necessary RTK-GNSS correction data. The transmission from GNSS reference station to GNSS rover was realized with UHF radio modem "Satelline Easy Pro", which offers different setup possibilities, to fulfil the Hungarian as well as the Austrian telecommunication regulations.

Remark: The use of UMTS modems for receiving real-time correction data for precise VRS-GNSS positioning failed due to bad UMTS coverage at the border region (Austria-Hungary) (Heine et al. 2013).

A 6-parameter motion sensor IXBLUE/IXSEA Octans was used to provide highly accurate true heading, motion, speed, and acceleration data. This inertial measurement unit (IMU) consists of gyrocompass and motion sensor, and delivers attitude information with an accuracy of 0.1° on heading and 0.01° on roll and pitch.

On the survey vessel, the transducers of the acoustic system were placed on the outside of the hull; situated at the starboard bow, the starboard beam, the port bow, and the port beam (Fig. 1b). The GNSS-antenna and the IMU where placed amidships. The offsets (lever arm), between all sensors, were defined by

an X, Y, and Z offset from the GPS antenna as the origin for all measurements.

The integration of the GNSS/IMU measurements and lever arm information for the determination of position and attitude for each transducer, and finally the calculation of the lake bottom coordinates based on the acoustic measurements were realized by the use of the hydrographic data acquisition, navigation and processing software package QINSy (quality integrated navigation system) (QINSy 2014).

ETRS89 was selected to be the homogeneous coordinate reference system for all geodetic measurements on the lake within the GeNeSee project, whereas UTM33N is the commonly used cartographic projection. Transformation to the national horizontal and vertical geodetic datum can be done using transformation parameters and geoid data provided by the respective national mapping agencies.

### 3.2 *Acoustic System: Single Beam Echo Sounder (SBES)*

High frequency single beam echo sounder (Simrad 710-36) with a narrow 2.8 degree beam was used for detailed mapping of the water depth. Its high frequency of 710 kHz allows using a short pulse length providing fine range resolution. In areas with soft bottoms, it will detect the upper limit of mud.

Furthermore the nominal depth range minimum of 0.1 m allows carrying out detailed measurements of the very shallow shore zones.

### 3.3 *Acoustic System: Parametric Sub Bottom Profiler (SBP)*

Sediment profilers, also known as sub bottom profilers (SBP), are structurally similar to single-beam sounders, but working at lower frequencies and thus gathering vertical cross-sections of the inner sedimentary sea bed structure (Lurton 2002). Parametric echo sounders are based on the concept of non-linear generation of acoustic waves. During simultaneous transmission of two signals of slightly different high frequencies at high sound pressure, a new frequency arise, with a frequency equal to the difference between the two primary frequencies. The resulting low frequency signal allows a better bottom penetration and a high vertical resolution.

For determining the sediment layers in Lake Neusiedl an Innomar SES 2000 parametric sub bottom profiler was used. The device generates a low frequency between 4 kHz and 12 kHz based on primary frequencies of around 100 kHz. The system is able to achieve a resolution of about 5 cm, an accuracy of ± 2 cm + 0.02% of the water depth for the 100 kHz frequency, and about ± 4 cm + 0.02% of the water depth for the chosen low frequency of 10 kHz (Innomar 2005). This requires detailed information about the sound velocity for the penetration material, which ranges between 1450 m/s and 1900 m/s for saturated sediments (Santamarina et al. 2005).

### 3.4 *Acoustic System: Side Scan Sonar (SSS)*

Several projects at estuaries and shallow coastal zones have shown that side scan sonar in combination with results of sub-bottom profiling and bathymetry provides more details of the sedimentation process itself and verifies the classification (Nitsche et al. 2004, Schrottke et al. 2006).

200 kHz high-resolution side looking sonar for shallow water surveying were used for mapping the morphology of the lake bed. Two transducers (Simrad 200 kHz – 0.5° x 49°) were mounted at the port bow and the starboard bow respectively, looking athwart ships. The side scan sonar images have a pixel resolution of 10 cm and are displayed as monochrome images (Fig. 2). The grey scale variations represent “backscatter” energy received from the lake bed, with strong backscatter producing lighter tones and weak backscatter producing darker hues. This variation is caused by a complex range of factors, such as lake floor slope, topographic variability, grazing angle of insonification (geometry of the sensor-target system), physical characteristics of the target surface, e.g. surface roughness, and the variations in sediment composition (Ulrick 1983).

### 3.5 *Combination of Soil Physical Sensors in a Measuring System (CSPS)*

A complementary methodology of single-point measurements with a soil physical approach was used to support acoustic techniques for mud layer and lake bed mapping (KOGELBAUER et al. 2013). The designed system combines two commonly applied soil physical measurement techniques and provides reproducible physical values joined with a RTK-GNSS for dynamic, horizontal and vertical point positioning (Fig. 1c). The designed system enables the delineation of water, mud, and lake bed sediment layers. It utilizes three main components: 1.) a capacitive sensor (Hydra Probe, Stevens Water Monitoring System) to determine the water content in soft mud and a modified cone penetrometer (Eijkelkamp) to measure penetration resistance in compact mud layers and shallow lake bed sediments, 2.) the data acquisition system using a data logger (CRX23, Campbell) to process data from the sensors and a GNSS RTK, and 3.) developed C# based software for synchronizing sensor data and GNSS position.

The designed system is based on well-known and commonly applied sensors that provide physical values for comparative purpose. Moreover, it supports non-destructive in-situ measurements without cost and time consuming sampling effort. The synchronization with a RTK-GNSS enables rapid dynamic vertical measurements with highly accurate positioning. Thus, this non-acoustic system provides valuable ground truth information for the echo sounding layer delineation.

The Hydra Probe is based on frequency domain reflectometry (FDR) at 50 MHz and indirectly indicates volumetric water content $\theta$ ($m^3 \cdot m^{-3}$) by measuring the relative dielectric permittivity $\varepsilon_r$. The dielectric permittivity $\varepsilon_r$ enables the layer delineation of the water-mud interface by its significant difference, with $\varepsilon_r$ in air (1), Lake Neusiedl water (70 – 80), and solid particles (4 – 7). It was correlated to the water content by a site-specific laboratory calibration, which accounted for the variation of mud composition throughout the lake. The data pairs of $\varepsilon_r$ with $\theta$ were fitted to a third degree polynomial ($R^2 = 0.9877$) (1) (D'AMBOISE 2012).The Hydra Probe measurement error of $\varepsilon_r$ was ± 1.5%.

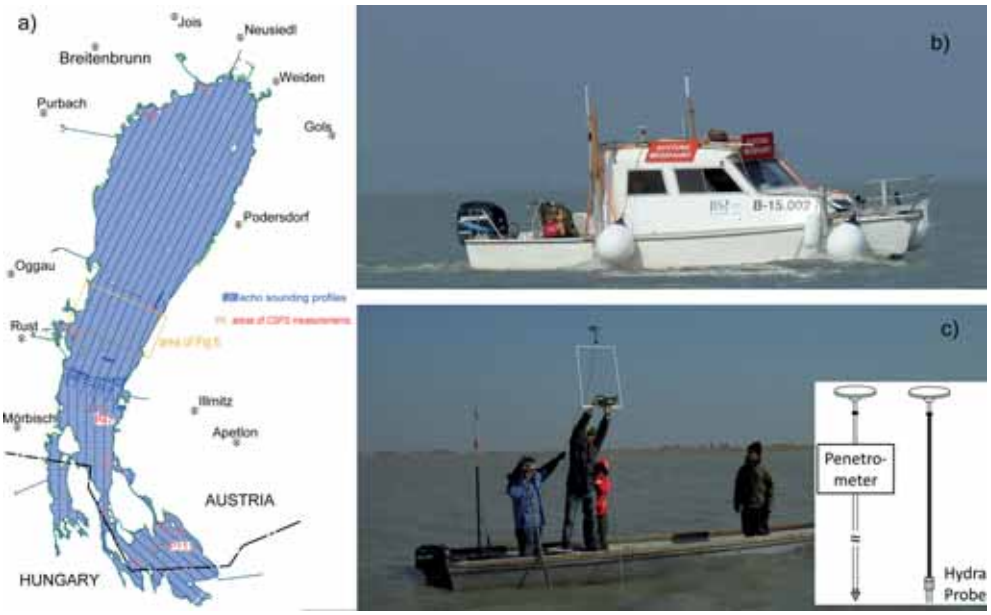


**Fig. 1:** a) Echo sounding profiles and distribution of calibration points, b) survey vessel, c) mud layer measurement with soil physical sensors system, i.e. penetrometer.

$$\theta = -0.087968 + 0.027307\ \varepsilon_r - 0.000356\ \varepsilon_r^2 + 2.34 \times 10^{-6}\ \varepsilon_r^3 \quad (1)$$

The cone penetrometer, the second sensor, measures the penetration resistance $PR_x$ (MPa), which is the force required to push forward the cone penetrometer through the soil (Bradford 1986). The laboratory calibration of the cone penetrometer related the output voltage $y$ (mV) from the penetrometer's force transducer with the applied weight. Hereby, a linear relation was obtained (2) with the base voltage $y_0$ (mV) and the cross sectional area of the cone $A_{p,x}$ (cm²) (Kogelbauer et al. 2013). Another factor for the probing rod weight $R_{p,x}$ was added. The conversion from mV to MPa was as proposed by Bradford (1986), where also the factor 0.09807 arises.

$$PR_x=((y-y_0+R_{p,x})/(29.82*A_{p,x}))*0.09807 \quad (2)$$

## 4 Survey and Data Collection

### 4.1 *General Echo Sounding Survey Setup*

The echo sounding measurements were realized along transects. The sounding lines run perpendicular to the assumed centre line of the lake bed, with a line spacing of 100 m. For quality control, lines of 500 m spacing running parallel to the lake bed centre were defined. Mistakes and gross errors as well as systematic errors are able to be detected at the intersection point of the transect lines.

Furthermore, surveying lines running parallel to the shore line had been defined to enable a comprehensive mapping of the shore zone by means of the side scan sonar.

The sounding lines and actual vessel position and vessel heading were visualized together at a navigation screen for the helmsman to steer a correct and steady course.

Sound velocity profiles (SVP) were measured frequently to correctly produce echo sounding depth measurements. Presence of unconsolidated material suspended in the water column affects the speed of sound propagation. Changing suspension situations due to swirl up of fine bottom sediments caused by waves, as well as the significant variations in water temperature during the survey (28 °C in August, 4 °C in November) requires sound velocity correction of the soundings, even for shallow water depths.

### 4.2 *Set-up and Measurement Procedure of the CSPS*

The Hydra Probe and the cone penetrometer were modified to enable measurements at the lake. For this application the Hydra Probe was mounted on a telescope rod with a GNSS antenna mounted on top. The modifications of the cone penetrometer were the direct connection of the strain gauge to the datalogger and the extension of the probing rod. The probing rod length of up to 5 m depended on the water depth and the possible penetration depth. The GNSS antenna was fixed on a frame at the penetrometer aligned with the penetrometer's cone tip. The detection of shallow layers with the penetrometer setup was restricted by factors such as the rod length, the lateral bending resistance of the rods determined by the rods' diameter, and muscular strength of the person in charge (Kogelbauer et al. 2013).

The designed system (CSPS, combination of soil physical sensors) was applied at the open water area for referencing echo sounding, at shallow water areas below 0.5 m to describe the shore line topography, and at the reed belt areas. The measurement procedure was similarly conducted at all sites using the sensors consecutively at the same site to create an instantaneously vertical profile in the soft mud and the consolidated lake bed sediments. The Hydra Probe measurement starts at the water surface, with the sensor head and its tines still in the air. After a few seconds the sensor is slowly inserted in the water and continuously submerged until no further penetration of the sensor is possible due to compacted mud. The penetrometer measurement starts at the mud layer, when first minimal pressure resistance is detected. The sensor is slowly submerged until the consolidated lake bottom. The pressure resistance rapidly increases when reaching more compacted mud and the shallow, consolidated lake bed sediments. Each sensor measurement was repeated at least three times for the same area to consider local variability

of the mud layer structure. At the open water surface the measurements were taken at predefined echo sounding reference points, using a small boat tied up by stakes. At the shore zone the measurements were taken along a short transect, starting with a point in the reed, going on at the transition from the reed to the open water surface, and then at the open water. This enables a description of the lake bed topography at the transition from the reed to the open water.

Mud cores were collected at some of the predefined echo sounding reference using a hand core sampler with polycarbonate core barrel. These samples had been analysed qualitatively (colour, roots) and quantitatively (particle size distribution, total and inorganic carbon, total nitrogen, pH, electrical conductivity, mineralogy) for the calibration of the CSPS sensors. In Tab. 1 the particle size distribution of the mud core samples of two reference points are listed. The percent by weight are given for the sand fraction S (from 2 mm to 0.063 mm), silt fraction U (from 0.063 mm to 0.002 mm), and clay fraction C (below 0.002 mm). The samples generally show high content of silt (0.002 mm to 0.05 mm) and clay (below 0.002 mm).

## 5 Results

The echo sounding campaigns resulted in a total of 2,000 km of transect measurements for SSS, SBES and SBP respectively. Approximately 4100 CSPS measurements are available for calibration purposes, complementing shallow areas (water depths below 50 cm) and shore line sediment layer composition and shore line morphology. More than 550 CSPS measurements are located at ten test areas of different mud accumulation, distributed over the lake area (Fig.1a), to account the distortion of acoustic signals.

According to the measuring campaigns the results can be classified as:

### SSS morphological information

Georeferenced side scan sonar (SSS) images: About 4000 SSS images were georeferenced using accurate positioning and attitude information from the RTK-GPS and IMU sensors. Due to a medium water depth of 1.4 m,

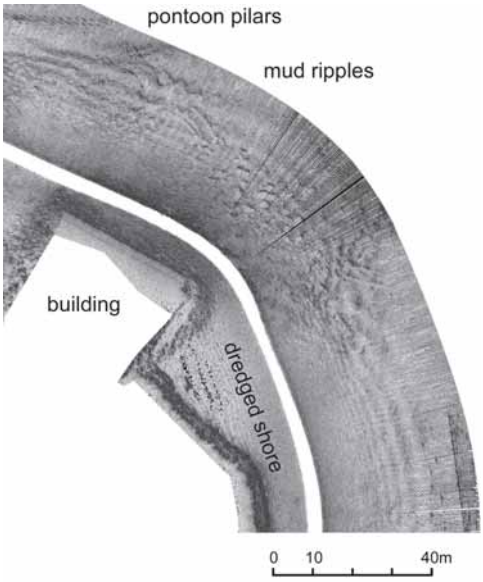


**Fig. 2:** Side scan sonar image showing mud ripples and man-made structures.

**Tab. 1:** Particle size distribution of the core samples at the reference points P47 and P111 (masl = metres above sea level).

| | Elevation (masl) | | p(S) (%) | p(U) (%) | p(C) (%) |
|---|---|---|---|---|---|
| **P47** | 113.40 | 113.56 | 5.6 | 54.6 | 39.8 |
| | 113.56 | 113.64 | 1.6 | 45.1 | 53.3 |
| | 113.64 | 113.72 | 2.2 | 41.9 | 55.9 |
| **P111** | 114.19 | 114.23 | 1.4 | 47.1 | 51.5 |
| | 114.23 | 114.28 | 4.1 | 44.5 | 51.4 |

the suitable sonar image strip width is limited to approximately 30 m. Information about the transition zone from the lake bottom to the reed area as well as manmade structures, pontoon pillars, dredged harbours etc., and mud surface morphology is given in detail. The main differences in the side scan backscatter of the mud surface represent erosional, depositional and dynamic environments (Fig. 2).

## High frequency echo sounding depth measurements of the mud surface layer

2,000 km of echo sounding depth measurements surveyed with high frequency sensors of 710 kHz and 100 kHz, and at low frequency of 10 kHz are available. The high frequency data show clearly a distinct reflection at the water-mud interface and enables the calculation of an accurate mud surface layer (Fig. 3).

## CSPS data and 10 kHz Sub Bottom Profiler data for mud thickness determination

The 10 kHz frequency is penetrating well the sediments and displays also significant reflections of layers deeper in the subsoil.

For the interpretation and correct layer detection of the 10 kHz sub bottom data, it was necessary to apply proper sound velocities not only for the water column, but also for the mud layer and for the subsoil. This could be achieved by integrating CSPS measurements in the sub-bottom data processing. 61 reference points within ten zones of different mud accumulation were compared. All reference points (CSPS measurements) were placed at intersections of at least two echo-sounding transects.

The comparison shows, that the first reflection displayed in the echogram is approximately at the same height as the Hydra Probe delineates the water-mud interface by a sudden decline to smaller volumetric water content θ ($m^3 \cdot m^{-3}$). The second reflection representing the interface between mud and the cohesive lake bed sediment is corresponding to the first significant pressure resistance peak detected by the cone penetrometer.

The acoustic sound velocity for the sub bottom layer detection was adapted until the echo

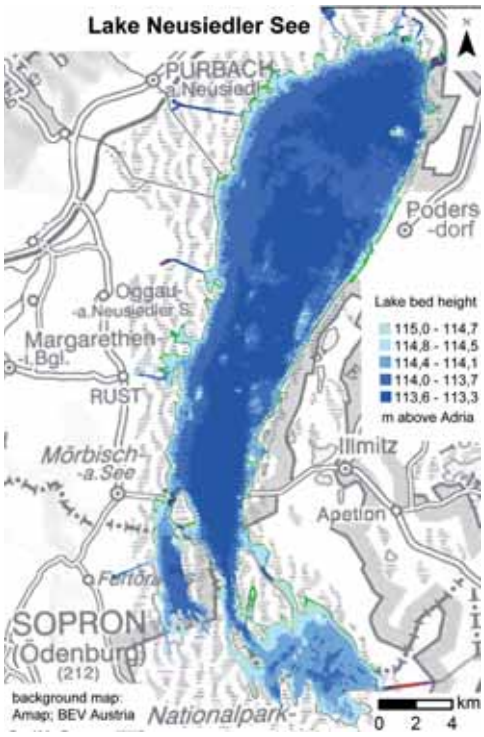


**Fig. 3:** Topography of the lake bed (mud surface).

sounding layers fitted with the CSPS layer delineation. After that, in spite of small differences, the hydro acoustic sub bottom data is providing reasonably good lake bed sediment structure information of Lake Neusiedl. As an example, reference points at two representative sites with different sediment layer composition (P47 high mud accumulation and P111 low mud accumulation), are shown in Figs. 4 and 5.

The CSPS measurements, left part in Figs. 4 and 5, of the Hydra Probe in water at almost constant θ of about 0.95 is interrupted by a sudden decline in θ to about 0.80 indicating the water-mud interface. The submersion end of the Hydra Probe sensor coincides with the point of detecting significant pressure resistance PR, consequently a continuous vertical mud-sediment profiling is gained with both sensors (Kogelbauer et al. 2013). In detail, the Hydra Probe measurements (ID47 and ID50; top blue scale) in Fig. 4 show a clear water-mud layer transition at 113.85 masl, where the

vol. water content θ suddenly decreases below 0.95. The penetrometer measurements (ID51 and ID53; bottom black scale) at point P47 detect two shallow top layers, which are also recorded by the echo sounder. The lake bottom is the significant penetration resistance peak of 1.2 MPa at 112.95 masl. The first penetration resistance peak at 0.6 MPa indicates already compacted mud. Thus the mud layer is about 0.9 m thick, ranging from the water-mud interface at 113.85 masl to the lake bottom at 112.95 masl, with an increasing degree of consolidation starting at 113.21 masl.

In contrast to a distinct mud layer at point P47, point P111 (Fig. 5) shows almost no mud layer and a highly consolidated lake bottom in the CSPS profile as well as in the echogram. The Hydra Probe measurements (ID4 and ID5) indicate only a very thin mud layer of about 8 cm at the water-mud interface height of 114.30 masl. The penetration resistance (ID7 and ID8) of the penetrometer rapidly increases indicating a highly consolidated layer that prevents further penetration. A high degree of consolidation is also indicated by the intensive red colour of the interfaces in the echogram.

The challenge for the establishment of a concise spatial dataset was the combination of SBES, SBP and CSPS in an optimum way to achieve the highest possible accuracy. Each dataset passed an individual quality check, based on classical statistics, removal of outliers, noise, and averages of repeated measurements. These datasets were then cross-referenced at approximately 61 calibration points, utilizing an interactive software tool, originally designed and programmed for the CSPS data smoothing and measurement analyses. In a further step cross referencing was performed using nearest neighbours of SBES and high frequency SBP data points. Hence, for each calibration point mud layer surface heights and thickness were obtained. Finally distortion factors for low frequency SBP readings were inversely calculated by comparing

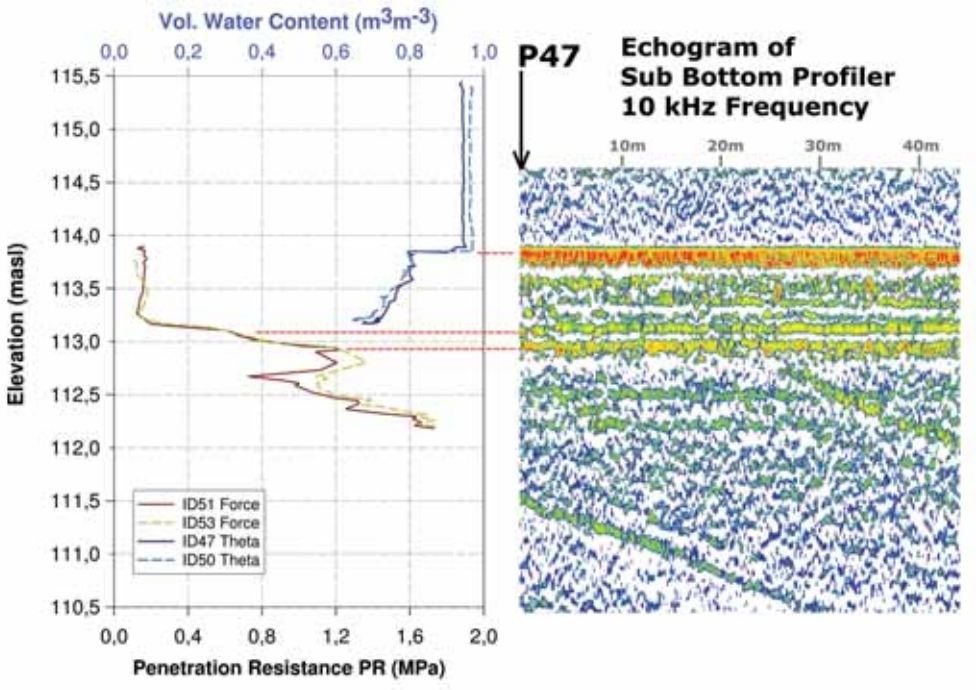


**Fig. 4:** Example of the layer validation by comparing the SBP echogram sequence (right) with the CSPS (left) at the reference point P47. The layering in the echogram coincides reasonably well with the CSPS interfaces. Strong reflections due to high impedance contrast indicated interfaces visualized by red-yellow.

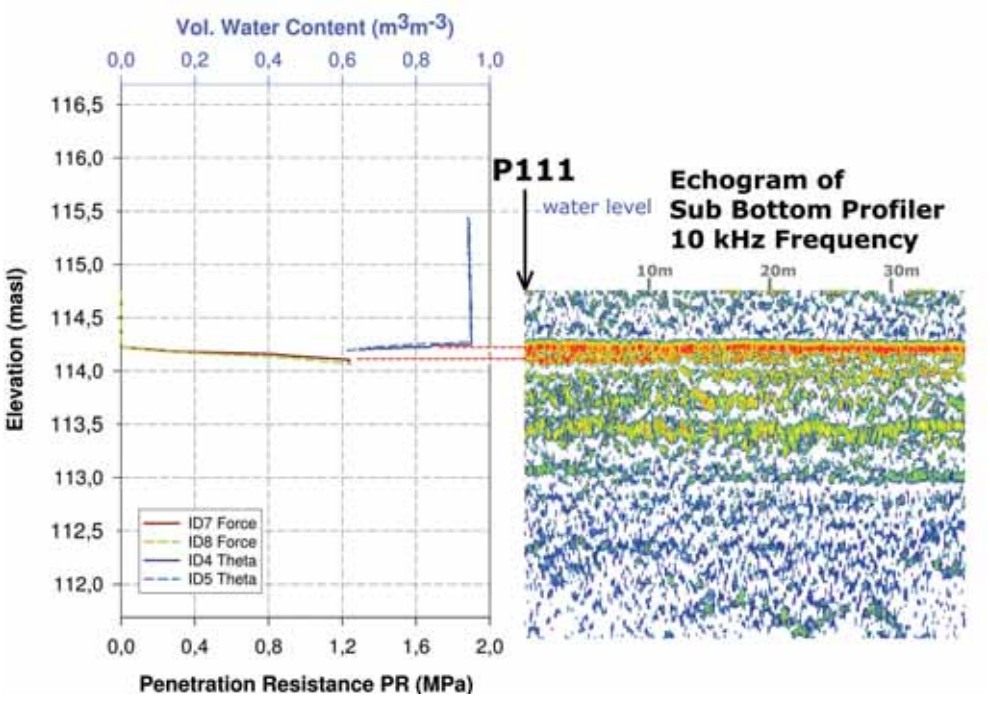


**Fig. 5:** Second example of layer validation at point P111 comparing the SBP echogram sequence (right) with the CSPS (left) showing little mud accumulation and a consolidated shallow lake bed.

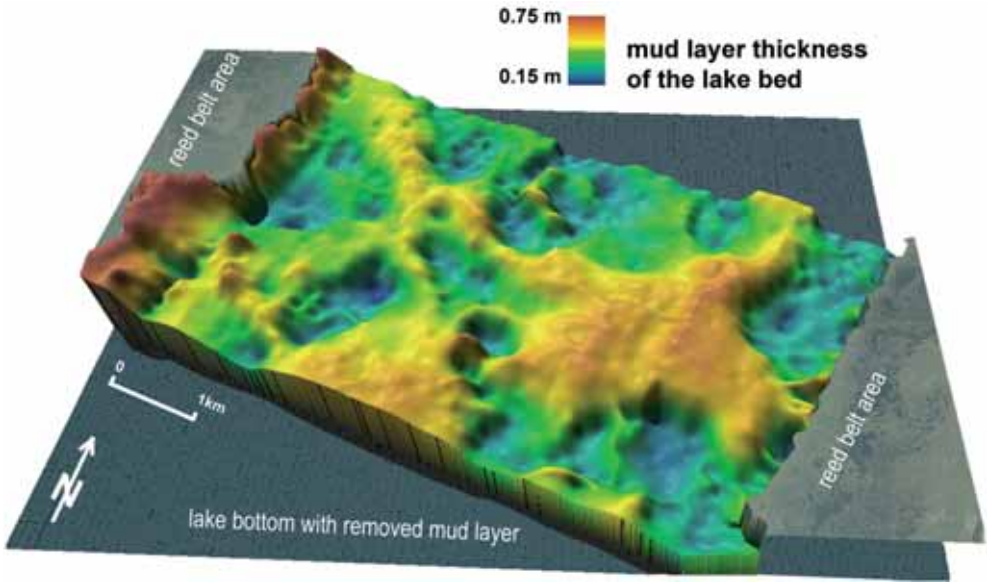


**Fig. 6:** Mud layer distribution and thickness at the central part of Lake Neusiedl, vertical exaggeration factor = 200.

the CSPS thickness and the SBP raw data. Thus the SBP data post processing was able to deliver a layer of consolidated sediments of the lake bottom within an accuracy of ± 5 cm. The difference between both layers is a good indicator for thickness and distribution of the mud layer of Lake Neusiedl (Fig. 6).

## 6 Discussion and Outlook

It could be proven that for the conditions of a shallow lake the water-mud interface can be reliably detected with SBES, SBP and CSPS. The results showed a very good agreement of these methods in the detection of the mud surface. The used SBP delivered suitable sediment layer images up to several metres. For an exact determination of the thickness of the mud layer, the distortion of the acoustic system could be calibrated with the readings of the CSPS. Repetitions of CSPS profile measurements proofed the reproducibility of data and reliability of the concept. Moreover, physical profile values are providing a continuous description of the depth of the sediment layer compositions.

Cross-referencing ensured the compensation of systematic errors of the echo sounding systems due to the density differences of water and mud layer. This procedure enabled the calculation of spatially distributed interface heights of high quality.

SSS images provide additional information for generating the shore line for the digital terrain model. The information about the shore line sediment layer composition and morphology is delineated from CSPS measurements at the transition zone from the open water body to the reed area.

The final result is a topographic dataset of the lake bottom and the mud layer, allowing generating high resolution digital terrain models (DTMs) of the lake.

## Acknowledgements

This project was supported by the European Regional Development Fund (ERDF) Cross-border Cooperation Programme Austria - Hungary 2007-2013. Reg. Nr. L00130, Acronym: “GeNeSee”.

## References

Bácsatyai, L., Csaplovics, E., Márkus, I. & Sindhuber, A., 1997: Digitale Geländemodelle des Neusiedler See-Beckens. – Wissenschaftliche Arbeiten aus dem Burgenland Band **97**, Burgenlandisches Landesmuseum, Eisenstadt, Österreich.

Bradford, J.M., 1986: Penetrability. – Klute, A. (ed.): Methods of Soil Analysis, Part 1, Physical and Mineralogical Properties. – Soil Science Society of America: 463–478, Madison, WI, USA.

Buchanan, L., 2005: Surveying in Fluid Mud. – Hydro International **9** (6). – http://www.hydro-international.com/issues/articles/id500-surveying_in_fluid_mud.html (13.2.2014).

Csaplovics, E., 1998: High resolution space imagery for regional environmental monitoring – status quo and future trends. – International Archives of Photogrammetry and Remote Sensing **32** (7): 211–216.

D’Amboise, C.J.L., 2012: Development of Profile Measurements Using a Frequency Domain Reflectometry Sensor in a Soft Sludge and Calibration for Use in the Neusiedler See. – M.Sc. Thesis, University of Natural Resources and Life Sciences, Vienna, Austria.

Eitzinger, J., Kubu, G., Formayer, H., Haas, P., Gerersdorfer, T. & Kromp-Kolb, H., 2009: Auswirkungen einer Klimaänderung auf den Wasserhaushalt des Neusiedlersees, Endbericht im Auftrag der Burgenlandischen Landesregierung vom 15. Juli 2005. – BOKU-Met Report 2009. ISSN 1994-4179, ISSN 1994-4187. – www.boku.ac.at/met/report/ (10.2.2014).

EuLakes vol. 2, 2013: European Lakes under Environmental Stressors. – Climate change and Future Risk, Project Report, 96 p.

Geschnatter, 2013: Die Wege des Wassers – Nationalpark Neusiedler See – Seewinkel. N1. April 2013. – www.nationalpark-neusiedlersee-seewinkel.at/tl_files/images/downloads/geschnatter/ Geschnatter2013_1.pdf (20.2.2014).

GeNeSee, 2011: Geodätische Neuerfassung des Systems Neusiedler See – Hanságkanal (GeNeSee). Projektantrag, Projektnummer L00130. Programm zur grenzüberschreitenden Kooperation Österreich-Ungarn 2007–2013. Universität für Bodenkultur Wien, 07.2011, Österreich.

Heine, E., Prokoph, A., Kogelbauer, I. & Loiskandl, W., 2013: Hydroakustische Erfassung der Morphologie und Sedimentschichtung des Neusiedler Sees. – Hanke, K. & Weinold, T. (Hrsg.): 17. Internationalen Geodätischen Woche Obergurgl, Herbert Wichmann Verlag, 2013, ISBN 978-3-87907-526-3.

Innomar Technologie GmbH, 2005: SES-2000 standard Parametric Sediment Echo Sounder: Users Guide.

Kogelbauer, I., Heine, E., D'Amboise, C., Müllebner, C., Sokol, W. & Loiskandl, W., 2013: Adaptation of Soil Physical Measurement Techniques for the Delineation of Mud and Lakebed Sediments at Neusiedler See. – Sensors **13** (12): 17067–17083, doi:10.3390/s131217067.

Loiskandl, W., Kogelbauer, I. & Nolz, R., 2012: Water and Landscape Management Aspects in the Neusiedler See Region. – Gastescu, P., Lewis, W. & Bretcan, J.P. (eds.): Water resources and wetlands. – ISBN: 978-606-605-038-8, Tulcea, Romania.

Lurton, X., 2002: An introduction to underwater acoustics: principles and applications. – Springer, Berlin, Heidelberg, ISBN 3-540-42967-0.

Missiaen, T., Slob, E. & Donselaar, M., 2008: Comparing different shallow geophysical methods in a tidal estuary, Verdronken Land van Saeftinge, Western Scheldt, the Netherlands. – Netherlands Journal of Geosciences, Geologie en Mijnbouw **87** (2): 151–164.

Nationalpark Neusiedler See – Seewinkel, 2012: www.nationalpark-neusiedlersee-seewinkel.at (10.2.2014).

Nitsche, F.O., Bell, R., Carbotte, S.M., Ryan, W.B.F. & Flood, R., 2004: Process-related classification of acoustic data from the Hudson River Estuary. – Marine Geology **209** (1): 131–145, ISSN 0025-3227.

QINSy, 2014: QINSy (Quality Integrated Navigation System). – http://www.qps.nl (15.6.2014).

Santamarina, J., Rinaldi, V., Fratta, D., Klein, K., Wang, Y., Cho, G. & Cascante, G., 2005: A Survey of Elastic and Electromagnetic Properties of Near-Surface Soils. – Near-Surface Geophysics: 71–88, eISBN: 978-1-56080-171-9, print ISBN: 978-1-56080-130-6.

Schmidt, J. & Csaplovics, E., 2011: Mapping the Austrian reed bed of Lake Neusiedl by means of airborne optical scanner imagery. – Csaplovics, E. & Schmidt, J. (eds): International Symposium on Advanced Methods of Monitoring Reed Habitats in Europe: pp. 55, ISBN: 978-3-941216-78-5.

Schönerklee, M., Kinner, P., Heiss, G., Soja, G., Friesl, W., Treitler, R., Schindler, J. & Kleissner, A., 2006: Neusiedler See – Tourismus mit Zukunft. – Wissenschaftliche Untersuchung zur Auswirkung des Wasserstandes des Neusiedler Sees innerhalb der Region Neusiedler See, Austrian Research Center Report U-0222.

Schrottke, K., Becker, M., Bartholomä, A., Flemming, B.W. & Hebbeln, D., 2006: Fluid mud dynamics in the Weser estuary turbidity zone tracked by high-resolution side-scan sonar and parametric sub-bottom profiler. – Geo-Marine Letters **26** (3): 185–198.

Soja, G., Züger, J., Knoflacher, M., Kinner, P. & Soja, A.M., 2013: Climate impacts on water balance of a shallow steppe lake in Eastern Austria (Lake Neusiedl).

Ulrick, R.J., 1983: Principles of Underwater Sound", McGraw-Hill, New York, NY, USA.

Address of the Authors:

Dr. Erwin Heine, University of Natural Resources and Life Sciences Vienna, Institute of Surveying, Remote Sensing and Land Information, Peter-Jordan-Straße 82, A-1190 Vienna, Austria, Tel.: +43-1-47654-5104, e-mail: erwin.heine@boku.ac.at

DI Ilse Kogelbauer, Univ. Prof. Dr. Willibald Loiskandl, Institute of Hydraulics and Rural Water Management, University of Natural Resources and Life Sciences, Vienna, Nußdorfer Lände 11, A-1190 Vienna, Austria, e-mail: {ilse.kogelbauer} {willibald.loiskandl}@boku.ac.at

M.Sc. Andreas Prokoph, Geomatik, HafenCity University, Hebebrandstraße 1, D-22297 Hamburg, Germany, Tel.: +49-40-42827-532

Manuskript eingereicht: März 2014
Angenommen: Juni 2014

PFG 2014 / 5, 0351 – 0367
Stuttgart, October 2014

Article

# Early Detection of Bark Beetle Infestation in Norway Spruce (*Picea abies*, L.) using WorldView-2 Data

Markus Immitzer & Clement Atzberger, Vienna, Austria

**Keywords:** WorldView-2, bark beetle infestation, tree vitality, green-attack, pre-visual detection, Norway spruce

**Summary:** In Central Europe and North America, bark beetle infestations cause considerable economic losses. If infested trees are not rapidly removed, large areas can be damaged. Removal of infested trees has to be done during the so-called "green-attack" stage, which is before the bark beetles move to other trees. Field surveys even if they are feasible are cost intensive and impractical if large areas have to be monitored. The aim of the study was to analyse the suitability of 8-band WorldView-2 satellite imagery for detecting bark beetle infestations of two intensity stages (e.g. "dead" and "green-attack") against "healthy" (non-attacked) trees. For classifying individual trees two classifiers, random forest and logistic regression, were evaluated. Despite the relative large class overlap in the spectral signatures, the sample trees (n = 600) could be assigned to the classes "dead", "green-attack", and "healthy" with an overall accuracy of about 75%. Producer's and user's accuracies of all classes were around 70%. The best result was obtained with random forests using the eight spectral bands of a WorldView-2 image acquired in July. With this dataset, an overall accuracy of 76% and a kappa coefficient of 0.61 were achieved. For the separation of the classes "healthy" and "green-attack", vegetation indices based on 2-band normalized differences as well as ratios yielded nearly as good results as the classification with all eight spectral bands. The best results were obtained by combining either the Green or Yellow band with the Near Infrared 1. With regard to individual bands, the Yellow and the Red band are defined as most important ones. We can conclude that 8-band WorldView-2 imagery has the potential for creating hotspot maps of infested trees or of trees with an increased risk of infestation. This could have positive implications for the forest practice.

**Zusammenfassung:** *Frühzeitige Erkennung von Borkenkäferbefall an Fichten mittels WorldView-2 Satellitendaten*. Borkenkäferepidemien führen in Europa und Nordamerika immer wieder zu großen ökonomischen Verlusten in der Forstwirtschaft. Um großflächige Ausbreitungen zu verhindern, müssen befallene Bäume rasch erkannt und entfernt werden. Die gezielte Entnahme der Bäume, bevor die Käfer ausgeflogen sind, ist schwierig, da die Bäume meist noch keine Verfärbung der Nadeln zeigen. Daher sind derzeit aufwändige und kostenintensive Feldbegehungen notwendig, um eine Ausbreitung des Schädlings zu vermeiden. In dieser Arbeit wurden sehr hochauflösende WorldView-2 Satellitendaten mit acht Spektralkanälen von zwei Aufnahmetagen untersucht, um Borkenkäferbefall frühzeitig zu erkennen. Dazu wurde versucht nicht befallene Bäume von befallenen jedoch noch nicht verfärbten („green-attack") und von bereits stark verfärbten bzw. abgestorbenen Bäumen auf Grund der spektralen Reflexion zu trennen. Hierbei wurden die Einzelbaumobjekte mittels Random Forest und Logistischer Regression klassifiziert. Trotz der großen Überschneidungen der spektralen Signaturen zwischen den Klassen „gesund", „befallen – ohne sichtbare Verfärbung" und „abgestorben" konnten diese mit Gesamtgenauigkeiten von rund 75% getrennt werden. Auch die Nutzer- und Produzentengenauigkeiten aller Klassen lagen dabei über 70%. Am besten konnten die Beispielbäume in der Aufnahme vom Juli klassifiziert werden, mit einer Gesamtgenauigkeit von 76% und einem kappa-Wert von 0.61. Zusätzlich wurden verschiedene Vegetationsindizes getestet. Dabei erzielten einzelne normalisierte Differenz- bzw. Verhältnis-Indizes nahezu gleich gute Ergebnisse wie Modelle mit allen acht Spektralkanälen. Die besten Ergebnisse wurden dabei mit Kombinationen des Grün- bzw. Gelb-Kanals mit dem Nahen Infrarot 1 Kanal erreicht. Bei den Modellen basierend auf einzelnen Kanälen brachten der Gelb- bzw. der Rot-Kanal die höchsten Genauigkeiten. Die erzielten Ergebnisse zeigen, dass

 www.schweizerbart.de
DOI: 10.1127/1432-8364/2014/0229 1432-8364/14/0229 $ 4.25

im Frühsommer aufgenommene WorldView-2 Szenen Potential für die frühzeitige Erkennung von Borkenkäferbefall aufweisen. Diese Tatsache könnte für die Visualisierung von befallenen Bäumen beziehungsweise von Bäumen mit hohem Befallsrisiko genutzt werden. Solche hotspot-Karten könnten eine große Unterstützung für die forstliche Praxis bei der Bekämpfung von Borkenkäferepidemien darstellen.

## 1 Introduction

Natural disturbances play an important and often positive role in forest ecosystems. At the same time, however, such disturbances cause great economic damage for forest owners. In Central-European forests windthrow and bark beetles are considered the most important abiotic and biotic disturbance agents in the last century (Schelhaas et al. 2003). After the big windthrows in Central Europe in the first ten years of this millennium ("Kyrill" in January 2007, "Paula" in January 2008, and "Emma" in March 2008), beetle infestations in Norway spruce (*Picea abies*, L.) forests increased dramatically (Tomiczek et al. 2011). Most likely, these problems will increase in the near future. For example, models based on climate change scenarios predict an increasing risk for bark beetle outbreaks (Netherer & Schopf 2010, Seidl et al. 2011, Overbeck & Schmidt 2012). As Norway spruce is the most valuable tree for European forestry, suitable monitoring methods have to be developed.

In Austria and other European countries, the ecological and economical most relevant bark beetle species are *Ips typographus*, L., and *Pityogenes chalcographus*, L.. Both are on Norway spruce and attack mainly weakened trees. To protect other trees, infested individuals have to be removed before the new larvae are fully developed and start to leave the trees for infesting neighbouring trees. An early detection of infested trees is therefore important to avoid mass outbreaks; best before (visually) discolorations are visible. Usually foresters have to look for early signs of infestation like boring dust around the base of trees (Krehan 2008). However, a regular large-scale control is too expensive and not practical. Remote sensing techniques are considered useful for an early detection of potentially infested hotspots.

Numerous studies, mainly in North America, pointed out the potential of remote sensing data for detection of (declining) health status of trees. Most of them analysed detection of Mountain Pine Beetles (*Dendroctonus ponderosae*, Hopkins) infestations on Lodgepole Pine (*Pinus contorta*, Dougl.) in Canada. While advanced stages of damage (so called "red-attack" and "grey-attack") can be detected easily, the early detection of an infestation (henceforth referred to as "green-attack") is problematic (Roberts et al. 2003, Skakun et al. 2003, Wulder et al. 2004, 2006a, 2006b, Coops et al. 2006). Due to the problems of early detection North American researchers focus their work on the analysis of areas around old "red attack" areas to locate new infestation hot spots (Wulder et al. 2009, Coggins et al. 2010, 2011).

An early detection of infested trees ("green-attack") would be a major breakthrough regarding the control, prevention and mitigation of large-scale outbreaks. For this reason investigations in the use of remote sensing for detection of infestation before visible discoloration ("green-attack", early detection) continues. Heath (2001) compared the spectral signatures (compact airborne spectrographic imager – CASI) of healthy, freshly infected ("green-attack") and previously infected ("red-attack") trees and found some trends in the spectra, partially confirming previous studies (e.g., Heller 1968, Hall 1981). The main problem was the large intra-class variability of the reflectance values hampering the separability of the different infestation classes. Similar results were achieved by Sharma (2007). For the identification of infestation he characterized the spectral bands between 900 nm and 1100 nm as the most essentially. He concluded that early detection could be possible under certain conditions. Cheng et al. (2010) were able to demonstrate effects of water deficit and changes in chlorophyll content of artificially stressed needles through wavelet analysis of reflection spectra measured in the laboratory. They found good statistical separability in the wavelength ranges between 950 nm and 1390 nm. These results

imply high potential for a cost effective and large-scale method for detection of health status classes of trees.

For the detection of large-scale bark beetle infestation, like in North America, satellite data with low (Eklundh et al. 2009) to medium resolution (Meigs et al. 2011, Meddens et al. 2013) can deliver adequate information. For early detection of mostly small-scale infestations in Central Europe the spatial resolution is very important (Lausch et al. 2013). With the new generation of very high resolution (VHR) satellite data, multispectral data with spatial resolutions in the metre range are available. Marx (2010) used bi-temporal RapidEye satellite images (mid-April to mid-June) for the detection of bark beetle infested spruce. The first image was used for the separation between spruce stands and deciduous trees. The second image was used for the separation of different attack classes within the spruce stands. In addition to the RapidEye spectral bands, different vegetation indices were included in the analysis. The reference data came from foresters who delineated infested (and healthy) areas in the field. Following experimental set-ups used in North America three infestations classes were classified: "healthy" (= "non-attacked"), "infested" ("green-attack") and "red" ("red-attack"). Classification was done by creating decision tree models. The classification results showed a good separation of the already discoloured trees ("red-attack"). The two classes "healthy" and "infestation" were frequently misclassified. Ortiz et al. (2013) used RapidEye and TerraSAR-X data, both acquired in May 2009, to detect bark beetle green-attack in southwest Germany. The RapidEye data achieved higher classification accuracies than the SAR data. The highest accuracy was achieved by combining the two datasets.

WorldView-2 data with higher spatial and spectral resolution have also been used for the detection of tree health status. Finnigan (2011), for example, used WorldView-2 data for the "red-attack" detection on Lodgepole pine. Filchev (2012) tried to map bark beetle stressed spruce in a Bulgarian Biosphere reserve. He used vegetation indices calculated from the eight WorldView-2 spectral bands. However, the results were not verified with field data.

In addition to satellite data, hyperspectral data from airborne platforms were evaluated for early detection of bark beetle infestations on spruce in several studies. Thereby early stages of infestation ("green-attack") could be detected (Fassnacht et al. 2012, 2014). Lausch et al. (2013) tried to detect very early stages of bark beetle infestation and even forecast infestation with one- or two-year old hyperspectral data. They found a tendency towards detectability of health status; however, they conclude that the achievable accuracies are too low for an application in forestry.

The aim of our study was to analyse the suitability of WorldView-2 imagery for detecting three bark beetle infestation classes on spruce: "dead" (red/grey-attack), "green-attack", and "healthy" (non-attacked) in Central Europe. WorldView-2 is the first commercial satellite providing data with very high spatial (2 m) and spectral (8 bands) resolution. Both factors are important for mapping tree species or health status of individual trees. Since foresters need an early recognition of infested areas remote sensing data were acquired early in summer. For evaluation of the image's acquisistion date, data from June and July were tested. Focus was set on identifying relevant spectral bands and vegetation indices for separating the classes "healthy" and "green-attack". The identification of relevant spectral bands has direct implications for practicers as the 4-band version of WorldView-2 data is much cheaper compared to the 8-band version. Ground truth data for the three classes were provided by local foresters through field inspection.

## 2 Data and Methods

### 2.1 *Study Site*

The study site covers approximately 1100 ha and is located in central Austria (47°28'N, 14°30'E) in the province of Styria (Fig. 1). The terrain is mountainous and extends from the montane to the subalpin life zone with an elevation ranging from 680 m and 2400 m above sea level. The annual rainfall is between

1250 mm and 1500 mm, with a maximum in July. The bedrocks are mainly base-poor silicates, quartz phyllites and gneisses. The potential natural forest community in the study site is a spruce-fir forest with admixture of beech, larch and sycamore maple (Kilian et al. 1994). The privately owned forests are commercially used focusing on timber production.

The study site is located next to Enns valley. In this region *Ips typographus*, L. and *Pityogenes chalcographus*, L. are the two most common bark beetle species on spruce. The logging statistics from the year 2010 of Styria reveals a substantial quantity of damaged timber (roughly 1 million cubic metre) caused by bark beetle attacks. This corresponds to approximately one-fifth of the total logging amount of that year. The huge impact of the bark beetle attacks was primarily a late consequence of heavy storm events in the preceeding years ("Kyrill", "Paula" and "Emma") (Fachabteilung 10C des Landes Steiermark – Forstwesen 2011).

## 2.2 *WorldView-2 Data*

The WorldView-2 satellite provides very high spatial resolution data with eight spectral bands. At nadir the ground resolution (GSD) is 50 cm for the panchromatic band (0.46 µm – 0.80 µm) and 200 cm for the multispectral bands. In addition to the four standard bands Blue (0.45 µm – 0.51 µm), Green (0.51 µm – 0.58 µm), Red (0.63 µm – 0.69 µm), and Near Infrared 1 (NIR 1, 0.77 µm – 0.90 µm), another four bands are available. The four additional bands are Coastal (0.40 – 0.45 µm), Yellow (0.59 µm – 0.63 µm), Red Edge (0.71 µm – 0.75 µm), and Near Infrared 2 (NIR 2, 0.86 µm – 1.04 µm). Further details about the sensor can be found on the website of the provider (Digital Globe 2014) and in Updike & Comp (2010). WorldView-2 data can be ordered either with the four conventional bands or (at higher costs) with all eight bands. The good suitability of WorldView-2 for tree species classification has already been shown (Immitzer et al. 2012a, Waser et al. 2014).

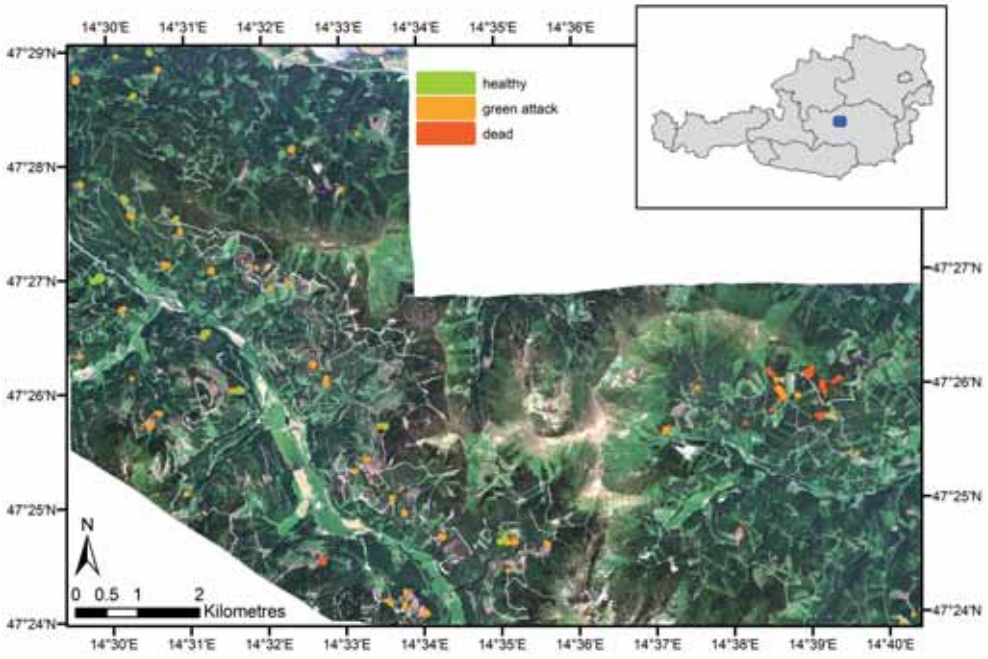


**Fig. 1:** WorldView-2 image (true-colour composite with the bands Red, Green, Blue) of the study site from June 2010. The locations of the reference data are shown in green ("healthy"), orange ("green-attack") and red ("dead"). The inlet indicates the position (blue) of the study site in the province of Styria in Austria.

For the purpose of the study, three WorldView-2 images with eight bands and processing level "Ortho Ready Standard" were obtained. The first image was acquired in June 2010. At that time the first generation of bark beetle was fully developed. The second image was taken in July and third in October, at the end of the growing season. All scenes were recorded under cloudless conditions over the study site. Detailed recording parameters can be found in Tab. 1. The third image was only used for confirming the location of reference data identified during field work. An image acquisition in October would be too late for early detection of "green-attack". Hence, only the two summer images (June and July 2010) were used for the classification exercise.

Before data analysis, the two summer scenes were atmospherically corrected, pansharpened and orthorectified. To derive top-of-canopy reflectance, the pixel gray values (digital numbers) were first converted into spectral 'at-sensor' radiance (Updike & Comp 2010) using the ENVI module (ENVI 4.8) FLAASH. The settings were chosen iteratively by checking the resulting reflectance values for plausibility. Optimal results were obtained with the following FLAASH settings: Atmospheric Model: Mid-Latitude Summer, Aerosol Model: Rural, Initial Visibility: 60 km (June) and 70 km (July). The atmospheric correction resulted in meaningful spectral reflectance signatures of the tree crowns. For visualisation purposes a pansharpening was performed to enhance the spatial resolution of the eight multispectral bands. Therefore, the HCS (Hyperspherical Color Space) algorithm (Padwick et al. 2010) implemented in ERDAS Imagine was used. Finally, both images, with 2 m and 0.5 m were orthorectified using a digital terrain model (5 m grid) and about 20 ground control points per scene. The coordinates of the control points were taken from a colour-infrared orthophoto with 0.5 m pixel size. The achieved average accuracy (RMSE) was about 1.8 pixels on images with 2 m pixel size.

## 2.3 *Reference Data*

As reference information we used groups of infested and healthy trees identified by experienced local forest staff through field inspections in the summer months. The tree groups were surveyed with GPS and marked on orthophotos. In most cases, the two classes were located near each other. So systematic differences in slope and azimuth (and consequently in illumination conditions) between the two classes can be excluded. Some of the infested trees were discoloured over the acquisition period. Others showed no visual changes between summer and autumn images. Most of the infested tree groups, however, were harvested by the foresters before the third image was acquired to prevent large-scale outbreaks.

Within the study we assumed that infestation by bark beetle (*Ips typographus*, L.) caused the discoloration of the trees. The trees were typically attacked early in spring or in the previous year. Healthy and infected trees display no visible differences in the true colour composites of the summer images (Fig. 2). Trees that are clearly discoloured in the summer images (June, July) were assigned to the class "dead" (red/grey-attack). We assume that these trees were attacked by bark beetle in one of the previous years and were already dead or almost dead in 2010. Fig. 2 shows sample images of the three data acquisition dates for the three infestation classes.

**Tab. 1:** Recording parameters of the three WorldView-2 images.

| | June | July | October |
|---|---|---|---|
| Acquisition date | 12 June 2010 | 10 July 2010 | 11 October 2010 |
| Scan direction | reverse | forward | forward |
| Mean satellite elevation | 76.8° | 65.6° | 66.7° |
| Mean satellite azimuth | 159.1° | 135.5° | 7.6° |
| Mean off nadir view angle | 11.8° | 21.4° | 20.9° |

Based on the reference polygons from field inspections and the two summer scenes, we selected in total about 600 reference trees within each image. In the June scene we manually delineated 257 "healthy", 272 "green-attacked", and 81 "dead" trees. In the July image 256 "healthy", 245 "green-attack", and 79 "dead" trees were identified. For each reference tree, we manually delineated the well-illuminated part of the tree crown to minimize shadow effects (Clark et al. 2005, Leckie et al. 2005, Greenberg et al. 2006, Immitzer et al. 2012a). It was not possible to automate the tree crown delineation because of strongly varying acquisition geometries.

To locate the sample trees, the pansharpened image with 0.5 m pixel size was displayed together with the multispectral image with 2 m pixel size both as colour-infrared composite (RGB: NIR 1, Red and Green). Then we selected the sun-lit pixels per tree crown in the multispectral image with 2 m pixel size and converted them to a polygon vector file. Finally, this file was used for extracting the spectral information from the corresponding WorldView-2 image. This workflow allowed a rapid

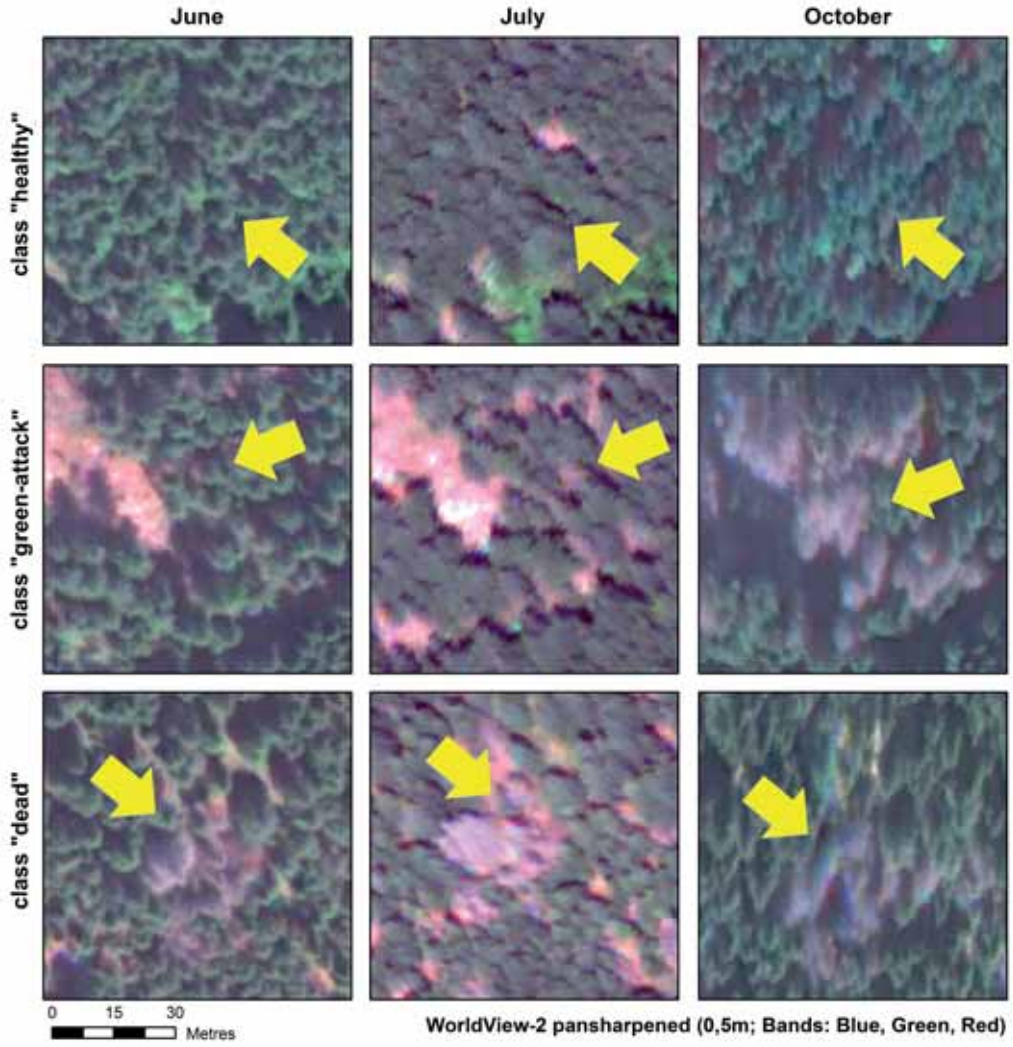


**Fig. 2:** Examples (marked with yellow arrows) of the three infestation classes ("healthy", "green-attack" and "dead") on pansharpened and atmospherically corrected summer and autumn WorldView-2 images.

selection and pixel-sharp demarcation of tree crowns (Immitzer et al. 2012b).

## 2.4 *Spectral Separation and Classification of Infestation Classes*

Based on the manually delineated tree crowns (section 2.3), the spectral values in the eight WorldView-2 bands were extracted and analysed. The mean values for each crown polygon were calculated and used for further analysis.

For separating the three infestation classes, we used the non-parametric, ensemble learning random forest (RF) classifier (Breiman 2001). The RF classifier is increasingly used for the classification of remote sensing data (Pal 2005, Immitzer et al. 2012a, Rodríguez-Galiano et al. 2012). Some of the advantages of this method are (I) it does not make any assumptions about data distribution and the collinearity in the data, (II) it does not require common covariance in the classes, (III) thanks to the integrated bootstrapping the accuracy estimates are obtained from independent samples, and (IV) it provides variable importance measures which can be helpful for feature selection (Breiman 2001, Liaw & Wiener 2002, Hastie et al. 2009, Immitzer et al. 2012a, Toscani et al. 2013). In our study, the following parameterization of the RF was used: 500 trees and two variables at each node (= the square-root of the total number of input variables) at each node. We created models using all eight, respectively, the four conventional WorldView-2 bands (Blue, Green, Red and NIR 1). We analysed the 2- and 3-class separability.

Although RF provides variable importance measures, logistic regression (LR) was used as an additional method to identify the most important spectral bands for separating the two most similar classes "green-attack" and "healthy". One advantage of LR is that models can also be built with only one explanatory variable, which is not meaningful with a decision tree-based method like RF. The drawback of LR is that it can only handle two-class problems. Using LR, we first created models with all eight spectral bands (baseline) and then with the four conventional ones. Next, every single band was used individually.

In addition to the eight spectral bands, we tested three categories of vegetation indices (Tab. 2), similar to other studies (Buschmann & Nagel 1993, Gitelson & Merzlyak 1994, Sims & Gamon 2002, Marx 2010). Within each category, all possible band combinations were tested. The first group of indices was obtained by calculating the difference and the second by calculating the ratio of two WorldView-2 bands, respectively. Analogously to the formula of the widely used NDVI (normalized difference vegetation index) (Rouse et al. 1973), normalized differences were calculated as a third group, again using all possible permutations.

To build LR models, we used bootstrap samples (random sampling with replacement) drawn from the original dataset (Efron 1979). With the generated model all undrawn samples were classified and the classification accuracy was then calculated. We repeated this procedure 500 times and used the majority votes of the iterations.

To evaluate the results of RF and LR we produced confusion matrices with the majority vote from all bootstrap iterations and calculated the producer's and user's accuracies for each class, the overall accuracy (correct classification rate), and Cohen's kappa coefficient (Cohen 1960).

For modelling R 3.0.2 (R Core Team 2013) was applied with the additional packages MASS (Venables & Ripley 2002), randomForest (Liaw & Wiener 2002), and caret (Kuhn et al. 2013).

**Tab. 2:** Formulas for indices calculation: $R_x$ and $R_y$ denote reflectance values of two different WorldView-2 bands. All possible permutations were tested. The indices were evaluated by logistic regression.

| Index type | Index formula |
|---|---|
| Difference indices | $R_y - R_x$ |
| Ratio indices | $\frac{R_x}{R_y}$ |
| Normalised difference indices | $\frac{R_y - R_x}{R_y + R_x}$ |

# 3 Results

## 3.1 *Spectral Signatures*

Fig. 3 shows the spectral signatures of the three infestation classes based on the July scene. The class "dead" shows higher reflectance values in the visible wavelength range and lower values in the near infrared compared to the two other classes. The differences between the classes "green-attack" and "healthy" are much smaller. The mean value of the class "green-attack" often lies between the average signatures of the two other classes. The largest distinctions between the classes "healthy" and "green-attack" appeared in the bands Yellow and Red. However, we found high within-class variances in all classes leading to significant class overlaps.

## 3.2 *Results of the Random Forest Classifier for the three Infestation Classes*

The RF classification of the three infestation classes based on the spectral data (all eight bands) produced very similar results for the two summer images: the overall accuracy with the June image was 74.4%, and with the July image 76.2%. Kappa coefficient was around 0.60 for both classifications. The con-

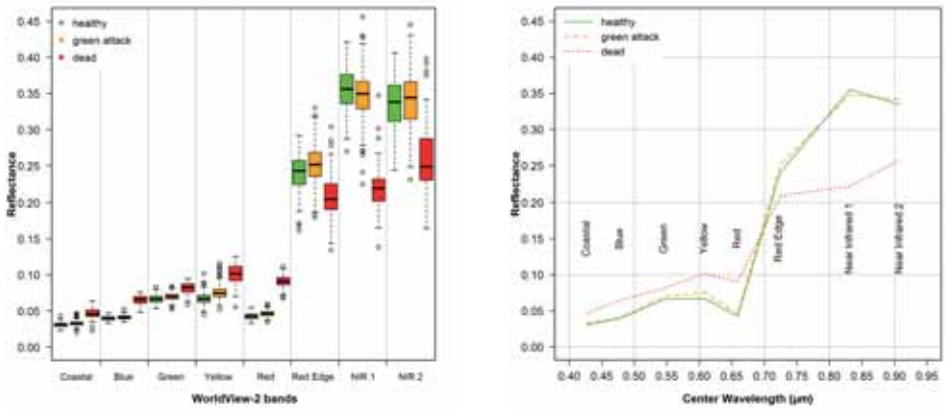


**Fig. 3:** Reflectance values of the three infestation classes "healthy", "green-attack" and "dead" based on the WorldView-2 image acquired on 10th July 2010: (a) boxplots and (b) spectral signatures (median values).

**Tab. 3:** Confusion matrix for the three classes "healthy", "green-attack", and "dead" using all eight bands of the WorldView-2 images from June and July, respectively, and the random forest classifier (independent bootstrapping results).

| | Field data | | | | | | | | | |
|---|---|---|---|---|---|---|---|---|---|---|
| | healthy | | green-attack | | dead | | Σ | | User's acc. | |
| Classified as | June | July | June | July | June | July | June | July | June | July |
| Healthy | 167 | 185 | 65 | 67 | 0 | 0 | 232 | 79 | 0.720 | 0.734 |
| Green-attack | 90 | 71 | 207 | 178 | 1 | 0 | 298 | 249 | 0.695 | 0.715 |
| Dead | 0 | 0 | 0 | 0 | 80 | 79 | 80 | 252 | 1.000 | 1.000 |
| Σ | 257 | 256 | 272 | 245 | 81 | 79 | 610 | 580 | | |
| Producer's acc. | 0.650 | 0.723 | 0.761 | 0.727 | 0.988 | 1.000 | Overall acc. | | 0.744 | 0.762 |

fusion matrices in Tab. 3 show that the class "dead" can be nearly perfectly separated from the two other classes. Producer's (PA) and user's accuracy (UA) for the class "healthy" was for the two images in the order of ≥ 72% (except PA for June image: 65.0%). Similar values were obtained for the class "green-attack", with however somewhat higher PA (73% – 76%) and lower UA (70% – 72%). Between the two summer images, only small differences could be detected. The PA of the July image was higher for the class "healthy" (72.3% vs. 65.0%) and for the class "green-attack" lower (76.1% vs. 72.7%) compared to the June image.

The use of the four conventional bands instead of all eight bands resulted in a decrease of classification accuracy for both images. The obtained overall accuracy for June was 71.6% (kappa 0.53) and those for July 70.2% (kappa 0.51).

### 3.3 *Separation of the Classes "Healthy" and "Green-attack"*

The bootstrapped results using RF and LR for separating the classes "healthy" and "green-attack" are shown in Tab. 4 to Tab. 8. The colours indicate the level of accuracy (based on kappa coefficients), increasing from white to green. As expected, the models without the easily separable class "dead", showed lower classification accuracies compared to the 3-class problem. Using all eight bands, both classes "healthy" and "green-attack" could be correctly assigned with an accuracy of around 70% with both approaches (RF and LR) and both images. The models based on the four conventional bands showed generally lower classification precision, except the LR model using the June data (Tab. 4).

The models with single spectral bands achieved significantly lower results, particularly for the June image (Tab. 5). When assessed individually, the Red and Green bands were most significant in the June image. In the July image, the drop in accuracy was less pronounced. Here, the Yellow band showed the highest accuracy, closely followed by the Red band. The two bands almost reached an accuracy of 70%, which is comparable with those of the LR models with the four conventional bands. For both summer images, the worst results were obtained using solely the bands in the near infrared. The Red Edge band had little discriminative power when used alone.

The results obtained from LR models using single bands could be confirmed with the two importance measures derived from RF model

**Tab. 4:** Overall accuracies and corresponding kappa coefficients (in brackets) from random forest (RF) and logistic regression (LR) models to separate "healthy" and "green-attack" samples using all eight and the four conventional spectral bands of WorldView-2 images acquired in June and July (independent bootstrapping results).

| | RF – eight bands | RF – four bands | LR – eight bands | LR – four bands |
|---|---|---|---|---|
| June | 0.703 (0.405) | 0.682 (0.364) | 0.713 (0.424) | 0.726 (0.451) |
| July | 0.737 (0.473) | 0.659 (0.318) | 0.711 (0.424) | 0.693 (0.384) |

**Tab. 5:** Overall accuracies and corresponding kappa coefficients (in brackets) from logistic regression models to separate "healthy" and "green-attack" samples using single bands of the WorldView-2 images acquired in June and July (independent bootstrapping results).

| | Coastal | Blue | Green | Yellow | Red | Red Edge | NIR 1 | NIR 2 |
|---|---|---|---|---|---|---|---|---|
| June | 0.493 (-0.036) | 0.631 (0.260) | 0.656 (0.311) | 0.626 (0.250) | 0.658 (0.315) | 0.531 (0.056) | 0.518 (0.031) | 0.484 (-0.048) |
| July | 0.583 (0.164) | 0.565 (0.127) | 0.635 (0.269) | 0.693 (0.384) | 0.669 (0.337) | 0.575 (0.149) | 0.543 (0.082) | 0.523 (0.043) |

**Tab. 6:** Overall accuracies and corresponding kappa coefficients (in brackets) from logistic regression models to separate "healthy" and "green-attack" samples using difference indices from the WorldView-2 images acquired in July (below the diagonal) and in June (above the diagonal), (independent bootstrapping results).

| Band | Coastal | Blue | Green | Yellow | Red | Red Edge | NIR 1 | NIR 2 |
|---|---|---|---|---|---|---|---|---|
| Coastal | - | 0.643 (0.284) | 0.648 (0.295) | 0.628 (0.254) | 0.643 (0.284) | 0.520 (0.034) | 0.533 (0.062) | 0.497 (-0.021) |
| Blue | 0.511 (0.018) | - | 0.624 (0.246) | 0.567 (0.131) | 0.624 (0.246) | 0.503 (-0.004) | 0.505 (0.000) | 0.486 (-0.057) |
| Green | 0.551 (0.099) | 0.593 (0.185) | - | 0.539 (0.075) | 0.539 (0.073) | 0.482 (-0.064) | 0.473 (-0.082) | 0.469 (-0.077) |
| Yellow | 0.699 (0.396) | 0.667 (0.332) | 0.653 (0.304) | - | 0.471 (-0.086) | 0.467 (-0.091) | 0.473 (-0.071) | 0.457 (-0.111) |
| Red | 0.603 (0.203) | 0.661 (0.320) | 0.499 (-0.011) | 0.637 (0.272) | - | 0.474 (-0.078) | 0.474 (-0.069) | 0.454 (-0.117) |
| Red Edge | 0.559 (0.117) | 0.575 (0.148) | 0.569 (0.136) | 0.507 (0.007) | 0.557 (0.112) | - | 0.478 (-0.066) | 0.478 (-0.056) |
| NIR 1 | 0.551 (0.099) | 0.561 (0.119) | 0.585 (0.167) | 0.615 (0.228) | 0.581 (0.159) | 0.681 (0.361) | - | 0.514 (0.020) |
| NIR 2 | 0.505 (0.005) | 0.505 (0.006) | 0.499 (-0.009) | 0.471 (-0.074) | 0.495 (-0.018) | 0.517 (0.029) | 0.597 (0.194) | - |

**Tab. 7:** Overall accuracies and corresponding kappa coefficients (in brackets) from logistic regression models to separate "healthy" and "green-attack" samples using ratio indices from the WorldView-2 images acquired in July (below the diagonal) and in June (above the diagonal) (independent bootstrapping results).

| Band | Coastal | Blue | Green | Yellow | Red | Red Edge | NIR 1 | NIR 2 |
|---|---|---|---|---|---|---|---|---|
| Coastal | - | 0.616 (0.232) | 0.597 (0.194) | 0.618 (0.234) | 0.631 (0.262) | 0.509 (0.010) | 0.507 (-0.001) | 0.480 (-0.067) |
| Blue | 0.547 (0.091) | - | 0.586 (0.169) | 0.535 (0.066) | 0.629 (0.257) | 0.539 (0.074) | 0.582 (0.162) | 0.577 (0.151) |
| Green | 0.507 (0.002) | 0.533 (0.063) | - | 0.501 (-0.026) | 0.599 (0.198) | 0.597 (0.195) | 0.707 (0.412) | 0.637 (0.274) |
| Yellow | 0.627 (0.253) | 0.671 (0.340) | 0.647 (0.293) | - | 0.550 (0.098) | 0.654 (0.307) | 0.62 (0.236) | 0.648 (0.295) |
| Red | 0.547 (0.090) | 0.649 (0.296) | 0.639 (0.277) | 0.543 (0.083) | - | 0.641 (0.28) | 0.694 (0.385) | 0.671 (0.341) |
| Red Edge | 0.523 (0.037) | 0.497 (-0.014) | 0.521 (0.030) | 0.663 (0.323) | 0.581 (0.158) | - | 0.488 (-0.044) | 0.535 (0.063) |
| NIR 1 | 0.621 (0.238) | 0.607 (0.211) | 0.683 (0.364) | 0.711 (0.419) | 0.689 (0.376) | 0.687 (0.372) | - | 0.480 (-0.054) |
| NIR 2 | 0.553 (0.101) | 0.501 (-0.008) | 0.567 (0.129) | 0.667 (0.331) | 0.603 (0.202) | 0.583 (0.163) | 0.577 (0.155) | - |

(8 bands, 2 classes). Both importance measurements ("mean decrease in Gini" and "mean decrease in accuracy") ranked the Red and the Green band as the most important variables using the June image. For the July image the two top ranked bands were Yellow and Red.

Classification accuracies obtained by using difference indices are reported in Tab. 6 to Tab. 8. Only results for one band order are shown (wavelength band y > wavelength band x), as differences were either inexistent (difference and normalized difference indices) or very small (ratio indices).

Compared to the use of single spectral bands, the classification accuracy from difference indices was either stable (June) or slightly improved (July). Only few models show better results than a purely random model (kappa coefficient > 0). For both images, difference indices employing the Coastal band gave highest accuracies.

The use of ratios instead of differences between two spectral bands improved the separability of the two infestation classes (Tab. 7). Most of the models, however, showed very low kappa-values which denote unsatisfied model accuracy. Band ratios combining Near Infrared 1 with Green (June), respectively Yellow (July) resulted in mean overall accuracies nearly similar to models using all eight spectral bands. These models proofed significant (kappa values > 0.4). Comparable results were also obtained using normalized differences (Tab. 8). Again, combining bands in the near infrared with the bands Green or Red yielded best results. In the July image, Near Infrared 1 combined with Yellow performed also very well.

## 4 Discussion

In our study the WorldView-2 data showed the potential to detect spectral differences between "healthy" and bark beetle infected "green-attack" trees. However, the spectral differences between the two infestation classes are small and blurred by high within-class variances. As a result, classification accuracies (RF and LR) do not exceed 70% for these two classes. Studies using hyperspectral data also found significant overlaps between

**Tab. 8:** Overall accuracies and corresponding kappa coefficients (in brackets) from logistic regression models to separate "healthy" and "green-attack" samples using normalized difference indices from the WorldView-2 images acquired in July (below the diagonal) and in June (above the diagonal) (independent bootstrapping results).

| Band | Coastal | Blue | Green | Yellow | Red | Red Edge | NIR 1 | NIR 2 |
|---|---|---|---|---|---|---|---|---|
| Coastal | - | 0.611 (0.220) | 0.605 (0.207) | 0.62 (0.236) | 0.635 (0.268) | 0.514 (0.020) | 0.507 (-0.002) | 0.51 (-0.008) |
| Blue | 0.551 (0.100) | - | 0.582 (0.160) | 0.543 (0.079) | 0.635 (0.268) | 0.533 (0.066) | 0.571 (0.141) | 0.567 (0.135) |
| Green | 0.505 (-0.002) | 0.537 (0.071) | - | 0.509 (-0.011) | 0.601 (0.202) | 0.582 (0.166) | 0.705 (0.409) | 0.633 (0.268) |
| Yellow | 0.627 (0.253) | 0.675 (0.348) | 0.641 (0.280) | - | 0.558 (0.112) | 0.652 (0.304) | 0.637 (0.273) | 0.643 (0.285) |
| Red | 0.547 (0.090) | 0.649 (0.296) | 0.637 (0.272) | 0.543 (0.084) | - | 0.618 (0.237) | 0.682 (0.364) | 0.673 (0.347) |
| Red Edge | 0.521 (0.033) | 0.497 (-0.013) | 0.521 (0.030) | 0.663 (0.323) | 0.581 (0.158) | - | 0.469 (-0.081) | 0.535 (0.065) |
| NIR 1 | 0.621 (0.238) | 0.607 (0.211) | 0.683 (0.364) | 0.709 (0.415) | 0.699 (0.396) | 0.689 (0.377) | - | 0.509 (0.008) |
| NIR 2 | 0.553 (0.101) | 0.503 (-0.004) | 0.569 (0.133) | 0.675 (0.347) | 0.603 (0.202) | 0.579 (0.155) | 0.595 (0.190) | - |

the two most problematic infestation classes (Heath 2001, Lausch et al. 2013). On the contrary, in our study, the class of "dead" trees could be classified almost perfectly.

Despite the relatively large class overlap in the spectral signatures, the manually delineated trees could be assigned to the classes "dead", "green-attack", and "healthy" by supervised classification (random forests, RF) with an overall accuracy of about 75%. The producer's and user's accuracies of all classes were around 70%. The best result was obtained with RF using all eight spectral bands of the July image. With this dataset, an overall accuracy of 76.2% and a kappa coefficient of 0.609 were achieved. Using only the four conventional WorldView-2 bands (Blue, Green, Red and Near Infrared 1) generally resulted in a loss of discriminative power. For the separation of the classes "green-attack" and "healthy" using RF or logistic regression (LR) the best results were achieved with all eight bands. Only the LR model using the June data was an exception. This might be due to the fact that unsuitable variables can worsen a LR model, whereas RF can handle this.

The similar accuracies of the classes "green-attack" and "healthy" is maybe caused by the equal data distribution between these two classes in the reference data. In a real-world setting, the occurrence of the class "healthy" is usually considerably higher than those of the infested trees. As we had no a priori information regarding the class distribution within our study area, we opted for an equal sampling of the three classes. Possible errors in the reference data have also to be taken into account when interpreting our results.

Using RapidEye data, Marx (2010) was able to separate the three classes with an overall accuracy of 98.6%. However, in this study, 97% of the samples were healthy trees, thus euphemising the overall accuracy. Looking at the results for the classes "green-attack" and "dead" the accuracies of our study are in line with or even higher than those found by Marx (2010). The "green-attack" trees were classified by Marx (2010) with a user's accuracy of 76.5% and with a producer's accuracy of 40.9%, the values for "red-attack" (nearly equivalent to our class "dead") were 87.4% and 80.2%, respectively. Our results also outperform those of Ortiz et al. (2013) using RapidEye data for the green-attack detection. The user's and producer's accuracies in their study were 50.0% and 66.7%, respectively. The higher accuracies in our study may be due to the higher spatial resolution of the WorldView-2 images (2 m) compared with the RapidEye data (5 m). It has also to be noted that we only classified the well illuminated parts of the tree crowns. The high detectability of already advanced stages of bark beetle infestation based on WorldView-2 data is also consistent with the results from Finnigan (2011).

A question arising in bark beetle studies is whether the remote sensing data detects directly the infested trees or solely a certain pre-weakening. This pre-weakening of trees could increase the predisposition to bark beetle infestation. The detection of pre-weakening of spruces was also highlighted in the study by Lausch et al. (2013). They used one- and two-year old hyperspectral data to classify different infestation classes. Their best model achieved very similar results as our study. They classified the three classes "dry" (old bark beetle infestations), "infestation 2010" and "healthy" with an overall accurcy of 69.3% (kappa 0.54) using hyperspectral HyMap data from 2009. The user's and producer's accuracies of the class "dry" were nearly 90%, those of the other classes were around 60%, therefore, the infestation of 2010 could be forcasted with data from 2009.

With respect to the image acquisition date, we found only small differences between the June and July images. The accuracies obtained from 8-band RF classification in the June image were almost as good as the July image. Using LR and various 2-band vegetation indices, the June image gave only slightly lower accuracies compared to the July image. An early image acquisition as such in June would give the forest practitioners extra time to remove infested trees before the bark beetles spread out. However, this requires good acquisition conditions, e.g. cloud free conditions with low haze levels and near-nadir view angles. In practice, one recommendation could be to task an early image acquisition, e.g. June, but insisting on optimum conditions. If these cannot be met the acquisition window should be

extended, e.g. into July, until suitable weather conditions are encountered.

Remarkably, for the separation of the classes "healthy" and "green-attack", some vegetation indices based on 2-band normalized differences and ratios yielded nearly as good results as the classification with all eight spectral bands. The best results were obtained with the bands Green and Near Infrared 1 from the June image and Yellow and Near Infrared 1 from the July image, respectively. The new bands Red Edge and Near Infrared 2 achieved significantly worse results. The use of spectral indices does not only permit an easy visualization of data compared to eight band data but also results in a simplified modelling, significantly reducing the necessary computer power and storage requirements. Possibly, the usage of 2-band vegetation indices reduces negative impacts related to illumination differences and topographic effects. However, these aspects were not studied in the present work.

Numerous studies identified bands from the green peak up to the Red Edge region as relevant for an early detection of plant stress induced by bark beetle infestation or air pollution (Stone et al. 2001, Lawrence & Labus 2003, Entcheva Campbell et al. 2004, Fassnacht et al. 2012, 2014, Lausch et al. 2013). This was also confirmed by our investigation, where the bands Red / Green (June) and Yellow / Red (July) showed the highest prediction power in the models with single bands. The same bands were identified by RF as the most important ones. In our study however, the Red Edge band was amongst the worst performing bands within the visible spectral range.

Regarding alternative data sources, WorldView-2 images have a few advantages compared to classical aerial images as well as hyperspectral datasets. One advantage of WorldView-2 data compared to hyperspectral imagery is its higher spatial resolution and large-scale mapping capacity. Lausch et al. (2013), for example, identified a problem of mixed information using hyperspectral data with a spatial resolution of 4 m. In their study it was pointed out that a spatial resolution of about 1 m would be interesting for mapping purposes at tree level. On the other hand, imaging spectroscopy certainly permits the detection of more subtle absorption features, which are not present in the rather coarse bands of the WorldView-2 sensor (Schlerf et al. 2010). Aerial images usually have a very high spatial resolution and are clearly cheaper than WorldView-2 data. But the number of spectral bands is smaller and radiometric inhomogeneity in the data makes large-scale applications difficult. However, it still has to be checked if the four additional WorldView-2 bands are more beneficial for the early detection of bark beetle infestation or the higher spatial resolution of aerial images. Aside from data with high spectral and high spatial resolution, multitemporal data (Meigs et al. 2011, Meddens et al. 2013) as well as multi-sensor data (Ortiz et al. 2013) can increase classification accuracy.

## 5 Conclusion and Outlook

The study showed that WorldView-2 satellite data may be useful for large-scale applications aiming at the detection of advanced as well as early bark beetle infestation with remote sensing data. However, the data does not permit to reliably identify each tree at the "green-attack" stage of infestation. Nonetheless, the data might be suitable to create hotspot maps of infested trees and of trees with an increased risk of infestation. Such maps would be an important information gain for the forest practice and would probably lead to an increase in efficiency of bark beetle infestation control.

Remotely sensed maps of bark beetle infestation could also positively contribute to the bark beetle modelling community. Both, the information from advanced bark beetle infestation (dead trees) with high confidence level, as well as the less reliable information from green-attack trees could constitute essential input data in bark beetle models. For example, it can be expected that the combination of maps showing green-attack and dead trees with predisposition models (Netherer & Nopp-Mayr 2005) could increase the prediction accuracy of such models. Remotely sensed maps can also be used as an alternative to cost intensive inventory data for detailed GIS modelling approaches of bark beetle infestation similar to the work described in Rossi et al. (2009).

With respect to our methodology, the spectral separability, positioning of reference polygons on the image, processing time and data volume needs further analysis. For further studies, it is also recommended to improve the collection of reference data. A more precise localisation of the trees in the field or a delineation of the individual crowns on the remote sensing images would make the localization of the trees less time consuming. In addition, a detailed description of the infestation stage, such as boring dust emission, start of the tree crown discoloration, and so on, would be helpful.

It was shown that mainly the four conventional bands (Blue, Green, Red and Near Infrared 1) and derived indices positively contributed to the separation of the infestation classes. Amongst the four new bands of WorldView-2, only the Yellow band had importance. For this approach it would be interesting to analyse the potential of other remote sensing data, e.g. digital aerial images. Furthermore, the potential of spectral regions not covered by the WorldView-2 satellite should be analysed. Therefore, for further studies applying hyperspectral data with very high spatial resolution is recommended. In this way, one could also test newer parameterizations of the Red Edge feature for detecting bark beetle infestation classes (Cho et al. 2008). In our study, the so-called Red Edge band of WorldView-2 did not positively contribute to the class separability.

This study and previous studies on tree species discrimination (Immitzer et al. 2012a, 2012b) have shown that the classification accuracy can be increased, if only the well-lit parts of the crowns are used. So far, the delineation of the crown has been made manually. For an operational, large-scale application this procedure must be automated. Initial tests of different segmentation algorithms were promising but not yet used.

The bulk of the above mentioned suggestions are addressed in an actual joint research project together with Bavarian State Institute of Forestry (LWF), German Aerospace Center (DLR), Bavaria State Forest Enterprise (BaySF) and Austrian State Forest Enterprise (ÖBf) with study areas in Bavaria and Austria. We are planning detailed analyses of time series both of WorldView-2 and airborne hyperspectral data (HySpex) with very high spatial resolution for observing vitality loss of artificially stressed trees.

## Acknowledgements

The study was partly funded by the EU-program of rural development (LE 07-13). The authors thank Günther Bronner and Bernhard Pfandl (Umweltdata GmbH) for WorldView-2 images and reference data. We thank Tatjana Koukal for her valuable comments on the manuscript.

## References

Breiman, L., 2001: Random forests. – Machine learning **45** (1): 5–32.

Buschmann, C. & Nagel, E., 1993: In vivo spectroscopy and internal optics of leaves as basis for remote sensing of vegetation. – International Journal of Remote Sensing **14** (4): 711–722.

Cheng, T., Rivard, B., Sánchez-Azofeifa, G.A., Feng, J. & Calvo-Polanco, M., 2010: Continuous wavelet analysis for the detection of green attack damage due to mountain pine beetle infestation. – Remote Sensing of Environment **114** (4): 899–910.

Cho, M.A., Skidmore, A.K. & Atzberger, C., 2008: Towards red-edge positions less sensitive to canopy biophysical parameters for leaf chlorophyll estimation using properties optique spectrales des feuilles (PROSPECT) and scattering by arbitrarily inclined leaves (SAILH) simulated data. – International Journal of Remote Sensing **29** (8): 2241–2255.

Clark, M.L., Roberts, D.A. & Clark, D.B., 2005: Hyperspectral discrimination of tropical rain forest tree species at leaf to crown scales. – Remote Sensing of Environment **96** (3-4): 375–398.

Coggins, S.B., Coops, N.C. & Wulder, M.A., 2010: Improvement of low level bark beetle damage estimates with adaptive cluster sampling. – Silva Fennica **44** (2): 289–301.

Coggins, S.B., Coops, N.C. & Wulder, M.A., 2011: Estimates of bark beetle infestation expansion factors with adaptive cluster sampling. – International Journal of Pest Management **57** (1): 11–21.

Cohen, J., 1960: A coefficient of agreement for nominal scales. – Educational and Psychological Measurement **20** (1): 37–46.

Coops, N.C., Johnson, M., Wulder, M.A. & White, J.C., 2006: Assessment of QuickBird high spatial resolution imagery to detect red attack damage due to mountain pine beetle infestation. – Remote Sensing of Environment **103** (1): 67–80.

Digital Globe, 2014: White Paper – The benefits of the 8 spectral bands of WorldView-2. – http://digitalglobe.com/ (7.7.2014).

Efron, B., 1979: Bootstrap Methods: Another Look at the Jackknife. – The Annals of Statistics **7** (1): 1–26.

Eklundh, L., Johansson, T. & Solberg, S., 2009: Mapping insect defoliation in Scots pine with MODIS time-series data. – Remote Sensing of Environment **113** (7): 1566–1573.

Entcheva Campbell, P.K., Rock, B.N., Martin, M.E., Neefus, C.D., Irons, J.R., Middleton, E.M. & Albrechtova, J., 2004: Detection of initial damage in Norway spruce canopies using hyperspectral airborne data. – International Journal of Remote Sensing **25** (24): 5557–5583.

Fachabteilung 10C des Landes Steiermark – Forstwesen, 2011: Fichtenborkenkäfersituation 2011. – http://www.agrar.steiermark.at/cms/beitrag/10435428/12717247/ (4.9.2011).

Fassnacht, F.E., Latifi, H. & Koch, B., 2012: An angular vegetation index for imaging spectroscopy data – Preliminary results on forest damage detection in the Bavarian National Park, Germany. – International Journal of Applied Earth Observation and Geoinformation **19:** 308–321.

Fassnacht, F.E., Latifi, H., Ghosh, A., Joshi, P.K. & Koch, B., 2014: Assessing the potential of hyperspectral imagery to map bark beetle-induced tree mortality. – Remote Sensing of Environment **140:** 533–548.

Filchev, L., 2012: An Assessment of European Spruce Bark Beetle Infestation Using WorldView-2 Satellite Data. – European SCGIS Conference "Best practices: Application of GIS technologies forconservation of natural and cultural heritage sites", Sofia, Bulgaria.

Finnigan, L., 2011: Evaluating the Utility of Eight Band Worldview-2 Imagery in the Detection of Red Attack. 8-Band Research Challenge, DigitalGlobe. – http://dgl.us.neolane.net/res/img/bee83c5d3c55789b4bf6f23e4f309a8a.pdf (16.1.2012).

Gitelson, A. & Merzlyak, M.N., 1994: Spectral reflectance changes associated with autumn senescence of Aesculus hippocastanum L. and Acer platanoides L. leaves. Spectral features and relation to chlorophyll estimation. – Journal of Plant Physiology **143** (3): 286–292.

Greenberg, J.A., Dobrowski, S.Z., Ramirez, C.M., Tull, J.L. & Ustin, S.L., 2006: A bottom-up approach to vegetation mapping of the Lake Tahoe Basin using hyperspatial image analysis. – Photogrammetric Engineering and Remote Sensing **72** (5): 581–589.

Hall, P.M., 1981: Remote sensing of Douglas-fir trees newly infested by bark beetles. – Master thesis, University of British Columbia, Vancouver, BC, Canada.

Hastie, T., Tibshirani, R. & Friedman, J., 2009: The elements of statistical learning: Data mining, inference, and prediction. – Second Edition, 768 S., Springer, New York, NY, USA.

Heath, J., 2001: The detection of mountain pine beetle green attacked lodgepole pine using Compact Airborne Spectrographic Imager (CASI) data. – Master thesis, University of British Columbia, Vancouver, BC, Canada.

Heller, R., 1968: Previsual detection of ponderosa pine trees dying from bark beetle attack. – Fifth Symposium on Remote Sensing of Environment: 387–434, University of Michigan, USA.

Immitzer, M., Atzberger, C. & Koukal, T., 2012a: Tree species classification with Random Forest using very high spatial resolution 8-band WorldView-2 satellite data. – Remote Sensing **4** (9): 2661–2693.

Immitzer, M., Atzberger, C. & Koukal, T., 2012b: Eignung von WorldView-2 Satellitenbildern für die Baumartenklassifizierung unter besonderer Berücksichtigung der vier neuen Spektralkanäle. – PFG – Photogrammetrie, Fernerkundung, Geoinformation **2012** (5): 573–588.

Kilian, W., Müller, F. & Starlinger, F., 1994: Die forstlichen Wuchsgebiete Österreichs – Eine Naturraumgliederung nach waldökologischen Gesichtspunkten. 60 S., Forstliche Bundesversuchsanstalt, Wien, Österreich.

Krehan, H., 2008: Das ABC der Borkenkäferbekämpfung an Fichte. – Borkenkäfer, BFW Praxis Information **17:** 17–18, http://bfw.ac.at/030/pdf/1818_pi17.pdf (24.9.2011).

Kuhn, M., Wing, J., Weston, S., Williams, A., Keefer, C., Engelhardt, A. & Cooper, T., 2013: caret: Classification and Regression Training. R package version 6.0-30. http://cran.r-project.org/package=caret (7.7.2014).

Lausch, A., Heurich, M., Gordalla, D., Dobner, H.-J., Gwillym-Margianto, S. & Salbach, C., 2013: Forecasting potential bark beetle outbreaks based on spruce forest vitality using hyperspectral remote-sensing techniques at different scales. – Forest Ecology and Management **308:** 76–89.

Lawrence, R. & Labus, M., 2003: Early Detection of Douglas-Fir Beetle Infestation with Subcanopy Resolution Hyperspectral Imagery. – Western Journal of Applied Forestry **18** (3): 202–206.

Leckie, D.G., Tinis, S., Nelson, T., Burnett, C., Gougeon, F.A., Cloney, E. & Paradine, D., 2005: Issues in species classification of trees in old growth conifer stands. – Canadian Journal of Remote Sensing **31** (2): 175–190.

Liaw, A. & Wiener, M., 2002: Classification and regression by randomForest. – R news **2** (3): 18–22.

Marx, A., 2010: Erkennung von Borkenkäferbefall in Fichtenreinbeständen mit multi-temporalen RapidEye-Satellitenbildern und Data-mining-Techniken. – PFG – Photogrammetrie, Fernerkundung, Geoinformation **2010** (4): 243–252.

Meddens, A.J.H., Hicke, J.A., Vierling, L.A. & Hudak, A.T., 2013: Evaluating methods to detect bark beetle-caused tree mortality using single-date and multi-date Landsat imagery. – Remote Sensing of Environment **132:** 49–58.

Meigs, G.W., Kennedy, R.E. & Cohen, W.B., 2011: A Landsat time series approach to characterize bark beetle and defoliator impacts on tree mortality and surface fuels in conifer forests. – Remote Sensing of Environment **115** (12): 3707–3718.

Netherer, S. & Nopp-Mayr, U., 2005: Predisposition assessment systems (PAS) as supportive tools in forest management – rating of site and stand-related hazards of bark beetle infestation in the High Tatra Mountains as an example for system application and verification. – Forest Ecology and Management **207** (1–2): 99–107.

Netherer, S. & Schopf, A., 2010: Potential effects of climate change on insect herbivores in European forests – General aspects and the pine processionary moth as specific example. – Forest Ecology and Management **259** (4): 831–838.

Ortiz, S., Breidenbach, J. & Kändler, G., 2013: Early Detection of Bark Beetle Green Attack Using TerraSAR-X and RapidEye Data. – Remote Sensing **5** (4): 1912–1931.

Overbeck, M. & Schmidt, M., 2012: Modelling infestation risk of Norway spruce by Ips typographus (L.) in the Lower Saxon Harz Mountains (Germany). – Forest Ecology and Management **266:** 115–125.

Padwick, C., Deskevich, M., Pacifici, F. & Smallwood, S., 2010: WorldView-2 Pan-Sharpening. – ASPRS 2010 Annual Conference, San Diego, CA, USA.

Pal, M., 2005: Random forest classifier for remote sensing classification. – International Journal of Remote Sensing **26:** 217–222.

R Core Team, 2013: R: A language and environment for statistical computing. – R Foundation for Statistical Computing, Vienna, Austria. – http://www.r-project.org/ (7.7.2014).

Roberts, A., Dragicevic, S., Northrup, J., Wolf, S., Li, Y. & Coburn, C., 2003: Mountain pine beetle detection and monitoring: remote sensing evaluations. – BC Forest Innovation Investment Operational Research Report with Reference to Recipient Agreement R2003-0205. – http://homepage.agrl.ethz.ch/sewolf/PDF/MPB_ForestInovationInvestment-Report_2003.pdf (22.6.2011).

Rodríguez-Galiano, V.F., Chica-Olmo, M., Abarca-Hernandez, F., Atkinson, P.M. & Jeganathan, C., 2012: Random Forest classification of Mediterranean land cover using multi-seasonal imagery and multi-seasonal texture. – Remote Sensing of Environment **121:** 93–107.

Rossi, J.-P., Samalens, J.-C., Guyon, D., van Halder, I., Jactel, H., Menassieu, P. & Piou, D., 2009: Multiscale spatial variation of the bark beetle Ips sexdentatus damage in a pine plantation forest (Landes de Gascogne, Southwestern France). – Forest Ecology and Management **257** (7): 1551–1557.

Rouse, J., Haas, R., Schell, J. & Deering, D., 1973: Monitoring vegetation systems in the Great Plains with ERTS. – Third ERTS symposium, NASA SP-351: 309–317, Washington, DC, USA.

Schelhaas, M.-J., Nabuurs, G.-J. & Schuck, A., 2003: Natural disturbances in the European forests in the 19th and 20th centuries. – Global Change Biology **9** (11): 1620–1633.

Schlerf, M., Atzberger, C., Hill, J., Buddenbaum, H., Werner, W. & Schüler, G., 2010: Retrieval of chlorophyll and nitrogen in Norway spruce (Picea abies L. Karst.) using imaging spectroscopy. – International Journal of Applied Earth Observation and Geoinformation **12** (1): 17–26.

Seidl, R., Schelhaas, M.-J. & Lexer, M.J., 2011: Unraveling the drivers of intensifying forest disturbance regimes in Europe. – Global Change Biology **17** (9): 2842–2852.

Sharma, R., 2007: Using multispectral and hyperspectral satellite data for early detection of mountain pine beetle damage. – PhD thesis, University of British Columbia, Vancouver, BC, Canada.

Sims, D.A. & Gamon, J.A., 2002: Relationships between leaf pigment content and spectral reflectance across a wide range of species, leaf structures and developmental stages. – Remote Sensing of Environment **81** (2–3): 337–354.

Skakun, R.S., Wulder, M.A. & Franklin, S.E., 2003: Sensitivity of the thematic mapper enhanced wetness difference index to detect mountain pine beetle red-attack damage. – Remote Sensing of Environment **86** (4): 433–443.

Stone, C., Chisholm, L. & Coops, N., 2001: Spectral reflectance characteristics of eucalypt foli-

age damaged by insects. – Australian Journal of Botany **49** (6): 687–698.

Tomiczek, C., Cech, T.L., Fürst, A., Hoyer-Tomiczek, U., Krehan, H., Perny, B. & Steyrer, G., 2011: Forest Protection Situation 2010 in Austria (in German with English summary). – Forstschutz aktuell **52:** 3–9.

Toscani, P., Immitzer, M. & Atzberger, C., 2013: Texturanalyse mittels diskreter Wavelet Transformation für die objektbasierte Klassifikation von Orthophotos. – PFG – Photogrammetrie, Fernerkundung, Geoinformation **2013** (2): 105–121.

Updike, T. & Comp, C., 2010: Radiometric use of WorldView-2 imagery. – DigitalGlobe, Longmont. – http://www.digitalglobe.com/downloads/Radiometric_Use_of_WorldView-2_Imagery.pdf (7.5.2012).

Venables, W.N. & Ripley, B.D., 2002: Modern applied statistics with S. – Fourth Edition, 495 S., Springer, New York, NY, USA.

Waser, L.T., Küchler, M., Jütte, K. & Stampfer, T., 2014: Evaluating the Potential of WorldView-2 Data to Classify Tree Species and Different Levels of Ash Mortality. – Remote Sensing **6** (5): 4515–4545.

Wulder, M.A., Dymond, C.C. & Erickson, B., 2004: Detection and monitoring of the mountain pine beetle – Information Report BC-X-398. Canadian Forest Service, Victoria, BC, Canada. – http://www.for.gov.bc.ca/hfd/library/documents/bib92565.pdf (15.9.2011).

Wulder, M.A., Dymond, C.C., White, J.C., Leckie, D.G. & Carroll, A.L., 2006a: Surveying mountain pine beetle damage of forests: A review of remote sensing opportunities. – Forest Ecology and Management **221** (1–3): 27–41.

Wulder, M.A., White, J.C., Bentz, B., Alvarez, M.F. & Coops, N.C., 2006b: Estimating the probability of mountain pine beetle red-attack damage. – Remote Sensing of Environment **101** (2): 150–166.

Wulder, M.A., White, J.C., Carroll, A.L. & Coops, N.C., 2009: Challenges for the operational detection of mountain pine beetle green attack with remote sensing. – Forestry Chronicle **85** (1): 32–38.

Addresses of the Authors:

Markus Immitzer & Clement Atzberger, University of Natural Resources and Life Sciences, Vienna (BOKU), Institute of Surveying, Remote Sensing and Land Information, Peter-Jordan-Straße 82, A-1190 Vienna, Tel.: +43-1-47654-5100, Fax: +43-1-47654-5142, e-mail: {markus.immitzer}{clement.atzberger}@boku.ac.at

Manuskript eingereicht: März 2014
Angenommen: Juli 2014

PFG 2014 / 5, 0369–0381
Stuttgart, October 2014

Article

# Crop Water Requirements on Regional Level using Remote Sensing Data – A Case Study in the Marchfeld Region

Nikolaus Neugebauer & Francesco Vuolo, Vienna, Austria

**Keywords:** irrigation, crop water requirements, evapotranspiration, satellite image, remote sensing, DEIMOS-1

**Summary:** This research presents an operative application of satellite–based technologies to estimate crop water requirements (CWR) on regional level. The study is located in the agricultural area of Marchfeld (Lower Austria) and focuses on the year 2012. Agricultural production in this region requires irrigation which draws its resources from the groundwater. Due to its impact on hydrology and environment this practice necessitates close monitoring and management. In this process the CWR is an important piece of information, which can be derived from satellite data. We used multi-temporal (6 acquisitions, with an average revisit time of 16 days) and multi-spectral (visible and near-infrared) imagery of the DEIMOS-1 satellite sensor data in combination with local agro-meteorological measurements. In a first step, the leaf area index (LAI) and albedo maps were derived from atmospherically corrected satellite data. Those were used to generate maps of potential evapotranspiration ($ET_p$) by direct application of the Penman-Monteith equation. Then, we produced a crop mask of the areas potentially irrigated. This was achieved by using an unsupervised image classification approach in combination with a post-classification analysis of the time-series of the crop development. Rain gauges data from a number of weather stations were spatially interpolated to produce a map of precipitation (P). Finally, the crop water requirements were calculated as the difference between $ET_p$ and the precipitation and aggregated over 10-day interval periods. Reference evapotranspiration ($ET_o$) for the growing period resulted in 391 mm. The extent of irrigated crops covered an area of 21,278 ha with a maximum $ET_p$ of 5.6 mm/day at the end of June. The total crop water requirement resulted in 34.26 million m³ for the year 2012.

**Zusammenfassung:** *Berechnung des Pflanzenwasserbedarfs für Sommerfeldfrüchte mittels Fernerkundungsdaten. Eine Fallstudie in der Marchfeld-Region.* Diese Arbeit präsentiert eine Berechnung des Pflanzenwasserbedarfes auf regionaler Ebene. Die Studie wird innerhalb der landwirtschaftlichen Region Marchfeld (Österreich) für das Jahr 2012 durchgeführt. Die landwirtschaftliche Produktion dieser Region ist definiert durch Feldbewässerung, die ihre Ressourcen aus dem Grundwasser bezieht. Der Einfluss auf die hydrologischen- und Umweltbedingungen macht eine genaue Beobachtung dieser Anwendung unumgänglich. Der Pflanzenwasserbedarf ist dabei eine wichtige Information, sowohl für die Beobachtung als auch für operationelle Entscheidungen. Die Analyse basiert auf multi-temporalen (6 Bildaufnahmen, 16 Tage Wiederholzyklus), multispektralen (sichtbares Licht und nahes Infrarot) Satellitenbildaufnahmen des DEIMOS-1 Sensors und lokalen agro-meteorologischen Daten. Zuerst wurde der Blattflächenindex (Leaf Area Index – LAI) und die Albedo aus den atmosphärisch korrigierten Satellitenbildern berechnet. Mit diesen Daten wurden durch eine direkte Anwendung der Penman-Monteith Gleichung Karten der potentiellen Evapotranspiration erstellt. Mit einer unüberwachten Klassifikation der zeitlichen Pflanzenentwicklung und einer nachfolgenden Analyse wurde die räumliche Verteilung von Sommerfeldfrüchten ermittelt. Weiters wurden Niederschlagsdaten von elf Wetterstationen interpoliert, um eine räumliche Abschätzung der Niederschlagsverteilung zu erhalten. Zuletzt wurde der Wasserbedarf der Sommerfeldfrüchte als Differenz der potentiellen Evapotranspiration und des Niederschlages berechnet und in 10-Tages-Intervallen aggregiert. Das Untersuchungsgebiet wies während der Vegetationsperiode eine totale $ET_0$ von 391 mm auf. Die Produktion von Sommerfeldfrüchten nahm eine Fläche von 21.278 ha in Anspruch und erreichte eine maximale $ET_p$ von 5,6 mm/Tag. Der gesamte Pflanzenwasserbedarf für Sommerfeldfrüchte innerhalb der Marchfeld-Region im Jahr 2012 war 34,26 Mio. m³.


www.schweizerbart.de
DOI: 10.1127/1432-8364/2014/0230
1432-8364/14/0230 $ 3.25

## 1 Introduction

Irrigated agricultural land has a high productive capacity producing between 30% to 50% of the world food crop on 17% of all arable land (Seckler et al. 1999). Efficient management of water resources is of particular importance considering that 70% of global freshwater withdraws are done by agriculture. The last decades have seen a growth in use of water for irrigation, which is predicted to further increase (Collins et al. 2009). Adjacent to nutrient management, efficient water management is considered to be the main component that can contribute to production increases (45% to 70% for most crops) thus providing future food security in a sustainable way (Mueller et al. 2012).

The need for irrigation arises when precipitation does not compensate the water loss caused by evapotranspiration (ET) of the plant surface. Usually, farmers and irrigation managers will aim to meet crop water requirement (CWR), defined as the deficit between ET loss and precipitation, by applying irrigation to achieve optimal crop development and yield (Allen et al. 1998). Water is taken from available sources, e.g. rivers and groundwater, and extensive infrastructure, such as canals, damns, water reservoirs, pumps, is needed to make water accessible for irrigation. An example is the Marchfeld region in Austria where irrigation is deployed since the 1970s. Between the years 1986 and 2004 the "Marchfeldkanal-Projekt" was realized in response to dropping groundwater levels. This canal system diverts water from the Danube River and conveys it to the Marchfeld region to make it accessible for irrigation practice. The method can result in considerable effects on the surrounding environment like biodiversity losses due to lowered groundwater tables or pollution of rivers by agricultural inputs (David et al. 2000). Further problems are limited water supply for downstream users, soil erosion and nutrient elution (Shanan 1987, David et al. 2000). In the Marchfeld the main issues are the regulation of groundwater levels and the dilution of nitrate into the groundwater. These problems deserve special recognition since the resources are also used as industrial, domestic and drinking water.

In the Marchfeld region the withdrawal of water for irrigation is currently approximated by measurements of the groundwater level. Field to catchment scale estimates of water requirements are important in the assessment of regional water consumption and groundwater depletion and could help to improve estimates of irrigation withdrawal. This information can be used to coordinate allocation of resources in irrigation, like volumes of water and investments in infrastructure, and in the compilation of water management plans to achieve an increased efficiency in the water use (Pereira et al. 2002).

Crop development is one of the driving factors determining water needs and it highly depends on spatial and temporal factors. A temporal variation is a result of vegetation dynamics over the growing season. Spatial variation is related to climatic conditions on large scale, and on smaller scale related to other factors like soil type and fertility, crop variety and management. Estimations of water requirements based on regional statistics, static crop maps and standard crop coefficients are not capable of accounting for this variability (Frenken & Gillet 2012). Therefore, precise estimations of water requirements need to take into account spatial and temporal information on the actual development of crops.

Crop development can be monitored using multi-spectral and multi-temporal observations from satellite platforms (Ozdogan et al. 2010). Current platforms are acquiring multispectral imagery in a spatial resolution precise enough for analysis of agricultural vegetation with suitable revisit intervals. For instance, the commercial Spanish satellite of the DMC (disaster monitoring constellation) DEIMOS-1 provides data in 3 spectral bands with a ground sampling distance (GSD) of 22 m and 2 – 3 days revisit time (Deimos-Imaging 2014). The freely available Landsat-8 satellite featuring 8 spectral bands provides 16 days revisit time and a GSD of 30 m. Sentinel-2, an upcoming European Space Agency (ESA) mission, will provide 13 spectral bands with a resolution of up to 10 m in a revisit interval of 2 – 3 days. These satellite sensors offer the possibility to monitor large crop areas in intervals (7 – 10 days) suitable for the calculation of CWR in a variety of agricultural conditions.

Other possible applications of EO data in agriculture are the implementation in crop models (Casa et al. 2012), monitoring of the nitrogen status (Scharf et al. 2002) and to predict yields (Jégo et al. 2012).

This paper focuses on the calculation of $ET_p$ and an estimation of the seasonal crop water requirements in the area of Marchfeld, an important agricultural region located in Lower Austria, where irrigation is regularly applied during summer months. Our approach combines daily agro-meteorological data from local stations and the processing of multi-spectral images based on the methodology described by D'Urso et al. (2001, 2010) using the Penman-Monteith approach (Allen et al. 1998). We used rain gauges data from eleven weather stations located in the region and 6 images with a spatial resolution of 22 m acquired with an average revisit time of 16 days. We performed an image classification using the satellite-based crop development curves as input feature to differentiate different types of crops. This was done to identify areas used for production of summer crops, which are most likely to be irrigated during the time of interest.

The paper presents the results of a case study and discusses the findings in the context of operative tools to support irrigation water management at regional scale.

## 2 Material

### 2.1 *Study Area*

Marchfeld is located in Lower Austria, north east of Vienna (Fig. 1). The average annual precipitation is 500 mm – 550 mm making it the driest region of Austria. Annual precipitation during the vegetation period (April – September) is 200 mm – 440 mm. Dry periods (time with no daily precipitation higher than 5 mm) of three weeks can occur averagely 5 times per year, longer dry periods of 30 – 34 days are a yearly occurrence (Neudorfer 2002). Modelling of future climatic development for Marchfeld and its surrounding regions suggests a decrease of precipitation volumes and an expected increase of likelihood for drought events (Pal 2004, Dubrovsky et al. 2008, Eitzinger et al. 2009, Trnka et al. 2009). The high average wind speed of about 3.5 m/s has an amplifying effect of the dry climate considering plant transpiration. The agricultural area has an extent of 60,000 ha of arable land of which more than 21,000 ha are regularly irrigated each year. The soil consists mainly of fertile aeolian slit deposit which, together with the pannonian climate, high solar radiation and flat terrain forms a well-qualified region for agricultural production. The main crops cultivated in summer are vegetables (11% of the crop area), sugarbeet (10%) and potatoes (7%). Cereal crop types are cultivated on about two-thirds of the crop area. Limitations to agricultural production are low precipitation and a predominantly low field water capacity of 70 mm and less. This means that the soil can hold only a low amount of water thus limiting availability to plants in dry periods.

Although Marchfeld is one of the driest regions in the country, it is still one of the primary producers of agricultural goods in Austria. This is possible due to the use of irrigation that is used to compensate scarce precipitation. The infrastructure of the "Marchfeldkanal Projekt" consists of 100 km of canal and 8 weirs which control surface water flow and height. To control groundwater levels 22 pumping stations and 7 infiltration basins were implemented. The cost of construction was 207.8 million Euro (Neudorfer & Weyermayer 2007). Water for application on field is pumped from the groundwater through wells. In this case decentralized, mobile pumps are run on diesel or less often by electricity. In some cases centralized pumping stations provide pressurized water via a distribution network. The majority of crops are irrigated from May until end of September. The only crop regularly irrigated afterwards (until mid-October) is spinach.

### 2.2 *Satellite Data*

In this study, we used satellite images acquired by DEIMOS-1, a satellite of the DMC (disaster monitoring constellation). DEIMOS-1 features a multi-spectral sensor providing 22 m resolution in 3 bands (NIR: 0.77 µm –

0.90 µm, Red: 0.63 µm – 0.69 µm, Green: 0.52 µm – 0.60 µm) with a revisit interval of 2 – 3 days. DEIMOS-1 was chosen because it offers a cost-effective solution to monitor crop development with suitable temporal, spatial and spectral resolution to work at field and district scales. Imagery was acquired on six different dates in 2012 to cover the growing season: June 17th, July 30th, August 1st and 20th, September 5th and 18th.

The imagery was provided orthorectified to a sub-pixel accuracy of about 10 m. The correction was performed by the data supplier using ground control points and the shuttle radar topography mission (SRTM v3) data as digital elevation model. An atmospheric correction using ATCOR (Richter 1998) was performed by the authors before further processing.

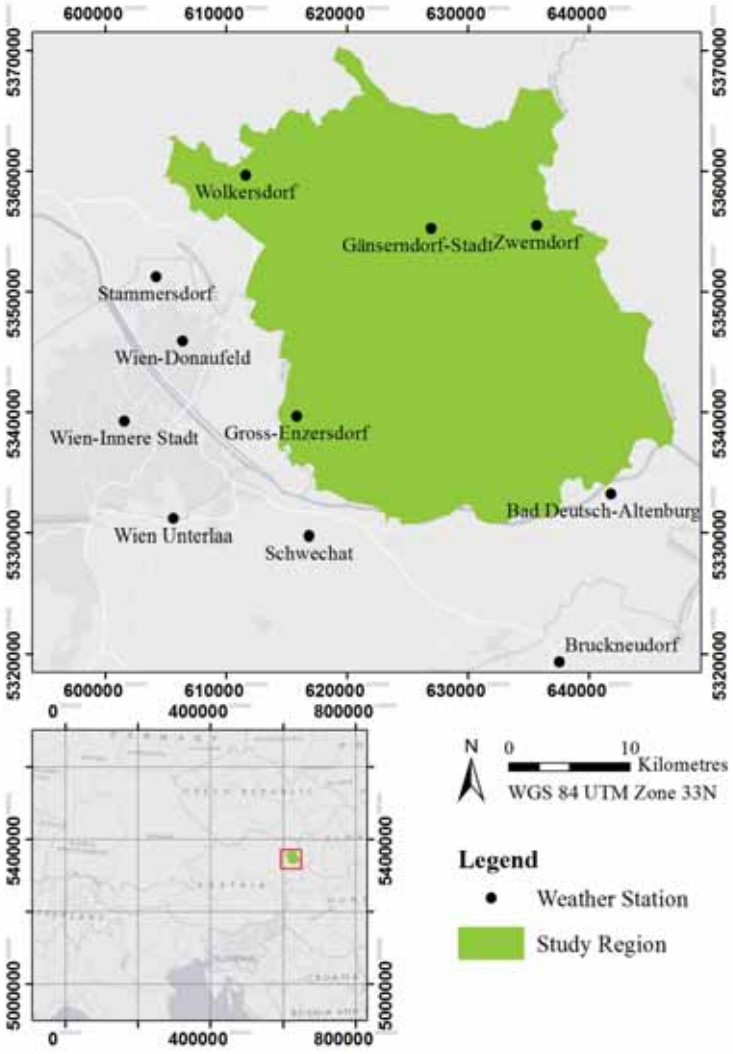


**Fig. 1:** Study area of Marchfeld (Lower Austria) and location of the weather stations used for the spatial interpolation of precipitation.

### 2.3 *Agro-Meteorological Data*

Precipitation was recorded at eleven weather stations in the region (Fig. 1). Fig. 2 reports the mean cumulated precipitation volumes of all eleven stations and the data for the stations which recorded the seasonal minimum (148 mm at Zwerndorf) and maximum (249 mm at Wien-Unterlaa) values. For the calculation of the reference evapotranspiration ($ET_0$), we considered solar radiation, air temperature, windspeed and air humidity recorded at the Zwerndorf station only.

## 3 Methods

### 3.1 *Calculation of Crop Water Requirements*

Crop water requirements are defined as the potential evapotranspiration ($ET_p$) of a cropped surface area, net of the precipitation (P):

$$CWR = ET_p - P \quad (1)$$

Precipitation (P) can be measured from local weather stations. A critical factor in the precise estimation of CWR is the potential evapotranspiration of crops. A review of different procedures for the determination of ET is given by Courault et al. (2005) and Verstraeten et al. (2008). The approach for mapping ET used in this study is based on the methodology proposed by D'Urso et al. (2001, 2010) using the FAO-56 Penman-Monteith equation (Allen et al. 1998). It consists of two main components. First we estimate the reference evapotranspiration ($ET_0$) based on the FAO-56 standards. $ET_0$ indicates the amount of water removed from a standard vegetation surface (grass) through the process of evapotranspiration. In this case, $ET_0$ is a function of meteorological factors (solar radiation, wind speed, temperature, air humidity), which can be measured by local weather stations, and crop specific factors (LAI, albedo and crop height – $h_c$), which are kept constant in relation to the theoretical reference surface (LAI = 2.88, albedo = 0.23, $h_c$ = 0.12 m).

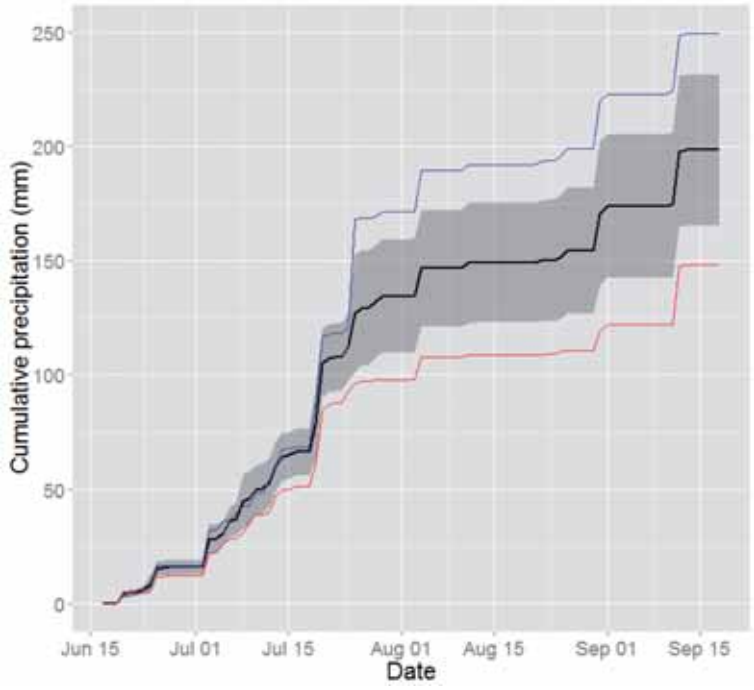


**Fig. 2:** Cumulated precipitation. The black line represents the mean value from all eleven weather stations, the shaded area is the standard deviation. Wien-Unterlaa recorded the total maximum of precipitation volumes (249 mm), Zwerndorf the minimum (148 mm).

$$ET_0 = \frac{0.408\Delta(R_n - G) + \gamma \frac{900}{T+273} u_2 (e_s - e_a)}{\Delta + \gamma(1 + 0.34)u_2} \quad (2)$$

$R_n$ = net radiation at the crop surface [MJ $m^{-2}$ $day^{-1}$],
G = soil heat flux density [MJ $m^{-2}$ $day^{-1}$],
T = mean daily air temperature at 2 m height [°C],
$u_2$ = wind speed at 2m height [m $s^{-1}$],
$e_s$ = saturation vapour pressure [kPa],
$e_a$ = actual vapour pressure [kPa],
$e_s - e_a$ = vapour pressure deficit [kPa],
$\Delta$ = slope vapour pressure curve [kPa $°C^{-1}$],
$\gamma$ = psychrometric constant [kPa $°C^{-1}$].

Subsequently the crop coefficient ($K_c$) is calculated. $K_c$ is defined as:

$$K_c = \frac{ET_p}{ET_0} \quad (3)$$

Traditionally, i.e. in non-satellite-based approaches, $K_c$ is calculated from measurements of actual evapotranspiration and contemporaneous $ET_0$ estimates. This way $K_c$ has been calculated for different conditions and is reported in tables for several crops. Tabulated data represents a fixed value suitable for comparing crop types under general conditions. Because crop development is subject to change in regard to management and environmental factors, the $K_c$ value should be dynamically adjusted to the actual conditions in order to achieve precise estimation of water requirement on field and regional scale.

In this study, we used the approach proposed by D'Urso et al. (2001, 2010) to estimate $ET_p$, where crop parameters used in the FAO-56 Penman-Monteith equation are replaced by LAI and albedo maps. LAI was calculated from the weighted difference vegetation index (WDVI) using the CLAIR model (Clevers 1989). A site specific model was calibrated and the satellite-based estimation of LAI was validated using ground measurements. The calibration procedure and results are presented in Vuolo et al. (2013). The surface albedo is substituted by the wavelength-integrated ground reflectance where wavelength gap regions are supplemented with interpolation (Richter & Schläpfer 2014). This calculation was performed using ATCOR module implemented in ERDAS Imagine. Crop height ($h_c$), which controls the resistance in canopy aerodynamic properties, was set to a constant value of 0.3 m, representing an average height for crops in the region. This was done because measurements of crop heights are not feasible for large areas over a time period of several months and a fixed value is considered to be a satisfactory compromise for the estimation of $ET_p$ (D'Urso & Calera Belmonte 2006).

To produce daily estimates of $ET_p$, $K_c$ maps were derived for each acquisition date (according to (2)) and they were temporally interpolated to obtain daily $K_c$ values from June 17th to September 18th. For this purpose, we used the "Whittaker Smoother" (Whittaker 1922, Eilers 2003, Atkinson et al. 2012). The smoothing parameter ($\lambda$) was set to 15. Subsequently, a daily estimation of $ET_p$ was performed by multiplying daily $K_c$ with corresponding daily $ET_0$ estimates. In a final step the total water requirements were aggregated in 10-day time steps.

### 3.2 *Spatial Interpolation of Precipitation*

To derive the variability of precipitation events over the region of interest, rain gauges data were spatially interpolated on a daily basis using the inverse distance weighted (IDW) method. IDW interpolation is a well performing method for interpolating precipitation and less complex to apply than the similar performing regression-kriging method (Wagner et al. 2012). The IDW algorithm was applied in MATLAB using a code provided by Fatichi (2012). The interpolation was set to take into account the 3 nearest neighbours of each point of measurements to produce a 22 m × 22 m grid corresponding to the $K_c$ raster dataset.

### 3.3 *Crop Category Classification*

The aim of the crop category classification was to identify the crop areas that are potentially irrigated. For this purpose, we defined two crop categories (summer and win-

ter crops) and used the summer crop areas to compute the total water requirements. The $K_c$ estimation from the satellite time series provided a quantification of the crop development over time which was used as an input feature in the image classification. In our case, the time series starting on June 17th covered the development of winter crops in their late or senescence stages. Likewise summer crops were recorded during their full development stage.

In a first step, non-agricultural areas such as urban, forest and water were identified using CORINE land cover (CLC) with a pixel size of 100 m (European Environment Agency 2006) and were removed from the $K_c$ dataset.

In a second step, an unsupervised image classification of the time series with an initial number of 12 clusters was performed. The 12 clusters were then aggregated to summer and winter crop classes based on a visual interpretation of the temporal crop coefficient development of each cluster. We introduced a third class (namely secondary crop) to account for double cropping systems, i.e. two or more crops in the same field during a single growing season.

## 4 Results

First we present the results of the summer crop area classification. This is followed by the results of analysis of the agro-meteorological data. The CWR is presented at the end of this section. $ET_p$ and CWR estimates were calculated considering summer crops only, because of the overlap between their development and the irrigation season. These were calculated on a daily basis and temporally aggregated to 10-day intervals. For ease of discussion, the considered reference period from June 17th to September 18th 2012 is referred to as the "growing season".

### 4.1 *Crop Area Estimation*

Results of the multi-temporal classification indicated that the total area used for crop production in Marchfeld was 60,691 ha. Summer crop cultivation accounted for 35% (21,278 ha) of the total crop area. Cultivation of secondary and winter crops accounted for 17,149 ha and 22,248 ha, respectively. An accuracy assessment of the crop map was performed using 140 random sampling points, which were visually interpreted using the crop development and colour composites. The class "summer crop" reached an accuracy of 90.5%. An error matrix for this class is given in Tab. 1.

The crop areas and the intensity of land use for summer crops were further analyzed based on the boundaries of administrative districts (Fig. 3). The region Andlersdorf dedicated most of its area to summer crop production (43% of the district area, 231 ha). The minimum of 5% (61 ha) was situated in Strasshof, a district consisting mainly of urban areas. The district of Groß-Enzersdorf had the largest total area of summer crop production with 2,245 ha (29% of the district area). The percentage of land use for summer crop cultivation within Marchfeld for each administrative district is given in Tab. 2.

### 4.2 *Analysis of Agro-Meteorological Data*

The average daily temperature recorded at Zwerndorf weather station ranged from 12.6 °C to 29.8 °C during the growing season.

**Tab. 1:** Error matrix of the crop mask classification.

| | | Reference data | | |
|---|---|---|---|---|
| | | **Summer** | **Other** | **User's accuracy** |
| **Classification result** | **Summer** | 38 | 4 | 90.5 % |
| | **Other** | 4 | 101 | 96.2 % |
| | **Producer's accuracy** | 90.5 % | 96.2 % | |
| | | **Overall accuracy** | 94.6 % | |

**Tab. 2:** Percentages of summer crop area to district area.

| Municipality | Area of summer crop cultivation (%) |
|---|---|
| Aderklaa | 27.2 |
| Andlersdorf | 43.1 |
| Angern an der March | 16.1 |
| Auersthal | 21.8 |
| Bockfließ | 19.2 |
| Deutsch-Wagram | 20.5 |
| Eckartsau | 23.0 |
| Engelhartstetten | 27.3 |
| Gänserndorf | 21.5 |
| Glinzendorf | 37.6 |
| Großebersdorf | 24.5 |
| Groß-Engersdorf | 30.3 |
| Groß-Enzersdorf | 29.4 |
| Großhofen | 29.0 |
| Groß-Schweinbarth | 12.8 |
| Haringsee | 33.3 |
| Lassee | 28.3 |
| Leopoldsdorf im Marchfelde | 33.4 |
| Mannsdorf an der Donau | 31.5 |
| Marchegg | 28.5 |
| Markgrafneusiedl | 15.0 |
| Matzen-Raggendorf | 12.9 |
| Obersiebenbrunn | 35.2 |
| Orth an der Donau | 22.9 |
| Parbasdorf | 36.7 |
| Pillichsdorf | 25.8 |
| Prottes | 16.5 |
| Raasdorf | 23.1 |
| Schönkirchen-Reyersdorf | 21.9 |
| Strasshof an der Nordbahn | 5.7 |
| Untersiebenbrunn | 25.6 |
| Weiden an der March | 23.7 |
| Weikendorf | 24.0 |
| Wolkersdorf im Weinviertel | 16.0 |

The average wind speed at 2 m height was 2.7 m/s ($\sigma = \pm 0.8$ m/s).

The reference ET reached a maximum value of 6.1 mm/day at the end of June. The minimum of 3.2 mm/day occurred at the beginning of September. The total $ET_0$ over the growing season was 391 mm (94 days). Fig. 3 reports the weekly averages of $ET_0$ in 2012 in relation to the averages of the years 2009 to 2011.

From the eleven stations, the highest amount of precipitation during the growing season was recorded in Wien-Unterlaa with 249 mm. The lowest volume was 148 mm at Zwerndorf. The interpolated measures of precipitations were aggregated to 10-day intervals and are presented in Tab. 3. Records of precipitation showed an expected eastward downtrend. Stations in the eastern part of the study area, i.e. Gänserndorf, Zwerndorf, Bad Deutsch-Altenburg and Bruck-Neudorf, recorded lower amounts of precipitation with a mean ($\mu$) of 163 mm and a standard deviation ($\sigma$) of $\pm$ 16 mm compared to stations in the western part ($\mu$ = 222 mm and $\sigma = \pm$ 16 mm). A comparison of average weekly values between 2012 and the years from 2009 to 2011 is given in Fig. 4.

## 4.3 *Crop Water Requirements*

The maximum water requirements for the growing season considering a timeframe of 94 days resulted in 34.26 million $m^3$, which corresponds to an average requirement of 3.8 million $m^3$ per 10-days ($\sigma = \pm$ 4.4 million $m^3$). The aggregation to 10-day intervals presented a maximum water requirement of 7.9 million $m^3$ in mid-August. Precipitation exceeded potential evapotranspiration during two of the 10-day periods. In this case, the surplus of water resulted in 4.7 million $m^3$ and 0.6 million $m^3$ at the end of July and in mid-September, respectively.

### Water requirements per district

The satellite-based calculation of water requirements was spatially aggregated to district level and normalized to the extent of the summer crop area per district to represent the spatial distribution of CWR. On average, the seasonal water requirement per district

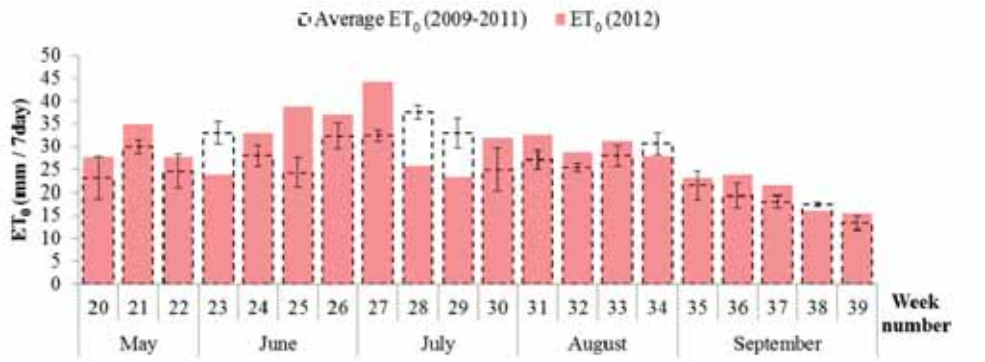


**Fig. 3:** Comparison between year 2012 and the average values measured in the last three years (2009 – 2011) for $ET_0$. The error bars indicate the standard deviation (1 time) within the four years (Zwerndorf).

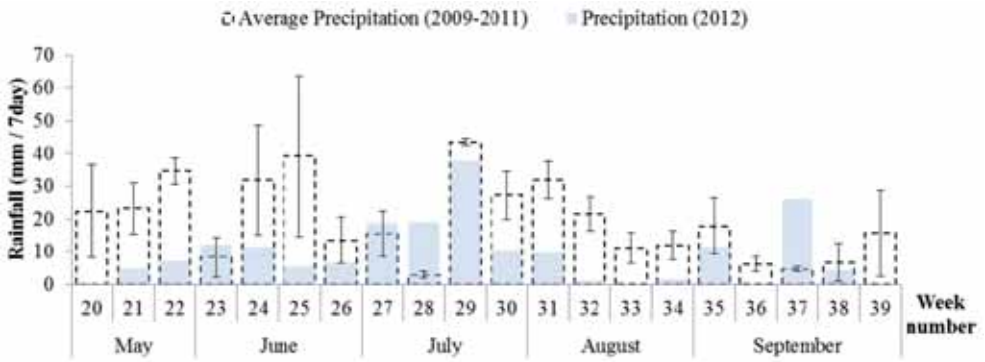


**Fig. 4:** Comparison between year 2012 and the average values measured in the last three years (2009 – 2011) for total rainfall. The error bars indicate the standard deviation (1 time) within the four years (Zwerndorf).

**Tab. 3:** Calculated values of reference evapotranspiration ($ET_0$), potential evapotranspiration of summer crops ($ET_p$), precipitation data and water requirements for the year 2012 from 17th of June to 18th of September; dates in the first column indicate starting points for 10-day intervals. Mean values (μ) and standard deviations (σ) refer to the spatial variation within the region of interest.

| | $ET_0$ (mm) | $ET_p$ (mm) | | Precipitation (mm) | | Water requirements of summer crops (million $m^3$) |
|---|---|---|---|---|---|---|
| | | μ | σ | μ | σ | |
| **June 17th** | 52.1 | 50.6 | 8.9 | 14.6 | 2.8 | 7.66 |
| **June 28th** | 61.4 | 56.0 | 13.6 | 19.4 | 5.0 | 7.87 |
| **July 9th** | 41.8 | 36.8 | 9.4 | 30.5 | 5.9 | 1.38 |
| **July 20th** | 36.6 | 32.0 | 7.7 | 55.0 | 14.1 | -4.77 |
| **July 31st** | 47.7 | 42.8 | 10.0 | 13.4 | 4.8 | 6.08 |
| **Aug. 11th** | 42.9 | 39.8 | 10.1 | 2.3 | 1.2 | 7.95 |
| **Aug. 21st** | 43.1 | 38.4 | 11.5 | 2.1 | 1.2 | 7.75 |
| **Sep. 1st** | 32.2 | 23.7 | 9.2 | 19.0 | 4.5 | 0.98 |
| **Sep. 11th** | 33.2 | 20.4 | 9.9 | 24.0 | 2.2 | -0.64 |
| **Overall** | 391 | | | | | 34.26 |

resulted in 1,523 m³/ha (σ = ± 288.4 m³/ha). The maximum CWR was observed in the district of Weiden an der March with a CWR of 1943 m³/ha. The minimum CWR of 968 m³/ha was observed in Pillichsdorf. Fig. 5 shows the spatial distribution of CWR.

## 5 Discussion and Conclusion

This study described an application of satellite-based technologies combined with agrometeorological data and spatial modelling to estimate water requirements during the irrigation period in the agricultural region of Marchfeld (Austria) for the year 2012. Reference evapotranspiration was calculated using the FAO-56 Penman-Monteith equation (Allen et al. 1998) and meteorological data recorded on-site. For a spatial estimation of precipitation events data from eleven rain gauges in the region of interest were interpolated. A time series of DEIMOS-1 imagery was acquired to follow the crop development during the growing season. Derived LAI and albedo maps were used to calculate the crop coefficient maps based on an approach proposed by D'Urso et al. (2001, 2010). The crop co-

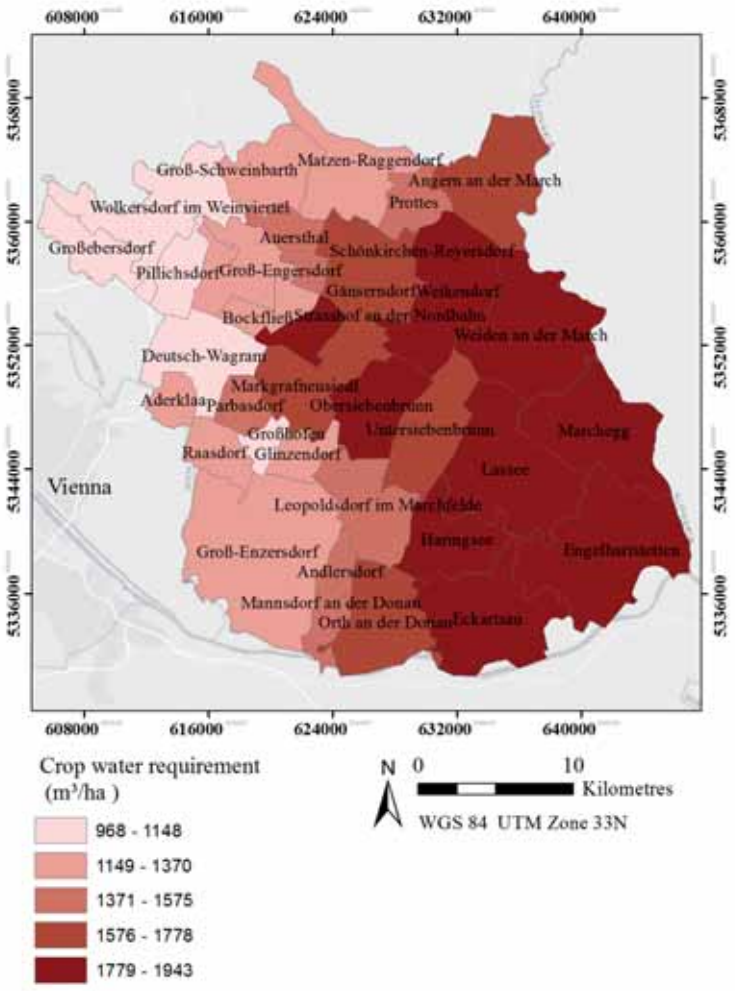


**Fig. 5:** Crop water requirements (m³/ha) of summer crops per district in Marchfeld for the growing season 2012.

efficient maps were temporally interpolated to derive daily estimations of crop development. Subsequently reference evapotranspiration and satellite-based $K_c$ data were used to calculate potential evapotranspiration on a pixel-basis. The satellite time series was further used to classify the agricultural surface in winter or summer crops. The land cover map and the pixel-based potential evapotranspiration were used to calculate the total water requirements of summer crops.

Results indicated that the total area extent of summer crop production in the year 2012 was 21,278 ha with a total potential evapotranspiration of 340 mm. The total precipitation for the observed time period was 180 mm calculated as the average within the study area resulting in total water requirements for summer crops of 34.26 million $m^3$ (in 94 days; 368,429 $m^3$/day on average). This represents the maximum level of water needs in the region for the year 2012.

Contemporaneous measurements of the actual water withdraws were not available for the same reference period. A coarse comparison is only possible considering the aggregated data per season and the estimations of groundwater withdrawal from the "Marchfeldkanal Betriebsgesellschaft", the company responsible for the canal infrastructure. The estimation is based on measurements of the fluctuations of groundwater levels for representative measurements points. The Marchfeldkanal Company estimates the withdrawal for irrigation purposes by limiting the time frame to summer periods where distinct drops in the groundwater levels can be observed. The timeframe of the measurements varies between 55 days (1995) and 162 days (2012). The resulting estimation for agricultural irrigation for the years from 1991 to 2008 ranges between 7.5 million $m^3$ (year 2005) and 45.1 million $m^3$ (year 2000). For the year 2012, the estimation of water withdrawal was 35 million $m^3$ considering a timeframe of 162 days starting at the end of April (Neudorfer 2013).

For the Marchfeld region water regulation is a major management and resource issue which is closely monitored at groundwater level (Neudorfer & Weyermayer 2007). Knowledge of the regional water requirement and its spatial and temporal distribution provide an important base for further decision making processes. Closer examination of the water deficit at field level can help to develop a more precise framework for the implementation and regulation of water management practices. Current assessments of this variable in the Marchfeld region are based on local point measurements and are thus fixed to small scale calculations (Cepuder & Nolz 2007).

In his publication about "Accounting for Water Use and Productivity" Molden (2006) identifies three levels of water use: "[…] a use level such as an irrigated field or household, a service level such as an irrigation or water supply system, and a water basin level that may include several uses". *EO* data can help to bridge the gaps between these levels since water deficits can be assessed in detail on large scale in relatively short time steps.

Estimations of regional water requirements similar to the presented research were performed in a recent study by Akdim et al. (2014) for the Doukkala area in western Morocco. In addition to the regional calculation of water deficit this publication further surveys the water withdrawal for irrigation by measurements at central pumps. In doing so, the authors identified times of water deficits, the applied irrigation and the occurrence of mismatches between the two. For Marchfeld the volume of water withdrawal for irrigation on regional level is difficult to obtain due to the decentralized network of pumping stations, their individual management and data privacy issues. Similar to the study of Akdim et al. (2014) it would allow quantifying the adequacy of water allocation in certain times or areas, an important topic worldwide as emphasized by Wallace (2000). The estimation of regional water deficit in Marchfeld is a first step towards this direction. The lack of comparable data emphasizes the need for expanded research activities on this topic.

## Acknowledgements

The study was supported by the Austrian Space Application Programme (ASAP) in the context of the project 'EO4Water – Application of Earth observation technologies for rural water management' (www.eo4water.com).

## References


Akdim, N., Alfieri, S., Habib, A., Choukri, A., Cheruiyot, E., Labbassi, K. & Menenti, M., 2014: Monitoring of Irrigation Schemes by Remote Sensing: Phenology versus Retrieval of Biophysical Variables. – Remote Sensing **6** (6): 5815–5851.

Allen, R.G., Pereira, L.L., Raes, D., Smith, M. & Ab, W., 1998: Crop evapotranspiration – Guidelines for computing crop water requirements. – http://www.fao.org/docrep/x0490e/x0490e00.htm (9.7.2014).

Atkinson, P.M., Jeganathan, C., Dash, J. & Atzberger, C., 2012: Inter-comparison of four models for smoothing satellite sensor time-series data to estimate vegetation phenology. – Remote Sensing of Environment **123:** 400–417.

Casa, R., Varella, H., Buis, S., Guérif, M., De Solan, B. & Baret, F., 2012: Forcing a wheat crop model with LAI data to access agronomic variables: Evaluation of the impact of model and LAI uncertainties and comparison with an empirical approach. – European Journal of Agronomy **37** (1): 1–10.

Cepuder, P. & Nolz, R., 2007: Irrigation management by means of soil moisture sensor technologies. – Journal of Water and Land Development **11** (1): 79–90.

Clevers, J.G.P.W., 1989: Application of a weighted infrared-red vegetation index for estimating leaf Area Index by Correcting for Soil Moisture. – Remote Sensing of Environment **29:** 25–37.

Collins, R., Kristensen, P. & Thyssen, N., 2009: Water resources across Europe-confronting water scarcity and drought. – European Environment Agency.

Courault, D., Seguin, B. & Olioso, A., 2005: Review on estimation of evapotranspiration from remote sensing data: From empirical to numerical modeling approaches. – Irrigation and Drainage Systems **19** (3–4): 223–249.

D'Urso, G., 2001: Simulation and management of on-demand irrigation systems: a combined agrohydrological and remote sensing approach. – Wageningen University Press 174, Netherlands.

D'Urso, G. & Calera Belmonte, A., 2006: Operative Approaches To Determine Crop Water Requirements From Earth Observation Data: Methodologies And Applications. – AIP Conference Proceedings: 14–25.

D'Urso, G., Richter, K., Calera, A., Osann, M.A., Escadafal, R., Garatuza-Pajan, J., Hanich, L., Perdigao, A., Tapia, J.B. & Vuolo, F., 2010: Earth Observation products for operational irrigation management in the context of the PLEIADeS project. – Agricultural Water Management **98** (2): 271–282.

David, B., Elen, C., Janer, D., Silke, E., Erik, P.J., Jose, S.-V. & Consuelo, V.-O., 2000: The environmental impacts of irrigation in the European Union. – Dwyer, J. (ed.): A report to the Environment Directorate of the European Comission.

Deimos-Imaging, 2014: Our satellite: DEIMOS-1. – http://www.deimos-imaging.com/technology/our-satellite-deimos-1 (14.2.2014).

Dubrovsky, M., Svoboda, M.D., Trnka, M., Hayes, M.J., Wilhite, D.A., Zalud, Z. & Hlavinka, P., 2008: Application of relative drought indices in assessing climate-change impacts on drought conditions in Czechia. – Theoretical and Applied Climatology **96** (1–2): 155–171.

Eilers, P.H.C., 2003: A Perfect Smoother. – Analytical Chemistry **75** (14): 3631–3636.

Eitzinger, J., Kersebaum, K.C. & Formayer, H., 2009: Landwirtschaft im Klimawandel: Auswirkungen und Anpassungsstrategien für die land- und forstwirtschaftlichen Betriebe in Mitteleuropa. – 1. Auflage, 376 S., Agrimedia, Müncheberg.

European Environment Agency 2006: CORINE Land Cover. – http://www.eea.europa.eu/publications/COR0-landcover (16.12.2013).

Fatichi, S., 2012: Inverse Distance Weight for MATLAB. – http://www.mathworks.com/matlabcentral/fileexchange/24477-inverse-distance-weight (30.6.2014).

Frenken, K. & Gillet, V., 2012: Irrigation water requirement and water withdrawal by country. – http://www.fao.org/nr/water/aquastat/water_use_agr/index.stm (1.7.2014).

Jégo, G., Pattey, E. & Liu, J., 2012: Using Leaf Area Index, retrieved from optical imagery, in the STICS crop model for predicting yield and biomass of field crops. – Field Crops Research **131:** 63–74.

Molden, D.J., 2006: Accounting for Water Use and Productivity. – International Irrigation Management Institute (May): 1–16.

Mueller, N., Gerber, J., Johnston, M., Ray, D., Ramankutty, N. & Foley, J., 2012: Closing yield gaps through nutrient and water management. – Nature **490** (7419): 254–257.

Neudorfer, W., 2002: Wasserschutz und Lebensader Marchfeldkanal. – 1. Auflage, 174 S., Deutsch-Wagram, Österreich.

Neudorfer, W., 2013: personal communication.

Neudorfer, W. & Weyermayer, H., 2007: Securing groundwater use and reestablishing the water balance by artificial recharge of groundwater in the region of Marchfeld, Austria. – Water Practice & Technology **2** (3): 1–7.

Ozdogan, M., Yang, Y., Allez, G. & Cervantes, C., 2010: Remote Sensing of Irrigated Agriculture: Opportunities and Challenges. – Remote Sensing **2** (9): 2274–2304.

Pal, J.S., 2004: Consistency of recent European summer precipitation trends and extremes with future regional climate projections. – Geophysical Research Letters **31** (13): 1–4.

Pereira, L.S., Oweis, T. & Zairi, A., 2002: Irrigation management under water scarcity. – Agricultural Water Management **57** (3): 175–206.

Richter, R., 1998: Correction of satellite imagery over mountainous terrain. – Applied Optics **37** (18): 4004–4015.

Richter, R. & Schläpfer, D., 2014: Atmospheric / Topographic Correction for Airborne Imagery. – ATCOR-4 User Guide, Version 6.3.1.

Scharf, P.C., Schmidt, J.P., Kitchen, N.R., Sudduth, K.A., Hong, S.Y., Lory, J.A. & Davis, J.G., 2002: Remote sensing for nitrogen management. – Journal of Soil and Water Conservation **57** (6): 518–524.

Seckler, D., Amarasinghe, U., Molden, D., de Silva, R. & Barker, R., 1999: World Water Demand and Supply, 1990 to 2025: Scenarios and Issues. – International Water Management Institute, Colombo, Sri Lanka.

Shanan, L., 1987: The impact of irrigation. – SCOPE **32:** 115–132.

Trnka, M., Dubrovský, M., Svoboda, M., Semerádová, D., Hayes, M., Žalud, Z. & Wilhite, D., 2009: Developing a regional drought climatology for the Czech Republic. – International Journal of Climatology **29** (6): 863–883.

Verstraeten, W.W., Veroustraete, F. & Feyen, J., 2008: Assessment of Evapotranspiration and Soil Moisture Content Across Different Scales of Observation. – Sensors **8** (1): 70–117.

Vuolo, F., Neugebauer, N., Bolognesi, S., Atzberger, C. & D'Urso, G., 2013: Estimation of Leaf Area Index Using DEIMOS-1 Data: Application and Transferability of a Semi-Empirical Relationship between two Agricultural Areas. – Remote Sensing **5** (3): 1274–1291.

Wagner, P.D., Fiener, P., Wilken, F., Kumar, S. & Schneider, K., 2012: Comparison and evaluation of spatial interpolation schemes for daily rainfall in data scarce regions. – Journal of Hydrology **464:** 388–400.

Wallace, J., 2000: Increasing agricultural water use efficiency to meet future food production. – Agriculture, Ecosystems & Environment **82** (1-3): 105–119.

Whittaker, E.T., 1922: On a New Method of Graduation. – Edinburgh Mathematical Society **41:** 63–75.

Address of the Authors:

Nikolaus Neugebauer & Francesco Vuolo, University of Natural Resources and Life Sciences, Vienna (BOKU), Institute of Surveying, Remote Sensing and Land Information, Peter-Jordan-Straße 82, A-1190 Wien, Österreich, Tel.: +43-1 47654 5138, Fax.: +43-1 47654 5142, e-mail: {nikolaus.neugebauer} {francesco.vuolo}@boku.ac.at

Manuskript eingereicht: März 2014
Angenommen: Juli 2014

PFG 2014 / 5, 0383–0392
Stuttgart, October 2014

Article

# Analysing Phenological Characteristics Extracted from Landsat NDVI Time Series to Identify Suitable Image Acquisition Dates for Cannabis Mapping in Afghanistan

Matteo Mattiuzzi, Coen Bussink & Thomas Bauer, Vienna, Austria

**Keywords:** illicit crop monitoring, cannabis, NDVI, phenology, seasonality, senescence

**Summary:** Since 2009, the United Nations Office on Drugs and Crime (UNODC) has carried out various annual surveys of cannabis cultivation in Afghanistan. The mapping of cannabis fields is based on very high resolution satellite imagery. The image acquisition dates have a strong influence on whether cannabis can be visually differentiated from other crops. Expert knowledge shows that the ideal acquisition dates are at the end of the growing period (senescence) of cannabis. For future surveys a method was developed to predict the optimum observation dates independent of temporal differences of the phenology. The study includes an analysis of Landsat-based NDVI time series and the calculation of information about the senescence stages of cannabis and other vegetation. The approach was applied to four test sites in Afghanistan.

**Zusammenfassung:** *Analyse phänologischer Eigenschaften basierend auf Landsat NDVI Zeitreihen für die Bestimmung geeigneter Zeitpunkte für die Aufnahme von Satellitenbildern für die Kartierung von Cannabis in Afghanistan.* Das Büro für Drogen- und Verbrechensbekämpfung der Vereinten Nationen (UNODC) führt seit 2009 jährlich eine Auswertung der Anbaufläche von Cannabis in Afghanistan durch. Die Kartierung von Cannabisfeldern erfolgt mit Hilfe von sehr hochauflösenden Fernerkundungsdaten. Der Aufnahmezeitpunkt der Daten ist sehr bedeutend dafür, ob Cannabis von anderen Feldfrüchten visuell eindeutig unterschieden werden kann. Nach Expertenansicht liegt dieser Zeitpunkt am Ende der Wachstumsperiode (Seneszenz) von Cannabis. Für zukünftige Auswertungen wurde eine Methode entwickelt, den idealen Aufnahmezeitpunkt unabhängig von zeitlichen Unterschieden der Phänologie im Voraus zu bestimmen. Der Ansatz umfasst eine Analyse von NDVI Zeitreihen basierend auf Landsat-Daten und die Ableitung von Informationen über die Seneszenz-Phasen von Cannabis und anderen Pflanzen. Die Methode wurde in vier Testgebieten in Afghanistan angewandt.

## 1 Introduction

Illicit crops like cannabis, opium poppy and coca bush form the basis for highly lucrative narcotic drug production. Illicit crop cultivation (cannabis and opium poppy) in Afghanistan takes place in areas where insecurity and insurgencies are prevalent and is strongly linked with organized criminal networks (Unodc 2013a). Policy measures to tackle the problem require an integrated approach of stabilization measures, creating opportunities for alternative development and law enforcement. In order to ascertain the impact of these measures, the United Nations Office on Drugs and Crime monitors illicit crop production, providing technical assistance to its member states on methodology. One of the key components to estimate plant-based drug production is the area under cultivation, which is mostly done with the help of satellite images and appropriate statistical techniques. These estimations face various challenges and in particular the optimum timing of the satellite imagery.


www.schweizerbart.de
DOI: 10.1127/1432-8364/2014/0231
1432-8364/14/0231 $ 2.50

This is especially difficult for monitoring cannabis in Afghanistan due to the possible confusion with other crops.

Up until now UNODC has conducted four annual cannabis surveys in Afghanistan to determine the area under cultivation (2009 – 2012). In addition UNODC has been conducting annual opium poppy surveys in Afghanistan since 1994 and since 1999 with satellite imagery. For estimating the area, UNODC used satellite imagery that were acquired for locations based on a spatial sampling approach. The very high resolution satellite images (VHR) obtained on a single acquisition date were used to identify cannabis fields (Fig. 1) and to calculate the area under cultivation, which was extrapolated to a larger cannabis risk area (Unodc 2013b). Reliable information on the growing cycle of cannabis plants (phenology) is essential for the selection of the ideal acquisition time of the VHR images. Within the growing cycle that is subject to seasonal and regional variations, an attempt is made to try and find the most appropriate time for the acquisition of the satellite images where the illicit crop can best be identified and distinguished from other vegetation by means of a visual interpretation. According to local UNODC experts in Afghanistan cannabis is harvested later than most other crops.

Studies on the mapping of cannabis are often directed towards the early detection of plants in order to guide eradication campaigns, e.g. by mapping of potential high-risk areas to reduce the search area (Lisita et al. 2013). There are various unpublished studies but only a few scientific publications on detection through remote sensing using spectral differences detected from aerial platforms or hyperspectral images. Daughtry & Walthall (1998) and Azaria et al. (2012) identified specific spectral ranges that are optimum for differentiating cannabis from other crops that are at their best when the cannabis fields have dense canopies. Although there is a lot of informal knowledge on the behaviour of cannabis plants and how they are affected by the environment and cultivation practices, as far as the authors could verify, there is no scientific literature on monitoring the phenology of cannabis with remote sensing time series.

Phenology is defined as the study of the timing of recurring plant life cycle events that are driven by environmental factors (Morisette et al. 2009). The documentation of the timing of phenological events often relies on visual observations in the field. In order to collect data on phenology over large geographic areas, measurements of reflected electromagnetic radiation from the land surface can be used. The timing of recurring changes in reflectance is defined as land surface phenology (Hanes et al. 2014). In this paper "phenology" refers to this term. Information on phenology as derived from remotely sensed images differ from conventional phenology data in that the information relates to the aggregated characteristics of the vegetation within the areal unit measured by satellite sensors. Phenological changes can be monitored by means of remote sensing as plants change in appearance and structure during their growth cycle.

The analysis as described in this paper is based on the normalized difference vegetation

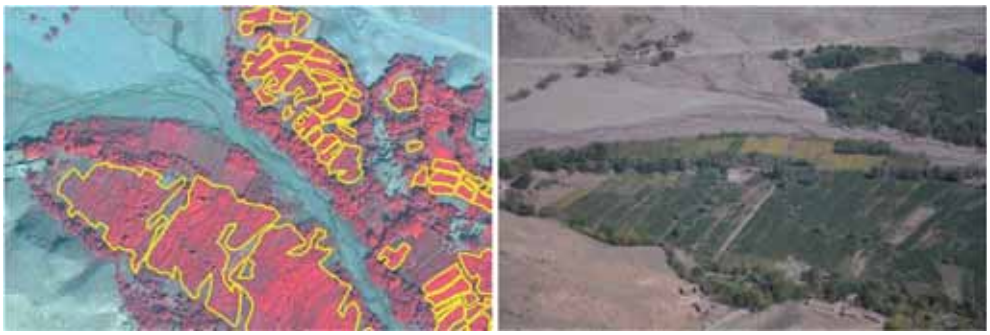

**Fig. 1:** Left: cannabis fields at flowering stage, as seen on a colour infra-red (CIR) satellite image, right: as seen from helicopter in Nangarhar province in 2012 (Unodc 2013).

index (NDVI). The NDVI is a mathematical combination of the Red and the NIR (near-infrared) band. Annual time series of satellite-derived vegetation indices and biophysical metrics that incorporate the reflectance of the NIR and the red wavelengths generally capture the spectral changes associated with leaf growth and senescence in the large areal units monitored by the sensor (Hanes et al. 2014). In order to better distinguish cannabis from other plants and to determine the ideal acquisition dates for VHR images, focus is laid on a more detailed analysis of the senescence. During the onset of senescence, deterioration of cell walls in the mesophyll tissue produces a distinctive decline in infrared reflectance; an accompanying increase in visible brightness may be the result of decline in the abundance and effectiveness of chlorophyll as an absorber of visible radiation (Campbell & Wynne 2006). This leads to a significant decrease of NDVI values.

While many studies have analysed phenological trends in general (e.g. Morisette et al. 2009), only a few studies have focussed on information on senescence derived from remotely sensed images. Jönsson & Eklundh (2004) for example developed a method to determine the number of seasons or seasonal parameters, e.g., the beginning or the end of the season. Zhang et al. (2003) used MODIS and AVHRR data for modelling the key phenological phases: green up, maturity, senescence and dormancy. A software tool developed by Lange & Doktor (2013) can also be used to determine such parameters.

The objective of this paper is to test whether the cannabis phenology in different regions in Afghanistan is different from the general vegetation at the end of the growing season, when cannabis can best be identified on VHR satellite imagery. In addition, the research looks at whether the development of cannabis in comparison to the general vegetation provides a basis for the development of a forecasting tool to determine the best dates for VHR image acquisition. This is done by analysing two parameters: i) the time span between the dates when the differences of the NDVI values of cannabis and non-cannabis vegetation reach a maximum; and ii) the maximum number of occurrences of senescence within each test site. The maximum difference of NDVI between cannabis and non-cannabis is expected to be the date where cannabis is most easily distinguishable. The maximum number of

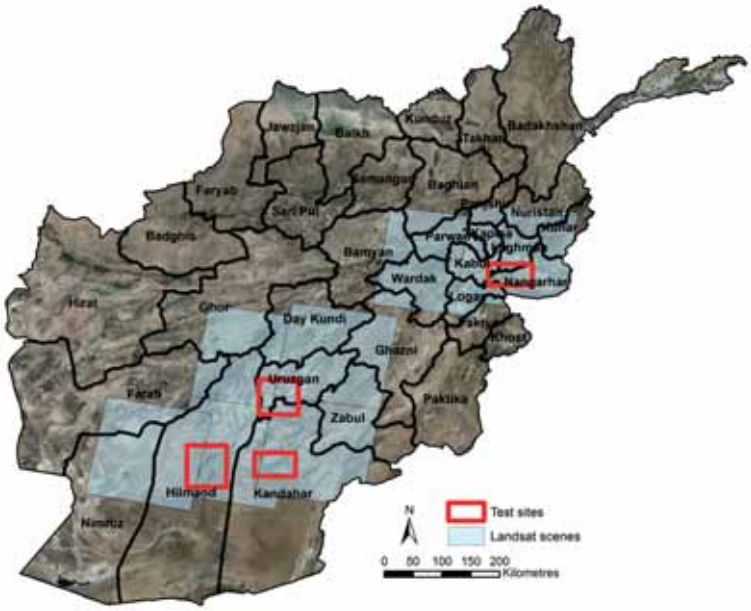


**Fig. 2:** Test sites in Afghanistan and Landsat scenes necessary to cover the areas.

occurrences of senescence is used to define a comparable phenological stage sensitive to seasonal changes between the years.

## 2 Study Area

Cannabis in Afghanistan is mostly (almost 90%) grown as an irrigated, annual monocrop, whereas the remaining 10% of the cannabis growing farmers cultivate cannabis in combination with other crops or on bunds (UNODC 2011). Cannabis flowers have the highest concentration of the active chemical drug components (cannabinoids like tetrahydrocannabinol) and the time of flowering is dependent on the age and variety of the plant, change in the photosynthetic period and environmental conditions. Cannabis plants usually start flowering after two months of growth but the abundant flowering starts when darkness (night length) exceeds approximately 11 hours per day. The flowering stage lasts between 4 and 12 weeks, depending on environmental conditions (CLARKE 1993). Outdoor cannabis cultivation in temperate zones like Afghanistan takes place in the summer season (March – September) and the life cycle of cannabis in Afghanistan is 5 – 6 months. From interviews with Afghan farmers, it is known that the planting season for cannabis starts between March and May/June. The plants are harvested from September/October to November/December depending on the region (UNODC 2013b). Cannabis is harvested when parts of the plants have already started deteriorating. Four test sites were selected in the provinces of Hilmand, Kandahar, Nangarhar and Uruzgan that represent the major cannabis growing areas in Afghanistan (Fig. 2). The northern growing provinces were not included since this region is a mountainous area where the matching of the reference dataset with the Landsat time series is highly challenging. The test sites are mainly flat, irrigated areas surrounded by desert.

## 3 Methodology

### 3.1 *Data*

The analysis was carried out using a time series of archived medium resolution satellite images. In this case all available data of the Landsat series (Landsat 5 TM and Landsat 7 ETM+) are acquired for the period between September 2008 and July 2012. Landsat was chosen as it offers free available data with a relatively high spatial resolution, and the continuity of acquisition is guaranteed for the coming years with the new Landsat 8 data. The time series are based on Landsat 5 TM and Landsat 7 ETM+ (SLC-off) and were downloaded from the USGS Earth Explorer (EARTH EXPLORER 2014). Fig. 2 shows the Landsat scenes necessary to cover the test sites. In total 7 different scene locations were needed. Landsat 5 TM could only be used until November 2011. The temporal resolution of each Landsat is 16 days resulting in a revisiting time of 8 days with both sensors. Additionally, in Afghanistan the overlapping areas from images of neighbouring Landsat orbits are covering more than 50 % of each scene (approximately 30 % on each side) leading to data for additional dates (LANDSAT 7 2012). For the period approximately 230 Landsat scenes per test site were downloaded and processed.

Landsat 7 ETM+ and Landsat 5 TM have very similar spectral bands. To produce a NDVI the Red (band 3) and the NIR (band 4) are required. The Red bands of both sensors have the identical spectral wavelength, the NIR is in Landsat 7 ETM+ with 0.77 µm to 0.90 µm slightly narrower compared to 0.76 µm to 0.90 µm in Landsat 5 TM. Since the difference is small it can be assumed that the impact can be neglected.

As reference data polygon data representing the cannabis fields (as shown in Fig. 1) were made available by UNODC. The polygons were delineated by UNODC staff based on VHR satellite images taken during the growing seasons of 2009, 2010 and 2011. Therefore, no geometric adjustment of the Landsat data was necessary as Landsat images fit with the reference data.

### 3.2 *Data Pre-Processing*

In order to process accurate NDVI values, spectral data were transformed from digital numbers which is basically top-of-atmosphere radiance with bias and gain introduced for storage optimisation to top-of-atmosphere reflectance using the R package "Remote Sensing" (R Core Team 2012, Mattiuzzi et al. 2012a). In a second step the data has been cropped and mosaicked to the extent of the test sites (Fig. 2). This was done using utilities of the geospatial data abstraction library (Gdal 2012). The NDVI values were filtered to reduce the impact of noise, cloud cover, missing data (Landsat 7 ETM+ SLC-off) and to derive smooth curves at regular temporal intervals. For filtering the „Modified Whittaker Smoother" (Atzberger & Eilers 2011) was chosen as the method allows filtering data without information on pixel quality. This method is based on two assumptions (Chen et al. 2004): i) that the NDVI time-series follows an annual cycle of growth and decline as the index is primarily related to vegetation density and plant vigour; and ii) that clouds and poor atmospheric conditions depress NDVI values, requiring that sudden drops in NDVI, which are not compatible with the gradual process of vegetation change, are regarded as noise and will be removed. Filtering was carried out with the MODIS package available in R (Mattiuzzi et al. 2012b).

### 3.3 *Analysis of the Phenology and the Senescence*

The result of the pre-processing is a yearly stack of layers of which NDVI graphs can be derived highly reflecting phenological stages at certain locations (Fig. 3 right).

Fig. 3 left shows the locations of cannabis fields in Kandahar. A VHR satellite image (colour infrared) acquired on November 15 in 2010 is used as a background image. The yellow polygons indicate cannabis fields as visually interpreted by UNODC experts. At the highlighted green marker the NDVI values are read out of the NDVI layer stack based on Landsat data and displayed as a graph (Fig. 3 right). The example clearly shows two peaks within a year. In most locations, where cannabis was identified, two crops occur within a year. On those fields the first peak can be identified at the end of March/beginning of April (winter crop) and in August/September (summer crop) a second peak occurs. The second peak represents cannabis while the first peak relates to other crops. The yellow points mark the main phenological stages: start of the season (local minimum NDVI at the beginning

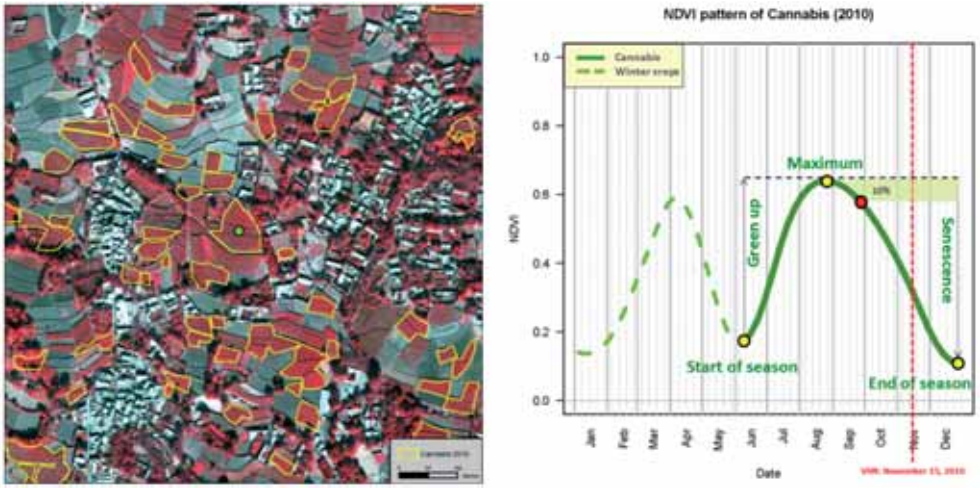


**Fig. 3:** Left: WorldView-2 satellite image (CIR; © DigitalGlobe Inc., all rights reserved) and cannabis polygons, right: NDVI curve with phenological indicators at one pixel location for 2010.

of green up), maximum (highest NDVI value) and end of season (local minimum NDVI at the end of senescence). A senescence of 10% is the point where the NDVI decreases by 10% of the cycle amplitude. The threshold was set to 10% in order to ensure an early detection of the declining phase of the NDVI values. This value is used for the subsequent analysis. The dashed red line represents the acquisition date of the VHR satellite image as used for the visual interpretation in 2010.

The best acquisition date of VHR satellite images when cannabis can be distinguished from other crops is expected to be at the date when the maximum difference in the NDVI occurs. Theoretically this can be at any time within the growing cycle but the aim is to determine the best date at the end of the growing season when cannabis can best be differentiated through visual interpretation. In order to forecast this optimal date without knowing the location of cannabis, the phenology of all active summer vegetation at the test sites is further investigated. The basic idea is to focus on the timing of senescence of all active summer vegetation pixels including cannabis in the test regions and to draw conclusions on the timing of NDVI differences.

The usage of the senescence for the prediction has been selected as it is expected that the senescence stage is closely related to the NDVI differences at the end of the growing cycle. The period between the maximum number of occurrences of early senescence (active summer vegetation, which can include cannabis sites) and maximum difference in NDVI (between cannabis and non-cannabis) is estimated based on two of the three available years, e.g. 2009 and 2010, using the average number of days of these years. This time period is then added to the date of the maximum number of occurrences of early senescence (active summer vegetation) in the year of the forecast, in this case 2011. The maximum number of occurrences of senescence is used to determine the general land surface phenology and training years are used to determine how the NDVI of cannabis behaves compared to the rest of the vegetation.

The time of the maximum NDVI was calculated for the summer period only. Within each geographic region 5000 random points were selected which have a NDVI maximum of at least +0.3 in the period of 40 days before and after the day where cannabis (mean) reaches its maximum. A NDVI value between 0.0 and +0.2 indicates a very low or no photosynthetic activity. The underlying assumption is to select those pixels with consistent active vegetation within the cannabis growing period. It is assumed that within a region the composition of planted crops is relatively stable in the years. The selected points can by chance also include cannabis pixels. This is because for the prediction of the senescence of cannabis in the following year no information about cannabis will be given. Therefore, two out of the three years were used to learn how the phenology of cannabis behaves in comparison to the general senescence of all crops in the region. For the remaining year the phenological stage of cannabis was predicted using the knowledge derived from the other years.

Based on the NDVI curves of the summer period the senescence was derived using the R package "phenex" (Lange & Doktor 2013). The date of the senescence was determined in the following way: In a first step the amplitude of the vegetation period was calculated using the minimum and maximum NDVI values found in the green up phase of the summer crop. The date of senescence refers to the point where the NDVI values decrease after the maximum by a given threshold of the NDVI amplitude (see Fig. 3 right), in this case 10% as mentioned before.

The distance between the date of the maximum senescence intensity of active summer vegetation (see red dashed line in Fig. 4) and the date of the maximum NDVI difference (black solid line) was calculated. The mean difference of the chosen reference years was then added to the maximum senescence intensity of active summer vegetation in the prediction. The number of occurrences of senescence is used as an indicator if the phenology in the test regions has changed from one year to another. For the subsequent analysis only reliable cannabis pixels were taken into account, the selection was done by using only those pixels that are fully contained by a cannabis reference polygon.

## 4 Results

The main outcome of this study is shown by region in the following figures. In the lower part of each graph the intensity of senescence is shown over time for active summer vegeta-

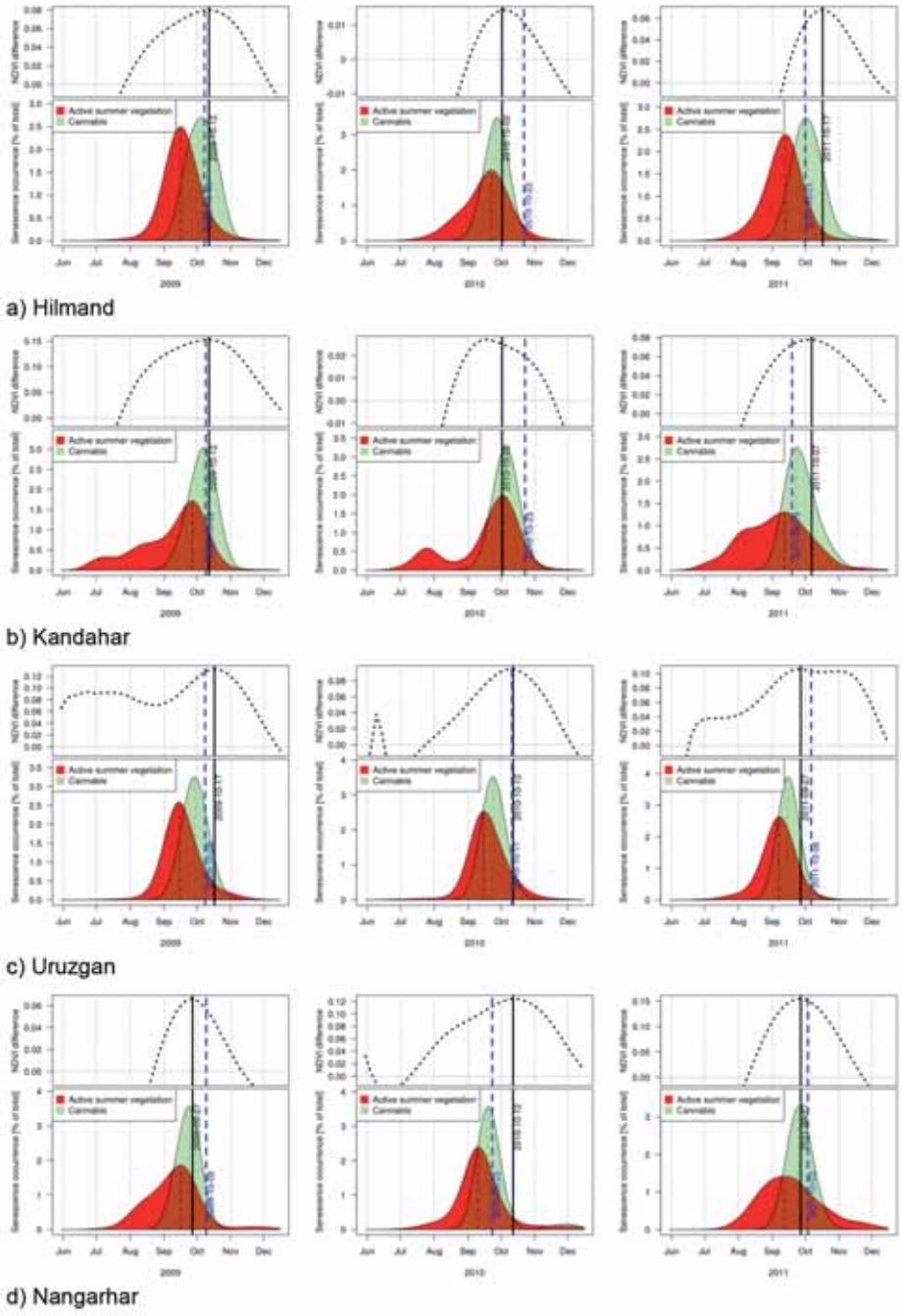


**Fig. 4:** Differences in NDVI and timing of senescence by region for 2009, 2010 and 2011 (lines: black solid = date of maximum NDVI difference, blue dashed = predicted maximum NDVI difference).

tion (red) and cannabis (green). In most cases it can be seen that cannabis reaches its maximum number of senescence occurrences later than the active summer vegetation. This confirms the experience of UNODC interpreters that cannabis is harvested later than other crops. The upper part shows the difference in NDVI (subtraction of non-cannabis from cannabis) and the bold black vertical line indicates the date of the maximum difference. The NDVI difference in Kandahar 2010 reaches its maximum earlier than the maximum number of occurrences of senescence. Therefore, the optimum date has been shifted to the maximum number of occurrences of senescence of the active summer vegetation.

The dashed blue lines in the graphs represent the predicted maximum NDVI difference (predicted ideal acquisition date). The calculation is based on the two other years. Comparing this with the date of the actual maximum NDVI difference (black line) gives information about the validity of the assumption for this study. The differences between the two dates in 2011 is 18 days for Hilmand, 17 days for Kandahar, 7 days for Uruzgan and 9 days for Nangarhar. A time range can be derived, taking into account the difference of the previous years. For Hilmand this time range can then be defined between 4 to 20 days, for Kandahar between 3 to 21 days, for Uruzgan between 1 to 10 days and for Nangarhar between 7 to 13 days.

## 5 Conclusions and Discussion

This research shows the usefulness of using Landsat time series to determine differences in crop phenology for the monitoring of cannabis in Afghanistan. The graphs depicting the development of the vegetation consistently show that cannabis tends to reach the stage of senescence later than other active summer vegetation. It is not known whether this depends on the type of vegetation, e.g. crop types, management of the crops or the ecophysiological circumstances in Afghanistan. The identified pattern supports the perception of the experts that undertake the identification of cannabis fields in the VHR satellite images, however it should be systematically monitored by the survey team if the date of maximum difference in NDVI corresponds with the date when cannabis can be best interpreted in the VHR satellite images. This information will be essential for optimising the programming of the VHR satellite images.

The method presented here to find the optimum acquisition date shows that in most cases the predictions based on the timing of senescence of the active summer vegetation strongly correspond with the optimum dates calculated from the actual NDVI values. Differences between predicted and actual dates range from 1 to 21 days. Although for operational purposes these time ranges are acceptable, it should be looked at more closely whether this method of prediction yields better results than other methods, e.g. using the start of the vegetation activity (green up) or simply using the mean date of maximum NDVI difference.

A limitation is the lack of an independent dataset to verify if the number of maximum occurrences of senescence reliably reflects the shifts in the timing of phenology. A deeper investigation, for example on test sites with ground based weather stations, could explain factors that influence phenological stages.

A strong limitation for developing and testing the method was that the predictions are based on two observations only. It would require longer time series to obtain more robust results, e.g. by including subsequent cannabis surveys. When this research was conducted another cannabis survey was finalised, which can give additional data to enhance the analysis.

Attention should be paid to the selection of cannabis pixels, as the median cannabis field size is only slightly larger than a Landsat pixel thereby reducing the number of usable cannabis reference pixel drastically. For this reason, many pixels had to be left out from the analysis because of probable mixed signatures. In the near future, images from Sentinel-2 (launch planned in 2015) could be used for this purpose offering a spatial resolution of 10 m. Another benefit of Sentinel-2 is the very high temporal resolution (5 days) which would lead to a more accurate computation of phenological phases.

One problem that this study faced was also the lack of information on the cultivation of

other crops. Information on crops growing in the same season would help to understand the difference between cannabis and crops with similar growing cycles. A crop by crop analysis could also help to detect which crops are causing problems in the prediction.

Future research can focus on what can be learned from the NDVI difference plots (Fig. 4, upper parts). The dates derived from this graph should be interpreted as an optimum within a time range and not as a single date. Experts with better knowledge of the crop types in the regions could interpret graphs from previous years. Similar NDVI difference patterns between the years could indicate that similar crops were grown and therefore represent a better prediction. Another aspect is to focus on a more detailed analysis of the regional senescence patterns in order to determine the point in time within the year when a reliable prediction of the ideal acquisition date is feasible.

## Disclaimer

The views expressed herein are those of the authors and do not necessarily reflect the views of the United Nations.

## References


Atzberger, C. & Eilers, P.H.C., 2011: Evaluating the effectiveness of smoothing algorithms in the absence of ground reference measurements. – International Journal of Remote Sensing **32:** 3689–3709.

Azaria, I., Goldschleger, N. & Ben-Dor, E., 2012: Identification of Cannabis plantations using hyperspectral technology. – Israel Journal of Plant Sciences **60** (1): 77–83.

Campbell, J.B. & Wynne, R.H., 2006: Introduction to remote sensing. – 5th edition, 667 p., Guilford Press, New York, NY, USA.

Chen, J., Jönsson, P., Tamura, M., Gu, Z., Matsushita, B. & Eklundh, L., 2004: A simple method for reconstructing a high-quality NDVI time-series data set based on the Savitzky-Golay filter. – Remote Sensing of Environment **91:** 332–344.

Clarke, R.C., 1993: Marijuana Botany: An Advanced Study: The Propagation and Breeding of Distinctive Cannabis. – Ronin Publishing, Berkeley, CA, USA.

Daughtry, C.S.T. & Walthall, C.L., 1998: Spectral discrimination of Cannabis sativa L. leaves and canopies. – Remote Sensing of Environment **64:** 192–201.

Earth Explorer, 2014: http://earthexplorer.usgs.gov (2.7.2014).

Gdal, 2012: Geospatial Data Abstraction Library: Version 1.9.1. Open Source Geospatial Foundation, Land surface phenology. – http://www.gdal.org (2.7.2014).

Hanes, J.M., Liang, L. & Morisette, J.T., 2014: Land surface phenology. – Hanes, J.M. (ed.): Biophysical Applications of Satellite Remote Sensing. – 230 p., Springer, Berlin.

Jönsson, P. & Eklundh, L., 2004: TIMESAT – A program for analysing time-series of satellite sensor data. – Computers and Geosciences **30:** 833–845.

Landsat 7, 2012: Landsat 7 Science Data Users Handbook. – http://landsathandbook.gsfc.nasa.gov (2.7.2014).

Lange, M. & Doktor, D., 2013: phenex: Auxiliary functions for phenological data analysis. R package version 1.0-3. – http://CRAN.R-project.org/package=phenex (2.7.2014).

Lisita, A., Sano, E.E. & Durieux, L., 2013: Identifying potential areas of Cannabis sativa plantations using object-based image analysis of SPOT-5 satellite data. – International Journal of Remote Sensing **34:** 5409–5428.

Mattiuzzi, M., Chemin, Y., Laborte, A. & Hijmans, R.J., 2012a: Remote Sensing. R package version 0.4.9/r260. – http://R-Forge.R-project.org/projects/remotesensing (2.7.2014).

Mattiuzzi, M., Verbesselt, J., Hengl, T., Klisch, A., Evans, B. & Lobo, A., 2012b: MODIS download and processing package. Processing functionalities for (multi-temporal) MODIS grid data. R package version 0.5-3/r276. – http://R-Forge.R-project.org/projects/modis (2.7.2014).

Morisette, J.T., Richardson, A.D., Knapp, A.K., Graham, E.A., Abnatzoglou, J., Wilson, B.E., Breshears, D.D., Henebry, G.M., Hanes, J.M. & Liang, L., 2009: Tracking the rhythm of the seasons in the face of global change: phenological research in the 21st century. – Frontiers in Ecology and the Environment **7** (5): 253–260.

R Core Team, 2012: R: A language and environment for statistical computing. R Foundation for Statistical Computing, Vienna, Austria. ISBN 3-900051-07-0. – http://www.R-project.org (2.7.2014).

UNODC, 2011: Afghanistan – Cannabis Survey 2010. – United Nations Office on Drugs and Crime, Vienna, Austria.

UNODC, 2013a: Afghanistan – Opium survey 2013. – United Nations Office on Drugs and Crime, Vienna, Austria.

UNODC, 2013b: Afghanistan – Survey of Commercial Cannabis Cultivation and Production 2012. – United Nations Office on Drugs and Crime, Vienna, Austria.

ZHANG, X., FRIEDL, M.A., SCHAAF, C.B., STRAHLER, A.H., HODGES, J.C.F., GAO, F., BRADLEY, R.C. & HUETE, A., 2003: Monitoring vegetation phenology using MODIS. – Remote Sensing of Environment **84:** 471-475.

Addresses of the Authors:

MATTEO MATTIUZZI & THOMAS BAUER, University of Natural Resources and Life Sciences, Vienna (BOKU), Institute of Surveying, Remote Sensing and Land Information, Peter-Jordan-Straße 82, A-1190 Vienna, Tel.: +43-1-47654-5100, Fax: +43-1-47654-5142, e-mail: {matteo.mattiuzzi}{t.bauer}@boku.ac.at

COEN BUSSINK, United Nations Office on Drugs and Crime, Statistics and Surveys Section, Trends Monitoring and Analysis Programme, PO Box 500, A-1400 Vienna, Tel.: +43-1-26060-4165, Fax: +43-1-26060-74165, e-mail: coen.bussink@unodc.org

Manuskript eingereicht: März 2014
Angenommen: Juli 2014

PFG 2014 / 5, 0393–0407
Stuttgart, October 2014

Article

# Improving Land Cover Maps in Areas of Disagreement of Existing Products using NDVI Time Series of MODIS – Example for Europe

Francesco Vuolo & Clement Atzberger, Vienna, Austria

**Keywords:** classification, land cover, random forest, accuracy / confidence, time series, NDVI

**Summary:** Regional to global scale land cover (LC) information is one of the most important inputs to various models related to global climate change studies, natural resource use and environmental assessment. This paper presents a methodology to derive land cover maps using time series of moderate-resolution imaging spectroradiometer (MODIS) 250 m normalized difference vegetation index (NDVI). An example for Europe is produced using the random forest (RF) classifier. For the accuracy assessment, the overall performance of our classification product (BOKU, Universität für Bodenkultur) is compared to the one of three existing LC maps namely GlobCover 2009, MODIS land cover 2009 (using the IGBP classification scheme) and GLC2000. Considered GlobCover and IGBP, the assessment is further detailed for areas where these two maps agree or disagree. The BOKU map reported an overall accuracy of 71%. Classification accuracies ranged from 78% where IGBP and GlobCover agreed to 63% for areas of disagreement. Results confirm that existing LC products are as accurate as the BOKU map in areas of agreement (with little margin for improvements), while classification accuracy is substantially better for the BOKU map in areas of disagreement. Two pixel-based measures of confidence of classification were derived, which showed a strong correlation with classification accuracy. The study also confirmed that RF provides an unbiased estimation of the error (out-of-bag) and therefore eliminates the need for an independent validation dataset.

**Zusammenfassung:** *Verbesserung von Landbedeckungskarten in Gebieten widersprüchlicher Grundlagen mit Hilfe der NDVI-Zeitreihe von MODIS – Beispiel für Europa.* Verlässliche regionale bis globale Informationen über die aktuelle Landbedeckung sind von größter Bedeutung für Fragen des Klimaschutzes, des Managements natürlicher Ressourcen sowie für Umweltbewertungen. Der vorliegende Beitrag beschreibt ein innovatives Verfahren, um Landbedeckungskarten aus Zeitreihendaten des Umweltsatelliten MODIS in 250 m Bodenauflösung zu generieren. Das überwachte Klassifikationsverfahren basiert auf multiplen Entscheidungsbäumen (Random Forest Classifier) und verwendet Informationen über den temporalen Verlauf der fernerkundlich erfassten Vegetationsdichte (NDVI). Um die Qualität unserer europäischen Landbedeckungskarte zu evaluieren, wird ein Vergleich mit drei existierenden globalen Landbedeckungskarten durchgeführt: GlobCover 2009, MODIS Land Cover 2009 (IGBP) und GLC2000. Als Referenz dient ein aus Google Earth generierter Referenzdatensatz basierend auf der visuellen Interpretation einer großen Anzahl von Referenzpunkten. Für die vergleichende Evaluierung wird zwischen Gebieten mit und ohne Übereinstimmung zwischen IGBP und GlobCover Produkten unterschieden. Die Landbedeckungskarte der Universität für Bodenkultur (BOKU) erreicht eine Gesamtgenauigkeit von 71%. Die Klassifikationsgenauigkeit variert dabei zwischen 78%, wenn IGBP und GlobCover übereinstimmen, und 63% in Gebieten ohne Übereinstimmung der zwei Vergleichskarten. Die BOKU Landbedeckungskarte zeigt in Gebieten ohne Übereinstimmung zwischen IGBP und GlobCover eine deutliche Verbesserung der Klassifikationsgenauigkeit. Die pixelweise generierten Konfidenzmaße zeigen darüber hinaus eine deutliche Korrelation mit der erzielten Klassifikationsgenauigkeit. Damit erhält der Nutzer ein detailliertes Bild über die zu erwartende Unsicherheitsmarge. Die Studie bestätigt, dass Random Forest eine ausgewogene (unbiased) Einschätzung der Fehler (out-of-bag) bietet.


www.schweizerbart.de
DOI: 10.1127/1432-8364/2014/0232
1432-8364/14/0232 $ 3.75

## 1 Introduction

Reliable and regularly updated land cover (LC) maps at medium spatial resolution and with regional-to-global coverage are required by land administrators, natural resource managers and scientists working in climate and environmental modelling (Hibbard et al. 2010). During the past 15 years, various international initiatives have been focused on the operational production of land cover products using satellite-based observations at a range of temporal and spatial resolutions. For instance, the European Commission's Joint Research Centre coordinated the realization of the global land cover 2000 (GLC2000) map using SPOT vegetation data at 1 km for the year 2000 (Bartholomé & Belward 2005). At higher spatial resolution, the European Space Agency (ESA) promoted the GlobCover project (Arino et al. 2008) to produce a global land cover map for the year 2005 and 2009 using MERIS data at 300 m pixel size. The land cover team at the Boston University recently released the Collection 5 of the MODIS global land cover type product (MCD12Q1) (Friedl et al. 2002, 2010). The product has a spatial resolution of 500 m (1 km in collection 4) and includes LC products obtained with five different classification systems, among them the International geosphere-biosphere programme (IGBP) and the University of Maryland (UMD) classifications. Of particular interest for the meteorological community is the ECOCLIMAP by Météo France (Masson et al. 2003), with a recent release of an improved version for Europe at 1 km resolution (ECOCLIMAP-II/Europe) (Faroux et al. 2013). ECOCLIMAP-II/Europe builds on existing land cover maps such as GLC2000 and CORINE land cover 2000 (Bossard et al. 2000) and on the analysis of leaf area index data from MODIS and of normalized difference vegetation index (NDVI) data from SPOT vegetation covering the period 1999 – 2005. Within the ESA's climate change initiative (CCI), a new set of global LC maps are also being generated using multi-sensor and multi-year observations (Landcover 2014).

Many studies have focused on dataset harmonization (Herold et al. 2006, 2009), intercomparison (Herold et al. 2008, Pflugmacher et al. 2011, Vintrou et al. 2012) and synergy to improve the consistency of existing products (See & Fritz 2006, Jung et al. 2006, Pérez-Hoyos et al. 2012, Vancutsem et al. 2013) or to extend their domain of application (Faroux et al. 2013). Despite the growing number of datasets, improved methods and joint efforts, land cover classification remains a challenging task due to the intrinsic high variability of class signatures at regional and global scales, together with the mixed pixel issues and class definition limitations. Most studies seem to agree that an improvement is possible by combining multiple input features (spectral- and temporal-observations), stratifications, e.g. based on climatological products, different classification approaches and by exploiting synergies between existing land cover products.

Interestingly, See & Fritz (2006) described a methodology to identify hotspots of disagreement between existing land cover products and to geographically focus reclassification efforts. Liu et al. (2004) noted that high agreement between two different classifiers can lead to a higher accuracy. This trend was confirmed by Vuolo & Atzberger (2012) where it was experimentally demonstrated that areas of thematic agreement between two existing land cover maps are more reliable in terms of classification accuracy compared to areas of disagreement. Moreover, the work of Vuolo & Atzberger (2012) showed that the classification performance of areas of disagreement could be notably improved using time series of NDVI from MODIS.

The scope of this paper is to extend the concept explored in Vuolo & Atzberger (2012) focusing on a larger dataset and including an additional land cover product for comparison. The paper is structured in three main components. First, we present the overall performance of our classification product (BOKU) and of three existing LC maps namely GlobCover 2009, MODIS land cover 2009 (using the IGBP classification scheme) and GLC2000. For this first comparison, validation focused on an independent dataset (visual interpretation of a large number of sample plots in Google Earth) not used during the training phase. BOKU map was derived using a smoothed and gap-filled time series of MODIS 250 m NDVI (average of multi-year

data centred on the year 2009) and the random forest (RF) classifier. Classification was stratified considering major European biogeographical regions. Then, we assessed the accuracy for the areas of agreement and of disagreement between the existing LC maps. For this detailed analysis we considered GlobCover and IGBP because they are produced with a similar spatial resolution and refer to the same year (2009) as the BOKU map. Finally, we produced a pan-European LC map and analysed the spatial pattern and the confidence of classification in relation to existing products. For this task, we exploited the entire reference dataset and based the accuracy assessment on the bootstrapped error estimates obtained during the training process.

## 2 Materials and Methods

A methodology is described for producing reliable land cover maps focusing on broad (here seven) LC classes. Only a few broad LC classes were chosen i) to provide a practical separation between managed vegetation and natural vegetation, and ii) to keep some flexibility and not preclude the possibility of comparisons with other LC schemes. The LC definitions used in this study and the corresponding MODIS IGBP (2009), GlobCover 2009 and GLC2000 class codes are provided in Tab. 1.

Multi-temporal MODIS NDVI observations were used to characterize the variations in growth patterns and phenology of different vegetation covers (Rodriguez-Galiano et al. 2012b). The image classification was performed by the machine learning random forest (RF) algorithm, which is an ensemble of decision trees.

### 2.1 *Satellite Data and Pre-Processing*

The input data used in this study consisted of 16-day NDVI composites from MODIS with a 250 m pixel size. The MODIS NDVI composite is a Level 3 product, calculated from the Level 2 daily surface reflectance product (MOD09 and MYD09 series) (Vermote et al. 2002). Data were aggregated using the constrained view angle – maximum value composite (CV-MVC) compositing method in a 16-day interval (Huete et al. 2002). The MODIS NDVI is currently available from Terra and Aqua platforms (MOD13Q1 and MYD13Q1) and the combined use of the two satellites provides time series with 8-day frequency.

In this study, we selected the year 2009 as the pivotal year and considered a MODIS time series of five years from the start of 2007 to the end of 2011. The CV-MVC time series were smoothed and interpolated to daily time steps based on a state-of-the-art Whittaker smoother (Atzberger & Eilers 2011a, 2011b, Atkinson et al. 2012). The smoothing/gap filling takes into account MODIS quality flags and the exact composite date of each pixel. For

**Tab. 1:** Land cover (LC) class codes and descriptions after aggregation of GlobCover 2009, GLC2000 and MODIS IGBP 2009 products. Water was not classified but taken from a water mask made for the MODIS satellite sensor data.

| Generalized Land Cover Class | GlobCover 2009 Class | GLC2000 Class | MODIS IGBP 2009 Class | Description |
|---|---|---|---|---|
| Cropland | 11,14,20,30 | 23,16,17,18 | 12, 14 | Agriculture and managed vegetation |
| Deciduous forest | 50,60 | 2,3 | 3, 4 | Close to open deciduous broadleaf trees |
| Evergreen forest | 70,90 | 4 | 1, 2 | Close to open evergreen needleleaf trees |
| Mixed forest | 100 | 6,9 | 5 | Mixed broadleaf and needleleaf trees |
| Shrubland | 110,130,150 | 11,12,14 | 6, 7, 8 | Shrub and sparse herbaceous |
| Grassland | 120,140 | 13 | 9, 10 | Herbaceous vegetation, rangeland |
| Urban/built up | 190 | 22 | 13 | Urban, mixed urban or artificial land |

purposes of filtering in near-real-time (NRT), shape constraints are used to minimize edge effects. The shape constraints are derived from the previous analysis of historical data. The processing ensures a significant reduction in high frequency noise and other artefacts resulting from undetected clouds and poor atmospheric conditions. The final product resulted in a filtered (smoothed and gap-filled) time series with a 7-day interval (52 observations per year) integrating data from MODIS Terra and Aqua platforms. The 5-year time series was summarized to provide 7-day inter-annual averages (n = 52) and the corresponding standard deviations (n = 52) for the period 2007 – 2011. The 104 multi-temporal observations representing the inter-annual averages and standard deviations centred on the year 2009 provided the main input for the land cover classification. The various steps of the time series data processing are exemplified in Fig. 1 for one arbitrarily selected MODIS pixel.

## 2.2 *Reference Dataset*

Similar to Vuolo & Atzberger (2012), the reference dataset was generated by visual interpretation of high spatial resolution images available in Google Earth (GE). The reference data was subsequently used to train the classification algorithm, to validate the results and to compare our map with existing LC products. A software toolbox was used to assist the display of GE images and to add the visually determined LC label to each of the surveyed point. This process was supported by the visualization of the temporal curves of NDVI values for each point under survey. Two quality indicators were also assigned: i) the confidence of interpretation, and ii) the homogeneity of the area under interpretation. The first index categorizes the uncertainties arising while interpreting the high spatial resolution images. The second index expresses the level of pixel homogeneity observed in the GE high spatial resolution images. A description of the toolbox and quality flags can be found in Vuolo & Atzberger (2012).

In our first study Vuolo & Atzberger (2012), we considered 1235 samples randomly selected over three core test sites in Europe (Austria, France and Macedonia). For the purpose of the present paper, we extended this reference dataset to a total number of 6383 points (1235 samples acquired from the previous study, 2526 acquired over seven additional core test sites and 2622 points to cover the remaining territory). The selection procedure was based on a random stratified sampling of Europe's main biogeographical regions (EEA 2012). Fig. 2 shows the extent of the study site. The regions considered were: *Alpine* (1), *Continental* (5), *Mediterranean* (7), *Pannonian* (8), *Atlantic* (10) and *Boreal* (11). The number of samples for each region and land cover class are presented in Tab. 2.

To reduce thematic errors in the reference dataset caused by the visual interpretation and spatial mismatch in the comparison of existing LC datasets, reference points that were qualified as 'Low homogeneity' and/or 'unsure' (n = 1717) were excluded from further analysis.

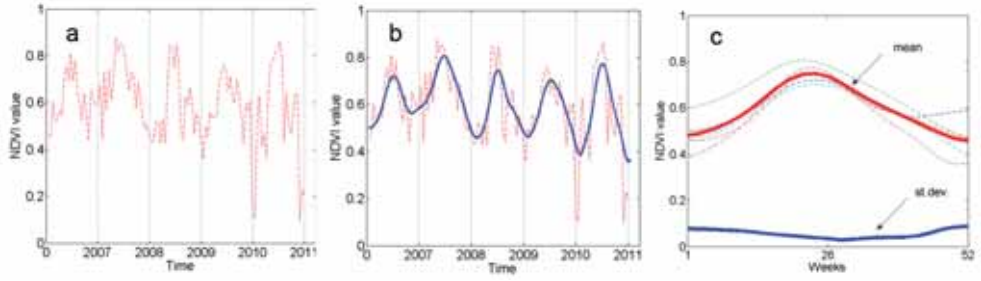


**Fig. 1:** a, b: Example of NDVI time series before and after filtering, c: temporal aggregation. Data smoothing was achieved in one step from year 2006 to 2011 using the Whittaker smoother as implemented at BOKU. The 104 features used for classification are shown in c: 52 mean values and 52 corresponding standard deviations.

The final dataset ($n_{tot}$ = 4666) was randomly split into two subsamples (training and validation). The first was solely used to train the classification algorithm. Only the validation samples were used to evaluate the classification algorithm and to perform an intercomparison with existing LC products.

**Tab. 2:** Number of samples of the reference dataset for each biogeographical region and land cover type. The randomized division of reference samples into training (n = 2342) and validation data (n = 2324) was done by class for each region.

| | Biogeographical region | | | | | | Total no. samples |
|---|---|---|---|---|---|---|---|
| | 1 | 5 | 7 | 8 | 10 | 11 | |
| Cropland | 78 | 695 | 450 | 59 | 186 | 68 | **1536** |
| Deciduous F. | 105 | 203 | 115 | 28 | 34 | 17 | **502** |
| Evergreen F. | 247 | 98 | 144 | 10 | 142 | 178 | **819** |
| Mixed F. | 124 | 231 | 67 | 7 | 49 | 122 | **600** |
| Shrubland | 103 | 25 | 194 | 1 | 42 | 14 | **379** |
| Grassland | 176 | 61 | 67 | 2 | 164 | 14 | **484** |
| Urban | 34 | 144 | 79 | 13 | 58 | 18 | **346** |
| ***Total no. samples*** | **867** | **1457** | **1116** | **120** | **675** | **431** | **4666** |
| Area ($km^2$) | 710 | 1959 | 1375 | 146 | 943 | 1016 | × 1000 |
| Sample / $km^2$ | 1.2 | 0.74 | 0.81 | 0.82 | 0.72 | 0.42 | |

## 2.3 *Classification Algorithm*

The land cover classification was performed by the machine learning random forest (RF) algorithm, which is an ensemble of decision trees. It uses bootstrap aggregating, i.e. bagging, to create different training subsets to produce a diversity of trees, each providing a classification result. The output class is obtained as the majority vote of the outputs of a large number of individual trees (Breiman 2001).

The algorithm produces an internal unbiased estimate of the generalization error, using the so-called 'out-of-bag' (OOB) samples (which are not included in the training subset) and provides a measure of the input features importance through random permutation. The randomized sampling leads to increased stability and better classification accuracy compared to a single decision tree approach. RF has been successfully applied in several classification problems achieving good results (Gislason et al. 2006, Rodriguez-Galiano et al. 2012a, Conrad et al. 2013, Toscani et al. 2013).

In this study we used a Matlab implementation of RF (Liaw & Wiener 2002, Abhishek

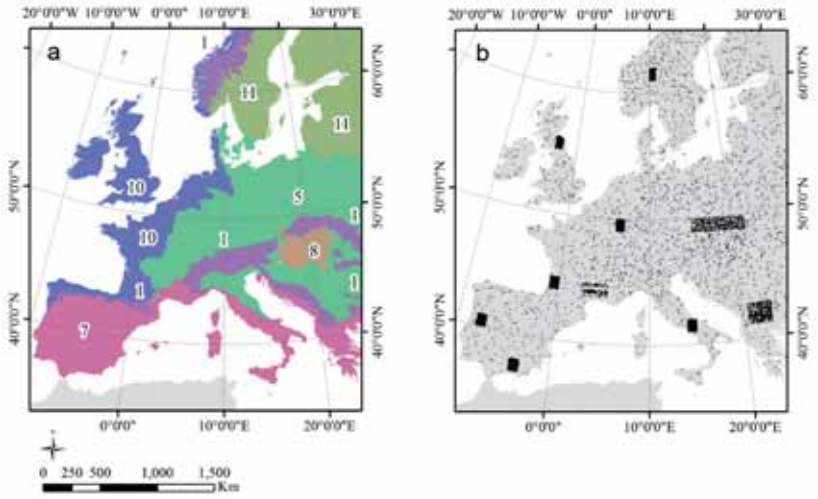


**Fig. 2:** a: Map of the biogeographical regions used for the stratification of the land cover classification, b: Reference dataset. The regions considered in this study were: Alpine (1), Continental (5), Mediterranean (7), Pannonian (8), Atlantic (10) and Boreal (11). The study area comprises most of the European area with a geographic extent from 10°00'W to 30°00'E and 35°00'N to 70°00'N. Regions with higher density of sampling points correspond to "core sampling sites".

2009). The software requires the setting of two parameters that are i) the number of trees to be grown in the run (*ntree*) and ii) the number of features used in each split (*mtry*). Several studies demonstrated that the default model parameters provide satisfactory results (Liaw & Wiener 2002, Díaz-Uriarte & Alvarez de Andrés 2006). We tested various combinations of *ntree* and *mtry*, which did not significantly affect the classification results. Therefore, as suggested in the software manual (Breiman & Cutler 2003), *mtry* was set equal to the square-root of the total number of input features (*mtry* = 10) using a sufficient number of trees (1000 in our case) so that adding more trees does not result in a significant performance gain.

### 2.4 *Accuracy Assessment and Classification Confidence Score*

The classification performance was based on common statistical measures (Foody 2002) derived from the classification error matrix, using solely validation samples. The selected statistical measures included the overall accuracy (OA), the producer's accuracy (PA) and the user's accuracy (UA). The two-side confidence intervals (CI) for the OA were calculated at 95% confidence level using the normal approximation method (Brown et al. 2001) including a continuity correction. The statistical significance of the differences between the pairs BOKU-GlobCover and BOKU-IGBP was evaluated with the McNemar's test with continuity correction (Siegel 1956).

The OOB error was used to assess the performance of the final pan-European LC map, which was generated using the entire reference dataset (training and validation samples). Two pixel-level measures of confidence of land cover classification were also obtained. A confidence score was calculated as the proportion of votes of the winning class to the total number of trees used in the classification. The higher the score, the more confident we are that a class is correctly classified. The second measure indicates the margin calculated as the proportion of votes for the winning class minus the proportion of votes of the second class.

## 3 Results

### 3.1 *Accuracy of Land Cover Classification*

The overall accuracies (OA) for the four LC maps produced by BOKU, IGBP, GlobCover and GLC2000 are presented in Tab. 3 for each biogeographical region and combined for all regions. Compared to the independent set of validation samples, BOKU achieved an OA of 71% (95% CI: 69% – 73%). The maps produced by IGBP, GlobCover and GLC2000 reported significantly lower OA ranging between 57% (GLC2000) and 63% (IGBP). From the numbers reported in Tab. 3 we calculated the percentage of increase or decrease of the overall accuracy of BOKU with respect to the other LC products. In this comparison, BOKU resulted 13%, 24% and 17% more accurate than IGBP, GlobCover and GLC2000, respectively. According to the two-tailed P-value, differences are considered to be extremely statistically significant ($p < 0.001$).

Regarding the six strata, and for all LC products, the *Boreal* biogeographical region was the least accurately classified. The *Alpine* biogeographical was inaccurately classified in all products, except BOKU. For the two mentioned regions GlobCover yielded the lowest accuracy. Results are not surprising since data samples in these two regions presented a lower level of confidence in the visual interpretation (due to the limited availability of high resolution images especially for the *Boreal* region) and a lower quality in the MODIS data input. The highest classification accuracies were ob-

**Tab. 3:** Overall accuracy for BOKU, IGBP (2009), GlobCover (2009) and GLC2000 for each biogeographical region and combined. All numbers refer to the independent validation dataset not used during training.

| | BOKU | IGBP | GlobCover | GLC2000 |
|---|---|---|---|---|
| *Alpine (1)* | 74% | 58% | 47% | 52% |
| *Continental (5)* | 75% | 70% | 64% | 61% |
| *Mediterranean (7)* | 67% | 61% | 58% | 63% |
| *Pannonian (8)* | 83% | 79% | 63% | 76% |
| *Atlantic (10)* | 72% | 56% | 60% | 71% |
| *Boreal (11)* | 58% | 58% | 49% | 52% |
| **Combined regions** | **71%** | **63%** | **57%** | **61%** |

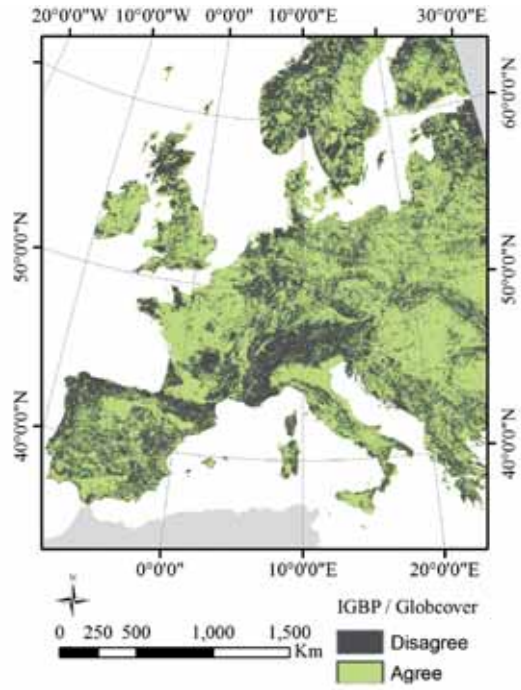


**Fig. 3:** Thematic agreement and disagreement between MODIS IGBP 2009 and GlobCover 2009.

tained for the *Pannonian* biogeographical region. The range of classification accuracies for the different LC products was larger for *Alpine* region (47% – 74%), compared to *Boreal* region (49% – 58%) region. For all regions, BOKU gave the highest OA.

The class-specific accuracies were analysed using the combined dataset. The error matrices are presented in Tab. 4. In details, *Cropland* reported a very high accuracy for most of the LC products, with producer's and user's accuracies greater than 70% in all cases. BOKU reported a very high producer's accuracy for *Cropland* (86%), indicating a good identification for all points visually interpreted as this class. Errors in the user's accuracy were often due to confusion with *Shrubland* and *Urban*. This result indicates that BOKU produces an overestimation of *Cropland* class with a commission error of 22%. A similar PA was observed in IGBP, with lower user's accuracies due to confusion of *Cropland* with *Deciduous Forest* and *Grassland* class. Regarding forest LC classes for BOKU, *Deciduous Forest* class was classified with producer's and user's accuracies of 67%, being often confused with *Mixed Forest* class. *Evergreen Forest* presented a higher accuracy with a producer's and user's accuracies greater than

**Tab. 4:** Error matrix and statistical measures for BOKU, IGBP 2009, GlobCover and GLC2000. All numbers refer to the independent validation dataset not used during training.

| | Reference | | | | | | | | |
|---|---|---|---|---|---|---|---|---|---|
| **BOKU** | C | DF | EF | MF | S | G | U | ∑ | UA |
| Cropland (C) | **660** | 12 | 18 | 14 | 50 | 44 | 50 | 848 | 78% |
| Decid. F. (DF) | 11 | **166** | 6 | 48 | 5 | 8 | 2 | 246 | 67% |
| Evergr. F. (EF) | 22 | 15 | **304** | 56 | 19 | 15 | 1 | 432 | 70% |
| Mixed F. (MF) | 23 | 47 | 51 | **172** | 2 | 12 | 0 | 307 | 56% |
| Shrubland (S) | 18 | 2 | 13 | 1 | **90** | 17 | 3 | 144 | 63% |
| Grassland (G) | 19 | 6 | 16 | 7 | 13 | **145** | 0 | 206 | 70% |
| Urban (U) | 14 | 1 | 1 | 0 | 10 | 5 | **127** | 158 | 80% |
| ∑ | 767 | 249 | 409 | 298 | 189 | 246 | 183 | 2341 | |
| PA | 86% | 67% | 74% | 58% | 48% | 59% | 69% | | |

OA 71% (95% C.I.: 69%–73%)

| | Reference | | | | | | | | |
|---|---|---|---|---|---|---|---|---|---|
| **IGBP (2009)** | C | DF | EF | MF | S | G | U | ∑ | UA |
| Cropland (C) | **650** | 83 | 15 | 38 | 18 | 77 | 25 | 906 | 72% |
| Decid. F. (DF) | 3 | **83** | 3 | 24 | 1 | 2 | 0 | 116 | 72% |
| Evergr. F. (EF) | 9 | 12 | **219** | 45 | 11 | 13 | 7 | 316 | 69% |
| Mixed F. (MF) | 27 | 63 | 106 | **176** | 7 | 12 | 3 | 394 | 45% |
| Shrubland (S) | 49 | 6 | 41 | 10 | **143** | 62 | 20 | 331 | 43% |
| Grassland (G) | 13 | 1 | 17 | 2 | 5 | **41** | 1 | 80 | 51% |
| Urban (U) | 13 | 1 | 1 | 0 | 0 | 1 | **126** | 142 | 89% |
| ∑ | 764 | 249 | 402 | 295 | 185 | 208 | 182 | 2285 | |
| PA | 85% | 33% | 54% | 60% | 77% | 20% | 69% | | |

OA 63% (95% C.I.: 61%–65%)

| | Reference | | | | | | | | |
|---|---|---|---|---|---|---|---|---|---|
| **GlobCover** | C | DF | EF | MF | S | G | U | ∑ | UA |
| Cropland (C) | **573** | 28 | 12 | 17 | 20 | 52 | 41 | 743 | 77% |
| Decid. F. (DF) | 43 | **146** | 50 | 103 | 8 | 19 | 6 | 375 | 39% |
| Evergr. F. (EF) | 5 | 8 | **215** | 46 | 35 | 8 | 1 | 318 | 68% |
| Mixed F. (MF) | 7 | 25 | 84 | **96** | 8 | 5 | 0 | 225 | 43% |
| Shrubland (S) | 70 | 12 | 39 | 11 | **99** | 74 | 7 | 312 | 32% |
| Grassland (G) | 55 | 28 | 6 | 23 | 13 | **80** | 3 | 208 | 38% |
| Urban (U) | 8 | 0 | 2 | 0 | 0 | 4 | **124** | 138 | 90% |
| ∑ | 761 | 247 | 408 | 296 | 183 | 242 | 182 | 2319 | |
| PA | 75% | 59% | 53% | 32% | 54% | 33% | 68% | | |

OA 57% (95% C.I.: 55%–60%)

| | Reference | | | | | | | | |
|---|---|---|---|---|---|---|---|---|---|
| **GLC2000** | C | DF | EF | MF | S | G | U | ∑ | UA |
| Cropland (C) | **630** | 51 | 34 | 28 | 23 | 55 | 62 | 883 | 71% |
| Decid. F. (DF) | 33 | **144** | 26 | 58 | 12 | 18 | 5 | 296 | 49% |
| Evergr. F. (EF) | 21 | 16 | **260** | 101 | 24 | 20 | 2 | 444 | 59% |
| Mixed F. (MF) | 15 | 27 | 56 | **98** | 20 | 8 | 1 | 225 | 44% |
| Shrubland (S) | 17 | 6 | 14 | 1 | **92** | 51 | 7 | 188 | 49% |
| Grassland (G) | 46 | 5 | 15 | 10 | 10 | **89** | 3 | 178 | 50% |
| Urban (U) | 2 | 0 | 1 | 2 | 1 | 3 | **102** | 111 | 92% |
| ∑ | 764 | 249 | 406 | 298 | 182 | 244 | 182 | 2325 | |
| PA | 82% | 58% | 64% | 33% | 51% | 36% | 56% | | |

OA 61% (95% C.I.: 59%–63%)

70%. *Mixed Forest* was often confused with *Deciduous* or *Evergreen Forest.* This trend was observed in all LC products, with additional confusion occurring between forest LC classes and *Cropland*, in particular in IBGP, with an omission error of 67%.

*Shrubland* presented the lowest PA in BOKU being often confused with *Cropland* and *Evergreen Forest* classes. This class was overestimated with a commission error of 37%. *Grassland* was classified with a producer's accuracy of nearly 60% and a user's accuracy of 70%. BOKU notably improved the classification accuracy for this class compared to the other LC products. Regarding *Urban* class, all LC products provided a good user's accuracy (> 80%), with GlobCover and GLC2000 achieving the best results. We observed an omission error of about 20% – 30% due to confusion of this class with *Cropland.*

### 3.2 *Accuracy for Areas of Agreement and Disagreement*

The classification accuracy was also evaluated separately for samples where GlobCover and IGBP maps agreed and where these maps disagreed. For this detailed analysis we considered only GlobCover and IGBP because they have a similar spatial resolution (300 m and 500 m pixel size) and refer to the same year (2009). The map of the areas of agreement and disagreement between these two products is presented in Fig. 3. The OA for BOKU, IGBP and GlobCover are presented in Tab. 5 for each

**Tab. 5:** The overall accuracy for IGBP, GlobCover and BOKU for areas of agreement and of disagreement between IGBP and GlobCover, respectively. The OA was assessed using the independent validation dataset (n = 2324 samples, of which 1230 were in agreement and 1094 in disagreement).

| | IGBP = GlobCover | | | Total no. of samples | IGBP ≠ GlobCover | | | Total no. of samples |
|---|---|---|---|---|---|---|---|---|
| | **IGBP** | **GlobCover** | **BOKU** | | **IGBP** | **GlobCover** | **BOKU** | |
| *Alpine (1)* | 65% | 65% | 80% | 226 | 50% | 27% | 68% | 206 |
| *Continental (5)* | 88% | 88% | 84% | 415 | 46% | 31% | 63% | 311 |
| *Mediterranean (7)* | 78% | 78% | 73% | 299 | 43% | 36% | 59% | 257 |
| *Pannonian (8)* | 93% | 93% | 96% | 28 | 60% | 37% | 70% | 30 |
| *Atlantic (10)* | 80% | 80% | 72% | 157 | 27% | 43% | 71% | 180 |
| *Boreal (11)* | 76% | 76% | 68% | 105 | 41% | 22% | 49% | 110 |
| **Combined regions** | **79%** | **79%** | **78%** | 1230 | **43%** | **33%** | **63%** | 1094 |

**Tab. 6:** The overall accuracy (combined regions) for IGBP, GlobCover and BOKU for all possible combinations of agreement among the three land cover products.

| | IGBP | GlobCover | BOKU | Total no. of samples |
|---|---|---|---|---|
| IGBP = GlobCover = BOKU | 90% | 90% | 90% | 941 |
| IGBP = BOKU ≠ GlobCover | 70% | 16% | 70% | 449 |
| IGBP ≠ BOKU = GlobCover | 19% | 72% | 72% | 316 |
| IGBP = GlobCover ≠ BOKU | 44% | 44% | 40% | 289 |
| IGBP ≠ GlobCover ≠ BOKU | 26% | 15% | 44% | 329 |

biogeographical region and combined. Results for areas of agreement and disagreement are presented separately.

In areas where GlobCover and IGBP agreed (n = 1230), we found an overall classification accuracy (combined regions) of 80% for IGBP / GlobCover and of 79% for BOKU. Percentage differences between BOKU and the combination of IGBP / GlobCover were not statistically significant ($p > 0.05$). Regarding the disagreement samples (n = 1094), we observed a general decrease in OA. However, this reduction was only modest for BOKU (from 71% to 63%) compared to the dramatic drop in

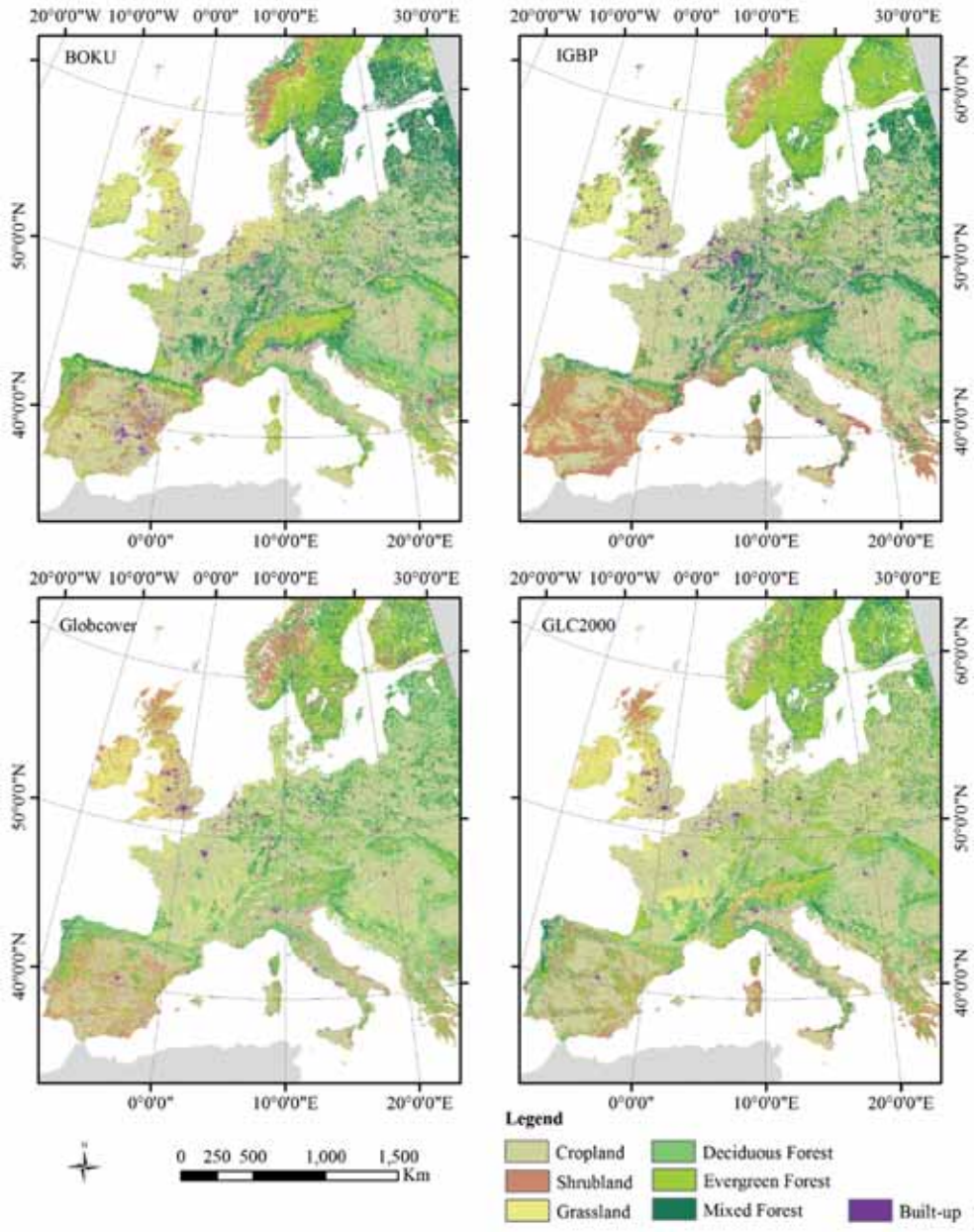


**Fig. 4:** BOKU, IGBP, GlobCover and GLC2000 land cover maps.

overall classification accuracy for GlobCover and IGBP. For example, in the case of IGBP, the overall classification accuracy dropped from 63% to 44%. For GlobCover the OA decreased from 57% to 33%. Hence, for the disagreement samples, BOKU resulted 43% and 95% more accurate compared to IGBP and GlobCover, respectively. Particularly remarkable improvements were achieved for *Atlantic*, *Alpine* and *Boreal* regions (Tab. 5).

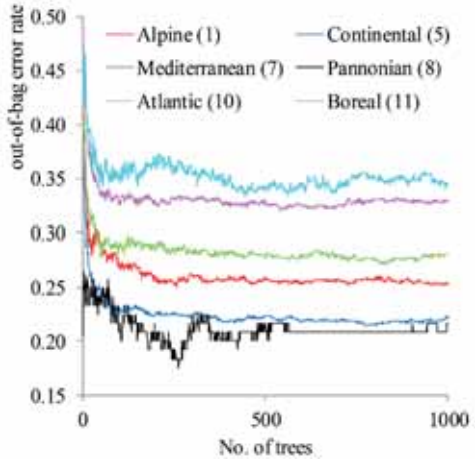


**Fig. 5:** Cumulative out-of-bag (OOB) error rate for the BOKU LC map for each biogeographical region. It shows how the OOB error changes while adding more trees to the ensemble classifier.

Classification results were further investigated considering all possible combinations of agreement (and disagreement) among the three LC products and they are presented in Tab. 6 for the combined biogeographical regions. In the case of a complete agreement (n = 941), we found an overall classification accuracy of 90%, which notably decreases where all products disagree (n = 329). Where BOKU agrees either with IGBP or with GlobCover, it achieved an OA greater than 70% indicating that our LC classification is more accurate (from 63% up to 72%) in the case of agreement with at least one of the two other LC products. Finally, the OA resulted slightly higher for the pair IGBP / GlobCover where they are in disagreement with BOKU. However, this latter combination presented the lower number of events (n = 289).

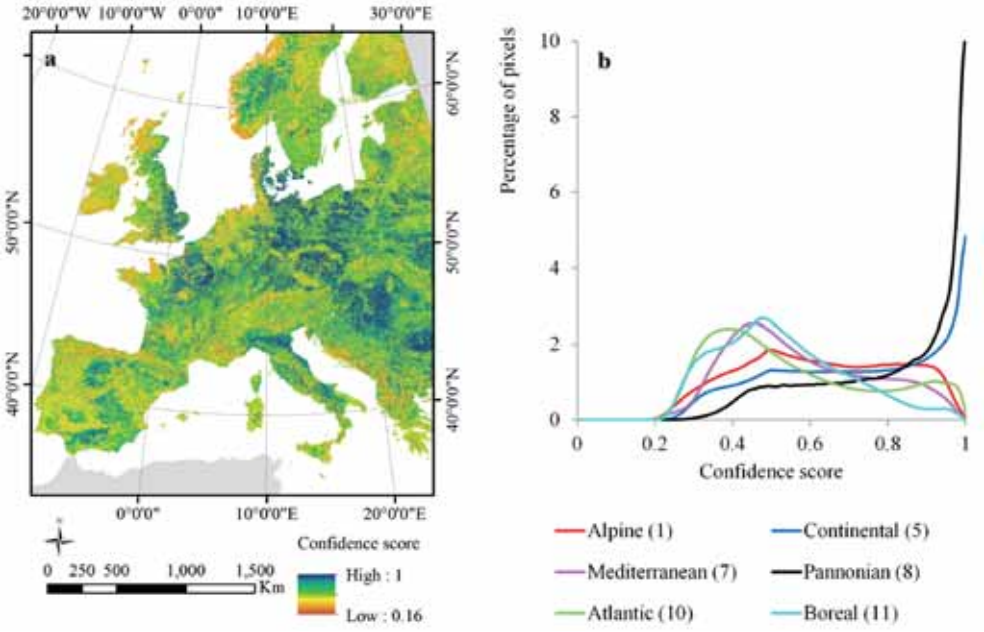


**Fig. 6:** a: Confidence scores for the BOKU LC map, b: Distribution of the confidence score values for the six biogeographic regions (number of bins = 100). A value of 1 indicates that all classification trees voted for the same class (maximum possible score). With seven LC classes, the theoretical minimum is 1/7.

### 3.3 *Map Production*

For producing the final map, we exploited the entire reference dataset ($n_{tot}$ = 4666) without splitting data in training and validation samples. Fig. 4 illustrates the BOKU map along with IGBP, GlobCover and GLC2000 products. Fig. 5 shows the cumulative OOB error rate for each biogeographical region over the 1000 classification trees.

The total accuracy was obtained as the last element of the OOB error rate minus one. The combined region achieved an average accuracy of 72% (versus 71% with the independent dataset) and of 75% (Alpine), 78% (Continental), 67% (Mediterranean), 78% (Pannonian), 72% (Atlantic) and 65% (Boreal), respectively. It is interesting to notice that these figures were comparable to the accuracy measures obtained from the independent validation dataset (first column in Tab. 3). The analysis of our dataset confirmed that the OOB error rate provides an unbiased estimation of the error and therefore eliminates the need for an independent validation dataset (Breiman 2001). However, we acknowledge that these accuracy measures might not be directly comparable with the OA obtained with the independent validation dataset since a different number of samples was used.

Fig. 6 shows the confidence score map and spatial distribution of score values. A score of

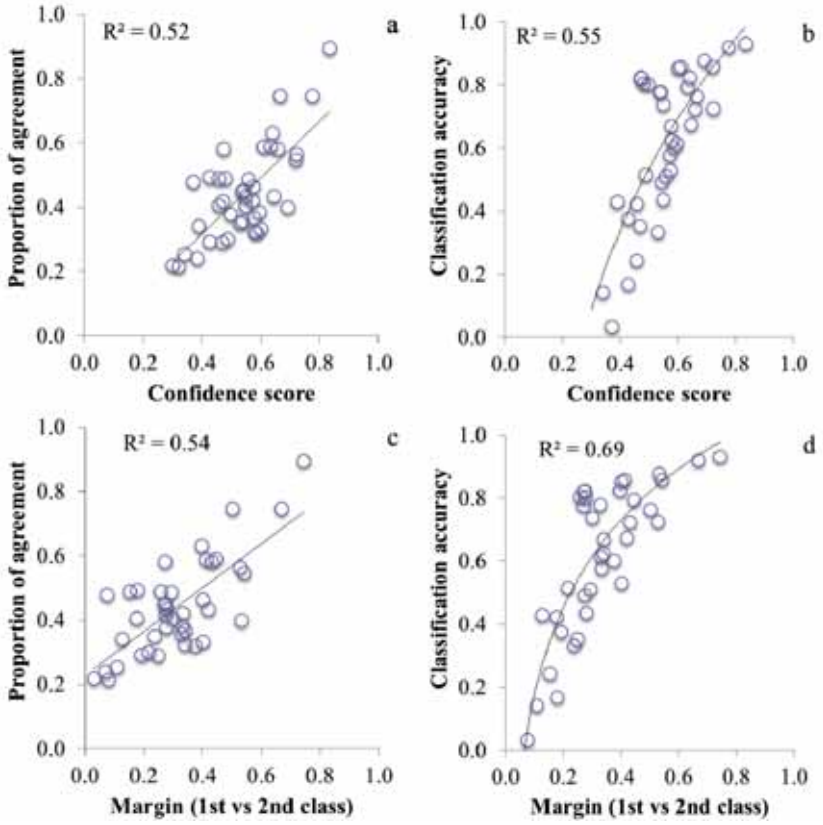


**Fig. 7:** a: Relationship of the confidence score with the proportion of agreement, b: Relationship of the confidence score with the classification accuracy, c: Relationship of the margin (defined as the difference in votes between the winning class and the second best class) with the proportion of agreement, d: Relationship of the margin with the classification accuracy. Each point represents the average value of one of the seven land cover classes within each of the six biogeographical regions (n = 42).

1 indicates that all classification trees voted for the same class, achieving the highest possible confidence.

Comparing Figs. 4 and 6, we notice that the pattern of the confidence score shows some spatial correlation with the land cover type and a clear positive trend with the class-specific accuracies. For instance, *Cropland* achieved a higher confidence score (0.70 ± 0.22 with a PA of 86%) compared to *Grassland* (0.49 ± 0.16 with a PA of 59%). A spatial correlation was also observed with the areas of agreement and disagreement between IGBP and GlobCover (Fig. 3).

Fig. 7a and b show the relationship between the confidence score and the proportion of pixels in agreement ($R^2 = 0.52$) and the classification accuracy ($R^2 = 0.55$), respectively. Similarly, Fig. 7c and d show the scatterplots between the classification margin and the proportion of pixels in agreement ($R^2 = 0.54$) and the classification accuracy ($R^2 = 0.69$), respectively. In all cases we observed a correlation showing that an increase in the confidence score corresponds also to an increase in the proportion of agreement and in the classification accuracy. For this comparison we used the producer's accuracy obtained from the independent validation dataset for each region.

## 4 Conclusions

This work evaluated the land cover (LC) classification performance of the random forest classifier using moderate-resolution imaging spectroradiometer (MODIS) 250 m normalized difference vegetation index (NDVI) time series at pan-European scale. The classification performance was compared to the overall accuracies of three existing products, GlobCover 2009, MODIS Land Cover Type IGBP 2009 and GLC2000. In particular, results were evaluated with respect to pixels in agreement and disagreement between GlobCover 2009 and MODIS IGBP 2009, i.e. 300 m and 500 m pixel size respectively. All results were obtained using harmonized legends with seven land cover classes. This disjoint analysis was performed to evaluate possible improvements in classification accuracy where existing maps are inconsistent (disagreement).

The results presented here expand our previous work (Vuolo & Atzberger 2012) and confirmed that there is a high potential in using multi-year (here 2007 – 2011, centred on the year 2009) time-series of MODIS 250 m NDVI for land cover classification. NDVI-derived BOKU LC maps achieved an overall accuracy of 71%. When comparing our results with the accuracy achieved by MODIS IGBP, GlobCover and GLC2000 aggregated to seven LC classes, we observed that BOKU LC map clearly outperforms these three (global) land cover products (see Tab. 4).

The findings at pan-European scale confirm that the classification accuracy of areas of agreement is systematically higher compared to areas where two (or more) maps disagree. Moreover, results demonstrated that in the case of the BOKU LC classification, the accuracy of data points for areas of disagreement was notably improved towards 43% and to 95% compared to IGBP and GlobCover, respectively (see Tab. 5). As expected, an improvement for agreement points was difficult to achieve, confirming that currently available LC products are already relatively accurate in areas of agreement (79% in our assessment and 90% where IGBP, GlobCover and BOKU agree).

Additionally, we analysed the consistency of two measures of confidence of classification, namely confidence score and margin. The two measures were obtained at pixel-level as direct outputs of the (ensemble) decision trees. We observed a clear relationship between the proportion of agreement/disagreement, accuracy and the confidence score/margin (see Fig. 7). Our results confirmed that these measures provide a reliable indication of confidence in classification for each pixel (Immitzer et al. 2012). For instance, the spatial pattern of the confidence score showed spatial correlation with the land cover type and – more importantly – a clear positive trend with the class-specific accuracies.

Regarding the bootstrapped error estimates obtained from the out-of-bag (OOB) samples, it is interesting to notice that these figures were comparable to the accuracy measures obtained from the independent validation dataset. Therefore, the analysis confirmed that the OOB error rate provides an unbiased es-

timation of the error and eliminates the need for an independent validation dataset (Breiman 2001).

Given the currently available global datasets, the users of LC products should in our opinion focus on combining existing maps and identify areas of agreement and disagreement. The accuracy of areas of spatial disagreement could then be improved based for example on the methodology proposed in this study. The proposed methodology can be easily generalized to different legend definitions or levels of land cover detail. This will help maximizing the overall accuracy of the resulting final land cover map as confirmed by our study.

Similar to several other studies (Jung et al. 2006, Kaptué Tchuenté et al. 2011, Fritz et al. 2011, Pflugmacher et al. 2011), our work confirmed that there is no clear preference of one LC product compared to others. A selection will always have to be based on a specific purpose or application.

Steps to further improve the accuracy of land cover maps include, for instance, ensembles of different algorithms for map production based on multi-source datasets (Benediktsson et al. 2007). Subsequently, these maps can be combined and synthetized in one product based on decision fusion rules (Waske & Benediktsson 2007, Udelhoven et al. 2009).

## References


Abhishek, J., 2009: Classification and Regression by randomForest-matlab. – https://code.google.com/p/randomforest-matlab/ (12.12.2013).

Arino, O., Bicheron, P., Achard, F., Latham, J., Witt, R. & Weber, J.-L., 2008: GlobCover: The most detailed portrait of Earth. – European Space Agency Bulletin **2008** (136): 24–31.

Atkinson, P.M., Jeganathan, C., Dash, J. & Atzberger, C., 2012: Inter-comparison of four models for smoothing satellite sensor time-series data to estimate vegetation phenology. – Remote Sensing of Environment **123** (0): 400–417.

Atzberger, C. & Eilers, P.H.C., 2011a: A time series for monitoring vegetation activity and phenology at 10-daily time steps covering large parts of South America. – International Journal of Digital Earth **4** (5): 365–386.

Atzberger, C. & Eilers, P.H.C., 2011b: Evaluating the effectiveness of smoothing algorithms in the absence of ground reference measurements. – International Journal of Remote Sensing **32** (13): 3689–3709.

Bartholomé, E. & Belward, A.S., 2005: GLC2000: a new approach to global land cover mapping from Earth observation data. – International Journal of Remote Sensing **26** (9): 1959–1977.

Benediktsson, J.A., Chanussot, J., Fauvel, M., Haindl, M., Kittler, J. & Roli, F., 2007: Multiple Classifier Systems in Remote Sensing: From Basics to Recent Developments. – Springer, Berlin, Heidelberg.

Bossard, M., Feranec, J. & Otahel, J., 2000: CORINE land cover technical guide: Addendum 2000. – http://www.dmu.dk/fileadmin/Resources/DMU/Udgivelser/CLC2000/technical_guide_addenum.pdf (2.7.2014).

Breiman, L., 2001: Random Forests. – Machine Learning **45** (1): 5–32.

Breiman, L. & Cutler, A., 2003: Setting up, using, and understanding random forests V4.0. – University of California, Department of Statistics. – http://www.stat.berkeley.edu/~breiman/Using_random_forests_v4.0.pdf (2.7.2014).

Brown, L.D., Cai, T.T. & Dasgupta, A., 2001: Interval Estimation for a Binomial Proportion. – Statistical Science **16** (2): 101–133.

Conrad, C., Rahmann, M., Machwitz, M., Stulina, G., Paeth, H. & Dech, S., 2013: Satellite based calculation of spatially distributed crop water requirements for cotton and wheat cultivation in Fergana Valley, Uzbekistan. – Global and Planetary Change **110:** 88–98.

Díaz-Uriarte, R. & Alvarez de Andrés, S., 2006: Gene selection and classification of microarray data using random forest. – BMC bioinformatics **7** (1): 3.

EEA 2012: Biogeographic regions in Europe. – http://www.eea.europa.eu/data-and-maps/figures/biogeographical-regions-in-europe-1 (24.1.2014).

Faroux, S., Kaptué Tchuenté, A.T., Roujean, J.-L., Masson, V., Martin, E. & Le Moigne, P., 2013: ECOCLIMAP-II/Europe: a twofold database of ecosystems and surface parameters at 1 km resolution based on satellite information for use in land surface, meteorological and climate models. – Geoscientific Model Development **6** (2): 563–582.

Foody, G.M., 2002: Status of land cover classification accuracy assessment. – Remote Sensing of Environment **80** (1): 185–201.

Friedl, M., McIver, D., Hodges, J.C., Zhang, X., Muchoney, D., Strahler, A., Woodcock, C., Gopal, S., Schneider, A., Cooper, A., Baccini, A., Gao, F. & Schaaf, C., 2002: Global land cover mapping from MODIS: algorithms and early

results. – Remote Sensing of Environment **83** (1–2): 287–302.

Friedl, M.A., Sulla-Menashe, D., Tan, B., Schneider, A., Ramankutty, N., Sibley, A. & Huang, X., 2010: MODIS Collection 5 global land cover: Algorithm refinements and characterization of new datasets. – Remote Sensing of Environment **114** (1): 168–182.

Fritz, S., See, L., McCallum, I., Schill, C., Obersteiner, M., Marijn Hannes Havlík, P., Achard, F.F., van der Velde, M. & Boettcher, H., 2011: Highlighting continued uncertainty in global land cover maps for the user community. – Environmental Research Letters **6** (4), http://iopscience.iop.org/1748-9326/6/4/044005/fulltext/ (8.7.2014).

Gislason, P.O., Benediktsson, J.A. & Sveinsson, J.R., 2006: Random Forests for land cover classification. – Pattern Recognition Letters **27** (4): 294–300.

Herold, M., Hubald, R. & Di Gregorio, A., 2009: Translating and evaluating land cover legends using the UN Land Cover Classification System (LCCS). – Workshop Report at FAO, GOFC-GOLD 43, Jena.

Herold, M., Mayaux, P., Woodcock, C.E.E., Baccini, A. & Schmullius, C., 2008: Some challenges in global land cover mapping: An assessment of agreement and accuracy in existing 1 km datasets. – Remote Sensing of Environment **112** (5): 2538–2556.

Herold, M., Woodcock, C.E., Mayaux, P., Belward, A.S., Latham, J. & Schmullius, C., 2006: A joint initiative for harmonization and validation of land cover datasets. – IEEE Transactions on Geoscience and Remote Sensing **44** (7): 1719–1727.

Hibbard, K., Janetos, A., van Vuuren, D.P., Pongratz, J., Rose, S.K., Betts, R., Herold, M. & Feddema, J.J., 2010: Research priorities in land use and land-cover change for the Earth system and integrated assessment modelling. – International Journal of Climatology **30** (13): 2118–2128.

Huete, A., Didan, K., Miura, T., Rodriguez, E.P., Gao, X. & Ferreira, L.G., 2002: Overview of the radiometric and biophysical performance of the MODIS vegetation indices. – Remote Sensing of Environment **83** (1–2): 195–213.

Jung, M., Henkel, K., Herold, M. & Churkina, G., 2006: Exploiting synergies of global land cover products for carbon cycle modeling. – Remote Sensing of Environment **101** (4): 534–553.

Kaptué Tchuenté, A.T., Roujean, J.-L. & De Jong, S.M., 2011: Comparison and relative quality assessment of the GLC2000, GlobCover, MODIS and ECOCLIMAP land cover data sets at the African continental scale. – International Journal of Applied Earth Observation and Geoinformation **13** (2): 207–219.

Immitzer, M., Atzberger, C. & Koukal, T., 2012: Tree Species Classification with Random Forest Using Very High Spatial Resolution 8-Band WorldView-2 Satellite Data. – Remote Sensing **4** (9): 2661–2693.

Landcover, 2014: http://www.esa-landcover-cci.org/ (7.7.2014).

Liaw, A. & Wiener, M., 2002: Classification and Regression by randomForest. – R news **2** (December): 18–22.

Liu, W., Gopal, S. & Woodcock, C.E., 2004: Uncertainty and Confidence in Land Cover Classification Using a Hybrid Classifier Approach. – Photogrammetric Engineering & Remote Sensing **70** (8): 963–971.

Masson, V., Champeaux, J.-L., Chauvin, F., Meriguet, C. & Lacaze, R., 2003: A Global Database of Land Surface Parameters at 1-km Resolution in Meteorological and Climate Models. – Journal of Climate **16** (9): 1261–1282.

Pérez-Hoyos, A., García-haro, F.C.C.F.J. & San-Miguel-Ayanz, J., 2012: A methodology to generate a synergetic land-cover map by fusion of different land-cover products. – International Journal of Applied Earth Observation and Geoinformation **19:** 72–87.

Pflugmacher, D., Krankina, O.N., Cohen, W.B., Friedl, M.A., Sulla-Menashe, D., Kennedy, R.E., Nelson, P., Loboda, T.V., Kuemmerle, T., Dyukarev, E., Elsakov, V. & Kharuk, V.I., 2011: Comparison and assessment of coarse resolution land cover maps for Northern Eurasia. – Remote Sensing of Environment **115** (12): 3539–3553.

Rodriguez-Galiano, V.F., Chica-Olmo, M., Abarca-Hernandez, F., Atkinson, P.M. & Jeganathan, C., 2012a: Random Forest classification of Mediterranean land cover using multi-seasonal imagery and multi-seasonal texture. – Remote Sensing of Environment **121:** 93–107.

Rodriguez-Galiano, V.F., Ghimire, B., Rogan, J., Chica-Olmo, M. & Rigol-Sanchez, J.P., 2012b: An assessment of the effectiveness of a random forest classifier for land-cover classification. – ISPRS Journal of Photogrammetry and Remote Sensing **67:** 93–104.

See, L. & Fritz, S., 2006: A method to compare and improve land cover datasets: Application to the GLC-2000 and MODIS land cover products. – IEEE Transactions of Geoscience and Remote Sensing **44** (7): 1740–1746.

Siegel, S., 1956: Nonparametric statistics for the behavioral sciences. – McGraw-Hill series in psychology McGraw-Hill, New York, NY, USA.

Toscani, P., Immitzer, M. & Atzberger, C., 2013: Wavelet-based texture measures for object-based classification of aerial images. – PFG – Photogrammetrie, Fernerkundung, Geoinformation **2013** (2): 105–121.

Udelhoven, T., van der Linden, S., Waske, B., Stellmes, M. & Hoffmann, L., 2009: Hypertemporal Classification of Large Areas Using Decision Fusion. – IEEE Geoscience and Remote Sensing Letters **6** (3): 592–596.

Vancutsem, C., Marinho, E., Kayitakire, F., See, L. & Fritz, S., 2013: Harmonizing and Combining Existing Land Cover/Land Use Datasets for Cropland Area Monitoring at the African Continental Scale. – Remote Sensing **5** (1): 19–41.

Vermote, E.F., El Saleous, N.Z. & Justice, C.O., 2002: Atmospheric correction of MODIS data in the visible to middle infrared: first results. – Remote Sensing of Environment **83** (1–2): 97–111.

Vintrou, E., Desbrosse, A., Bégué, A., Traoré, S., Baron, C. & Lo Seen, D., 2012: Crop area mapping in West Africa using landscape stratification of MODIS time series and comparison with existing global land products. – International Journal of Applied Earth Observation and Geoinformation **14** (1): 83–93.

Vuolo, F. & Atzberger, C., 2012: Exploiting the Classification Performance of Support Vector Machines with Multi-Temporal Moderate-Resolution Imaging Spectroradiometer (MODIS) Data in Areas of Agreement and Disagreement of Existing Land Cover Products. – Remote Sensing **4** (12): 3143–3167.

Waske, B. & Benediktsson, J.A., 2007: Fusion of Support Vector Machines for Classification of Multisensor Data. – Geoscience and Remote Sensing, IEEE Transactions on **45** (12): 3858–3866.

Address of the Authors

Dr. Francesco Vuolo & Prof. Dr. Clement Atzberger, University of Natural Resources and Life Sciences, Institute of Surveying, Remote Sensing and Land Information (IVFL), Peter-Jordan-Straße 82, A-1190 Wien, Tel.: +43-1-47654-5100, Fax.: +43-1-47654-5142, e-mail: {francesco.vuolo} {clement.atzberger} @boku.ac.at

Manuskript eingereicht: März 2014
Angenommen: Juli 2014

PFG 2014 / 5, 0409–0421
Stuttgart, October 2014

Article

# Evaluating Phenological Metrics derived from the MODIS Time Series over the European Continent

Anja Klisch & Clement Atzberger, Vienna, Austria

**Keywords:** MODIS, Whittaker smoother, phenology, start of season, change detection

**Summary:** Regularly updated and consistent time series of the normalised difference vegetation index (NDVI) are important data sources for environmental monitoring. BOKU has setup an operational processing chain for a large European window (40° x 40°) using the Moderate Resolution Imaging Spectroradiometer (MODIS) NDVI with a 16-day compositing period and 250 m ground resolution from the year 2000 onwards. Recently, this MODIS time series has been compared with the newly released GIMMS NDVI3g dataset derived from National Oceanic and Atmospheric Administration (NOAA) satellites with (1/12)° spatial and bi-monthly temporal resolution (Atzberger et al. 2014). The NDVI time series has shown an overall moderately good agreement. However, when deriving phenological metrics from both time series, the start of season exhibited large discrepancies, which could be partly related to differences in the temporal NDVI profiles. With the present study, the validation efforts are continued. We focus on evaluating the start of season (SOS) data derived from MODIS NDVI from 2003 to 2011 with (1/12)° spatial resolution using the extraction algorithm implemented at BOKU. The study particularly considers the spatial and temporal variability over the European continent and Maghreb by comparing them with other published results. The spatial pattern of the SOS at a continental level showed a good agreement with previous work of Han (2012). A moderate ($R^2$ = 0.53) and good ($R^2$ = 0.79) relationship between SOS and altitude could be established along transects in Scandinavia. Inter-annual SOS anomalies derived for the island of Ireland coincided very well with the research results of O'Connor et al. (2012). A good agreement ($R^2$ = 0.90) for all pixels and years in Europe and Maghreb could be reported when compared with results of the state-of-the-art TIMESAT software (Jönsson & Eklund 2004).

**Zusammenfassung:** *Ableitung und Evaluierung phänologischer Kenngrößen aus MODIS-Zeitreihen für den Europäischen Kontinent.* Regelmäßig aktualisierte und konsistente Zeitreihen des normalisierten differenzierten Vegetationsindex (NDVI) sind eine wichtige Voraussetzung für die Überwachung und Modellierung von Umweltprozessen in großen Untersuchungsgebieten. Basierend auf NDVI-Zeitreihen des Moderate Resolution Imaging Spectroradiometer (MODIS) wurde an der BOKU eine Prozessierungskette für ein Europäisches Fenster (40° x 40°) aufgesetzt. Die MODIS-NDVI-Zeitreihen liegen seit 2000 als 16-Tages-Komposite mit einer räumlichen Auflösung von 250 m vor. Diese Zeitreihe wurde unlängst mit den GIMMS NDVI3g Daten der National Oceanic and Atmospheric Administration (NOAA) Satelliten verglichen, die zweimonatlich mit (1/12)° räumlicher Auflösung zur Verfügung stehen (Atzberger et al. 2014). Die NDVI-Zeitreihen zeigten eine gute Übereinstimmung. Allerdings ergaben sich relativ große Unterschiede bei dem daraus abgeleiteten Wachstumsbeginn, die sich nur z. T. auf Unterschiede in den NDVI-Profilen zurückführen lassen.

In der vorliegenden Arbeit werden diese Untersuchungen fortgesetzt. Es wird der Wachstumsbeginn (start of season, SOS) der Jahre 2003 bis 2011 näher analysiert. Die SOS-Daten wurden aus den räumlich degradierten MODIS-NDVI-Zeitreihen (1/12)° für Europa und Maghreb extrahiert. Im Fokus der Analyse steht dabei die Beurteilung der in den Daten abgebildeten räumlichen und zeitlichen Variabilität durch den Vergleich mit bereits veröffentlichen Studien. Auf europäischer Ebene zeigte das räumliche Muster des SOS eine gute Übereinstimmung mit den Ergebnissen von Han (2012). Weiterhin konnte eine mäßige ($R^2$ = 0.53) und gute ($R^2$ = 0.79) Abhängigkeit des SOS von der Geländehöhe entlang von zwei Profilen in Skandinavien festgestellt werden. Zwischenjährliche SOS-Anomalien in Irland stimmten sehr gut mit den Ergebnissen von O'Connor et al. (2012) überein. Schließlich wurden die SOS mit Ergebnissen der State-of-the-Art TIMESAT-Software (Jönsson & Eklund 2004) verglichen. Auch hier wurde eine gute Übereinstimmung über alle Pixel ($R^2$ = 0.90) in Europa und Maghreb erreicht.

 www.schweizerbart.de
DOI: 10.1127/1432-8364/2014/0233 1432-8364/14/0233 $ 3.25

## 1 Introduction

The University of Natural Resources and Life Sciences in Vienna (BOKU) has setup an operational processing chain for a large European window (40° x 40°) using the Moderate Resolution Imaging Spectroradiometer (MODIS) normalised difference vegetation index (NDVI) with a 16-day compositing period and 250 m ground resolution from the year 2000 onwards. It provides consistently back-processed and near real-time NDVI products with quality information on a weekly basis. This NDVI time series is used at BOKU to derive regularly updated thematic products such as land cover (Vuolo & Atzberger 2012, 2014), phenological metrics (Atzberger et al. 2014) or drought indicators. At the same time, efforts are undertaken for creating 'combined' historical archives of NDVI from different sensors and adding new sensors such as Proba-V and Sentinel-2 to yield long lasting consistent time series.

To support these activities, we have started to compare and evaluate the NDVI products of the processing chain in several aspects. Recently, this MODIS time series has been compared with the newly released Global Inventory Modeling and Mapping Studies (GIMMS) NDVI3g dataset derived from National Oceanic and Atmospheric Administration (NOAA) satellites (Pinzón 2013). The GIMMS NDVI3g time series is covering the time period from 1981 to 2011 with (1/12)° spatial and bi-monthly temporal resolution. The comparative analysis comprised the data distribution, the spatial and temporal agreement of the NDVI itself as wells as derived phenological metrics such as the start and maximum of growing season (Atzberger et al. 2014). The NDVI time series has shown an overall moderately good agreement. The same holds for the maximum of season. However, the start of season (SOS) exhibited large discrepancies which were partly related to the fact that the temporal GIMMS NDVI3g profiles start rising earlier in the year than those of MODIS. The results suggested that further analysis and validation of phenological indicators is necessary.

The present paper addresses this issue while continuing the analysis previously undertaken when comparing the GIMMS and MODIS data (Atzberger et al. 2014). Its aim is to extract and evaluate phenological metrics from MODIS NDVI time series at the spatial resolution of GIMMS over Europe and Maghreb for the years 2003 – 2011. In contrast to ground based phenological observations, these time series refer to the aggregated response of a particular vegetated land surface extent (pixel) that comprises different levels of phenology e.g. individual plant, community, population and landscape. The time series also includes influences of atmospheric contamination, cloud cover, snow cover, soil wetness, and bidirectional viewing effects. Thus, we conceptually distinguish between plant phenology and land surface phenology (LSP). The present study follows the definition of White et al. (2009), who consider LSP as the study of the spatio-temporal development of the vegetated land surface as revealed by satellite sensors. The start of season is retrieved from the NDVI time series by means of the widely used relative threshold approach e.g. Jönsson & Eklundh (2002), Delbart et al. (2006), van Leeuwen (2008), White et al. (2009).

The objective of the study is to examine the plausibility of spatial and temporal patterns in the calculated SOS in the study area. Results are also checked against published results of other research teams.

## 2 Materials and Methods

The time series of satellite derived NDVI has been used for extracting land surface phenology metrics in many previous studies such as Reed et al. (1994), Moulin et al. (1997), Jönsson & Eklundh (2002), Stöckli & Vidale (2004), Beck et al. (2006), White et al. (2009), de Beurs & Henebry (2010). Most frequently derived metrics are displayed in Fig. 1. The current study focuses on retrieving SOS with the relative threshold approach that is implemented at BOKU. Its principle is illustrated in Fig. 1**.** The timing of the start of season occurs when the NDVI increases 20% of the seasonal amplitude from the seasonal minimum. It was out of scope of this study to explore more than one algorithm. Nevertheless, a comparison against the results obtained with the TIME-

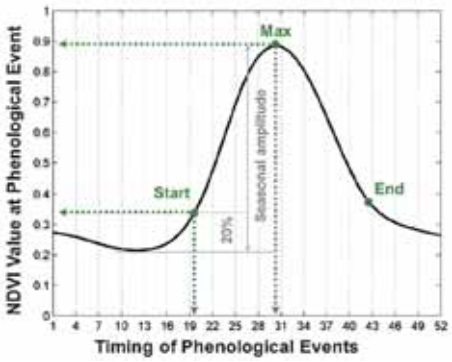


**Fig. 1:** Basic phenological metrics that can be extracted at particular events of a growing season (start of season, maximum/peak of season, end of season) from time series of satellite data (NDVI = normalised difference vegetation index). The principle of extracting start of season (SOS) by means of the relative threshold approach (20% of seasonal amplitude) is also displayed.

SAT software Jönsson & Eklundh (2002, 2004) is part of the current study. The TIMESAT software includes the relative threshold approach as well. Moreover, it can be considered as state-of-the-art and has been widely used in studies e.g. Beck et al. (2007), van Leeuwen (2008), O'Connor et al. (2012).

### 2.1 *Satellite Data and Pre-Processing*

The study's dataset included MOD13Q1 and MYD13Q1 NDVI collection 5 products of the MODIS Terra and Aqua satellites from the Land Processes Distributed Active Archive Center (LP DAAC) from the year 2000 onwards. These products are gridded level-3 data in approximately 250 m spatial resolution in Sinusoidal projection with a temporal resolution of 16 days (Terra 16-day period starting Day 001, Aqua 16-day period starting Day 009). The level-3 data are calculated from the level-2G daily surface reflectance gridded data (MOD09 and MYD09 series) using the constrained view angle – maximum value composite (CV-MVC) compositing method (Solano et al. 2010).

The MODIS products were processed within an operational BOKU processing chain comprising the following main steps:

1. downloading, mosaicking, re-projecting to geographic coordinates (datum WGS84) using nearest neighbour resampling, and image cropping to a dedicated tile system with a spatial resolution of approximately 0.002232°;
2. application of a standardised filtering for reducing the possible impact of undetected clouds and poor atmospheric conditions. The entire NDVI time series per pixel is smoothed in a single step.

The operational filtering step uses the Whittaker smoother (Eilers 2003, Atzberger & Eilers 2011a, 2011b) for smoothing and interpolating the data to daily NDVI values. It takes into account the quality of the data and the compositing day of the year for each pixel and time step based on the MODIS VI quality assessment science dataset (Solano et al. 2010). For a detailed description of the filtering procedure and settings see Atzberger et al. (2014). Only every seventh image corresponding to "Mondays" is stored as a 7-day dataset out of the resulting daily NDVI values. The 7-day interval reduces the storage load of the archive but permits an easy restoration of daily data for further applications at a later time, e.g. assuming a linear trend between consecutive Mondays. For instance, phenological metrics were extracted from daily NDVI time series allowing a better description of the timing of events.

Similar to the study reported in Atzberger et al. 2014, we used a spatially aggregated MODIS dataset consistent with the recently released GIMMS dataset at (1/12)° resolution. The spatially degraded dataset diminished the computational load that is needed to derive and evaluate phenological metrics at European scale. The spatial aggregation comprised the following processing steps:

1. averaging/resampling the smoothed MODIS data to the (1/12)° grid excluding pixels flagged as water;
2. masking all pixels that represent water in at least one time step of either MODIS or GIMMS time series (ignoring inland water bodies);
3. expanding the mask by one pixel to avoid possible artifacts.

## 2.2 *Study Area*

The study region covers an area of approximately 18 million km², of which more than 12 million km² is land surface (Fig. 2). The climate in the area varies between polar and arid according to the Koeppen climate classification (Kottek et al. 2006). Precipitation and temperatures show a large gradient from the fully humid to very dry Sahara desert and from polar tundra to cold/hot arid (Kottek et al. 2006). Land cover comprises a large number of different classes including cropland, deciduous, evergreen and mixed forest, shrub cover, grassland and bare areas (Friedl et al. 2010, Vuolo & Atzberger 2012).

Resulting from this huge spatial variability of the landscape and climatic conditions, one can identify a variety of growing seasons that are reflected in the spatio-temporal pattern of the NDVI. Fig. 2 depicts typical spatial patterns of the NDVI values at four different

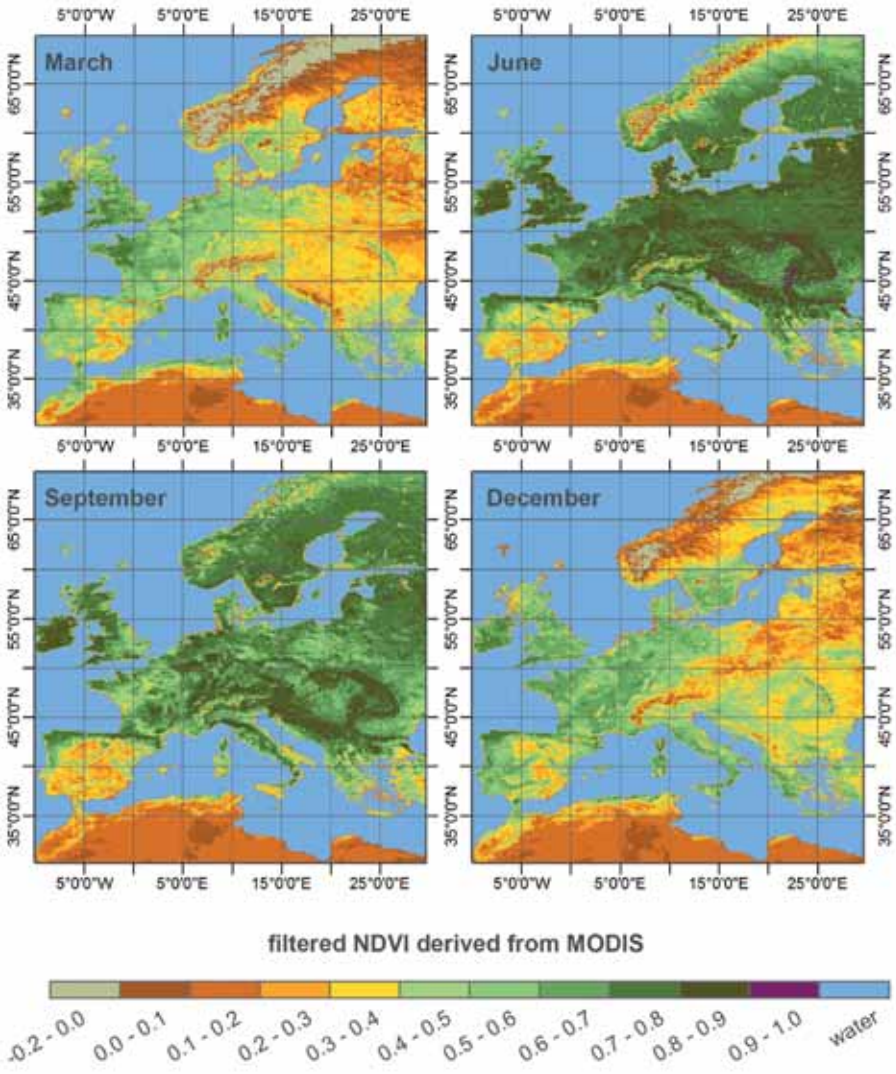


**Fig. 2:** Observed NDVI (normalised difference vegetation index) pattern in Europe/Maghreb throughout the year 2005 derived from MODIS, top left: March (week 12), top right: June (week 24), bottom left: September (week 37) and bottom right: December (week 50).

times in the year of 2005. It is complemented by exemplary temporal profiles of different land cover/land use types in different parts of the study area (Fig. 3).

The typical growing season of vegetation, e.g. deciduous forest, shrub cover, grassland, in wide parts of Central, Northern and Eastern Europe exhibits the onset of greenness in spring, maximum in summer and end of season in autumn. However, there are special cases such as shifted (earlier) seasons in Southern Europe/Maghreb, the occurrence of bimodal growing seasons and mixed cases, i.e. no clear distinction between growing seasons from year to year/strongly varying seasons, that should be considered when implementing a method for extracting land surface phenology. Particularly mixed cases will always be difficult to treat, but the present study focuses on distinguishing three basic cases:

- unimodal season: starting in spring/summer spanning to autumn, e.g. Fig. 3 mixed forest profiles of Sweden and Austria, crop in Italy;
- unimodal season: starting in autumn spanning to spring, e.g. Fig. 3 crop in Morocco;
- bimodal season: 1st cycle starting in spring spanning to summer, 2nd cycle starting in summer/autumn to winter, e.g. Fig. 3 mixed cropland and natural vegetation in France.

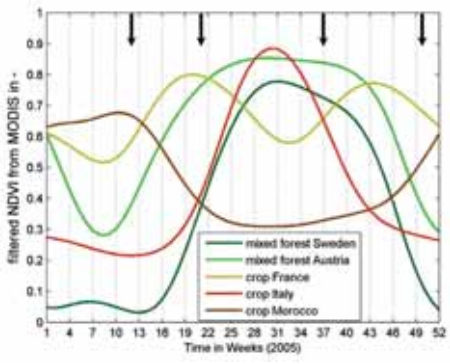


**Fig. 3:** Typical NDVI (normalised difference vegetation index) time profiles in Europe/Maghreb throughout the year 2005 derived from MODIS (black arrows indicate the timing of the NDVI maps in Fig. 2).

## 2.3 *Extraction of Phenological Metrics from the NDVI Time Series*

### BOKU implementation

Land surface phenological metrics were extracted for areas having a maximum NDVI of at least 0.3. The implemented approach allows detecting both uni- and bimodal growing seasons. In case of bimodal growing seasons, however, we extracted/evaluated only the metrics of the first season. The selected approach is able to manage seasons spanning over different years. For this paper, the extraction has been summarised in four steps, yet a detailed description can be found in Atzberger et al. (2014):

1. detecting the number of cycles by means of auto-correlation information;
2. focussing on the first cycle of the season in case of multiple cycles;
3. defining a temporal search window for each growing season depending on the number of detected cycles based on the moment of minimum and the moment of maximum; so to identify a reasonable and reproducible minimum. We decided to use the steepest preceding increase as a criterion;
4. detecting start and end of season (SOS/EOS) using a relative threshold of 20% of the seasonal amplitude (Fig. 1).

The extraction procedure detected the growing seasons from 2003 to 2011. This restriction was necessary as growing seasons might span different in the years as shown in Fig. 3 for Morocco. For example, valid starts of the growing season of 2003 can range from beginning of July 2002 (-183) to end of June 2003 (181) counted in days of the year (DOY). If values occurred outside the defined start ranges, it was checked if they could belong to a different season.

### TIMESAT implementation and data processing

The TIMESAT software (version 3.0) (Jönsson & Eklundh 2002, 2004) was employed to derive a second SOS dataset for comparison. The software provides an adaptive Savitzky-Golay filtering, an asymmetric Gaussian or double logistic model fit for filtering the data.

The number of potential annual seasons is determined by analysing a fitted model function. It can be controlled by a user defined threshold (season parameter) that can be applied region-specific by using a land cover map and setting a different season parameter for the land cover classes (for details see Eklundh & Jönsson 2009). The seasonality parameters such as the time of the start and end of the season are calculated for each growing season respective the number of annual time steps. The SOS is extracted at the time, when the NDVI has increased to a user defined level of the seasonal amplitude. The results of the processing are stored in a binary file. To retrieve annual SOS images, a time window containing the season must be defined.

As the MODIS NDVI data were already filtered and stored as a 7-day dataset, the parameters of the Savitzky-Golay filter were set to a window size of one using the NDVI time series from 2002 to 2011 with 52 annual time steps and adding 2011 as additional year to the end of the time series. To make sure that the growing seasons of each pixel were treated in the same way as with the BOKU approach, the season parameter was defined for two land cover classes separately: 1 for unimodal growing seasons and 0 for bimodal growing seasons. In both cases, the relative threshold of 0.2 was applied. The time window of the annual growing seasons was fixed for the entire study area in a way that it accounted for seasons spanning two calendar years. For instance, to cover the growing seasons of 2003, the window was defined from the first week of July 2002 until the last week of June 2004.

Due to different approaches in defining the timing of the growing season in both implementations, the SOS had to be adjusted before comparing them. Thus, both SOS datasets were re-assigned to the calendar day and year when they actually occurred. The resulting SOS images ranged between 1 and 366. Special attention was paid when inter-comparing years for pixels where starts may fall into different years (see section 3.3).

## 3 Results and Discussion

### 3.1 *Spatial Consistency of the Start of the Growing Season*

Maps of the start of season (SOS) were derived for each year from 2003 to 2011 yielding up to nine SOS estimates per pixel (see section 2.3). The median of SOS across Europe/Maghreb is shown in Fig. 4 left. As an example for the observed inter-annual variability, the SOS of 2005 is also displayed (Fig. 4 right).

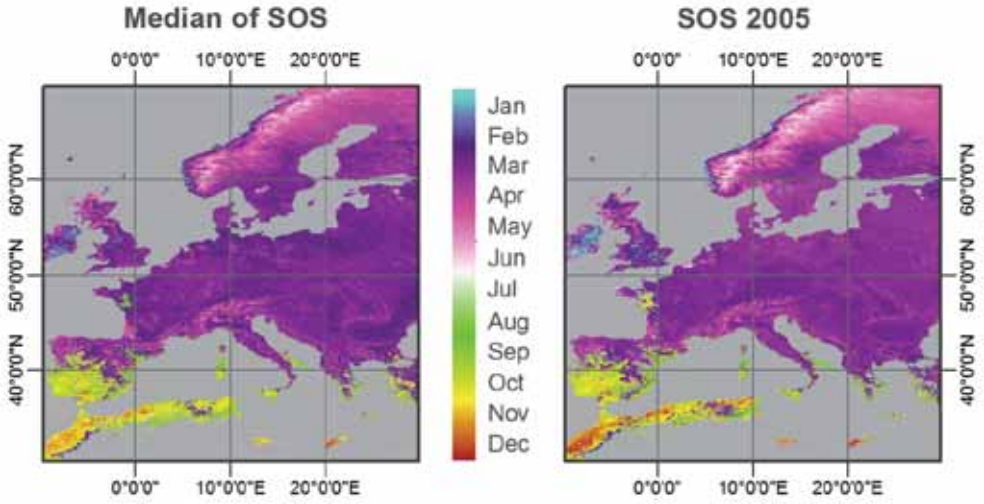


**Fig. 4:** Spatial pattern of the start of season (SOS) derived from MODIS NDVI time series, left: median of the SOS over the years (2003 – 2011), right: SOS of the year 2005.

Overall, the observed spatial pattern shown in Fig. 4 reflects well existing gradients within Europe resulting from the combined impact of land cover, latitude, altitude, temperature and rainfall regimes (Stöckli & Vidale 2004). Light purple to white colours indicate late starts from May to June and predominantly appear in forests, shrub cover or grassland in mountainous areas e.g. Scandinavia, the Alps, the Pyrenees and the Carpathian Arc. Earlier starts with dark purple colours (March to April) appear at lower altitudes e.g. to the north of the Alps and to the east of the Carpathian Mountains. Very early starts (January to February) are visible in oceanic Ireland. Southern Spain, the coastal regions of southern Europe and Maghreb show a distinct earlier SOS due to their particular temperature and precipitation patterns (October to December). A very similar map was derived from a SPOT-VEGETATION NDVI time series averaged over seven years (1999 – 2005) at 1 km spatial resolution by Han (2012), confirming the results of this study. Interestingly, both studies reveal a SOS as late as August/September for a distinct patch in the Pays de la Loire region of France (see small yellowish spot at the Atlantic coast of France).

O'Connor et al. (2012) examined the spatio-temporal patterns of the SOS across Ireland using medium resolution imaging spectrometer (MERIS) global vegetation index (MGVI) at 1.2 km spatial resolution (2003 – 2009) and the TIMESAT software. The derived map highlights SOS variations according to CORINE land cover 2000 and 2006. Considering the differences in spatial resolution between our study and O'Connor et al. (2012), we found again a close agreement in the spatial pattern of the mean of SOS. In addition, the spatial link between the SOS and the land cover type is apparent. Later SOS (April – May; pink colours) in the west and southeast of the island agree with the land cover types peat bogs as well as moors and heaths. On the contrary, pastures show the earliest SOS (January – February) with turquoise to purple colours.

To further examine the plausibility of our SOS map, the relation between altitude and SOS was analysed for two transects in Scandinavia (Fig. 5). In Scandinavia, GIMMS data already have been successfully used by Karlsen et al. (2002, 2009) to derive phenological maps and to relate them to traditional vegetation zone maps. To examine the relation between altitude and the SOS in the present study, the SOS pixels were chosen based on a simplified (recoded) land cover type 1 product MCD12Q1 v005 from MODIS (Friedl et al. 2010, Vuolo & Atzberger 2012). Only pixels

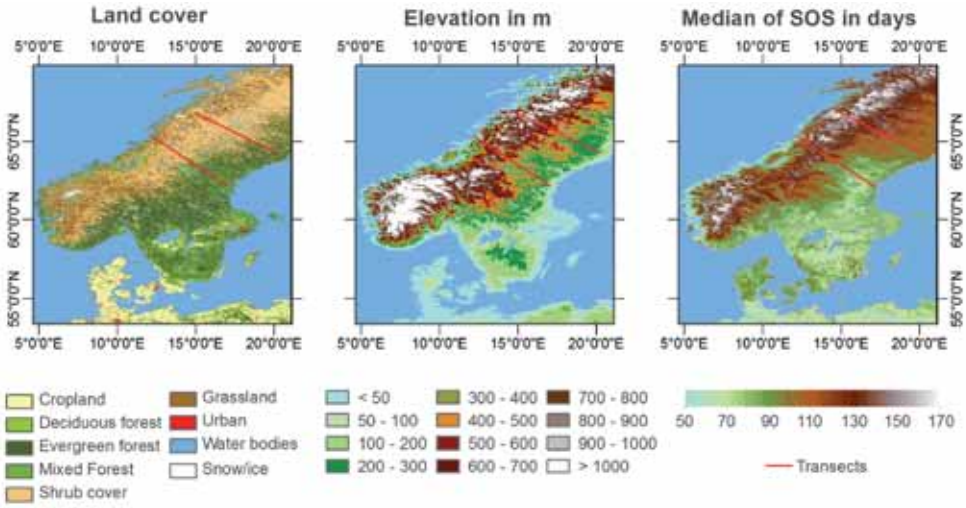


**Fig. 5:** Left: spatial pattern of recoded land cover type 1 product MCD12Q1 v005 from MODIS (Friedl et al. 2010, Vuolo & Atzberger 2012), centre: mean elevation (NOAA 1988), right: median of SOS (start of season) for Scandinavia. In all maps, the location of the transects is included.

labelled as deciduous forest, mixed forest or shrub cover were selected from this simplified map. Fig. 5 shows the location of transects, the land cover types (left), the average elevation map (NOAA 1988) (centre) and the derived median of the SOS (right). For this figure, the SOS colour scheme has been adopted to resemble the elevation map.

Similar spatial patterns can be observed in Fig. 5, centre and right, between elevation and SOS. The starts extracted by the BOKU approach are found to vary between March and May (DOYs 60 – 151) and generally increase with altitude. Compared to the results of Karlsen et al. (2002), our SOS results appear anticipated by about one month. However, the overall spatial pattern of SOS (as shown in Fig. 5 right) agrees with their results very well. The observed bias can be related to diverse definitions of the relative threshold when extracting the SOS. Karlsen et al. (2002) used the 18 year mean NDVI value for each pixel whereas our approach identifies the 20% seasonal amplitude, which is reached earlier.

The relationship of the median of the SOS (2003 – 2011) and the altitude along the two transects of Fig. 5 are plotted in Fig. 6. The southern and northern transects yield moderate (0.53) and good results (0.79) respectively in terms of $R^2$. For the northern (southern) transect, we found for each 100 m elevation difference a 6 days (7 days) increase of the SOS. This supports Hopkins' empirical law (for the US) between the timing of spring growth and elevation which states that the SOS is delayed 3 – 4 days for every 100 m increase (Hopkins 1920, Reader et al. 1974, Fisher & Mustard 2007). Our results also compare well with Dunn (2009) reporting equally high numbers of up to 7 days delay for study sites in the Rocky Mountains derived from MODIS data at 1 km spatial resolution.

The lower $R^2$ for the southern transect (Fig. 6 left) was confirmed when regressing individual years to altitude. The annual $R^2$ values range between 0.41 and 0.56. The lower $R^2$ result from stronger variations of the SOS at lower altitudes (eastern part of the southern transect) cannot primarily be explained by a change of elevation.

### 3.2 *Temporal Consistency of the Start of the Growing Season*

The analysis of the temporal consistency of the SOS was checked for the period 2003 to 2011. As already shown in Atzberger et al. (2014), the range of the SOS per pixel across the nine years varies between 17 and 35 days ($25^{th}$ and $75^{th}$ percentiles) in Europe, with a median of 24 days. Again, we checked our data against the study of O'Connor et al. (2012) in Ireland, where a 10-day composited time series of MGVI data from 2003 to 2009 was used. For the comparison, the mean SOS of the MODIS data was plotted for the same years (2003 – 2009) in Fig. 7. It was found that the individual years of both studies fit visually quite well (not shown). Likewise, when annu-

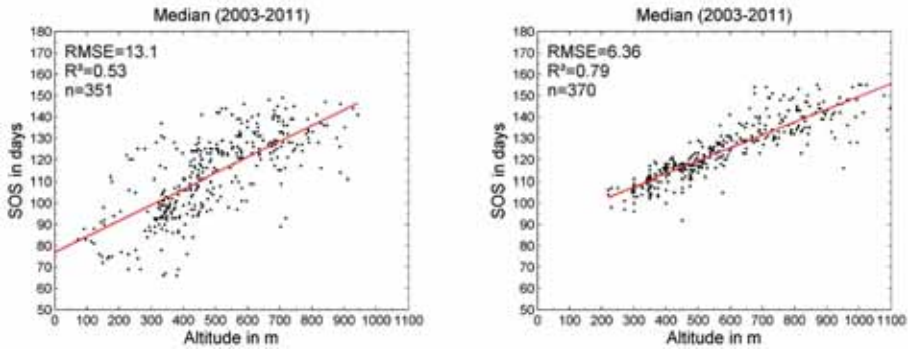


**Fig. 6:** Scatterplot between the SOS (start of season) and the altitude for the two transects shown in Fig. 5, left: southern transect, right: northern transect. The resulting linear regression lines are displayed in red.

al anomalies were calculated with respect to the mean SOS and grouped into classes of ten days, spatio-temporal patterns similar to the ones described in O'Connor et al. (2012) were found (Fig. 7). Individual years highlighted by O'Connor et al. (2012) were also evident in our data. For example, O'Connor et al. (2012) highlighted an SOS later than average in 2004 and 2006 due to an unusual cold winter and/or spring. For 2009, a later SOS in the south and an earlier SOS in the north was reported by O'Connor et al. (2012). A noticeably early SOS occurred in 2005 and 2007. The mentioned anomalies can be well retrieved in the MODIS derived SOS maps (Fig. 7).

The most striking event in our data was found in 2010, when the SOS of the entire island was strongly delayed by 38 days on average due to an exceptionally cold winter as reported by the Irish Meteorological Service (Met Éireann 2010). However, this year was not covered by the data of O'Connor et al. (2012).

### 3.3 *Comparison with the Results of TIMESAT*

To highlight similarities and differences between our approach and alternative methods, the widely used TIMESAT software (Jönsson & Eklundh 2002, 2004) was employed to extract the SOS from the MODIS data with respect to the growing seasons from 2003 to 2011. The SOS derived from TIMESAT and BOKU are compared by calculating the difference between the median of SOS in both datasets (Fig. 8, left).

Particularly in regions with SOS at the end/at the beginning of the year, e.g. Maghreb, starts may fall into different years for the compared approaches resulting in anomalous great differences, e.g. SOS differences > 100 days. Thus, special attention was paid to these cases. Before calculating the SOS difference, 365 (days) was subtracted from the SOS values close to the end of the year yielding in negative starts.

As shown in Fig. 8 left, light to dark blue colours indicate an earlier SOS in the TIMESAT results compared to the BOKU results, whereas orange to dark red colours represent later SOS for TIMESAT. As both implementations use the relative threshold approach, one can observe very similar results in large parts of Central and Eastern Europe with differences within ± 5 days (ca. 85% of pixels). Larger differences (ca. 15%) result from earlier SOS for TIMESAT, which occur predominantly in Northern and Central Europe, e.g. Scotland, Norway, Sweden, Germany, Poland, but also in Southern Spain and Maghreb (Fig. 8,

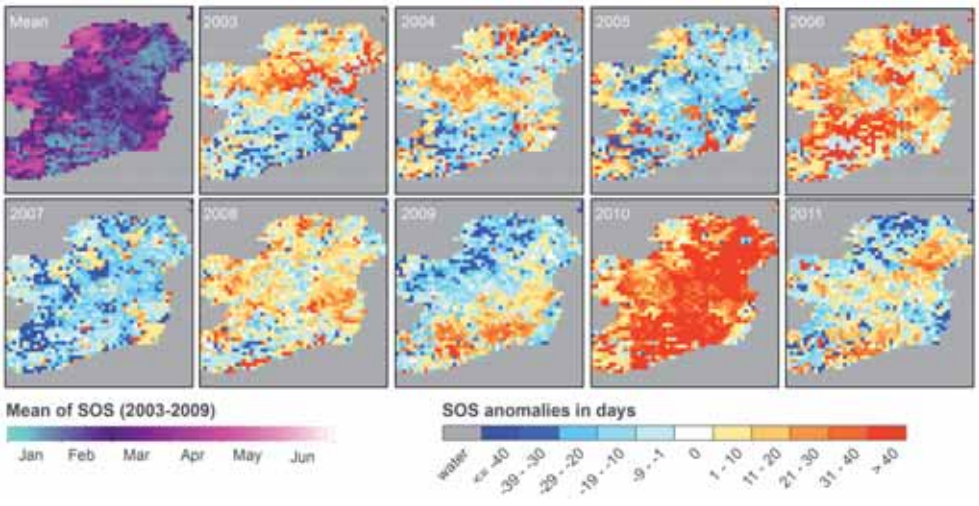


**Fig. 7:** Mean SOS (start of season) (2003 – 2009) and annual SOS anomalies (year – mean) for the island of Ireland. Note the two different colour scales.

left). The average absolute difference between TIMESAT and BOKU over all years and pixels is only four days.

A scatterplot of the SOS from both implementations for all pixels of all considered years is shown in Fig. 8, right. Only the ordinate of the scatterplot ranges from negative to positive SOS values, as most of the above mentioned SOS corrections affected the starts extracted from TIMESAT. The calculated $R^2$ between both SOS time series of 0.90 confirms their good agreement. Most of the cases that diverge from the 1:1 line have earlier SOS for TIMESAT and thus appear below this line.

The SOS differences between both implementations can be related to different approaches of dealing with seasonal minima. TIMESAT always refers to the minimum between the consecutive maxima of two growing seasons. The seasonal amplitude is calculated respective the average of the left and right minimum values (Jönsson & Eklundh 2004). The BOKU algorithm tries to consider possible "noise" at the beginning of the season, e.g. small green peaks in winter due to the growing of winter crops. Thus, the algorithm searches for the steepest preceding increase and defines the minimum at the beginning of the identified increase (see section 2.3). The amplitude is just determined relative to the left minimum.

## 4 Conclusions

The present study was meant to continue research regarding phenological metrics from MODIS NDVI time series previously described in Atzberger et al. (2014). The study focused on the start of the growing season from 2003 to 2011 and results are compared against other published results. To exclude misinterpretations solely due to an erroneous implementation of the selected threshold approach, the SOS results of the BOKU implementation have been compared with results of the state-of-the-art TIMESAT software. The intention here was to check the plausibility of the own results as well as highlight existing differences and agreements worth to consider in further developments and work at BOKU. From the above, the main findings and conclusions can be summarised as follows:

- The averaged SOS (median) in Europe showed a good agreement with a previous work of Han (2012). This confirms the spatial consistency of the derived SOS.
- The relationship of the median of the SOS and the altitude at pixel level along two transects in Scandinavia yielded moderate ($R^2 = 0.53$) to good results ($R^2 = 0.79$). The observed positive correlation between altitude and SOS is well documented in the literature.

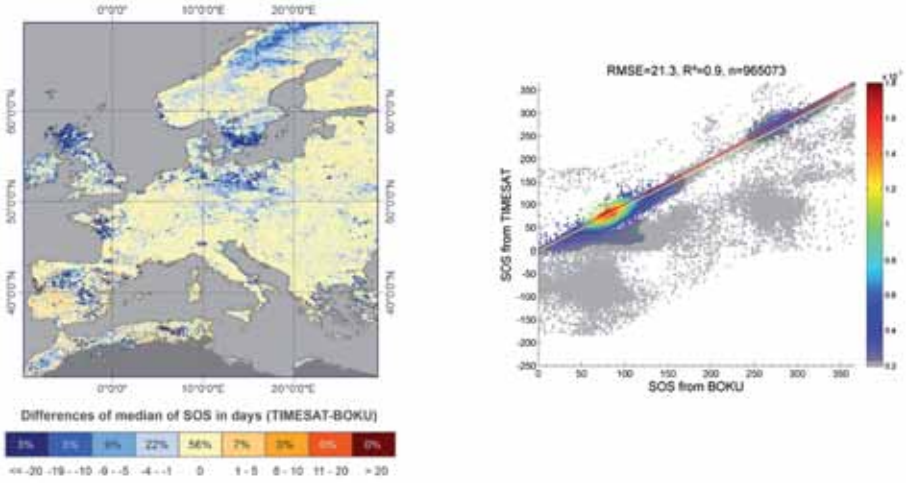


**Fig. 8:** Comparison of the start of season (SOS) derived from MODIS 2003 – 2011, left: difference of median SOS between TIMESAT and BOKU; right: scatterplot of SOS between TIMESAT (y-axis) vs. BOKU (x-axis) derived from the full image extent, also shown are the 1-to-1 line (red) and the regression line (light yellow), increasing densities from light grey to blue to yellow to red.

- Very good agreements of the inter-annual anomalies were found for the island of Ireland respective the study of O'Connor et al. (2012). The given resolution of (1/12)° of the MODIS time series deemed suitable for visual and magnitude comparison. However, this spatial resolution cannot fully reflect the same spatial variation as shown in O'Connor et al. (2012) with 1.2 km.
- The particularly cold winter of 2009/2010 and its impact on the SOS in Ireland, with an average delay of more than 30 days, could be successfully reproduced with the MODIS time series. This shows that such events can be possibly detected and mapped in near-real-time.
- A good agreement with minor differences for 85% of the temporally averaged SOS pixels over Europe and Maghreb with results of the TIMESAT software was found. The average absolute difference to the TIMESAT results over all years and pixels is only four days. This indicates that the derived SOS maps would not be markedly different using another algorithm.
- Difference in the SOS to TIMESAT result from different implementations of the relative threshold approach. Their impact has to be carefully analysed in the future.

A first attempt was made to evaluate the BOKU implementation for extracting SOS with ca. 8 km spatial resolution NDVI data. This exercise will be repeated at full spatial resolution of MODIS NDVI with 250 m. Future studies should focus on validating satellite-derived land surface phenological indicators. Long lasting and relatively dense phenological networks, e.g. Austria, Germany, could be used to evaluate satellite-derived maps against field observations as already shown by e.g. Soudani et al. (2008), Bradley et al. (2009), Liang et al. (2011).

## Acknowledgements

The MODIS MOD13Q1, MYD13Q1, MCD12Q1 and MOD09Q1 data were obtained through the online Data Pool at the NASA Land Processes Distributed Active Archive Center (LP DAAC), USGS/Earth Resources Observation and Science (EROS) Center, Sioux Falls, South Dakota (https://lpdaac.usgs.gov/get_data). The computations of the standardized MODIS filtering for the European areas have been achieved using the Vienna Scientific Cluster (VSC). We thank Per Jönsson and Lars Eklundh for making the TIMESAT software available.

## References

Atzberger, C. & Eilers, P.H.C., 2011a: Evaluating the effectiveness of smoothing algorithms in the absence of ground reference measurements. – International Journal of Remote Sensing **32:** 3689–3709.

Atzberger, C. & Eilers, P.H.C., 2011b: A time series for monitoring vegetation activity and phenology at 10-daily time steps covering large parts of South America. – International Journal of Digital Earth **4:** 365–386.

Atzberger, C., Klisch, A., Mattiuzzi, M. & Vuolo, F., 2014: Phenological metrics derived over the European continent from NDVI3g data and MODIS time series. – Remote Sensing **6:** 257–284.

Beck, P.S.A., Atzberger, C., Høgda, K.A., Johansen, B. & Skidmore, A.K., 2006: Improved monitoring of vegetation dynamics at very high latitudes: A new method using MODIS NDVI. – Remote Sensing of Environment **100:** 321–334.

Beck, P.S.A., Jönsson, P., Høgda, K.-A., Karlsen, S.R., Eklundh, L. & Skidmore, A.K., 2007: A ground-validated NDVI dataset for monitoring vegetation dynamics and mapping phenology in Fennoscandia and the Kola Peninsula. – International Journal of Remote Sensing **28:** 4311–4330.

Bradley, C.R., Schwartz, M.D. & Xiao, X., 2009: Remote sensing phenology: Status and way forward. – Noormets, A. (ed.): Phenology of ecosystem processes. – Applications in Global Change Research: 231–246, Springer.

de Beurs, K.M. & Henebry, G.M., 2010: Spatiotemporal statistical methods for modelling land surface phenology. – Hudson, I.L. & Keatley, M.R. (eds.): Phenological research: Methods for environmental and climate change analysis: 177–208, Springer.

Delbart, N., Le Toan, L., Kergoat, L. & Fedotova, V., 2006: Remote sensing of spring phenology in boreal regions: A free of snow-effect method using NOAA-AVHRR and SPOT-VGT data (1982-2004). – Remote Sensing of Environment **101:** 52–62.

Dunn, A.H., 2009: Land surface phenology of North American Mountain Environments using the Terra Moderate Resolution Imaging Spectro-

radiometer. – Thesis, http://scholar.lib.vt.edu/theses/available/etd-07242009-213007/unrestricted/Thesis_Manuscript_AllisynHDunn.pdf (17.2.2014).

Eilers, P.H.C., 2003: A perfect smoother. – Analytical Chemistry **75:** 3631–3636.

Eklundh, L. & Jönsson, P., 2009: Timesat 3.0 Software Manual. – Lund University, Sweden.

Fisher, J.I. & Mustard, J.F., 2007: Cross-scalar satellite phenology from ground, Landsat and MODIS data. – Remote Sensing of Environment **109:** 261–273.

Friedl, M.A, Sulla-Menashe, D., Tan, B., Schneider, A., Ramankutty, N., Sibley, A. & Huang, X., 2010: MODIS collection 5 global land cover: Algorithm refinements and characterization of new datasets. – Remote Sensing of Environment **114:** 168–182.

Han, Q., 2012: Remote sensing-based quantification of spatial and temporal variation in canopy phenology of four dominant tree species. – Thesis, http://www.itc.nl/library/papers_2012/msc/nrm/qifeihan.pdf (17.2.2014).

Hopkins, A.D., 1920: The Bioclimatic Law. – Monthly Weather Review **48:** 355–365.

Jönsson, P.K. & Eklundh, L., 2002: Seasonality extraction by function fitting to time series of satellite sensor data. – IEEE Transactions on Geoscience and Remote Sensing **40:** 1824–1832.

Jönsson, P. & Eklundh, L., 2004: Timesat – a program for analyzing time-series of satellite sensor data. – Computers & Geosciences **30:** 833–845.

Karlsen, S.R., Høgda, K.A., Johansen, B., Elvebakk, A. & Tømmervik, H., 2002: Use of AVHRR NDVI data to map vegetation zones in northwestern Europe. – 29th International Symposium on Remote Sensing of Environment (ISRSE), 8–12 April 2002, Buenos Aires, Argentina.

Karlsen, S.R., Høgda, K.A., Wielgolaski, F.E., Tolvanen, A., Tømmervik, H., Poikolainen, J. & Kubin, E., 2009: Growing-season trends in Fennoscandia 1982–2006, determined from satellite and phenology data. – Climate Research **39:** 275–586.

Kottek, M., Grieser, J., Beck, C., Rudolf, B. & Rubel, F., 2006: World map of Köppen-Geiger climate classification updated. – Meteorologische Zeitschrift **15:** 259–263.

Liang, L., Schwartz, M.D. & Fei, S., 2011: Validating satellite phenology through intensive ground observation and landscape scaling in a mixed seasonal forest. – Remote Sensing of Environment **115:** 143–157.

Met Éireann, 2010: http://www.met.ie/climate-ireland/weather-events/Winter2009-10.pdf (17.2.2014).

Moulin, S., Kergoat, L., Viovy, N. & Dedieu, G. 1997: Global-scale assessment of vegetation phenology using NOAA/AVHRR satellite measurements. – Journal of Climate **10:** 1154–1170.

NOAA, 1988: Data Announcement 88-MGG-02, Digital relief of the Surface of the Earth. – NOAA, National Geophysical Data Center, Boulder, Colorado, 1988, http://www.eea.europa.eu/data-and-maps/data/world-digital-elevation-model-etopo5 (17.2.2014).

O'Connor, B., Dwyer, E., Cawkwell, F. & Eklundh, L., 2012: Spatio-temporal patterns in vegetation start of season across the island of Ireland using the MERIS global vegetation index. – ISPRS Journal of Photogrammetry and Remote Sensing **68:** 79–94.

Pinzón, J.E., 2013: Revisiting error, precision and uncertainty in NDVI AVHRR data: Development of a consistent NDVI3g time series. – Remote sensing, in preparation.

Reader, R., Radford, J.S. & Lieth, H., 1974: Modeling Important Phytophenological Events in Eastern North America. – Lieth, H. (ed.): Phenology and Seasonality Modeling, 444 p., Springer.

Reed, B.C., Brown, J.F., VanderZee, D., Loveland., T.R., Merchant, J.W. & Ohlen, D.O. 1994: Measuring phenological variability from satellite imagery. – Journal of Vegetation Science **5:** 703–714.

Solano, R., Didan, K., Jacobson, A. & Huete, A., 2010: MODIS vegetation index user's guide (MOD13 series), version 2.00, may 2010 (collection 5). – Vegetation Index and Phenology Lab, The University of Arizona, USA, http://vip.arizona.edu/documents/MODIS/MODIS_VI_UsersGuide_01_2012.pdf (17.2.2014).

Soudani, K., le Maire, G., Dufrêne, E., Francois, C., Delpierre, N., Ulrich, E. & Cecchini, S., 2008: Evaluation of the onset of green-up in temperate deciduous broadleaf forests derived from moderate resolution imaging spectroradiometer (MODIS) data. – Remote Sensing of Environment **112:** 2643–2655.

Stöckli, R. & Vidale, P.L., 2004: European plant phenology and climate as seen in a 20-year AVHRR land-surface parameter dataset. – International Journal of Remote Sensing **25:** 3303–3330.

van Leeuwen, W.J.D., 2008: Monitoring the effects of forest restoration treatments on post-fire vegetation recovery with MODIS multitemporal data. – Sensors **8:** 2017–2042.

Vuolo, F. & Atzberger, C., 2012: Exploiting the classification performance of support vector machines with multi-temporal moderate-resolution imaging spectroradiometer (MODIS) data in ar-

eas of agreement and disagreement of existing land cover products. – Remote Sensing **4:** 3143–3167.

Vuolo, F. & Atzberger, C., 2014: Improving Land Cover Maps in Areas of Disagreement of Existing Products using NDVI Time Series of MODIS - Example for Europe. – PFG – Photogrammetrie, Fernerkundung, Geoinformation, **5:** 393–407.

White, M.A., De Beurs, K.M., Didan, K., Inouyes, D.W., Richardson, A.D., Jensen, O.P., O'Keefe, J., Zhang, G., Neman, R.R., Van Leeuwen, W.J.D., Brown, J.F., De Wit, A., Schaepman, M., Lin, X., Dettinger, M., Bailey, A., Kimball, J., Schwartz, M.D., Baldocchi, D.D., Lee, J.T. & Lauenroth, W.K., 2009: Intercomparison, interpretation, and assessment of spring phenology in North America estimated from remote sensing for 1982 – 2006. – Global Change Biology **15:** 2335–2359.

Address of the Authors:

Anja Klisch & Clement Atzberger, University of Natural Resources and Life Sciences, Vienna, Institute of Surveying, Remote Sensing and Land Information, Peter-Jordan-Straße 82, A-1190 Wien, Tel.: +43-1-47654-5110, Fax: +43-1-47654-5142, e-mail: {anja.klisch} {clement.atzberger}@boku.ac.at

Manuskript eingereicht: März 2014
Angenommen: Juni 2014

PFG 2014 / 5, 0423–0434
Stuttgart, October 2014

Article

# Method Analysis for Collecting and Processing in-situ Hyperspectral Needle Reflectance Data for Monitoring Norway Spruce

Kathrin Einzmann, Wai-Tim Ng, Markus Immitzer, Vienna, Austria, Martin Bachmann, Nicole Pinnel, Weßling & Clement Atzberger, Vienna, Austria

**Keywords:** in-situ measurements, needle spectra, Norway spruce, portable spectroradiometer, tree vitality

**Summary:** Forest damage induced by bark beetle attacks can cause major economic losses in forestry. Hyperspectral remote sensing data and state of the art very high spatial resolution satellite data offer a great potential for assessing tree vitality. However, a better understanding of the effects of vitality decrease and its impact on the spectral behaviour of needles is needed. Filling this knowledge gap can make a significant contribution to improve the interpretation of remote sensing data. However, it is still unclear which method for needle spectra collection is most suitable. In this work, two methods for spectral reflectance measurements of Norway spruce needles using portable spectroradiometers were tested and analysed: using a classical fore optic and a so-called contact probe. The spectral reflectance data were evaluated with different statistical similarity measure techniques. Besides analysing the measurements themselves, the methods were compared in terms of their practicality. Furthermore, the impact of storage on the reflection behaviour was investigated. The spectral measurements were performed in the field as well as in a laboratory and repeated three times during the 2013 growing season. Based on the obtained results we recommend measuring needle samples with the contact probe of portable spectroradiometers.

**Zusammenfassung:** *Methodenanalyse zur Erfassung und Prozessierung hyperspektraler in-situ Nadelreflexionsdaten zum Monitoring von Fichten.* Durch Borkenkäferbefall hervorgerufene Waldschäden verursachen große ökonomische Schäden in der Forstwirtschaft. In hyperspektralen Fernerkundungsdaten sowie in räumlich sehr hoch aufgelösten Satellitendaten der neuesten Generation wird großes Potential für die Vitalitätsbeurteilung von Bäumen gesehen. Ein besseres Verständnis der Auswirkung von Vitalitätsverlusten auf die spektrale Reflexion von Nadeln könnte einen wesentlichen Beitrag zur Interpretation von Fernerkundungsdaten darstellen. Mit welcher Methode die Nadelspektren gemessen werden sollten, ist aber noch unklar. Die vorliegende Arbeit stellt zwei Methoden für die Messung spektraler Signaturen von Fichtennadeln mittels Feldspektroradiometer vergleichend gegenüber. Neben den Messergebnissen wurden die verwendeten Methoden auch hinsichtlich ihrer Praktikabilität untersucht. Zusätzlich wurden Auswirkungen von Lagerung auf das Reflexionsverhalten analysiert. Die spektralen Messungen fanden sowohl im Feld als auch im Labor statt und wurden in der Vegetationsperiode 2013 dreimal durchgeführt. Die Reflexionsspektren wurden statistisch ausgewertet und mittels Ähnlichkeitsmaßen verglichen. Auf der Basis der erzielten Ergebnisse und der einfacheren Handhabung wird empfohlen, die Samples mittels „contact probe“ zu messen.

## 1 Introduction

The characteristic spectral signature of a tree and its foliage provides valuable insights in its vitality and enables tree species identification through remote sensing (Blackburn 2002, Ustin et al. 2004, Asner et al. 2008). Leaf and needle spectral signatures are moreover useful for a detailed assessment of the plant's physiological status. Furthermore, the spectral re-


www.schweizerbart.de
DOI: 10.1127/1432-8364/2014/0234 1432-8364/14/0234 $ 3.00

flectance at canopy level is important for sensor design studies and various up-scaling tasks.

The acquisition and successful analysis of reflectance spectra from plant tissue of trees is, however, a complex task. Two fundamental problems have to be emphasized. First, it is in general difficult to collect representative leaf/needle samples, given the growth patterns of trees with a huge vertical extent, complicated 3D structures, and shading effects due to self-shading as well as neighbouring trees (Gastellu-Etchegorry et al. 1996, van Leeuwen & Huete 1996, Zarco-Tejada et al. 2004). Secondly, no generally accepted measurement protocol for collecting signatures of leaf/needle samples is available. For example, one may opt for measuring leaf samples directly after harvesting in the field. Alternatively, one may choose to cool the samples for later analysis in the lab. Leaf samples can be measured individually or as a stack of leaves, attached or removed from their twigs, etc. Additionally, a number of alternative measurement devices exist (Koch et al. 1990, Gamon & Surfus 1999, Stone et al. 2003, Malenovský 2006). For example, reflectance spectra can be acquired using lab and field spectroradiometers with or without fore optics, as well as contact probes.

This publication discusses two different methods for gathering spectral data with a portable spectroradiometer for monitoring the reflectance of Norway spruce (*Picea abies*, L.). We discuss methods for needle sample storage and preparation. Furthermore we evaluate the spectral data collection *in-situ* and in a laboratory environment and examine the influence of sample freshness. By doing so, we aim to positively contribute to a future harmonization and standardization of measurement protocols, so that outcomes of different studies can be better compared among each other. The findings of this research serve at the same time as a preliminary study to the German/Austrian VitTree project, evaluating different airborne as well as multi- and hyperspectral sensors for an automated assessment of tree vitality, especially for Norway spruce. Norway spruce is particularly important with respect to the early detection of bark beetle attacks using remote sensing data (Wulder et al. 2006, Lausch et al. 2013, Immitzer & Atzberger 2014, Fassnacht et al. 2014).

## 2 Materials and Methods

### 2.1 *Study Site and Needle Collection*

Norway spruce needles were collected during summer-fall 2013 from a 60 year and a 80–100 year old forest stand, located near Altötting (48°13'N, 12°43'E), southeast Germany.

Needle samples were taken from 16 sample trees by tree climbers (Fig. 1). According to other studies (Koch 1988, Schlerf et al. 2010) one to two branches from the sunlit part of the tree crown, between the 12th to 16th whorls, were cut down. From these branches needle samples from the past four growing seasons, ranging from 2010 to 2013, were collected. Directly after cutting down the branches, the needle samples were separated by year, stored in zip lock bags and refrigerated. This sampling method was repeated three times throughout the growing season of 2013 (Tab. 1).

After sample collection, the first spectral measurements were conducted directly in the

**Fig. 1:** Tree climber at work.

field using the contact probe (solely for needle age class 2012). The cut needle samples were then kept in a fridge and measured again the next day. Furthermore, from the same twig a sample was refrigerated overnight, cut the next day and measured with the same spectroradiometer used for the *in-situ* measurements.

The amount of collected samples showed a large variability. The needles from the last two growing seasons (2012 and 2013) were abundant and lush. This indicates excellent growing conditions for the past two years. On the contrary, the needles retrieved from growing year three and four were difficult to identify and collect due to the scarcity and limited size (Fig. 2). This indicates poorer growing conditions in 2010 and 2011.

For security reasons, tree climbers work in teams of two. To evaluate an alternative needle collection method we also tested the shooting of needles, which theoretically requires only one person. Using shotguns, smaller parts of the top branches were shot down. A plastic cover underneath the tree was used to collect the falling branches. Both tested methods, tree climbers and shooting, proved to be adequate in collecting needle samples. Both practices require highly trained staff. We finally preferred tree climbers as they offer increased sampling control and are capable to retrieve larger samples, necessary to collect needles from all four growing years.

## 2.2 *Needle Preparation*

Before running the spectral measurements, the needles were cut off the twigs and placed on a non-reflective plate. This plate was coated with 3M-optical black velvet paint (Fig. 3), to obtain pure needle spectra. The average weight per probe was about 5 g and approximate 5–6 twigs were used per sample. For each tree, the needles of the four last needle age classes were measured separately.

## 2.3 *Measurement Methods*

The day following the needle collection, needle spectra were measured in a laboratory environment. Two passive non-imaging ASD

**Tab. 1:** Needle sample acquisition dates and spectral measurements of different needle ages.

| Measurement | Acquisition date | Contact probe lab | Contact probe field | Contact probe lab next day | Fore optic lab | Fore optic lab twig |
|---|---|---|---|---|---|---|
| 1 | 16.07.2013 | Year 2010–13 | – | – | Year 2010–13 | - |
| 2 | 10.09.2013 | Year 2010–13 | Year 2012 | Year 2012 | Year 2010–13 | Year 2012 |
| 3 | 12.11.2013 | Year 2010–13 | Year 2012 | Year 2012 | Year 2010–13 | Year 2012 |


**Fig. 2:** Needle sample containing the last four growing seasons. Red lines were drawn for separating the different needle ages. The newest needles are found at the right (2013), while the needles at the left immerged in 2010. Note the poor needle growth in 2011 due to unfavourable climatic conditions.

**Fig. 3:** Cut needles (year 2013) on a black velvet painted plate.

FieldSpec®Pro (Analytical Spectral Devices, Inc., Boulder, CO, USA) spectroradiometer models were used covering a spectral range from 350 nm – 2500 nm.

Both instruments were kept at room temperature for multiple days and were switched on 30 minutes before measuring to increase stability of the measurement. The lamps were turned on at the same time. For the reflectance measurements, two different methods were tested: One used an 8° fore optic lens. The other used a contact probe. The two measurement methods were evaluated to identify possible advantages and disadvantages of the two methods.

**Tab. 2:** Parameter settings of the ASD instruments for the two different measurement methods.

| | Fore optic | Contact probe |
|---|---|---|
| Dark current readings | 80 | 20 |
| White Reflectance readings | 80 | 20 |
| Number of spectra averaged | 40 | 10 |
| Number of saved spectra per run | 2 | 2 |

**Fig. 4:** Measurement setup with 8° fore optic. Two light sources at a distance of 50 cm illuminate the surface at 45°.

## Fore optic lens

When using the 8° field-of-view fore optic lens, the distance between the plate and the fore optic was set to 15 cm. The plate, with the needle sample, was placed directly under the field-of-view of the fore optic. As light source, two Quartz halogen spotlights (with 45° angle) were used to illuminate the surface while minimizing shadows (Fig. 4). At the beginning of the measurements the spectroradiometer was optimized and after approximately every 15 minutes a white reference was taken using a Spectralon panel. Spectrum average was set to 40 (for details see Tab. 2). Per sample 16 spectra (eight double measurements) were taken, to prevent inaccurate measurements due to illumination effects. After each measurement the plate was turned approximately 90° clockwise to minimize possible effects of uneven sample placement and surface roughness.

Alternatively, we measured whole twigs from the samples of year 2012 (Fig. 5 right) instead of cut-off needles (Fig. 5 left).

**Fig. 5:** Different spectra measurement methods: needles with fore optic (left), needles with contact probe (middle) and interlocking twigs (year 2012) with fore optic (right). Note that the light source is an integral part of the contract probe.

### Contact probe

In addition to the laboratory measurements, the samples from year 2012 were measured *in-situ*, directly after the needle collection in the field. For this purpose a so-called contact probe was used (Fig. 5, middle). The contact probe is a mobile device with an integrated 100 W halogen reflectorized lamp. Spectrum average was set to 10, as opposed to 40 used by the fore optic (Tab. 2). Because it is imperative to hold the contact probe steady while pressing it against the needles, a smaller amount of spectrum averages is advantageous. For the calibration a white reference was run every time starting a new sample. Per sample, 16 needle spectra (eight double measurements) were taken. Between the measurements the contact probe was lifted and the needles on the plate rearranged.

Besides the *in-situ* measurements for needle age class 2012, we used the contact probe in a laboratory environment. In the laboratory all four needle age classes were measured with the settings given in Tab. 2. Furthermore the needles, which were measured in the field the day before, were remeasured. For details of all performed measurements see Tab 1.

## 2.4 *Spectral Corrections and Optimizations*

The 16 measurements of each sample were manually checked for outliers and spectra with visually appearing irregularities were removed. This occasionally occurred due to measurement and operator errors. After outlier removal, the measurements were processed with the AS toolbox, a software solution developed at DLR (Dorigo et al. 2006). First a Spectralon correction was applied to every spectrum. This corrects the fact that the Spectralon reference panel is not a truly Lambertian reflector with 100% reflectivity. Then offsets in the spectra were corrected. Such jumps occasionally occurred between the different detectors, VNIR (visible-near infrared), SWIR (shortwave infrared) 1 and SWIR 2. They are caused by a slight temporal change in calibration of the detectors but mainly by target inhomogeneity and fibre optic characteristic (Mac Arthur et al. 2012). For correction, we kept the spectra of the second detector constant and moved the curves of the remaining two units to match the SWIR 1 detector, until the jumps disappeared (additive correction).

From the corrected spectra, mean values and standard deviations were calculated. For all subsequent analysis, only these averaged spectra were used.

## 2.5 *Similarity Measures*

For comparing the differences in the reflectance spectra of the two measurement methods, different deterministic and stochastic similarity measures were calculated.

A widely used, simple and deterministic measure is the Euclidian distance (ED). The ED defines the distance between two pixel vectors

$$\mathrm{ED}(s_i, s_j) = \left\| s_i - s_j \right\| \equiv \left[ \sum_{l=1}^{L} (s_{il} - s_{jl})^2 \right]^{1/2} \quad (1)$$

with $s_i$ and $s_j$ being two spectral signatures of two pixel vectors $r_i$ and $r_j$ and $L$ is number of bands (Chang 2003).

Another deterministic measure is the sum of absolute differences (SAD), a way to quantify the difference of spectral signatures

$$\mathrm{SAD} = \sum_{i=0}^{M-1} \sum_{j=0}^{N-1} \left| S_{1(i,j)} - S_{2(i,j)} \right| \quad (2)$$

where the absolute values of $M$ x $N$ pixel windows in the reference spectra $S_{1(i,j)}$ and target spectra $S_{2(i,j)}$ are subtracted (Watman et al. 2004).

Furthermore, the Pearson's correlation coefficient (PCC) was calculated, which measures the linear dependence of two spectral signatures $x$ and $y$ of number of needle samples $n$:

$$\mathrm{PCC} = \frac{\sum xy}{\sqrt{\sum x^2 \sum y^2}} = \frac{\sum_{i=1}^{n} (x_i - \overline{x})(y_i - \overline{y})}{\sqrt{\sum_{i=1}^{n} (x_i - \overline{x})^2} \sqrt{\sum_{i=1}^{n} (y_i - \overline{y})^2}} \quad (3)$$

For hyperspectral image analysis another common measure is the spectral angle mapper (SAM), which calculates the angle between two spectra $s_i$ and $s_j$. It is an orthogonal projected-based measure sensitive to changes in spectral shape but insensitive to changes in overall brightness (Kruse et al. 1993, Chang 2003, Cho et al. 2010).

$$\mathrm{SAM}(s_i, s_j) = \cos^{-1} \frac{s_i \times s_j}{\|s_i\| \|s_j\|} \quad (4)$$

As stochastic similarity measure technique, the SID-SAM mixed measure was used. It combines the deterministic SAM with the stochastic spectral information divergence (SID) (Du et al. 2004). The SID gives information over the disparity between two pixel vectors in relation to their probability mass functions (Chang 2003):

$$\mathrm{SID}(r_i, r_j) = \mathrm{D}(r_i \| r_j) + \mathrm{D}(r_j \| r_i) \quad (5)$$

with $r_i$ and $r_j$ being two pixel vectors and D being the average discrepancy in the self-information of $r$ of band $l$.

The SID and SAM can be combined using the tangent named here as DU, which is calculated as followed:

$$\mathrm{DU} = \mathrm{SID}(s_i, s_j) \times \tan(\mathrm{SAM}(s_i, s_j)) \quad (6)$$

The advantage of this measure is that it makes two similar spectral signatures more alike and dissimilar signatures easier to distinguish (Du et al. 2004).

## 3 Results and Discussion

### 3.1 *Spectral Differences Between Needle Age Classes*

For every needle year class, spectral signatures were separately analysed, to detect differences between the years and the two measurement methods (fore optics and contact probe). The spectral needle age classes for one sample tree are shown in Fig. 6. Year 2013 had very good growing conditions. This prosper vitality is resulting in higher spectral reflectance in the near infrared. The spectral signatures of year 2010 and 2011 are much lower, due to their age and poorer growing conditions during these years.

Regarding the similarity measures of the four needle age classes (Fig. 7, columns (contact probe) and columns (fore optic)), year

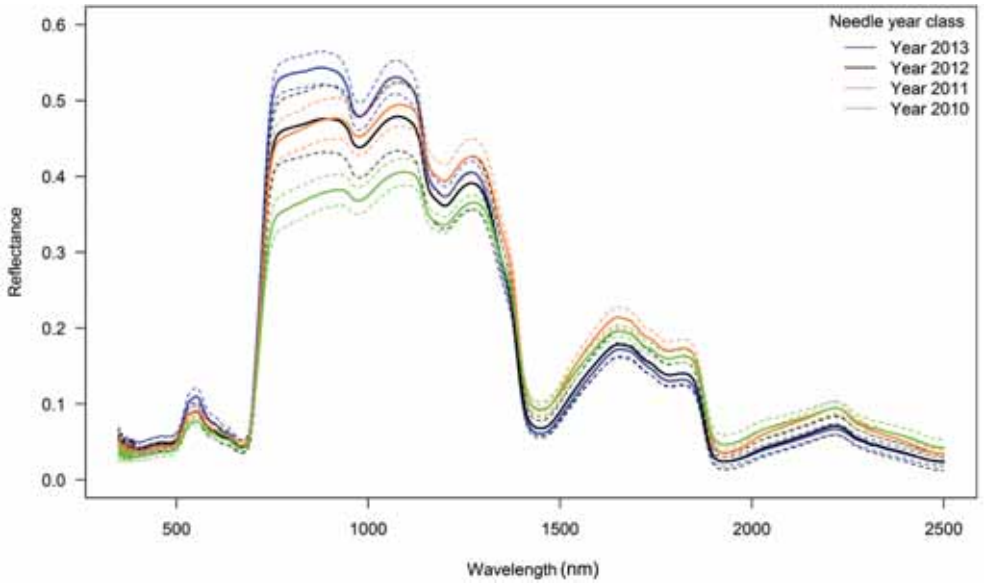


**Fig. 6:** Mean spectra of different needle age classes for one sample measured with contact probe (dotted lines: mean value +/- standard deviation).

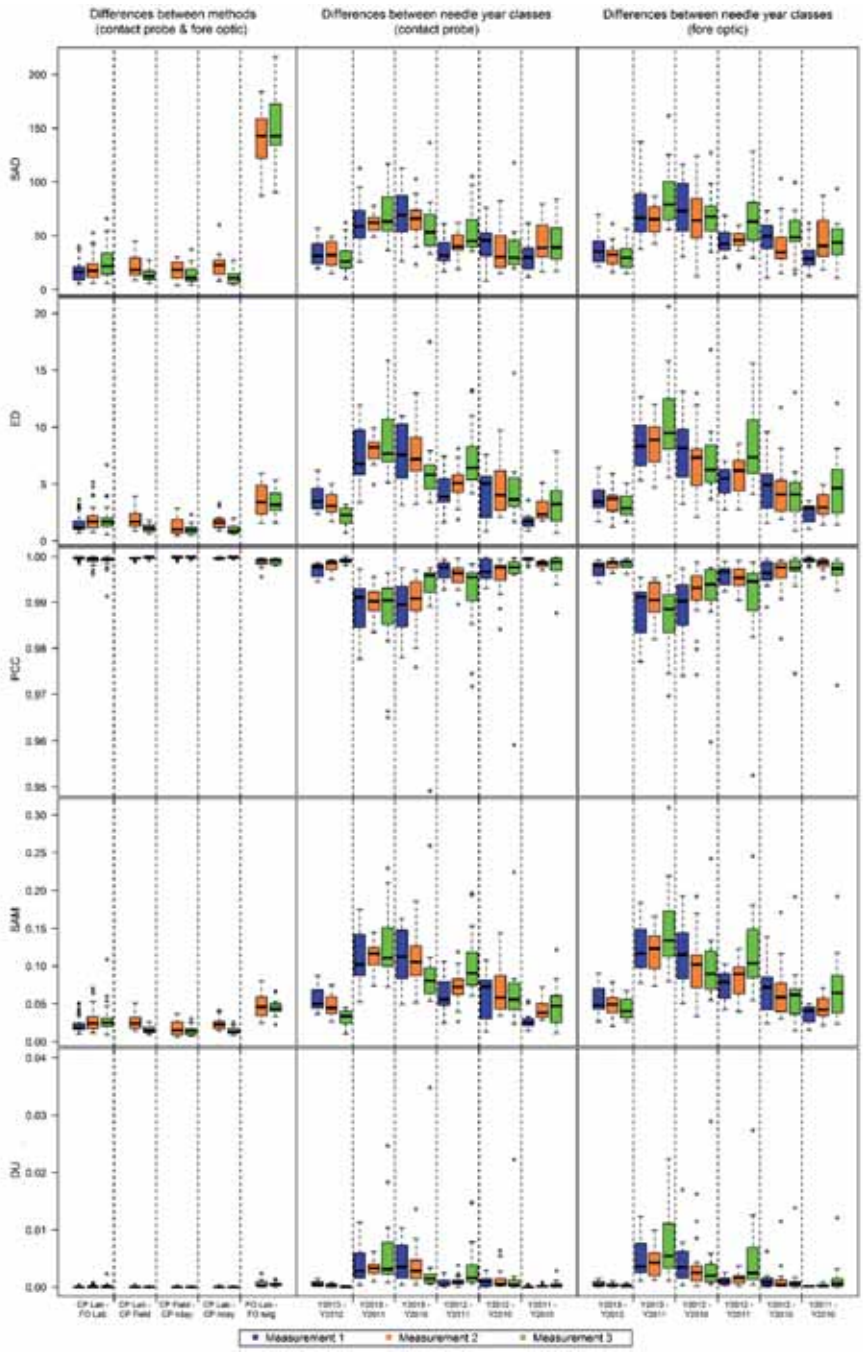


**Fig. 7:** Statistical analysis and applied similarity measures (SAD: sum of absolute differences, ED: Euclidean distance, PCC: Pearson's correlation coefficient, SAM: spectral angle mapper, and DU: mixed measure after Du et al. 2004) for different methods (CP: contact probe, FO: fore optic) and needle year classes (Y).

2012 and year 2013 have high agreement values as well as year 2010 and 2011, which is especially visible in the DU measure. When comparing the applied measurement methods both techniques yield similar levels (Fig. 7, middle and right columns as before), however, with lower variations for the contact probe measurements. Due to the differences in spectra between needle year classes, for time series analyses it is important to repeat measuring the same needle year classes.

## 3.2 *Spectral Differences Between in-situ and Cooled Samples*

When comparing the spectra of the fresh samples to the one day old samples, no major differences are noted in the spectral signal (Fig. 8). Likewise, no significant differences are visible between the fresh *in-situ* samples and the laboratory samples, which were cut and measured the next day.

## 3.3 *Differences Between Contact Probe and Fore Optic Measurements*

### Spectral differences between contact probe and fore optic

All similarity measures indicate little differences between the two methods (Fig. 7, column (contact probe & fore optic)). Hence, from a statistical point of view, both methods produce comparable results with only marginal differences. ED and SAM reveal analogous results. Overall illumination is not a highly influencing factor. The low DU values indicate similar results with both methods. Together this demonstrates that the contact probe and the fore optic are both suitable for measuring needle reflectance.

### Usability

A main difference between the two methods is the performance flexibility. The fore optic method requires a laboratory environment and an elaborate set up. The set up includes consistent illumination at a favourable angle and a

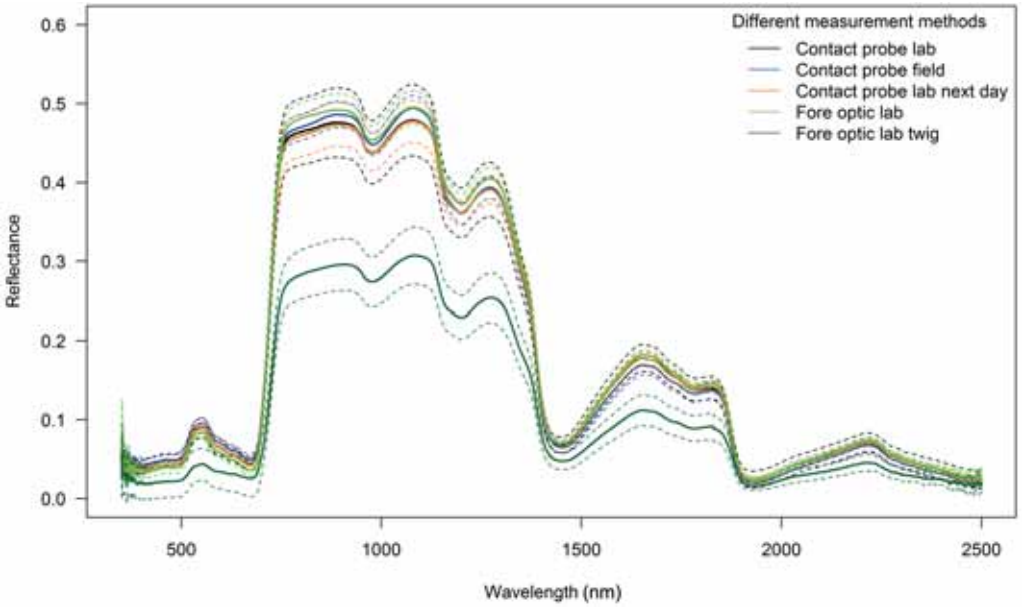


**Fig. 8:** Mean spectra of different measurement methods for one sample of needle age class 2012 (dotted lines: mean value +/- standard deviation).

construction covered with low reflective plastic foil to cancel out any spectral interference. In contrast to this, the contact probe measurements are straightforward and require fewer set up. Using the contact probe, no significant differences were noticed between the *in-situ* measurements and the laboratory measurements. We conclude that the contact probe offers increased mobility and flexibility, which allows sampling under different circumstances and with different states of needle freshness.

#### Measurement time

The two measurement methods differ markedly regarding the measurement time. As the number of spectrum averages collected for a given sample was set higher for the fore optic, the sampling with the contact probe was faster. In principle, it would be possible to reduce the amount of spectrum averages when using the fore optic. However, the contract probe measurements would still be less time consuming due to the speed of each consecutive measurement and the contact probe being more precise in handling. In our setting, the performance of the contact probe was faster, despite the white reference calibration was repeated after every sample. With the fore optic it was run only every 15 minutes.

#### Measurements in case of small sample size

In case of measuring a small sample size due to a poor growing season (2011 in Fig. 2), the contract probe proved to be more accurate compared to the fore optic as it requires fewer needles per sample. Collecting spectra from a small sample with the fore optic lens, proved to be challenging. When applying the fore optic on a thin layer of needles the measurements were considerably inconsistent due to the lack of an optically infinite thick layer. Whilst processing these signatures, quite many divergent measurements had to be removed, resulting in an average containing fewer samples with higher intra-sample variability.

### 3.4 *Spectral Differences Between Twigs and Cut Needles*

As expected, the spectra of cut needles revealed vast differences compared to the spectra of the twigs. The differences mainly arose from stronger shading effects when measuring the twigs, readily seen in the lower reflectance level across the visible-SWIR spectral region (Fig. 8). The spectral signature of the twig is also lower compared to the needle spectra, since the branch is also measured. At the same time, the within-sample standard deviation is considerably increased when measuring twigs instead of needles (Fig. 8).

Except SAD, all applied similarity measure techniques show a very high agreement between the spectral signatures of the needles compared with the twig spectra (Fig. 7). This indicates that the overall shape of the spectra is preserved. Due to the lower reflectance of twigs in contrast to needle spectra (Fig. 8), the SAD indicates a lower agreement. It must be noted that for measuring twigs a larger sample size is needed. For years with less needles, measuring whole twigs results in a much lower agreement. Layering the branches would for example be impractical for needle years 2011 and 2010, due to the lack of samples and inability to fully cover the field of view of the fore optic. Based on these findings we recommend the needle cutting method because of the increased spectral signal purity and more importantly the reduced sample size.

### 3.5 *Similarity Measures*

When comparing the similarity measure techniques, all methods show similar results, with only minimal variations. The ED and SAM reach nearly the same values, this occurs when the angle between the spectra is small and overall brightness differences are small (Du et al. 2004). The SAD is the only measure where smaller variations can be seen, mainly differences between the needle and twig measurement. This is caused by the off-set of the needle and twig spectra (Fig. 8).

## 4 Conclusion and Outlook

Our analysis indicates a number of advantages of measuring needle spectra with the contact probe. The contact probe can be easily applied both in the field as well as in the laboratory. Other advantages of conducting the measurement with the contact probe are its faster performance and its ability to collect spectra from also smaller sample sizes (Tab. 3). Furthermore, the contact probe measurements can be carried out *in-situ* independently of weather conditions, such as sun illumination and cloudiness, and without a fixed measurement setup, e.g. halogen lamps. In rainy conditions the needles can even be sampled in a car trunk. This flexible and user-friendly approach can be adapted to a wide range of projects.

The study confirmed former studies, which state that spectra of different needle age classes are significantly different. From a monitoring point of view – if based on needle spectra – it is thus very important to repeat measuring the same needle year classes. Otherwise there is a potential for misinterpreting the results. From a remote sensing perspective the strong influence of needle age is problematic, as needle measurements cannot simply be up-scaled to aircraft or satellite levels. For example, it is not clear which mixture of which needle age classes best corresponds to the integrated measurement of remote devices. One has also to consider that needles are usually only collected from the upper part of the crown (as in this study), whereas a remote sensor measures the integral part of the canopy. Additionally, for using these pure needle spectra as ground truth data or for up-scaling, one would also need to measure and take into account the tree's wooden parts (Malenovský 2006). Shadowing effects due to crown structure etc. are as well ignored when working at leaf scale (Schlerf et al. 2010).

**Tab. 3:** Comparison of the two measurement methods.

| | Spectral measurements | |
|---|---|---|
| | fore optic | contact probe |
| Accuracy | + | + |
| Speed | - | + |
| Flexibility | - | + |
| Handling small samples | - | + |

Based on our analysis, we cannot recommend measuring entire twigs instead of cut needles. When measuring spectra of twigs a bigger sample size is needed, which might not be sufficient for years with poor growing conditions. In addition, twig spectra show a higher variance compared to the single needle spectra due to illuminations effects and shadows, which occur when rotating the plate between each of the eight double measurements.

Two alternative needle collection methods were evaluated: tree climbers and the use of shotguns. Tree climbers were finally preferred as they offer increased sampling control and are capable to retrieve larger samples. Enough samples are necessary in particular for older needle ages and needles grown during unfavourable growing conditions. Shooting down small branches sometimes fails to deliver samples for several growing seasons. With this method mistakes can arise when the needles fail to fall on the plastic canvas. However, concerning the sample retrieval speed shooting is considerably faster. Cutting down one or two larger branches with three repetitions throughout the growing season, has also the potential to alter the vitality of the tree and influence its spectral signature. By removing only small parts of the foliage the adverse effects on the tree are negligible.

A more detailed analysis of the needle spectra is planned. This will include the interpretation of chemical analyses and the differences between stressed and unstressed needles. During the summer of 2013, half of the measured trees were artificially damaged by removing a strip of bark along the circumference of the trunk (roughly at breast height, see Fig. 1). This damage disrupts the nutrient flow and influences the vitality of the tree. The differences in spectra of the stressed and unstressed trees will be described in an upcoming publication. Therefore, needle sampling will be continued in the vegetation period 2014. Additionally, we have planned chemical analyses

in 2014 to create a better understanding of the differences in spectra and its chemical components.

## Acknowledgements

The study was part of the Project E54 "VitTree: Automated assessment of forest tree vitality using up-to-date optical satellite data with enhanced spectral and spatial resolution" funded by the Bavarian State Ministry of Food, Agriculture and Forestry. The authors thank the tree-climbing team, Alfred Wörle (LWF) and his colleagues, as well as Lea Henning (DLR) for the assistance in the field and in the spectral laboratory. We also thank Rudolf Seitz and Adelheid Wallner (LWF) for the organisation of the needle sampling campaigns.

## References

Asner, G.P., Jones, M.O., Martin, R.E., Knapp, D.E. & Hughes, R.F., 2008: Remote sensing of native and invasive species in Hawaiian forests. – Remote Sensing of Environment **112** (5): 1912–1926.

Blackburn, G.A., 2002: Remote sensing of forest pigments using airborne imaging spectrometer and LIDAR imagery. – Remote Sensing of Environment **82** (2–3): 311–321.

Chang, C.-I., 2003: Hyperspectral imaging: techniques for spectral detection and classification. – 400 p., Springer, New York, NY, USA.

Cho, M.A., Debba, P., Mathieu, R., Naidoo, L., Van Aardt, J. & Asner, G.P., 2010: Improving discrimination of savanna tree species through a multiple-endmember spectral angle mapper approach: Canopy-level analysis. – IEEE Transactions on Geoscience and Remote Sensing **48** (11): 4133–4142.

Dorigo, W., Bachmann, M. & Heldens, W., 2006: AS Toolbox & Processing of field spectra – user's manual, – Technical report, German Aerospace Center, DLR-DFD, Imaging Spectroscopy group, Wessling.

Du, Y., Chang, C.-I., Ren, H., Chang, C.-C., Jensen, J.O. & D'Amico, F.M., 2004: New hyperspectral discrimination measure for spectral characterization. – Optical Engineering **43** (8): 1777–1785.

Fassnacht, F.E., Latifi, H., Ghosh, A., Joshi, P.K. & Koch, B., 2014: Assessing the potential of hyperspectral imagery to map bark beetle-induced tree mortality. – Remote Sensing of Environment **140:** 533–548.

Gamon, J.A. & Surfus, J.S., 1999: Assessing leaf pigment content and activity with a reflectometer. – New Phytologist **143** (1): 105–117.

Gastellu-Etchegorry, J.P., Demarez, V., Pinel, V. & Zagolski, F., 1996: Modeling radiative transfer in heterogeneous 3-D vegetation canopies. – Remote Sensing of Environment **58** (2): 131–156.

Immitzer, M. & Atzberger, C., 2014: Early Detection of Bark Beetle Infestation in Norway Spruce (Picea abies, L.) using WorldView-2 Data. – PFG – Photogrammetrie, Fernerkundung, Geoinformation **2014** (5): 351–367.

Koch, B., 1988: Untersuchungen zur Reflexion von Waldbäumen mit unterschiedlichen Schadsymptomen auf der Grundlage von Labor- und Geländemessungen. – 195 p., Dissertation, Universität München.

Koch, B., Ammer, U., Schneider, T. & Wittmeier, H., 1990: Spectroradiometer measurements in the laboratory and in the field to analyse the influence of different damage symptoms on the reflection spectra of forest trees. – International Journal of Remote Sensing **11** (7): 1145–1163.

Kruse, F.A., Lefkoff, A.B., Boardman, J.W., Heidebrecht, K.B., Shapiro, A.T., Barloon, P.J. & Goetz, A.F.H., 1993: The spectral image processing system (SIPS)-interactive visualization and analysis of imaging spectrometer data. – Remote Sensing of Environment **44** (2-3): 145–163.

Lausch, A., Heurich, M., Gordalla, D., Dobner, H.-J., Gwillym-Margianto, S. & Salbach, C., 2013: Forecasting potential bark beetle outbreaks based on spruce forest vitality using hyperspectral remote-sensing techniques at different scales. – Forest Ecology and Management **308:** 76–89.

Mac Arthur, A., MacLellan, C. & Malthus, T., 2012: The Fields of View and Directional Response Functions of Two Field Spectroradiometers. – IEEE Transaction on Geoscience and Remote Sensing **50** (10): 3892–3907.

Malenovský, Z., 2006: Quantitative remote sensing of Norway spruce (Picea abies (L.) Karst.): Spectroscopy from needles to crowns to canopies. – 141 p., PhD Thesis, Wageningen University, Netherlands.

Schlerf, M., Atzberger, C., Hill, J., Buddenbaum, H., Werner, W. & Schüler, G., 2010: Retrieval of chlorophyll and nitrogen in Norway spruce (Picea abies, L. Karst.) using imaging spectroscopy. – International Journal of Applied Earth Observation and Geoinformation **12** (1): 17–26.

Stone, C., Chisholm, L.A. & McDonald, S., 2003: Spectral reflectance characteristics of Pinus ra-

diata needles affected by dothistroma needle blight. – Canadian Journal of Botany **81** (6): 560–569.

Ustin, S.L., Roberts, D.A., Gamon, J.A., Asner, G.P. & Green, R.O., 2004: Using imaging spectroscopy to study ecosystem processes and properties. – BioScience **54** (6): 523–534.

Van Leeuwen, W.J.D. & Huete, A.R., 1996: Effects of standing litter on the biophysical interpretation of plant canopies with spectral indices. – Remote Sensing of Environment **55** (2): 123–138.

Watman, C., Austin, D., Barnes, N., Overett, G. & Thompson, S., 2004: Fast sum of absolute differences visual landmark detector. – 2004 IEEE International Conference on Robotics and Automation, 2004, ICRA '04: 4827–4832.

Wulder, M.A., Dymond, C.C., White, J.C., Leckie, D.G. & Carroll, A.L., 2006: Surveying mountain pine beetle damage of forests: A review of remote sensing opportunities. – Forest Ecology and Management **221** (1–3): 27–41.

Zarco-Tejada, P.J., Miller, J.R., Harron, J., Hu, B., Noland, T.L., Goel, N., Mohammed, G.H. & Sampson, P., 2004: Needle chlorophyll content estimation through model inversion using hyperspectral data from boreal conifer forest canopies. – Remote Sensing of Environment **89** (2): 189–199.

Addresses of the Authors:

Kathrin Einzmann, Wai-Tim Ng, Markus Immitzer & Clement Atzberger, University of Natural Resources and Life Sciences, Vienna (BOKU), Institute of Surveying, Remote Sensing and Land Information, Peter-Jordan-Straße 82, A-1190 Vienna, Tel.: +43-1-47654-5100, Fax: +43-1-47654-5142, e-mail: {kathrin.einzmann} {tim.ng} {markus.immitzer} {clement.atzberger}@boku.ac.at

Martin Bachmann & Nicole Pinnel, German Aerospace Center (DLR), Earth Observation Center, German Remote Sensing Data Center, German Aerospace Center (DLR), D-82234 Weßling, Tel.: +49-8153-28-3325, Fax: +49-8153-28-3325, e-mail: {martin.bachmann}{nicole.pinnel}@dlr.de

Manuskript eingereicht: März 2014
Angenommen: Juni 2014

PFG 2014 / 5, 0435–0450
Stuttgart, October 2014

Article

# Generating Resistance Surfaces for Wildlife Corridor Extraction

Franz Suppan & Fredy Frey-Roos, Vienna, Austria

**Keywords:** wildlife ecology, resistance surface, remote sensing, GIS model, wildlife conservation

**Summary:** Experts of wildlife migration often delineate a corridor directly and solely from remote sensing images. Resistance surfaces on the other hand are an intermediate product, if the corridor should be extracted (semi-)automatically, by establishing a knowledge database about spatial behaviour of wildlife. The advantage of a spatial explicit knowledge database is the development of spatial rules in combination with wildlife behaviour, creating a basic database. This database should help to transfer discussions from different expert opinions to more concrete discussions about parameters of spatial rules. The aim of such a knowledge database is the ability to repeat/reproduce the experiment, the reduction of subjectivity of a single expert and the possibility to apply the same method for a large region on a detailed level. Furthermore, the automatic extraction of corridors allows the evaluation of different scenarios like the implementation of new wildlife passages. This study discusses the formulation of spatial rules for wildlife migration in a GIS to generate the basic information of a resistance surface. The application of this method is also discussed in a project called Alpine Carpathian Corridor, where the aim was to safeguard the wildlife migration corridor including intensively used areas (of the landscape).

**Zusammenfassung:** *Widerstandsmodelle für die Extrahierung von Wildtierkorridoren.* Wildtier-Experten können einen Wildtierkorridor oftmals direkt aus Fernerkundungsdaten auf Basis ihres Wissens extrahieren. Widerstandsmodelle stellen ein Zwischenprodukt dar, wenn der Korridor automatisiert extrahiert werden soll, um damit die Subjektivität des Experten zu reduzieren. Das basiert auf dem Aufbau einer Wissensdatenbank über das räumliche Verhalten von Wildtieren und die Formalisierung dieser Regeln in einem GIS. Der Vorteil dieser Quantifizierung ist die Nachvollziehbarkeit, die Anwendbarkeit auch für sehr große Gebiete bei einer hohen räumlichen Auflösung und die Übertragbarkeit des Regelwerkes bis zu einem bestimmten Grad auch auf andere Regionen. Bei dem Projekt Alpen-Karpaten-Korridor, bei dem es um die Vernetzung der beiden großen Lebensräume Alpen und Karpaten ging, fand die Formalisierung des Regelwerkes Anwendung. Die Herausforderung dabei war, einen Wildtierkorridor auch durch intensiv genutzte Bereiche der Landschaft zu führen und der Raumplanung geeignete Grundlagen für die Umsetzung des Korridors bereit zu stellen.

## 1 Introduction

In the last decades cultural landscapes were changing due to many factors like increasing infrastructure facilities, spatial expansion of settlement and industrial areas or intensified agriculture (e.g. Banko et al. 2004). One popular way of safeguarding wildlife is to declare corridors to enable the exchange between core areas of species habitat, to enhance gene flow or to reduce extinction risk (e.g. Hilty et al. 2006, Beier & Noss 1998, Vogt et al. 2007, Fleury & Brown 1997). For this reason, the safeguarding of even small, natural landscape features and their importance for wildlife and species migration became obvious (e.g. Andren 1994, Fahrig 2001, Baum et al. 2004, Kramer-Schadt et al. 2011). The composition of core areas and natural landscape patches, in interaction with mostly human induced disturbances of settlements or technical infrastructure, like road network, generates a complex


www.schweizerbart.de
DOI: 10.1127/1432-8364/2014/0235
1432-8364/14/0235 $ 4.00

landscape matrix for movement patterns (Forman & Godron 1986). The landscape connectivity describes the movement between these patches in a structural and functional way (Taylor et al. 1993). The wildlife corridor itself is part of the landscape connectivity, with focus on the connection between specified locations (Anderson & Jenkins 2006).

Corridor delineation in accordance with Beier & Loe (1992) can be based on different methods and input data (Abt & Sandfort 2011). Field surveys (e.g. Sawyer et al. 2009, Molinari & Molinari-Jobin 2001) or telemetry data (Musiega & Kazadi 2004) are visually interpreted or buffered. Due to the lack of quantitative individual based data for large regions, corridor extraction is commonly applied by using land cover information and their derived resistance values (e.g. Janin et. al. 2009, Rabinowitz et al. 2010, Driezen et al. 2007, Wang & Zeller 2009).

Main input data for a (semi-)automatic extraction of wildlife corridors are land cover, derived from different input data like aerial photographs, satellite images or cadastral maps. In addition ancillary data like fences, traffic density or road mitigation measurements are used. The land cover has to be transferred to resistance values to provide the possibility of modelling their suitability for wildlife migration (e.g. Rayfield et al. 2010). Additionally, the final resistance value depends on spatial interactions between adjacent land covers. The resistance surface models are finally used as input datasets for the application of different methods for corridor extraction like least cost path algorithms (e.g. Ray et al. 2002), circuit theory (McRae & Beier 2007) and graph theory (e.g. Goetz et al. 2009). A least cost path algorithm needs source and target regions and the map of resistance values in between. Starting from the source region, the resistance values are accumulated in that way, that the accumulated resistance values are minimized. This procedure is repeated for the target region. The accumulated resistance values are summarized for both regions. The lowest values of this summarisation indicate the route with the lowest accumulated resistance values from the source and the target region. Circuit theory is based on the same input data, resistance values and regions, and applies the method of electrical circuits known from electrical engineering. An advantage of circuit theory compared to least cost path algorithms is the extraction of multiple routes (Howey 2011). The application of graph theory creates a network, where the core habitats are knots. The connection between the knots known as the graphs and their attributes are computed using the resistance value map.

An extracted corridor can vary according to the selected method, but regardless which method is applied, the resistance value map is always the base for further computation. This study emphasises the importance of the resistance surface, independent of the selected method of corridor extraction. The study focusses on the creation of the resistance value maps and discusses the relationship of land cover classes and resistance values, their spatial relation and dependency, and the potential for establishing different scenarios, e.g. for the placement of mitigation measurements.

The application of this method will be presented by some of the results of the Alpine – Carpathian – Corridor project. The Alpine – Carpathian – Corridor project aims to re-establishing the wildlife corridor between two core areas in regions with intensive human activities. The numerous stakeholders: inhabitants, industry, forestry, hunters, etc. and their different interests in this region (e.g. Centrope 2014) make it necessary, to define the steps of corridor delineation in such a way, that it is broadly comprehensible. This requirement was established by the formulation of a knowledge database for wildlife movement and the consequential GIS model of the resistance surface as the base of this delineation.

## 2 Input Data

Land cover is considered as the main input dataset, because it provides fundamental information concerning the landscape matrix and spatial information about small patches of suitable areas for wildlife (Yadav et al. 2012). However, using only land cover based on remotely sensed images (considered as areal data) does not have to correspond with the general situation of landscape connectivity in this area (Brooks 2003) due to the fact

that features like fences or traffic density are barely recognizable in a 30 m spatial resolution dataset. Therefore, ancillary data will be used to refine the land cover. Nevertheless, the land cover provides not only groundwork for this study, but also provides information about the potential of landscape connectivity, which will be discussed in a follow up chapter. However, to evaluate landscape regarding its potential as well as its existing condition for connectivity, it is necessary to include features such as landscape elements with barrier function, e.g. fences and roads, and connection functions, such as mitigation measurements of fenced highways (over- and underpasses and their quality). In that way different scenarios of wildlife corridors can be established. These potential scenarios are determined by different regional planning actions, which influence the resistance value. Actions with increasing effect on the resistance value are changes from grassland to infrastructure but there are also actions with decreasing effect on the resistance value like the establishment of protected areas.

## 2.1 *Land Cover Data (areal)*

Land cover data is the basic spatial dataset for modelling landscape connectivity and wildlife migration. Presuming an accurate dataset, according to geometric and thematic aspects, essentially land cover data should be up-to-date and secondly as detailed as possible to provide the highest accurate resistance maps. However, main limitations are accessibility and costs. CORINE land cover data (Bossard 2000, European Environment Agency 2007a) is often used in wildlife studies because it is free of charge and easy to access. A disadvantage of this dataset for wildlife studies, at a scale of 1 : 50,000, is the degree of spatial generalisation. The raster dataset available dates from 2006, and has a spatial resolution of 100 m x 100 m (1 ha). However, the smallest delineated patches, the minimum mapping unit, are 25 ha (European Environment Agency 2007a) and 5 ha for land cover changes (European Environment Agency 2007a). CORINE land cover provides in that way useful data for habitat suitability models with focus on larger core areas, e.g. Falucci et al. (2007). For studying wildlife migration or connectivity between core areas, smaller patches of forest, hedges, grassland and their spatial configuration are essential. These smaller patches function as stepping stones, which are especially essential in landscapes with intensive agricultural activities, by improving the quality of a migration corridor. On the other hand, small and scattered patches of built-up areas can reduce and even stop migration. The spatial information of such small patches improves the quality and is therefore essential for the generation of accurate resistance maps.

In account of this insight/information, a homogeneous land cover dataset of about 10,000 km$^2$ was generated from multi-seasonal Landsat TM5 and Landsat ETM7+ images. Through this new land cover dataset, the spatial accuracy was improved to 30 m x 30 m and the minimum mapping unit was reduced to ~ 0.2 ha (2 pixels). As a result the extraction of smaller but important patches for wildlife migration was possible.

Fig. 1 demonstrates the advantage of the generated land cover dataset compared to the CORINE 2006 land cover raster. The homogeneous yellow area of non-irrigated arable land of CORINE 2006 contains smaller (less than 25 ha) but quite important features for the landscape connectivity of mammals (see also stepping stone theory, Mac Arthur & Wilson 1967, or metapopulation theory, Levins 1969). The colour scheme of the classes is in accordance with the colour table/palette suggested by the European Environment Agency (2007b). The black circles contain predominately woody patches, despite the most southeast circle contains partially built-up area. The features in the black circles are especially of importance for the GIS-model, because they have a spatial influence on their surroundings, according to Tab. 1. In our case, considering the main species of interest (red deer), forest eases the movement through its shelter function and built-up area hampers the movement by its disturbance function.

The total study area was covered by four standard scenes of Landsat (WRS-2 path/row: 190 26/27, 189 26/27). In total, 17 different Landsat scenes of 2009 were processed to reduce effects of cloud cover or uncertainties

due to phenological variation in the classification. By doing this the quality of the land cover data was improved, especially for important categories of the GIS-model for the resistance model. Each scene was classified with a k-nearest-neighbour (kNN) algorithm (Kouk-al et al. 2010) independently. Afterwards, the majority for each pixel was chosen as the final land cover class.

The necessary land cover classes for the wildlife study were defined independently from CORINE 2006 nomenclature in accordance with wildlife aspects. The list of land cover classes is summarized in Tab. 1.

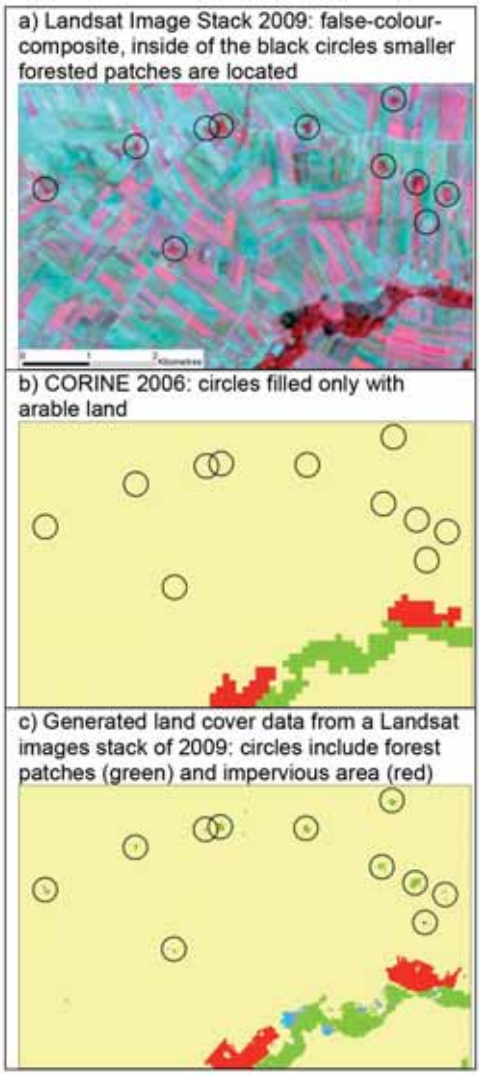


**Fig. 1:** Comparison of CORINE 2006 raster land cover data with the generated land cover dataset. Detail of an agriculture dominated landscape. Yellow: arable land, green: forest, red: settlement and impervious area, blue: water bodies and reed. The black circles are areas of interest (a: Landsat image, NASA Landsat Program 2009; b: CORINE land cover raster data, European Environment Agency; c: land cover derived from Landsat image).

## 2.2 *Ancillary Data*

Land cover derived from satellite images is usually limited to extensive objects which can be separated by their spectral properties (Lillesand & Kiefer 1994). Using only this information, the derived resistance map can provide information about the theoretical potential of the landscape for wildlife migration. Therefore, the suitability of resistance maps for describing the actual or future situation depends on the consideration of ancillary data. Ancillary data (e.g. Rogan et al. 2003) are typically linear or point features in the landscape with high impact on the permeability of landscapes, like roads, and attributes of these features, like traffic density. Additionally, data from regional planning can be implemented, for instance protection status or the rededication of arable land to built-up area.

The implementation of ancillary data is limited by its accessibility (costs, copyright, etc.) or can be collected through field work. These features of ancillary data have often only a small areal effect although they have a high impact on the connectivity. Common features are fences which impose a challenge to distinguish by means of remote sensing and have the potential to completely interrupt otherwise ideal wildlife corridors. Additionally, there is generally less public information available about fences. In this study the fences were located through field work, in combination with data from hunting associations and former projects. Especially, fences located around forest areas are critical: the positive effect of these forests and its surroundings is dissolved and is even degraded to inaccessible area, considering our main species of interest.

Highways and express roads require a fence by Austrian law and form therefore barriers.

**Tab. 1:** Land cover, their resistance values and spatial influence according to "area classes".

| Land cover | resistance value | SPI: spatial influence, R: resistance value |
|---|---|---|
| Forest | 0.01 – 0.2 | 900 – 10 000 m²: R 0.20 → SPI: 300 m<br>10 000 – 25 000 m²: R 0.15 → SPI: 700 m<br>25 000 – 50 000 m²: R 0.10 → SPI: 1 200 m<br>50 000 – 100 000 m²: R 0.05 → SPI: 1 350 m<br>> 100 000 m²: R 0.01 → SPI: 1 500 m |
| Reed, wetland | 0.2 | 0 |
| Grassland | 0.3 | 0 |
| Agriculture | 0.4 | 0 |
| Water body | 0.4 / 0.7 | 0.4: distance from river bank: 0 – 150 m<br>0.7: distance from river bank > 150 m |
| Vineyard | 0.6 | 0 |
| Quarry, etc. | 0.9 | 0 |
| Graveyard, fenced areas, etc. | 1 | 0 |
| Settlement, industrial areas | 1 | 900 – 13 500 m²: R 1.0 → SPI: 100 m<br>13 500 – 27 000 m²: R 1.0 → SPI: 200 m<br>27 000 – 90 000 m²: R 1.0 → SPI: 300 m<br>> 90 000 m²: R 1.0 → SPI: 500 m |

Here, wildlife passages are important features for migration (e.g. Clevenger et al. 2001). Wildlife mitigation measurements vary between small, existing bridges or underpasses to green bridges (Wöss et al. 2002), explicitly made for wildlife crossing. Not only the width and height of the wildlife passage are of importance, in addition aspects like the top surface of the passage floor, e.g. concrete or natural soil (Völk et al. 2001) influence wildlife passage. In Austria the Federal Road Administration (ASFINAG) is also legally engaged to keep these passages free from blockages, like storage of farming vehicles. These wildlife passages were qualitatively separated into four classes: useful, moderate, weak, not useful. This classification was based on field work in accordance with requirements of the wildlife species for migrating red deer (*Cervus Elaphus*).

Roads were considered as linear features and were accessed by open street maps (Open Street Map (and) contributors, CC BY-SA (Creative Commons, ShareAlike)). Due to high traffic density estimated by field work, unfenced roads were separated into three categories resulting in different resistance values.

## 3 Resistance Values

Consisting of land cover and ancillary data this information had to be transferred into a metric variable related to wildlife. This transformation is based on the demands of the selected species. However the parameters chosen for one single species are often in opposition to another species. This dilemma exists not only between large mammals and amphibians but in between different mammal species themselves. Red deer will cross rivers and water bodies without hesitation whilst lynx (*Lynx Lynx*) will attempt to avoid contact with water as long as possible.

Furthermore, the aim of this study is to discuss generating resistance maps for wildlife corridor extraction. Therefore, the resistance values have to be related to migration. This is a clear distinction to methods where the resistance is only the inverse of the suitability value (see e.g. Corridordesign 2007). Migrating wildlife has different needs than local non-migratory wildlife populations. Migrating wildlife is more sensitive to disturbances, like wind parks. Perceiving these as a combination of movement, noise and light effects, whereas local populations have adapted to the disturbance and can be even found grazing

beneath the wind turbines. For local population it is easier to find passages or underpasses at highways while migratory species requires guiding features, like hedge rows, to find and accept such mitigation measurements.

The resistance value is assumed as a function of land cover *in situ* and in the surrounding, giving the "stress" of crossing an area during migration. Furthermore, the resistance value is also depending on the local land use plans and protection status. A crux for working with resistance (low values are suitable for migration, high values restrain migration) is the definition of the resistance value for each land cover class.

The generated values and assumptions are based on previous studies of the Institute for Surveying, Remote Sensing and Land Information (e.g. Grillmayer et al. 2002 and Köhler 2005) in combination with the federal recommendations for public roads (FSV 2007) and additional expert knowledge (Völk et al. 2001).

### 3.1 *General*

In this study the main interest is on safeguarding the possibility of genetic exchange between species populations of the Alps and the Carpathians. Beside bears, wolves and lynx, red deer was the main target species and nearly fits the assumption for a generic focal species (Watts et al. 2010). Red deer is the most sensitive mammal considering landscape connectivity, i.e. closeness to forested areas, distance to settlements, and quality of wildlife passages. In comparison to red deer, bears have very low requirements for underpasses with a recommended passage height of 4 m (see Völk et al. 2001). Additionally, to calculate a resistance model a knowledge database of spatial rules is necessary. Especially the spatial behaviour of migrating species is of interest, not only of local populations. Therefore, track tracing data by itself is not enough for the formulation of the knowledge database. Collar data and gene samples of numerous migrating species are necessary, data which is hardly available for many species. Because red deer has a long tradition in research studies, expert knowledge was readily available and implemented to the knowledge database. A study of Köhler (2005) evaluates already basic values and spatial rules. Hence red deer was chosen as the species of interest and the resistance values and spatial rules are based on this knowledge database. The resistance value represents the average probability of crossing through a pixel of given length (here 30 m) and ranges from very low 0.01 to 1.

The small number of necessary land cover classes results from their relevance and their ability of quantification for wildlife migration. A low resistance value belongs to forested areas, while large, contiguous forest patches have the lowest value of 0.01. The value of 0 was not given, because even in appropriate areas there is still resistance for migration compared to core habitat. Furthermore, we did not give 0 values due to computational reasons. Reeds and wetlands have lower resistance values compared to grassland because of their sheltering function, especially larger reed zones. Agriculture, having a value in between the best and worst land cover, is definitely the most heterogeneous class, ranging from open, ploughed land without shelter and food to e.g. maize with useful shelter/protection and fodder availability. The value of 0.4 is here determined as an average. Vineyards might have a lower value of resistance although it is often protected by additional construction features and the ease of crossing is depending on the main orientation of the vineyard rows. While crossing along these rows is easier, the perpendicular crossing is more challenging and results therefore in a higher value compared to agriculture. While abandoned quarries sometimes serve as a refugium for wildlife, active quarries with fences, steep and slippery slopes, light and noise disturbances result in a value of 0.9. The resistance value of 1 indicates an absolute barrier, impermeable for wildlife. Still this category is subdivided in two categories due to their spatial influence.

The study area was dominated by three main categories: forest, agriculture and settlement areas.

Rules are based on expert knowledge of migratory red deer, unpublished collar and tracking data, despite the argument of Janin et al. (2009), that "*resistance is often arbitrarily established on the basis of expert knowledge*".

The values were defined considering regional, political and historical aspects as well as the features of the migrating species and not local populations. These values are a generalisation; the exact value will definitely fluctuate due to seasonality and differences in between years (especially agriculture), spatial arrangement (vineyards) or partial fencing (quarries) and the behaviour of the individual species. Nevertheless, in comparison to expert judgements alone the formulation of spatial explicit rules provides the opportunity for a basic understanding, which can be modified in the future.

## 3.2 *Spatial Effect of Resistance Values*

Land cover types can be separated in two groups by their spatial effect: Stationary features, those that affect only the area of their occurrence and features with additional spatial influence on their surrounding agricultural land and grassland belong to the first group. While water bodies alongside river banks are in general accepted by wildlife, larger water bodies more than 150 m away from the banks have higher resistance values. Contrary are features that influence the vicinity, either in a negative way by increasing the resistance value or in a positive way by decreasing the resistance value. Land cover with positive influence on adjacent land cover types for wildlife migration is forested area. The spatial range of the positive influence depends on the area of the considered forest patch. Land cover with negative spatial influence on the surrounding is settlement, where the range of spatial influence depends on the considered settlement area. Even small areas like farm houses have already the highest resistance value due to their disturbance potential.

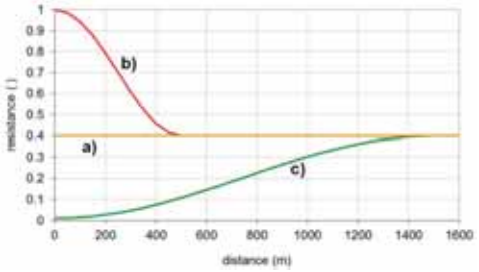


**Fig. 2:** Effect of spatial influence on agricultural land – profiles of resistance values for different adjacencies (left to 0 m); a) unaffected field – agricultural beside e.g. vineyard with a constant resistance value of 0.4; b) negative affected field (500 m) – large settlement (left of axis ordinate 0 m) nearby to agriculture – the resistance value descends from 1 to 0.4; c) positive affected field (1,500 m) – large forest (left of axis ordinate 0 m) nearby to agriculture – the resistance value gradually increases from 0.01 to 0.4.

The spatial effect is described in the last column of Tab. 1. A forest patch of 4 ha has a resistance value of 0.1. The spatial effect of this forest patch is effective up to a distance of 1,200 m. The positive influence of the land cover class will decrease from the borderline of the forest patch till the end of the spatial influence. Because the influence near the considered patch is in excess compared to the more distant locations it is not a linear function but a cosine function (see Fig. 2) between adjacent and more distant locations.

Working in a raster GIS with a distance raster for each area category of settlement or forest, the topological influence for the calculation of the resistance value can be considered as:

$$d_x = \left( 1 - \frac{\cos\left( \frac{dist}{dist_{\max,cat}} \times f_1 \right) + 1}{2} \right) \quad (1)$$

$d_x$ distance factor
dist distance from settlement
$dist_{max,\,cat}$ maximum distance for this area category of either settlement or forest
$f_1$ $180 / \pi$

for settlement influence:

$$R_{cal} = 1 - \left( \left( 1 - R_L \right) \times d_x \right) \quad (2)$$

for forest influence:

$$R_{cal} = R_{Start} + \left( \left( R_L - R_{Start} \right) \times d_x \right) \quad (3)$$

$R_{cal}$ calculated resistance value under consideration of the area category for settlement or forest

$R_L$ static, local resistance value, without neighbourhood effect

$R_{Start}$ resistance value of the considered forest patch $\rightarrow R_{Start} = f$ (forest patch area)

The calculations were performed for each area class of every land cover of Tab. 1 with spatial influence. If the spatial influences of different area classes are overlapping, the final resistance value was calculated according to the involved land cover class. Overlapping of different settlement area classes: the highest value will be assigned to the resistance surface. Overlapping of different forest area classes: the lowest value will be assigned to the resistance surface. If settlement and forest area classes are overlapping, the final resistance value will be calculated from the highest value of settlements and the lowest value from forest.

Furthermore, a positive spatial influence cannot cross a barrier, e.g. the positive influence of a large forest patch cannot reduce the resistance value on the other side of the highway – even if animals can sense the forest, they have no possibility to cross the barrier.

### 3.3 *Interaction between Different Spatial Influences*

Considering spatial influence leads automatically to complex interdependencies in natural landscapes and the issue of quantifying these interdependencies. The general rule was: if there is a negative spatial influence the positive influence cannot overrule it. However the negative influence will be reduced. The reduction values are estimated from collar data, expert interviews and field studies (Fig. 3).

Two land cover categories are able to reduce a negative influence: water bodies and forest. Water bodies can decrease the spatial influence of settlements by half of the original settlement value (see Fig. 3, profile b) from 500 m for large settlement areas to 250 m for smaller settlements. Forest patches decrease the negative spatial influence according to their size by two-thirds (see Fig. 3, profile c), finishing the negative influence at 170 m. Fig. 3, profile d, shows the effect of a forest patch adjacent to settlement, although being too small (100 m) to absorb all the spatial influence of the settlement. After 100 m of forest the spatial influ-

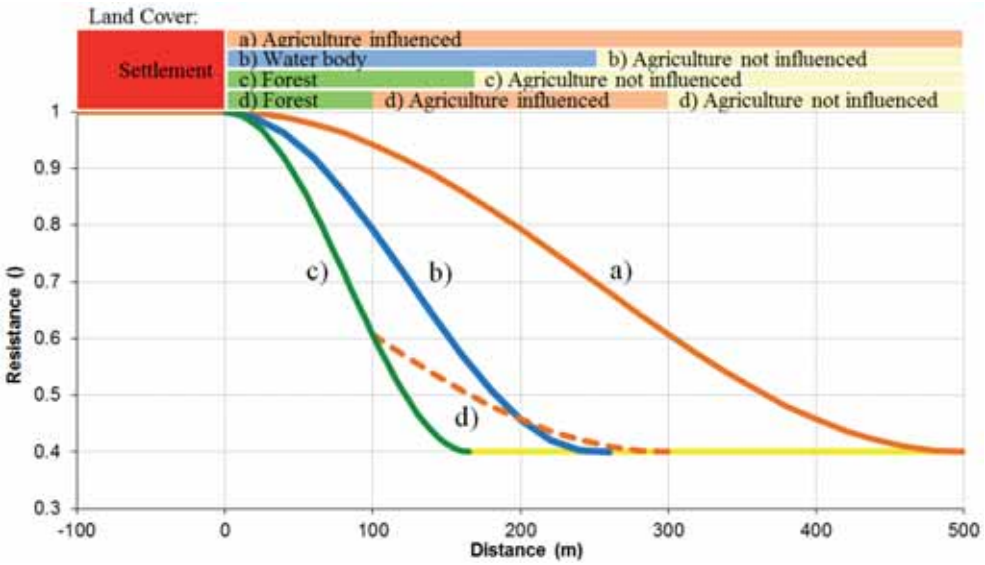


**Fig. 3:** Spatial "buffering" effect of different land covers and their interactions; top: land cover and their spatial extent; bottom: profiles of their resistance values; a) agriculture beside large settlement area: negative spatial influence for 500 m distance till agriculture has it original value of 0.4; b) between the settlement and agriculture a water body of 250 m width is located; c) between the settlement and agriculture a forest of nearly 170 m width is located; d) between the settlement and agriculture a forest of 100 m width is located.

ence of profile a) continues from the resistance value 0.6, resulting in a total spatial influence of 300 m for this spatial composition of large settlement – forest patch – agricultural land.

While the spatial influence of settlement on the surrounding can be reduced, the resistance value of the settlement area itself remains unchanged at the highest value of 1. On the other hand, for forested areas the spatial influence cannot be reduced to zero, however the resistance value of forested area itself can be increased through large settlement areas.

Roads and wildlife passages are considered at the end of creating a dataset of resistance values. Roads are separated in three categories: dirt roads with a resistance value of 0.3, because they can serve as "guiding" features, especially if they are covered with leaf litter. Paved roads receive a value of 0.6 and paved roads with heavy traffic a resistance value of 0.85. Because wildlife can come quite near to roads, especially with forest in the vicinity, even roads with high traffic intensity are not considered with negative spatial influence perpendicular to the main road axis. The resistance value can only increase, if overlapped by negative spatial influence of settlements, yet cannot decrease. Roads in forest remain with the same value as roads in agricultural fields.

Existing wildlife passages for crossing highways were surveyed and separated in four categories. Excellent, with resistance value of 0.3, providing enough width and suitable surface, moderate value 0.6 decreasing width and surface quality, and poor with value 0.9, including small widths, and decreasing quality due to paved roads or waterways. The fourth category is considered as not passable. New wildlife passages should belong to the excellent category.

Modelling connectivity is highly dependent on the availability and quality of geo input data. Especially linear barriers like roads, fences or paved riversides can easily interrupt the feasibility for wildlife migration. Additionally, in contrast to roads, such data is hardly available. By reason, that the hard barrier effect of fences it was necessary to collect this information through field studies. Fences can influence large forest patches and render them as inaccessible areas, e.g. due to enclosures. The ancillary data of fences is therefore required for statements about the status quo of landscape connectivity and have to be considered therefore as a required dataset.

Protected areas are the only land use category, beside forest, which is reducing the resistance value by 0.1 for forest, wetland, grassland and agriculture. The smallest resistance value is 0.01. Paved roads, settlement or fenced areas remain unchanged.

The creation of a resistance surface can be performed with any raster GIS with cost distance algorithms, in this study ArcGIS™ Spatial Analyst™ by Esri was used by writing Python scripts, simple text files provide the input parameters like resistance values and spatial influence distance.

### 3.4 *Combination of the Separate Geolayers and Different Scenarios*

For each category the resistance value was calculated and afterwards combined, to produce a single dataset. The combination rules between different land cover classes are:

- a positive spatial influence cannot cross a barrier, e.g. the positive influence of a large forest patch cannot reduce the resistance value on the other side of the highway,
- if there is an overlapping of negative influence layers from different area categories, the resistance value will be taken from the layer with the highest value,
- if there is an overlapping of positive influence layers from different area categories, the resistance value will be taken from the layer with the lowest value,
- if there is a negative spatial influence the positive influence cannot overrule it, but the negative influence will be reduced,
- road and wildlife passage datasets are the last layers in the sequence of overlapping. Especially for roads the resistance values can increase by nearby settlement area but cannot decrease. Wildlife passages are supposed to be unchangeable: even if the passage is located in forest area, the quality of the passage itself will not be improved.

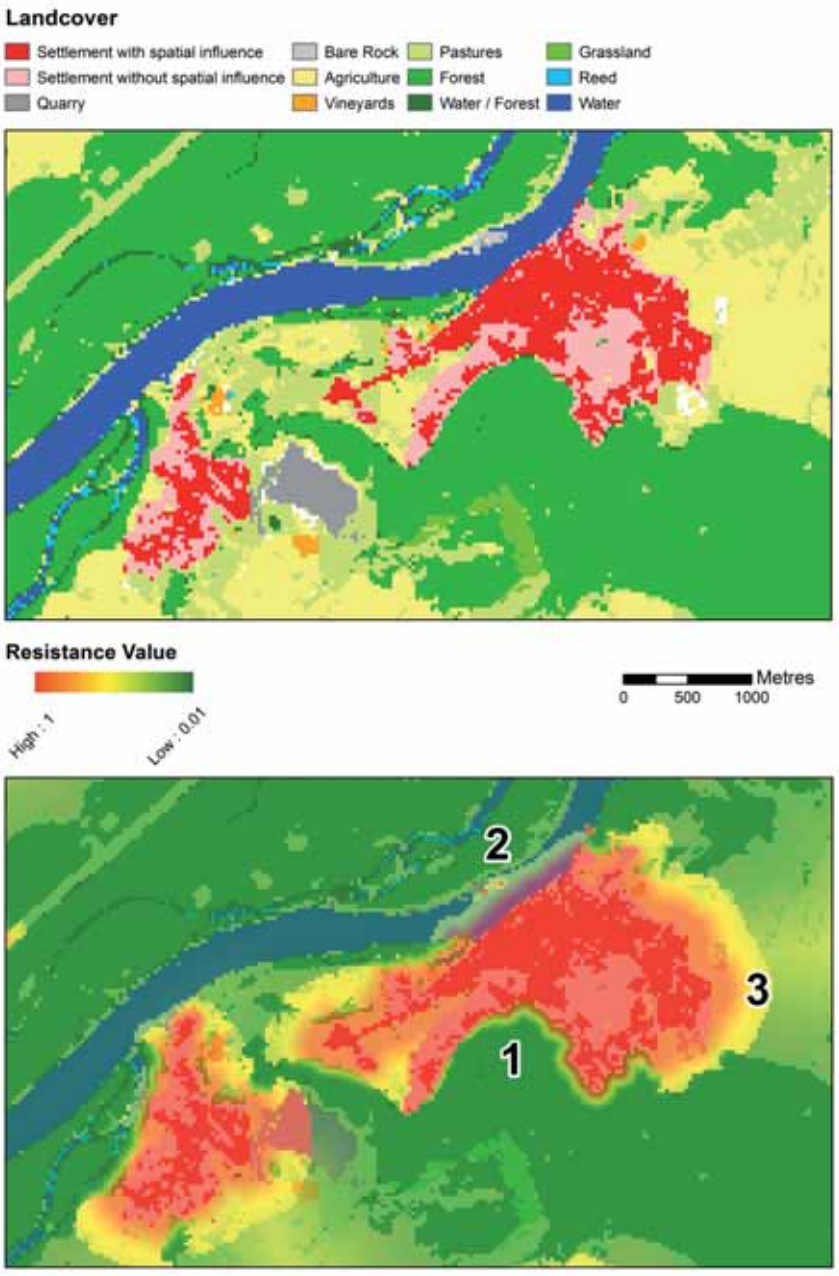


**Fig. 4:** Top: land cover map; bottom: resulting resistance map; red hue: negative spatial influence of settlement area; green hue: positive spatial influence of forest; location (1): settlement adjacent to forest: spatial influence of settlement reduced to one third of the original 500 m; location (2): settlement adjacent to water body: the negative influence of the settlement is river to half of the original value – on the opposite river side the riparian forest is not influenced by the settlement; location (3): Settlement adjacent to agriculture with the longest spatial influence.

## 4 Results

The method of generating different resistance value maps was applied in a study area, which covers both Austrian and Slovakian territory. Fig. 4 shows the effects of spatial interaction for the resistance map in detail in an area close to the river Danube. Here the spatial interactions of different land cover are demonstrated. The resistance value map can already be used to illustrate the spatial effect of spatial planning activities, like planting of forest area, independent of selected source and target regions for algorithms of corridor extraction.

The further figures focus on the result of different resistance surfaces for the corridor

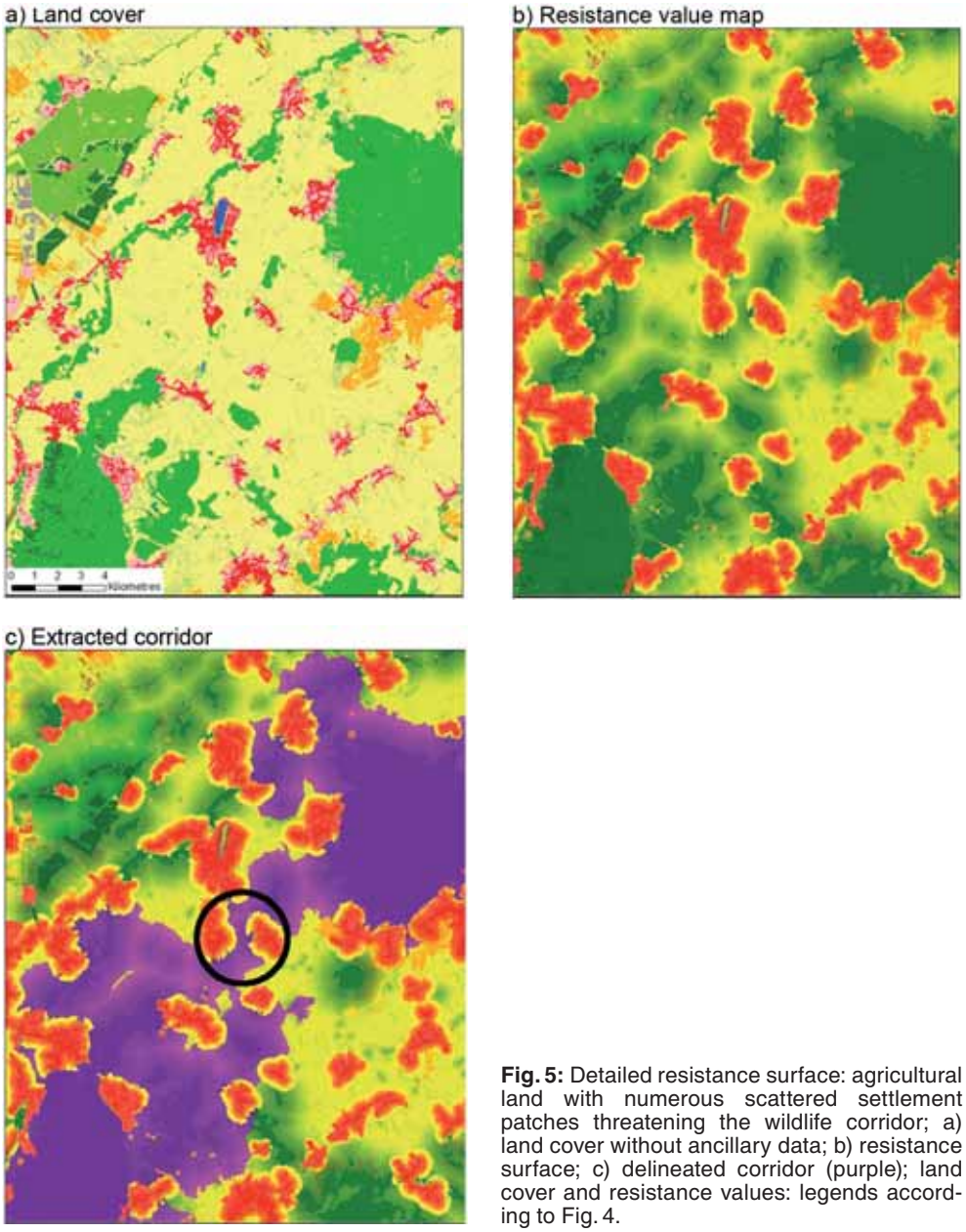


**Fig. 5:** Detailed resistance surface: agricultural land with numerous scattered settlement patches threatening the wildlife corridor; a) land cover without ancillary data; b) resistance surface; c) delineated corridor (purple); land cover and resistance values: legends according to Fig. 4.

delineation. The corridor delineation was exemplified by a least cost path algorithm, but any other algorithm might be used.

In Fig. 5 the forested core areas in the southwest and northeast corner should be connected. But the permeability of the landscape is reduced. Due to settlement agglomeration the resistance values are increased, not only for the settlement areas but also beyond the borders of the settlement. A corridor delineation (here with a least cost path algorithm) exemplifies this effect even more by showing the bottlenecks of the corridor. Fig. 5c (black circle) indicates where the width of the corridor decreases to less than 500 m but FSV (2007) recommends a corridor width of 500 m to 1,000 m between settlements. Here regional planning activities should be applied to halt at

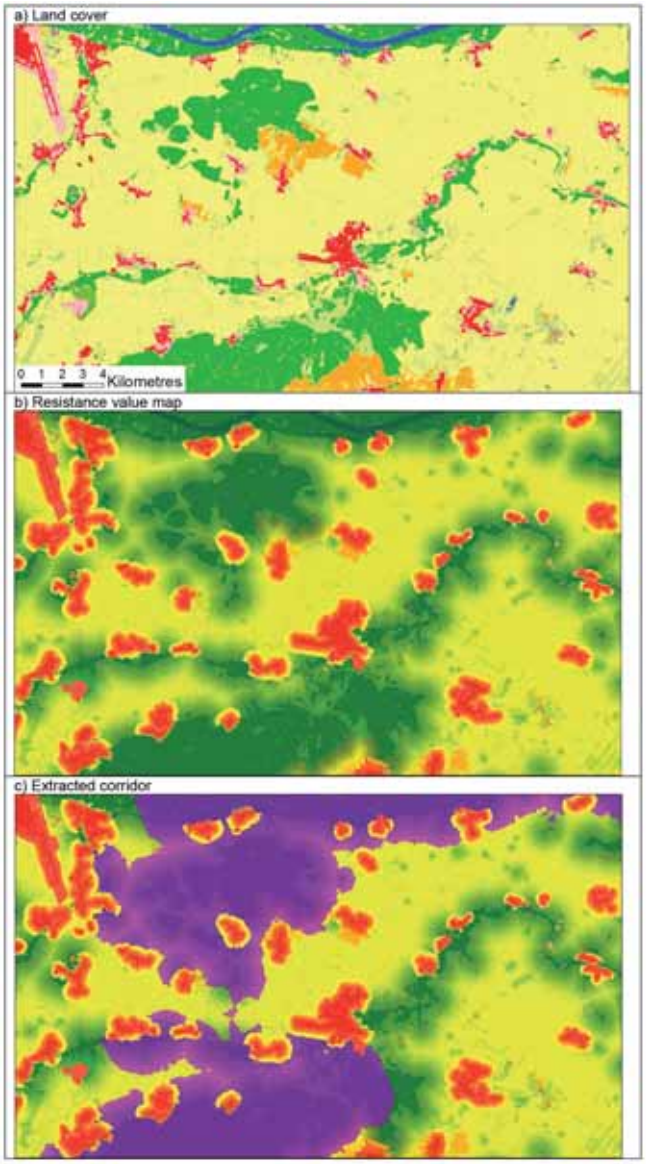


**Fig. 6:** Landscape potential; a) land cover without ancillary data; b) resistance surface; c) delineated corridor (purple); land cover and resistance values: legends according to Fig. 4.

least further expansion of the adjacent settlements. The implementation of forest patches in this area would not change the width of the corridor but helps to decrease the resistance values. In natural forest the minimum width of the corridor can even decrease to 100 m (FSV 2007). The consideration of the spatial effect of settlements is here essential. Without this consideration, the distance between the settlements is still above 500 m and seems to be wide enough for wildlife migration.

Fig. 6 indicates a bottleneck which prohibits wildlife migration. In the middle, from west to east a riparian corridor is situated. For the calculation of the resistance values only the land cover was implemented, without ancillary data like the layers of roads, wildlife passages, fences or spatial planning. Corridor delineation (here with a least cost path algorithm) demonstrates the shortest and "cheapest" (lowest accumulated resistance values) connection between north and south, with the bottleneck in arable land.

This layer combination for the resistance surface shows the spatial path of connection, without restrictions due to roads, fences, and other obstacles. Although it is an artificial construct, it indicates the "potential" of the landscape for connectivity. The layer combination is useful for regional planning regarding general decisions on land use. It shows where the landscape is well connected, neglecting limiting factors like roads and fences. This information can be useful for the placement of new wildlife passages and reduces the costs of implementing new forested patches in that way.

Fig. 7 shows the same area similar to Fig. 6 with the main intention, to connect the forested core areas from the south and north. The implementation of ancillary data (Fig. 7b) results in different resistance surface than Fig. 6, due to considering the highway as an absolute barrier, also existing wildlife passages are considered. Furthermore, large parts of the forest north of the highway are fenced and cannot be accessed by large mammals. The small red dots represent wind parks, which rises the resistance value and lowers the connectivity. The extracted corridor of the actual condition (Fig. 7c) is therefore diverted to the riparian corridor, where wind parks increase the hardship of wildlife migration.

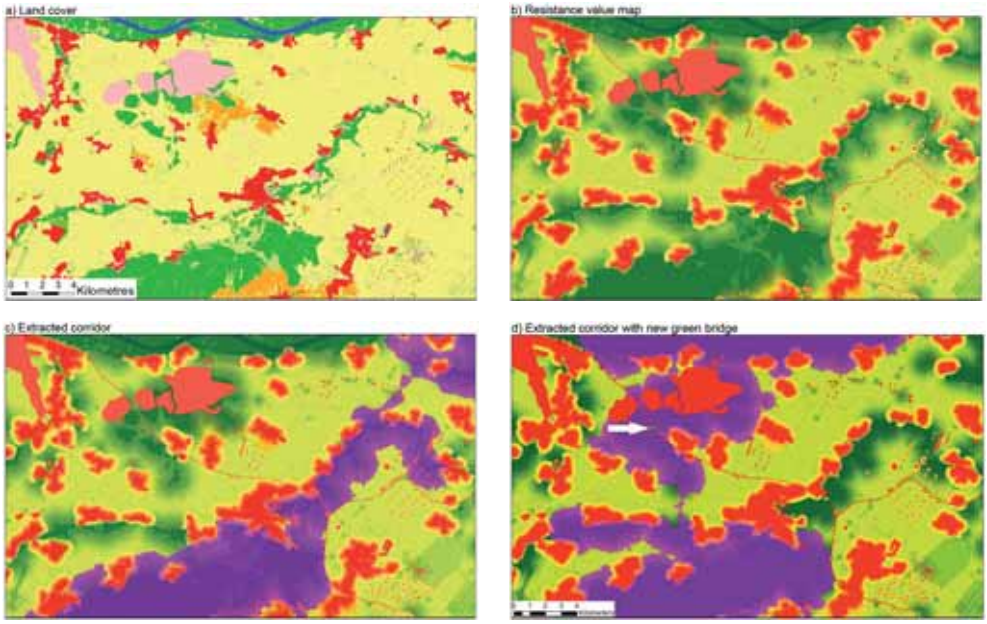


**Fig. 7:** Status quo and chances of enhancement; a) land cover and ancillary data; b) resistance surface; c) delineated corridor (purple); d) resistance surface like b) but considers a new mitigation measurement for crossing the highway (white arrow); purple: extracted corridor; land cover and resistance values: legends according to Fig. 4.

Fig. 7d shows the effect of considering a new location for a wildlife passage crossing the highway (white arrow). The rest of the landscape remains the same as for Fig. 7c. The acceptance of a wildlife passage for migration of animals depends not only on the quality of the passage itself but also on the circumstances of approaching this passage. Small forested patches or hedges function as guiding features in the landscape, providing also shelter. If these guiding features already exist, the acceptance of the wildlife passage will not even be faster but also additional costs for these features are avoided like the access to favoured parcels, planting, etc. are avoided. Fig. 6 provides this spatial information of existing landscape features supporting wildlife migration. The placement of the new wildlife passage inside the corridor area of Fig. 6 guarantees therefore an easier acceptance of the passage by wildlife. Additionally it reduces the costs of integration of the new passage in the landscape.

So the corridor extraction is depending on the quality of the resistance surface and the consideration of spatial effects and ancillary data. Beside the resistance surface, the extracted corridor is depending on the applied algorithm. Furthermore the initial regions have a substantial influence on the outcome (region locations, region shape, etc.).

A traditional least cost path algorithm is often used in wildlife analysis (Beier et al. 2009) it has its limitations in validating thresholds of ecological parameters. In addition it enhances only one path, the least cost path, even if there are more possibilities apparent (Pinto & Keitt 2009). Circuit theory on the other hand is often limited by hardware requirements because of large data processing demands.

## 5 Discussion

The Figs. 5 and 6 demonstrate the importance of the resistance surface. A delineated corridor, by applying a delineation algorithm, can only be as good as the basic input. The resistance surface functions as the basic input. Land cover data with proper spatial details is necessary, especially for land based wildlife movement, although incorporating ancillary data, like fences or wildlife passages, are crucial. The consideration of spatial interactions improves the account for regional planning actions. Despite the declaration of these spatial interdependencies is discussed in a controversial way in literature, the implementation in a GIS helps to understand the movements in a better way and provides the possibility to refine and adapt these spatial rules and assumptions for the future.

Due to the geometry of Landsat images, features smaller than 30 m x 30 m cannot be detected. But for future studies the new generation of satellite data such as Sentinel-2 with high temporal (three to five days) and high spatial resolution (10 m to 20 m) provides new opportunities. Temporal effects like seasonal and even diurnal differences of resistance values for agriculture become more accessible. To study seasonal effects more knowledge of animal behaviour will be needed like additional collar / GPS data and the quantification of these data to spatial rules. The knowledge database for generating resistance values demonstrated here, considers especially the spatial effect of extensive land covers. The inclusion of spatial effect for linear structures, like roads in combination with existing rules, might improve the quality of the resulting resistance value in some parts of the landscape but further research is needed.

## Acknowledgements

The project Alpine-Carpathian-Corridor ("ACC Basic" and "ACC Centrope") was funded by the European Commission in the European Territorial Cooperation Program Slovakia – Austria 2007 – 2013, Land Niederösterreich, Land Burgenland and the Austrian Federal Ministry of Agriculture, Forestry, Environment and Water Management. Constructive comments and suggestions made by the anonymous reviewer. Wai Tim Ng and Kathrin Einzmann helped to improve the article.

## References

Abt, K.M. & Sandfort, R., 2011: Landschaftsfragmentierung und tierökologische Korridore – Ein

Überblick zum aktuellen Forschungsstand sowie zu ökologischen, planerischen und rechtlichen Aspekten. – Forschungsprojekt Alpen Karpaten Korridor, Universität für Bodenkultur, Wien, Österreich.

Anderson, A. & Jenkins, C.N., 2006: Applying Nature's Design: Corridors as a Strategy for Biodiversity Conservation. – Columbia University Press, NY, USA.

Andren, H., 1994: Effects of habitat fragmentation on birds and mammals in landscapes with different proportions of suitable habitat – a review. – Oikos **71:** 355–366.

Banko, G., Kurzweil, A., Lexer, W., Mayer, S., Roder, I. & Zehtner, G., 2004: Status und Trends des quantitativen Flächenverbrauchs in Österreich. – Wissenschaft & Umwelt Interdisziplinär **8:** 43–52.

Baum, K.A., Haynes, K.J., Dillemuth, F.P. & Cronin, J.T., 2004: The matrix enhances the effectiveness of corridors and stepping stones. – Ecology **85:** 2671–2676.

Beier, P. & Loe, S., 1992: A checklist for evaluating impacts to wildlife movement corridors. – Wildlife Society Bulletin **20:** 434–440.

Beier, P. & Noss, R.F., 1998: Do habitat corridors provide connectivity? – Conservation Biology **12** (6): 1241–1252.

Beier, P., Majka, D.R. & Spencer, W.D., 2009: Uncertainty analysis of least-cost modeling for designing wildlife linkages. – Ecological Applications **19** (8): 2067–2077.

Brooks, C.P., 2003: A scalar analysis of landscape connectivity. – Oikos **102:** 433–439.

Bossard, M., Feranec, J. & Otahel, J., 2000: CORINE land cover technical guide – Addendum 2000 – Technical Report No. 40, European Environment Agency, Copenhagen, Denmark.

Centrope, 2014: Central European region. – http://www.centrope.com/en (1.7.2014).

Clevenger, A.P., Chruszcz, B. & Gunson, K.E., 2001: Highway Mitigation Fencing Reduces Wildlife-Vehicle Collisions. – Wildlife Society Bulletin **29** (2): 646–653.

Corridordesign, 2007: Overview of corridor modelling. – http://corridordesign.org/designing_corridors/corridor_modeling/ (7.7.2014).

Driezen, K., Adriaensen, F., Rondinini, C., Doncaster, C.P. & Matthysen, E., 2007: Evaluating least-cost model predictions with empirical dispersal data: a case-study using radiotracking data of hedgehogs (Erinaceus europaeus). – Ecological Modelling **209:** 314–322.

European Environment Agency, 2007a: CLC2006 technical guidelines. – EEA Technical report, No 17/2007, ISSN 1725-2237, http://www.eea.europa.eu/publications/technical_report_2007_17 (1.7.2014).

European Environment Agency, 2007b: Corine land cover 2006 classes and RGB color codes. – http://www.eea.europa.eu/data-and-maps/data/corine-land-cover-2006-raster-3/corine-land-cover-classes-and/clc_legend.csv (7.7.2014).

Fahrig, L., 2001: How much habitat is enough? – Biological Conservation **100:** 65–74.

Falucci, A., Maiorano, L. & Boitani, L., 2007: Changes in land-use/land-cover patterns in Italy and their implications for biodiversity conservation. – Landscape Ecology **22:** 617–631.

Fleury, A.M. & Brown, R.D., 1997: A Framework for the Design of Wildlife Conservation Corridors with Specific Application to Southwestern Ontario. – Landscape and Urban Planning **37** (8): 163–186.

Forman, R.T.T. & Godron, M., 1986: Landscape Ecology – Wiley, New York, NY, USA.

FSV (Oesterreichische Forschungsgesellschaft Strasse, Schiene, Verkehr), 2007: RVS 04.03.12 Wildschutz, Flora und Fauna an Verkehrswegen. – http://rvs.co.at/shop/produktdetail.aspx?ID Produkt= eafb2c26-1d55-4a0e-87bf-124cf7ab30fc (1.7.2014)

Grillmayer, R., Schacht, H. & Wöss, M., 2002: Forschungsprojekt Wildökologische Korridore. – Universität für Bodenkultur, Wien, Österreich.

Goetz, S.J., Jantz, P. & Jantz, C.A., 2009: Connectivity of core habitat in the Northeastern United States: Parks and protected areas in a landscape context. – Remote Sensing of Environment **113:** 1421–1429.

Hilty, J.A., Lidicker, Jr.W.Z., Merenlender, A. & Dobson, A.P., 2006: Corridor Ecology: The Science and Practice of Linking Landscapes for Biodiversity Conservation – Island Press, Washington, DC, USA.

Howey, M.C.L., 2011: Multiple pathways across past landscapes: circuit theory as a complementary geospatial method to least cost path for modelling past movement. – Journal of Archaeological Science Volume **38** (10): 2523–2535.

Janin, A., Lena, J.P., Ray, N., Delacourt, C., Allemand, P. & Joly, P., 2009: Assessing landscape connectivity with calibrated cost-distance modelling: predicting common toad distribution in a context of spreading agriculture. – Journal of Applied Ecology Volume **46** (4): 833–841.

Kramer-Schadt, S., Kaiser, T.S., Frank, K. & Wiegand, T., 2011: Analyzing the effect of stepping stones on target patch colonization in structured landscapes for Eurasian lynx. – Landscape Ecology **26:** 501–513.

Koukal, T., Adelmann, C., Bauerhansl, C. & Schneider, W., 2010: Vom Punkt zur Fläche – vom Pixel zur Karte: Klassifikation der Landbedeckung mit der kNN-Methode. – VGI – Österreichische Zeitschrift für Vermessung und Geoinformation **98:** 90–101.

Köhler, C., 2005: Habitatvernetzung in Österreich GIS Modellierung von Mobilitätswiderstandswerten für waldbevorzugende, wildlebende Großsäuger in Österreich. – Masterthesis, Institut für Vermessung, Fernerkundung und Landinformation (IVFL), BOKU – Universität für Bodenkultur, Wien, Österreich.

Levins, R., 1969: Some demographic and genetic consequences of environmental heterogeneity for biological control. – Bulletin of the Entomological Society of America **15:** 237–240

Lillesand, T.M. & Kiefer, R.W., 1994: Remote Sensing and Image Interpretation. – Third edition, Wiley, New York, NY, USA.

Mac Arthur, R.H. & Wilson, E.O., 1967: The theory of island biogeography. – Princeton University Press, Princeton, New Jersey, USA.

McRae, B.H. & Beier, P., 2007: Circuit theory predicts gene flow in plant and animal populations. – National Academy of Sciences of the USA **104:** 19885–19890.

Molinari, P. & Molinari-Jobin, A., 2001: Identifying Passages in the Southeastern Italian Alps for Brown Bears and Other Wildlife. – Bear Journal (Ursus) **12:** 131–134.

Musiega, D.E. & Kazadi, E.N., 2004: Simulating the East African wildebeest migration patterns using GIS and remote sensing. – African Journal of Ecology **42:** 355–362.

Pinto, N. & Keitt, T.H., 2009: Beyond the least-cost path: evaluating corridor redundancy using a graph-theoretic approach. – Landscape Ecology **24:** 253–266.

Rabinowitz, A. & Zeller, K.A., 2010: A range-wide model of landscape connectivity and conservation for the jaguar, Panthera onca. – Biological Conservation **143:** 939–945.

Ray, N., Lehmann, A. & Joly, P., 2002: Modelling spatial distribution of amphibian populations: a GIS approach based on habitat matrix permeability. – Biodiversity and Conservation **11:** 2143–2165.

Rayfield, B., Fortin, M.J. & Fall, A., 2010: The sensitivity of least-cost habitat graphs to relative cost surface values. – Landscape Ecology **25:** 519–532.

Rogan, J., Miller, J., Stow, D., Franklin, J., Levien, L. & Fischjer, C., 2003: Land-Cover Change Monitoring with Classification Trees Using Landsat TM and Ancillary Data. – Photogrammetric Engineering & Remote Sensing **69** (7): 793–804.

Sawyer, H., Kauffman, M.J., Nielson, R.M. & Horne, J. S., 2009: Identifying and prioritizing ungulate migration routes for landscape-level conservation. – Ecological Applications **19:** 2016–2025.

Taylor, P.D., Fahrig, L., Henein, K. & Merriam, G., 1993: Connectivity is a vital element of landscape structure. – Oikos **68:** 571–573.

Vogt, P., Riiters, K.H., Iwanowski, M., Estreguil, C., Kozak, J. & Soille, P., 2007: Mapping landscape corridors. – Ecological Indicators **7:** 481–488.

Völk, F., Glitzner, I. & Wöss, M., 2001: Kostenreduktion bei Grünbrücken durch deren rationellen Einsatz. – Straßenforschungsauftrag Nr. 3.195 des Bundesministeriums für Verkehr, Innovation und Technologie Straßenforschung, Heft **513**.

Wang, I.J., Savage, W.K. & Shaffer, H.B., 2009: Landscape genetics and least-cost path analysis reveal unexpected dispersal routes in the California tiger salamander (Ambystoma californiense). – Molecular Ecology **18:** 1365–1374.

Watts, K., Eycott, A., Handley, P., Ray, D., Humphrey, J. & Quine, C., 2010: Targeting and evaluating biodiversity conservation action within fragmented landscapes: an approach based on generic focal species and least-cost networks. – Landscape Ecology **25:** 1305–1318.

Wöss, M., Grillmayer, R. & Völk, F., 2002: Green bridges and wildlife corridors in Austria. – Zeitschrift für Jagdwissenschaft **48** (1): 25–32.

Yadav, P.K., Kapoor, M. & Sarmak, K., 2012: Land Use Land Cover Mapping, Change Detection and Conflict Analysis of Nagzira – Navegaon Corridor, Central India Using Geospatial Technology. – International Journal of Remote Sensing and GIS **1** (2): 90–98.

Addresses of the Authors:

Mag. Franz Suppan, University of Natural Resources and Life Sciences, Vienna (BOKU), Institute of Surveying, Remote Sensing and Land Information, Peter-Jordan-Straße 82, A-1190 Vienna, Tel. +43-1-47654-5118, e-mail: franz.suppan@boku.ac.at

Dr. Fredy Frey-Roos, University of Natural Resources and Life Sciences, Vienna (BOKU), Institute of Wildlife Biology and Game Management, Gregor-Mendel-Straße 33, A-1180 Vienna, e-mail: alfred.frey-roos@boku.ac.at

Manuskript eingereicht: März 2014
Angenommen: Juni 2014

PFG 2014 / 5, 0451 – 0464
Stuttgart, October 2014

Article

# Omnidirectional Perception for Lightweight MAVs using a Continuously Rotating 3D Laser

David Droeschel, Dirk Holz & Sven Behnke, Bonn

**Keywords:** MAVs, 3D laser scanner, scan registration, obstacle detection

**Summary:** Micro aerial vehicles (MAV) are restricted in their size and weight, making the design of sensory systems for these vehicles challenging. We designed a small and lightweight continuously rotating 3D laser scanner – allowing for environment perception in a range of 30 m in almost all directions. This sensor is well suited for applications such as 3D obstacle detection, 6D motion estimation, localisation, and mapping.
Reliably perceiving obstacles in the surroundings of the MAV is a prerequisite for fully autonomous flights in complex environments. Due to varying shape and reflectance properties of objects, not all obstacles are perceived in every 3D laser scan (one half rotation of the scanner). Especially farther away from the MAV, multiple scans may be necessary in order to adequately detect an obstacle. In order to increase the probability of detecting obstacles, we aggregate acquired scans over short periods of time in an egocentric grid-based map. We register acquired scans against this local map to estimate the motion of the MAV and to consistently update the map.
In experiments, we show that our approaches to pose estimation and laser scan matching allow for reliable aggregation of 3D scans over short periods of time, sufficiently accurate to improve detection probability without causing inaccuracies in the estimation of the position of detected obstacles. Furthermore, we assess the probability of detecting different types of obstacles in varying distances from the MAV.

**Zusammenfassung:** *Omnidirektionale Wahrnehmung für leichte MAVs mittels eines kontinuierlich rotierenden 3D-Laserscanners.* Dieser Artikel beschreibt einen kleinen und leichten kontinuierlich rotierenden 3D-Laserscanner, der für die dreidimensionale Wahrnehmung von Hindernissen auf einem Micro Aerial Vehicle (MAV) entwickelt wurde. Der Sensor ermöglicht eine nahezu omnidirektionale Wahrnehmung der Umgebung in einer Entfernung von bis zu 30 m.
Eine Voraussetzung für die vollständige Autonomie von MAVs in komplexen Umgebungen ist die zuverlässige Wahrnehmung von Hindernissen. Durch unterschiedliche Formen und optische Eigenschaften, wie Reflektanz, werden nicht alle Hindernisse in jedem Laserscan wahrgenommen. Speziell bei weiter entfernten Objekten sind mehrere Scans notwendig, um ein Hindernis zu detektieren.
Um die Detektionswahrscheinlichkeit zu erhöhen, werden Entfernungsmessungen des Sensors über kurze Zeitfenster in einer egozentrischen 3D Gitterkarte aggregiert. Neue 3D-Scans werden gegen diese Karte registriert, um die Eigenbewegung des Fluggeräts zu schätzen.
Experimente zeigen, dass der Ansatz zur Positionsbestimmung eine robuste Aggregation von 3D-Scans über kurze Zeitfenster ermöglicht. Dadurch wird die Detektionswahrscheinlichkeit erhöht, ohne Ungenauigkeiten in der Position erkannter Hindernissen zu verursachen.

## 1 Introduction

In recent years, lightweight micro aerial vehicles (MAV) such as quadrotors attracted much attention in the field of aerial robotics because of their relatively low cost, ease of control, and compatibility with everyday indoor and outdoor environments. The size and weight limitations of such platforms, however, pose a problem for the design of their sensory systems. Most of today's lightweight MAVs are equipped with ultrasound distance sensors and air pressure sensors for estimating height above the ground, inertial sensors for estimat-

 www.schweizerbart.de
DOI: 10.1127/1432-8364/2014/0236 1432-8364/14/0236 $ 3.50

ing attitude, magnetometers for estimating the heading direction, GPS for absolute position estimates (outdoors), and cameras, e.g. for estimating visual odometry. While these small and lightweight sensors provide valuable information, they do not suffice for obstacle detection and safe navigation. Only few systems are equipped with 2D laser range finders (LRF) that measure distances in a plane around the MAV (Tomić et al. 2012, Grzonka et al. 2009, Bachrach et al. 2009, Shen et al. 2011).

2D laser range sensors are widely used for mobile robots navigating on flat ground – due to their accurate distance measurements even in bad lighting conditions and their large field-of-view (FoV). For robots acting in 3D environments or driving on more complex terrain, three-dimensional laser scanning sensors are popular. For instance, many autonomous cars perceive obstacles by means of a rotating laser scanner with a 360° horizontal FoV, allowing for detection of obstacles in all directions (Urmson et al. 2008, Montemerlo et al. 2008). Up to now, such 3D laser scanners are rarely used on lightweight MAVs due to their payload limitations.

In order to enable navigation in complex 3D environments for lightweight MAVs, we designed a continuously rotating 3D laser scanner that is minimalistic in terms of size and weight and measures distances of up to 30 m in almost all directions. Fig. 1 shows the sensor mounted on our MAV.

We use the laser scanner to perceive obstacles around the MAV by aggregating the distance measurements over a short period of time in an MAV-centric local multiresolution 3D map. The map models occupancy in all directions around the MAV and, thus, can cope with dynamic obstacles and changing environments as the regions where changes take place are updated with high frequency. We estimate the 6D motion of the MAV – relative to the egocentric map – by registering 3D laser scans with this local map. Fig. 4 illustrates the architecture of our approach.

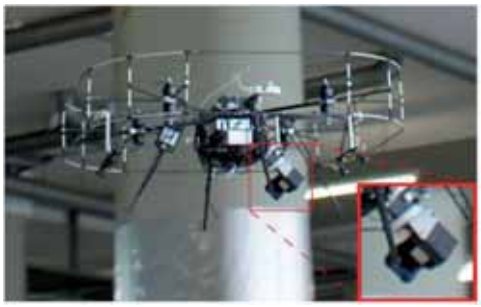

**Fig. 1:** The 3D laser scanner mounted on our MAV.

## 2 Related Work

The use of MAVs in recent remote sensing and robotics research varies largely in the level of autonomy – ranging from basic hovering and position holding (Bouabdallah et al. 2004) over trajectory tracking and waypoint navigation (Puls et al. 2009) to fully autonomous navigation (Grzonka et al. 2012). Similarly, the complexity of environments where MAVs operate ranges from flight arenas instrumented with motion capture systems and external computing, over outdoor flights in open spaces where GPS is available, to indoor flights in restricted spaces. Limiting factors for increasing the level of autonomy and/or the complexity of environments for lightweight MAVs are onboard sensing and onboard processing power.

Particularly important for fully autonomous operation of MAVs is the ability to perceive obstacles and avoid collisions. Most autonomous MAVs, however, cannot adequately perceive their surroundings and, hence, cannot avoid all collisions. Instead, collision detection is often restricted to the two-dimensional measurement plane of laser range finders (Grzonka et al. 2012) or to the limited FoV of forward-facing cameras (Mori & Scherer 2013, Ross et al. 2013). Most often, collision avoidance is neglected altogether, e.g. by flying in a certain height when autonomously flying between waypoints.

One way to extend the FoV for obstacle detection is to combine multiple sensors. Tomić et al. (2012), for example, present an autonomous MAV that perceives the environment using a stereo camera pair mounted in forward direction and a 2D laser range scanner mounted horizontally. Still, their perceptual field does not include the space below, above, and

behind the MAV. Most similar to our work is the work of Scherer et al. (2012) and Cover et al. (2013). The authors describe a system that is used to autonomously explore rivers using visual localisation and laser-based 3D obstacle perception. Similar to their approach, we aim at perceiving as much of the surroundings as possible in order to obtain almost omnidirectional obstacle detection.

In contrast to related approaches, we are able to aggregate distance measurements from consecutive 3D scans in an egocentric 3D multiresolution map and efficiently align new 3D scans with it to estimate the 6D motion of the MAV. By aggregating the scans, we obtain a higher measurement density in the map and a higher probability of detecting obstacles.

## 3 System Setup

Our platform is based on the open source *MikroKopter* octocopter kit, with a co-axial arrangement of rotors. The onboard computer (Intel Core i7-3820QM 2.7 GHz, 8 GB RAM) has ample computing power for sensor data processing and navigation planning. As middleware, we employ the Robot Operating System ROS (Quigley et al. 2009).

Besides the 3D laser scanner, our MAV is equipped with two stereo camera pairs (see Fig. 2) to estimate the motion of the MAV during scan acquisition.

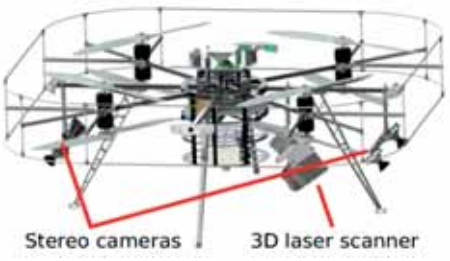


**Fig. 2:** CAD drawings of our MAV.

### 3.1 *3D Laser Scanner*

Our continuously rotating 3D laser scanner consists of a Hokuyo UTM-30LX-EW 2D laser range finder (LRF) which is rotated by a Robotis Dynamixel MX-28 servo actuator to gain a three-dimensional FoV. As shown in Fig. 3, the scanning plane is parallel to the axis of rotation, but the heading direction of the scanner is twisted slightly away from the direction of the axis in order to enlarge its FoV.

The 2D LRF is electrically connected by a slip ring, allowing for continuous rotation of the sensor. The axis of rotation is pitched downward by 45° in forward direction, which places the core of the MAV upwards behind the sensor as depicted in Fig. 3. Hence, the sensor can measure in all directions, except for a conical blind spot pointing upwards behind the robot.

The 2D laser scanner has a size of 62 mm × 62 mm × 87.5 mm and a weight of 210 g. Together with the actuator (72 g) and the slip ring, the total weight of the 3D scanner is approximately 400 g.

The Hokuyo LRF has an apex angle of 270° and an angular resolution of 0.25°, resulting

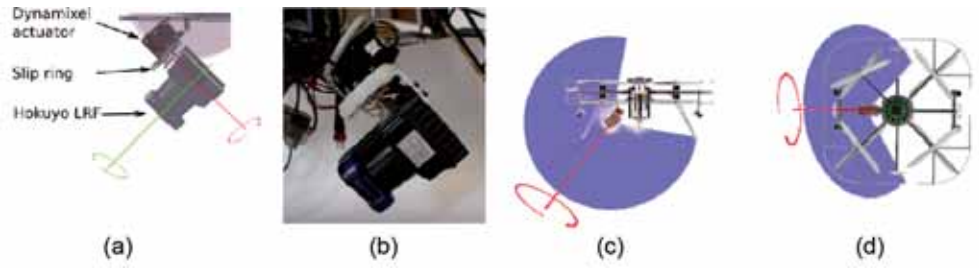


**Fig. 3:** (a) CAD drawings of our continuously rotating laser scanner. The Hokuyo 2D LRF is mounted on a bearing and rotated around the red axis. Its mirror is rotated around the green axis, resulting in a 2D measurement plane (blue). (b) Photo of the sensor. (c + d) CAD drawings illustrating the FoV of individual scans of the laser scanner (blue) from side and top view. The black dashed line illustrates the centre of the measurement plane. The 2D LRF is rotated around the red axis.

in 1080 distance measurements per 2D scan, called a *scan line*. The measurement accuracy is specified by the manufacturer with ± 30 mm at 0.1–10 m distance (± 50 mm at 10–30 m). The Dynamixel actuator rotates the 2D LRF at one rotation per second, producing 40 scan lines and 43,200 distance measurements per full rotation. Slower rotation is possible if a higher angular resolution is desired. For our setup, a half rotation leads to a full 3D scan of most of the environment. Hence, we can acquire 3D scans with up to 21,600 points with 2 Hz.

### 3.2 *Camera System*

The MAV is equipped with two stereo camera pairs pointing forward and backward with a pitch angle of 45° (see Fig. 2). Each stereo pair consists of two UEye 1221LE-M cameras with Lensagon BF2M15520 fisheye lenses. The lenses allow for a wide field-of-view up to 285° and the baseline between the cameras in a stereo pair is 20 cm. Image acquisition of all four cameras is initiated by a hardware trigger with 18 Hz, which allows for synchronised data acquisition. The hardware trigger is released by the onboard computer by using a general-purpose input/output. Thus, we gain time synchronisation between the clock on the onboard computer and the camera images. In addition, we also synchronise the internal clock of the Hokuyo laser scanner with the PC board by actively resetting the clock and then using time differences.

The mutual orientations of the cameras in a stereo pair are determined in advance with the method of Schneider & Förstner (2013). We calibrate the camera system to the laser scanner by manually labelling points in a laser scan and its corresponding pixel in the camera images. We select 50 scan points and their corresponding camera pixel, preferring spatially distributed points in corners and on edges in the scene. The 3D coordinates for the camera points are calculated as described in Schneider & Förstner (2013). The resulting transformation is calculated using singular value decomposition (SVD).

## 4 Preprocessing

In order to calculate a 3D point cloud from the scan lines originated by the LRF, a 3D point $P_l$ in the LRF's coordinate frame is transformed to $P_b$ in the base coordinate frame of the MAV by

$$P_b = T_l T_r T_c P_l \tag{1}$$

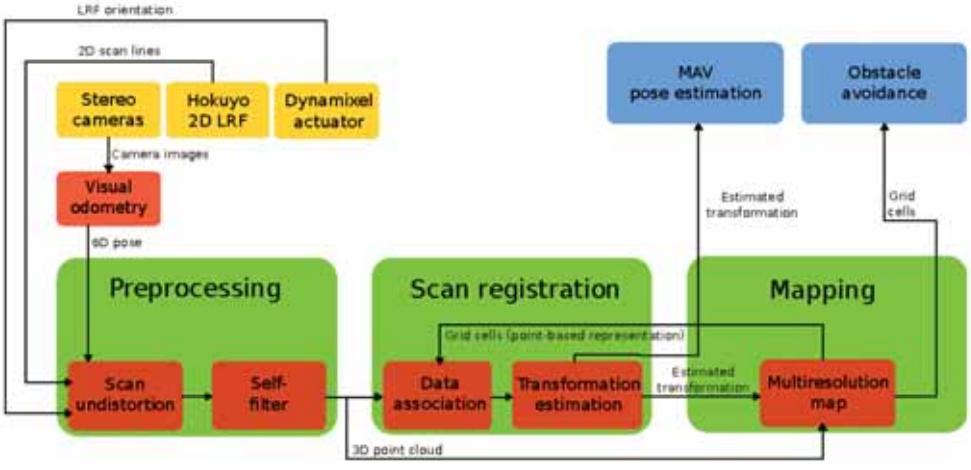


**Fig. 4:** An architectural overview of our system. The laser range finder (LRF) measurements are processed in preprocessing steps described in section 4. The resulting 3D point cloud is used to estimate the transformation between the current scan and the map as described in section 5. Registered scans are stored in a local multiresolution map.

Here, $T_l$ is a static transformation between the base frame of the MAV and the link where the 3D laser scanner is mounted and $T_c$ is the static transformation between the 2D LRF and the bearing. $T_r$ is a continuously changing transformation that takes into account the bearing's orientation. Its rotational parts are measured using the encoder positions reported by the Dynamixel actuator. Fig. 5 shows a resulting scan of an outdoor environment.

The offset between the scanned plane section and the rotation axis results in a different FoV for two different half rotations which is shown in Fig. 6a. In this way, occlusion from small parts of the MAV is reduced significantly.

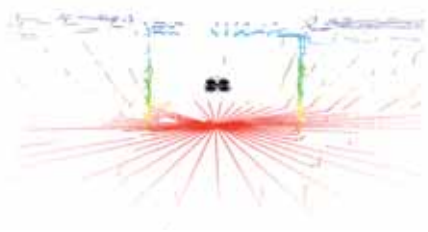

**Fig. 5:** A 3D scan of an outdoor environment acquired with our continuously rotating laser scanner. The colour of the points encodes the distance from the ground.

### 4.1 *Multi-Echo Detection*

The Hokuyo UTM-30LX-EW is able to measure up to three echoes of a single emitted light pulse. The number of echoes for a light pulse depends on the surface of the measured objects, i.e. shape and reflectivity. For example, transparent materials, vegetation or edges of buildings often yield more than one echo. Often, the second echo comes from a structure in the original pulse direction, behind a partial occlusion, which means that it can be treated as an additional distance measurement. Measurements from the first and the second echo are shown in Fig. 6b.

### 4.2 *Scan Aggregation*

Preprocessing raw laser scans to form 3D scans considers only the rotation of the scanner w.r.t. to the MAV. The motion of the MAV during acquisition is not taken into account (so far). As a consequence, the environmental structures measured in 3D scans are not consistent. In particular, first and last scan line appear considerably disconnected, structures in consecutive scans drift. We account for this effect by undistorting 3D scans in two steps.

First, measurements of individual scan lines are undistorted with regards to the rotation of the 2D LRF around the servo rotation axis (red axis in Fig. 3). Here, the rotation between

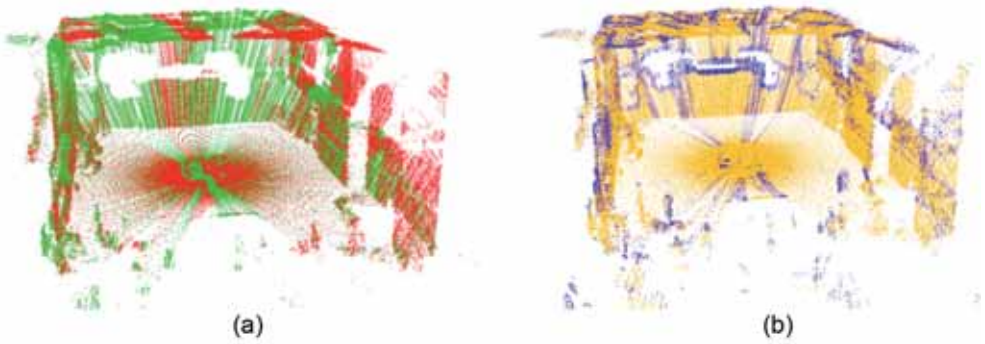


**Fig. 6:** Accumulated 3D scans of an indoor environment. (a) The colour encodes the different half rotations of the scanner. Moving the optical centre of the 2D laser range finder away from the rotation axis of the actuator results in different self-occlusions of the scans from the first (green) and the second (red) half rotation. (b) Measurements from first echo (yellow) and the second echo (purple). In case of partial occlusions, e.g. by the MAV itself, multi-echo detection leads to an increase of distance measurements.

the acquisition of two scan lines is distributed over the measurements by using spherical linear interpolation.

Second, we compensate for the motion of the MAV during acquisition of a full 3D scan. To this end, we incorporate a visual odometry estimate from the two stereo cameras. Here, a keyframe-based bundle adjustment is performed (Schneider et al. 2013) on the synchronised images with 18 Hz. Since the update rate of the 2D LRF is 40 Hz, we linearly interpolate between the estimates of the visual odometry.

The 6D motion estimate is used to assemble the individual 2D scan lines of each half rotation to a 3D scan. Fig. 7 illustrates the effect of scan undistorting.

### 4.3 *Self-Filter*

The laser range finder measures also points on the MAV. These points are excluded from further processing by checking the egocentric point coordinates (in the base coordinate frame of the MAV) against a simplified CAD model of the MAV. Furthermore, distance measurements that are most likely caused by the veiling effect when scanning the edge of an object are removed.

## 5 Scan Registration

We register 3D laser range scans with a local multiresolution map to estimate the motion of the MAV. After aggregating scans to a full 3D scan over one half rotation and transforming them to compensate for the sensor motion, the generated 3D scan is aligned to the so far built map by means of the iterative closest point (ICP) algorithm. The map is incrementally updated by inserting every registered 3D scan. It is initialised using the first 3D scan acquired.

Correspondences are assigned using the point-based representation in the cells of our local grid map (section 5.1) and the ICP algorithm estimates a transformation between the scan and the map, describing the displacement between them. We benefit from the mul-

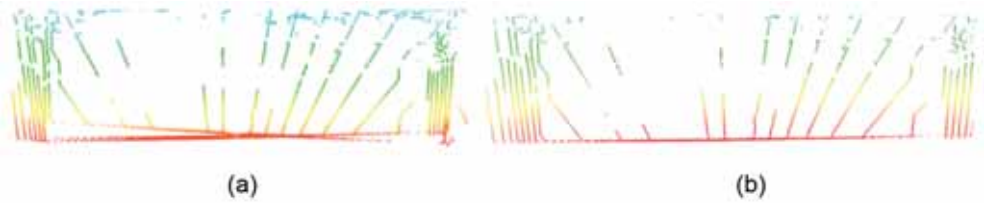


**Fig. 7:** Example of deskewing a 3D laser scan acquired in an indoor environment with flat ground from a side view. (a) Sensor movement during scan acquisition yields distorted 3D scans. (b) We deskew the scan based on the motion estimate.

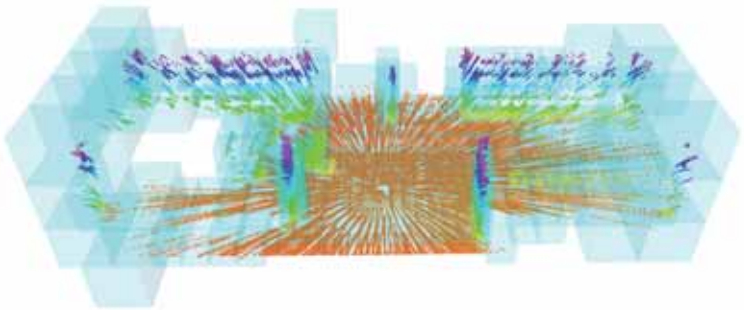

**Fig. 8:** A grid-based local multiresolution map with a higher resolution in the close proximity to the sensor and a lower resolution with increasing distance. The point colour encodes the distance from the ground.

tiresolution property of our map, which allows aligning a 3D scan in a coarse-to-fine approach. Hence, we start assigning correspondences and estimating the transformation at the coarsest level. The resulting transformation is used as initialisation for the registration on the next finer level and so forth.

### 5.1 *Local Multiresolution Map*

Distance measurements from the sensor are accumulated in a robot-centric 3D multiresolution map with increasing cell sizes from the MAV centre. The representation consists of multiple MAV-centred 3D grid-maps with different resolutions. On the finest resolution, we use a cell length of 0.25 m. Each grid-map is embedded in the next level with coarser resolution and doubled cell length. An example of a built local multiresolution map is shown in Fig. 8.

We use a hybrid representation, storing 3D point measurements along with occupancy information in each cell. Point measurements of consecutive 3D scans are stored in fixed-sized circular buffers, allowing for point-based data processing and facilitating efficient nearest-neighbour queries.

Fig. 9 shows a one-dimensional schematic illustration of the map organisation. We aim for efficient map management for translation and rotation. To this end, individual grid cells are stored in a circular buffer to allow shifting of elements in constant time. We interlace multiple circular buffers to obtain a map with three dimensions. The length of the circular buffers depends on the resolution and the size of the map. In case of a translation of the MAV, the circular buffers are shifted whenever necessary to maintain the egocentric property of the map. In case of a translation equal to or larger than the cell size, the circular buffers for respective dimensions are shifted. For sub-cell-length translations, the translational parts are accumulated and shifted if they exceed the length of a cell.

Since we store 3D points for every cell for point-based processing, individual points are transformed into the local coordinate frame of a cell when adding points, and back to the map's coordinate frame when accessing point coordinates. Every cell in the map stores a list of 3D points from the current and previous 3D scans. This list is also implemented by a fixed-sized circular buffer. If the capacity of the circular buffer is exceeded, old measurements are discarded and replaced by new measurements.

Since rotating the map would require moving all cells, our map is oriented independently of the MAV orientation. We maintain the orientation between the map and the MAV and use it to rotate measurements when accessing the map.

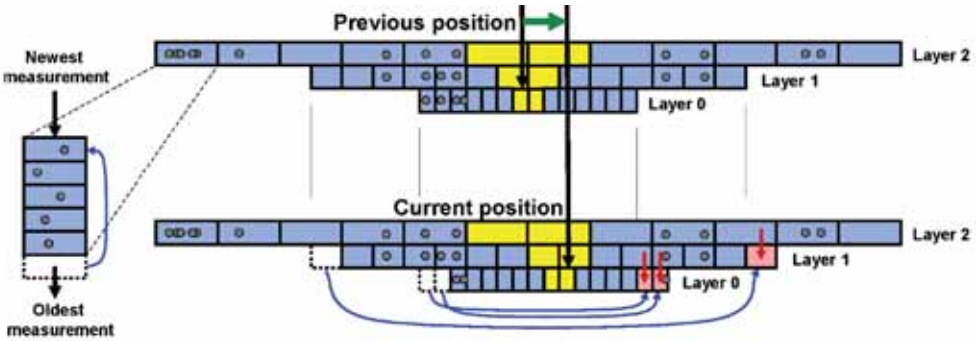


**Fig. 9:** One-dimensional schematic illustration of the hybrid local multiresolution map. Along with the occupancy information, every grid-cell (blue) maintains a circular buffer (left) with its associated measurement points (grey). The map is centred around the MAV and in case of a MAV motion, ring buffers are shifted according to the translational parts of the movement, maintaining the egocentric property of the map. Cells at coarser levels are used to initialise newly added cells (red arrows). Due to the implementation using ring buffers, cells vanishing on one side of the map become new cells at the other side (blue arrows).

Besides the scan registration approach for pose estimation and map updates, the map is used for obstacle avoidance and local navigation planning (Nieuwenhuisen & Behnke 2014).

## 5.2 *Data Association*

When using the ICP algorithm for scan registration, corresponding points between the model and the current point cloud are assigned, usually by building a space-partitioned data structure from the model point cloud. In contrast, we continuously maintain our data structure for efficient nearest-neighbour queries to assign correspondences. Every point from a newly acquired 3D scan is directly assigned to a cell in the map in constant time. The closest point in terms of the Euclidean distance from the point list of this cell is initially assigned as corresponding point.

As illustrated in Fig. 10, points in neighbouring cells might be closer to the measured point than the initially assigned point. Consequently, we extend the search to neighbouring cells, if the distance to the initial assignment is larger than the distance to the border of a neighbouring cell.

Since acquired 3D scans of the scene and the aggregated local map differ in terms of structure and point density, especially when parts of the scene have previously been occluded, individual assigned correspondences can be incorrect. These incorrect correspondences distort the transformation estimation and need to be filtered. We reject correspondences using the following criteria:

- *Asymmetric correspondences:* We check for symmetry in the assignments: for a correspondence from a scan point $d_i$ to a map point $m_i$, we check if $d_i$ is the closest point to $m_i$ in the scan point cloud. Otherwise, the correspondence is rejected.
- *One-to-many correspondences:* In case multiple points in the 3D scan correspond to the same point in the map, we keep only the one correspondence with the smallest point-to-point distance and reject all others.
- *Correspondence trimming:* Correspondences are rejected by only considering the best $\theta_t$ percent of the assigned correspondences (ranked by point-to-point distance).
- *Distance rejection:* Correspondences are rejected if the point-to-point distance exceeds a threshold $\theta_d$.

## 5.3 *Transformation Estimation*

With $N$ assigned corresponding point pairs ($m_i$, $d_i$), we determine the displacement between the points of a scan $d_i$ and the map points $m_i$ by finding a rigid transformation $T$ that minimises

$$E(\mathrm{T}) = \sum_{i=1}^{N} \left\| m_i - T d_i \right\|^2 \tag{2}$$

using a closed-form solution using singular value decomposition (Besl & McKay 1992).

In each ICP iteration, correspondences are re-assigned, the transformation best aligning the corresponding points is applied to the scan, and the following termination criteria are checked:

- $E(\mathrm{T})$ is smaller than a given threshold $\theta_r$,
- the difference between $T_k$ and $T_{k-1}$ is smaller than $\theta_e$ or
- the number of iterations exceeds $\theta_i$,

**Fig. 10:** Assigning point correspondences. Left: for every point of a 3D scan (blue), a corresponding map point (green) is initially assigned from the cell's point list (red line). Right: if the distance to neighbouring cells is smaller than the distance to the initial assignment, closer points might be found in the neighbouring cell (orange line).

where $T_k$ and $T_{k-1}$ are the estimated transformations from the current and the previous iteration, respectively.

## 6 Experiments and Results

Due to varying shape and reflectance properties of objects, not all obstacles are perceived in every 3D laser scan (one half rotation of the scanner). Especially farther away from the robot, multiple scans may be necessary in order to adequately detect an obstacle.

In experiments, we assess the probability of detecting different types of obstacles in varying distances from the MAV. Furthermore, we assess the quality of the produced local map. The intuitions behind these experiments are the following: if a certain object can only be perceived (at least once) in $n$ 3D laser scans, it is sufficient for reliable collision avoidance if our local mapping approach can reliably aggregate $n$ 3D laser scans without inducing inconsistencies in the egocentric obstacle map, e.g. blurring effects due to drifts in the pose estimates. Obviously, whether or not an obstacle can be avoided also depends on the distance to the obstacle and movement direction and speed of the MAV. Both can be neglected if the sensor is able to detect all types of obstacles in the immediate vicinity of the MAV (and the MAV is not flying too fast).

### 6.1 *Obstacle Detection Probabilities*

For assessing the probability of detecting objects in the vicinity of the robot, we have chosen seven test obstacles differing, amongst other characteristics, in size (diameter), colour and material (reflectivity), and transparency. Referring to the experiment setup in Fig. 11a, the objects are mounted on a tripod holder. The MAV is positioned with distances to the holder of 1 m to 10 m. For each distance, a total of 30 3D scans are captured. We visually inspect the acquired data and count the 3D scans in which at least a part of the object is visible in the distance measurements and estimate the average detection probability. For the estimation of the detection probabilities, we considered roughly the same lengths for all obstacles (1 m, which is also the minimum safety distance during navigation). That is, the probabilities primarily depend on diameter and reflection properties rather than object length.

As can be seen in the plots (Fig. 11b) and the detailed results (Fig. 11c), we are able to detect all types of obstacles at 1 m distance, and with an aggregation period of 10 s up to 3 m (for the transparent plexiglass tube). Obstacles with better visibility like the metal rod, the cardboard and plastic tubes, are reliably detected up to 10 m away from the robot.

Based on the achievable results, we distinguish, respectively, different obstacle types (and distances) and detection probabilities: objects that can be reliably detected when aggregating over 2.5 s (5 scans) are considered safe and easy to detect (green in Fig. 11c), obstacles that cannot be detected at least once in 10 s (20 scans) are considered especially dangerous and very hard to detect (red in Fig. 11), and obstacles of moderate detection probability (yellow in table in Fig. 11c) can be reliably handled by scan aggregation when not flying too fast.

### 6.2 *Scan Matching and Aggregation*

In a second experiment, we evaluate the accuracy of the scan registration in an indoor motion capture (MoCap) system. It provides accurate pose information of the MAV at high rates (100 Hz) but is restricted to a small capture volume of approximately 2 m × 2 m × 3 m. As error metric, the absolute trajectory error (ATE) is computed, based on the estimated and the ground-truth trajectory from the MoCap system. The reference implementation provided by Sturm et al. (2012) was used to compute the error. Throughout the experiments, we used five levels for the multiresolution map and a cell length of 0.125 m at the finest level, yielding a cell length of 2 m at the coarsest level.

The registration parameters (sections 5.2, 5.3) $\theta_r$, $\theta_i$ and $\theta_\varepsilon$ are manually determined. In this experiment, $\theta_r = 1$ cm, $\theta_\varepsilon = 0.001$ cm, $\theta_i = 15$, $\theta_d = 1$ m, and $\theta_t = 80\%$ showed best results.

The dataset for evaluation is a 50 seconds flight sequence containing 100 3D scans,

(a) Left: Six different object types, from left to right: cable (0.75 cm), aluminium broomstick (2.7 cm), plexiglass tube (5 cm), cardboard tube (7.5 cm), rectangular metal rod (4 cm), blue plastic tube (11 cm). Middle and right: experiment setup with object holder (black metal rod, 4 cm), measuring type and flying multicopter.

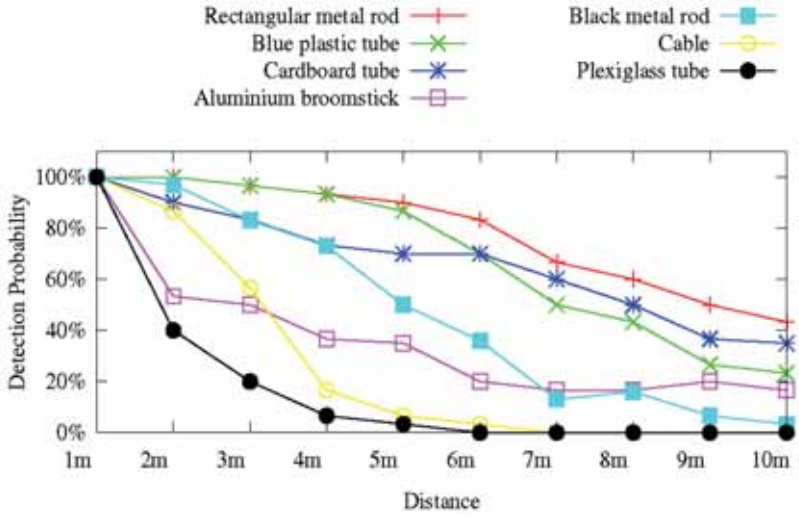


(b) Change of detection probabilities over increasing distance for the different objects (standing).

| Object | Distance | | | | | | | | | |
|---|---|---|---|---|---|---|---|---|---|---|
| | 1m | 2m | 3m | 4m | 5m | 6m | 7m | 8m | 9m | 10m |
| Rectangular metal rod | 100.0 | 100.0 | 96.6 | 93.3 | 90.0 | 83.3 | 66.6 | 60.0 | 50.0 | 43.3 |
| Blue plastic tube | 100.0 | 100.0 | 96.6 | 93.3 | 86.6 | 70.0 | 50.0 | 43.3 | 26.6 | 23.3 |
| Cardboard tube | 100.0 | 90.0 | 83.3 | 73.3 | 70.0 | 70.0 | 60.0 | 50.0 | 36.6 | 35.0 |
| Aluminium broomstick | 100.0 | 53.3 | 50.0 | 36.6 | 35.0 | 20.0 | 16.6 | 16.6 | 20.0 | 16.6 |
| Black metal rod | 100.0 | 97.0 | 83.0 | 73.0 | 50.0 | 36.0 | 13.0 | 16.0 | 6.6 | 3.3 |
| Cable | 100.0 | 86.6 | 56.6 | 16.6 | 06.6 | 03.3 | 00.0 | 00.0 | 00.0 | 00.0 |
| Plexiglass tube | 100.0 | 40.0 | 20.0 | 06.6 | 03.3 | 00.0 | 00.0 | 00.0 | 00.0 | 00.0 |

(c) Detailed detection probabilities in percent (standing MAV).

**Fig. 11:** Assessing the probabilities of detecting different types of objects in different distances, measured over 30 3D scans for each obstacle and distance. We count the 3D scans in which at least a part of the object is visible in the measurements and estimate the average detection probability.

where the MAV was controlled by a human operator, taking off and landing at two locations in the MoCap volume. The speed during the experiment was varying from 0.1 m/s to 1.1 m/s. Fig. 12 shows the ATE of our multiresolution scan registration method, compared to the MoCap trajectory.

In quantitative experiments, we compare our method to a state-of-the-art registration method, the Generalized-ICP (Segal et al. 2009). In addition, we evaluate the accuracy of the visual odometry that is used to undistort acquired 3D scans. The mean, standard deviation and maximum ATE of all three methods are summarized in Tab. 1. The results indicate that both scan registration methods improve the motion estimate from the visual odometry and that the trajectory generated by our method has a slightly lower ATE compared to the Generalized-ICP. The run-times of both methods for this experiment on a single core of an Intel Core i7-3820QM (2.7 GHz) processor, are also summarized in Tab. 1, showing that Generalized-ICP is computationally much more expensive than our method.

In a third experiment, we assess the quality of our grid-based map. Consecutive 3D scans are aligned with the map and 3D points are added to respective cells. Fig. 13 shows the point-based representation of the map at different time steps, accounting for an increasing density of the map after adding consecutive 3D scans. As obstacle, the blue plastic tube shown in Fig. 11a was used. The MAV was hovering at a height of 2 m with a distance to the obstacle of 8 m. The experiment shows that we can reliably and accurately track the MAV's movement over 10 s and aggregate the acquired 20 3D scans to a dense and sharp map.

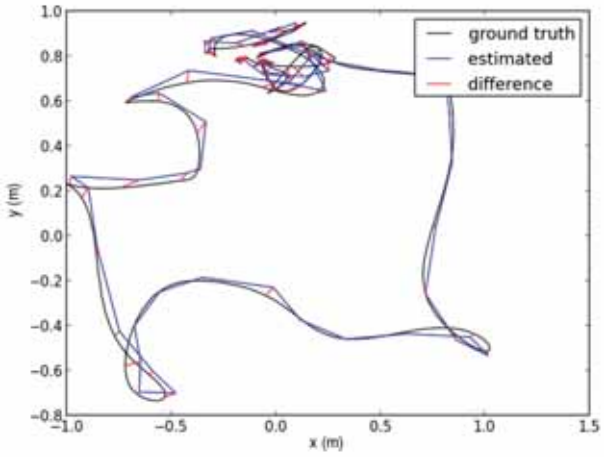


**Fig. 12:** Absolute trajectory error of the scan registration using the multiresolution map (blue) compared to ground-truth data from the MoCap system (black). Points of the trajectory are projected on the xy-plane.

**Tab. 1:** Absolute trajectory error (ATE) and run-time of our registration method, in comparison to visual odometry (VO), and Generalized-ICP (GICP). Referring to the root-mean-square error (RMSE), our approach achieves better results while being significantly faster.

| | ATE (m) | | | | run-time (ms) | |
|---|---|---|---|---|---|---|
| | RMSE | mean | median | max | mean | max |
| VO | 0.151 | 0.134 (± 0.059) | 0.129 | 0.324 | | |
| GICP | 0.033 | 0.030 (± 0.013) | 0.030 | **0.079** | 1432 (± 865) | 5673 |
| ours | **0.030** | **0.028** (± 0.015) | **0.026** | 0.093 | **311** (± 90) | **376** |

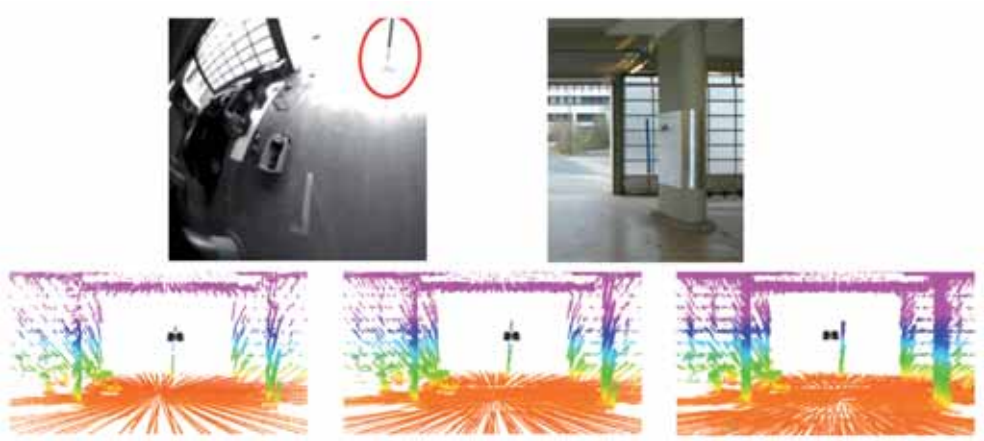

**Fig. 13:** Aggregating 3D scans in a scene of the third experiment. Photos show the sensed pole (red ellipse) and the surroundings from an on-board camera with fish-eye lens (top left) and an external camera (top right). Scan aggregation increases the detection probability and the point density in the map (bottom row, left to right: map after aggregating 5, 10, and 20 scans.

Since ground-truth data, e.g. from a MoCap system was not available in this experiment, we evaluate the different methods by inspecting the variation of points in a planar area. Fig. 14 shows a part of the floor in the resulting point-based representation from a side view. It can be seen that using scan registration decreases the thickness of the floor significantly, indicating an improved motion estimate. Similar to the results of the second experiment, the resulting floor patch generated by aggregating scans using our method is slightly thinner.

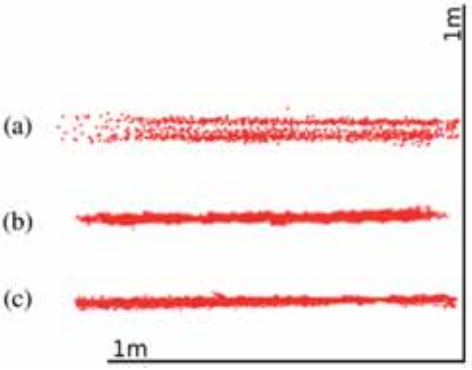


**Fig. 14:** A cut-out part of the floor from a side view after scan aggregation (length of the segments: 1 m). (a) using only visual odometry, (b) visual odometry combined with scan registration using Generalized-ICP, (c) visual odometry with our multiresolution scan registration.

Note that in normal operation, scans are only added if they properly align with the map, i.e., $E(\mathrm{T})$ is smaller than $\theta_r$ in (2). For this experiment, we added every scan to the map to have a fair comparison to the motion estimate from visual odometry.

## 7 Conclusion

We designed a small and lightweight continuously rotating 3D laser scanner that is particularly well suited for the use in MAVs. The sensor allows for measuring distances of up to 30 m in almost all directions with a minimal blind spot. For each light pulse, up to three echoes are reported which is advantageous in case of transparent material, vegetation, or edges of buildings.

We use the sensor to perceive obstacles in the vehicle's vicinity by building a grid-based obstacle map. We estimate the motion of our MAV by registering 3D laser scans with the map.

In experiments, we showed that our approaches to pose estimation and laser scan matching allow for reliably aggregating 3D scans over short periods of time, accurately enough to improve detection probability and without causing inaccuracies in the estimation of the position of detected obstacles.

Overall, we can build dense and sharp 3D obstacle maps and estimate the vehicle's trajectory by 3D scan registration.

As an outlook on ongoing and future work, we integrated the sensor in our MAV and conducted experiments with dynamical obstacles, showing that the MAV is able to omnidirectionally perceive obstacles and to react on them (Nieuwenhuisen et al. 2013).

## Acknowledgements

This work has been supported partially by grant BE 2556/7-1 of German Research Foundation (DFG).

## References

Bachrach, A., He, R. & Roy, N., 2009: Autonomous flight in unstructured and unknown indoor environments. – European Micro Aerial Vehicle Conference (EMAV): 1–8.

Besl, P.J. & McKay, N.D., 1992: A method for registration of 3-D shapes. – IEEE Transactions on Pattern Analysis and Machine Intelligence (PAMI) **14** (2): 239–256.

Bouabdallah, S., Murrieri, P. & Siegwart, R., 2004: Design and control of an indoor micro quadrotor. – IEEE International Conference on Robotics and Automation (ICRA): 4393–4398.

Cover, H., Choudhury, S., Scherer, S. & Singh, S., 2013: Sparse tangential network (SPARTAN): Motion planning for micro aerial vehicles. – IEEE International Conference on Robotics and Automation (ICRA): 2820–2825.

Grzonka, S., Grisetti, G. & Burgard, W., 2009: Towards a navigation system for autonomous indoor flying. – IEEE International Conference on Robotics and Automation (ICRA): 2878–2883.

Grzonka, S., Grisetti, G. & Burgard, W., 2012: A fully autonomous indoor quadrotor. – IEEE Transitions on Robotics **28** (1): 90–100.

Montemerlo, M., Becker, J., Bhat, S., Dahlkamp, H., Dolgov, D., Ettinger, S., Haehnel, D., Hilden, T., Hoffmann, G., Huhnke, B., Johnston, D., Klumpp, S., Langer, D., Levandowski, A., Levinson, J., Marcil, J., Orenstein, D., Paefgen, J., Penny, I., Petrovskaya, A., Pflueger, M., Stanek, G., Stavens, D., Vogt, A. & Thrun, S., 2008: Junior: The Stanford entry in the urban challenge. – Journal of Field Robotics **25** (9): 569–597.

Mori, T. & Scherer, S., 2013: First results in detecting and avoiding frontal obstacles from a monocular camera for micro unmanned aerial vehicles. – IEEE International Conference on Robotics and Automation (ICRA): 1750–1757.

Nieuwenhuisen, M. & Behnke, S., 2014: Hierarchical planning with 3D local multiresolution obstacle avoidance for micro aerial vehicles. – Joint International Symposium on Robotics (ISR) and the German Conference on Robotics (ROBOTIK): 598–604.

Nieuwenhuisen, M., Droeschel, D., Schneider, J., Holz, D., Läbe, T. & Behnke, S., 2013: Multimodal obstacle detection and collision avoidance for micro aerial vehicles. – European Conference on Mobile Robots (ECMR): 7–12.

Puls, T., Kemper, M., Kuke, R. & Hein, A., 2009: GPS-based position control and waypoint navigation system for quadrocopters. – IEEE/RSJ International Conference on Intelligent Robots and Systems (IROS): 3374–3379.

Quigley, M., Gerkey, B.P., Conley, K., Faust, J., Foote, T., Leibs, J., Wheeler, R. & Ng, A.Y., 2009: ROS: An open-source robot operating system. – ICRA Workshop on Open Source Software.

Ross, S., Melik-Barkhudarov, N., Shankar, K.S., Wendel, A., Dey, D., Bagnell, J.A. & Hebert, M., 2013: Learning monocular reactive UAV control in cluttered natural environments. – IEEE International Conference on Robotics and Automation (ICRA): 1765–1772.

Scherer, S., Rehder, J., Achar, S., Cover, H., Chambers, A.D., Nuske, S.T. & Singh, S., 2012: River mapping from a flying robot: state estimation, river detection, and obstacle mapping. – Autonomous Robots **32** (5): 1–26.

Schneider, J. & Förstner, W., 2013: Bundle Adjustment and System Calibration with Points at Infinity for Omnidirectional Camera Systems – PFG – Photogrammetrie, Fernerkundung und Geoinformation **2013** (4): 309–321.

Schneider, J., Läbe, T. & Förstner, W., 2013: Incremental real-time bundle adjustment for multi-camera systems with points at infinity. – ISPRS Archives of Photogrammetry, Remote Sensing and Spatial Information Sciences, XL-1/W2.

Segal, A., Haehnel, D. & Thrun, S., 2009: Generalized-ICP. – Robotics: Science and Systems (RSS) 5.

Shen, S., Michael, N. & Kumar, V., 2011: Autonomous multi-floor indoor navigation with a computationally constrained micro aerial vehicle. – IEEE International Conference on Robotics and Automation (ICRA): 2968–2969.

Sturm, J., Engelhard, N., Endres, F., Burgard, W. & Cremers, D., 2012: A benchmark for the evaluation of RGB-D SLAM systems. – IEEE/RSJ International Conference on Intelligent Robots and Systems (IROS): 573–580.

Tomić, T., Schmid, K., Lutz, P., Domel, A., Kassecker, M., Mair, E., Grixa, I., Ruess, F., Suppa, M. & Burschka, D., 2012: Toward a fully autonomous UAV: Research platform for indoor and outdoor urban search and rescue. – Robotics Automation Magazine, IEEE **19** (3): 46–56.

Urmson, C., Anhalt, J., Bae, H., Bagnell, J.A.D., Baker, C.R., Bittner, R.E., Brown, T., Clark, M.N., Darms, M., Demitrish, D., Dolan, J.M., Duggins, D., Ferguson, D., Galatali, T., Geyer, C.M., Gittleman, M., Harbaugh, S., Hebert, M., Howard, T., Kolski, S., Likhachev, M., Litkouhi, B., Kelly, A., Mcnaughton, M., Miller, N., Nickolaou, J., Peterson, K., Pilnick, B., Rajkumar, R., Rybski, P., Sadekar, V., Salesky, B., Seo, Y.-W., Singh, S., Snider, J.M., Struble, J.C., Stentz, A.T., Taylor, M., Whittaker, W.R.L., Wolkowicki, Z., Zhang, W. & Ziglar, J., 2008: Autonomous driving in urban environments: Boss and the urban challenge. – Journal of Field Robotics Special Issue on the 2007 DARPA Urban Challenge, Part I, **25** (8): 425–466.

Addresses of the Authors:

David Droeschel, Dirk Holz & Prof. Dr. Sven Behnke, Autonomous Intelligent Systems Group, Computer Science Institute VI, University of Bonn, Friedrich-Ebert-Allee 144, D-53113 Bonn, e-mail {droeschel}{holz}@ais.uni-bonn.de, behnke@cs.uni-bonn.de

Manuskript eingereicht: Januar 2014
Angenommen: Juli 2014

# Berichte von Veranstaltungen

## Gemeinsame Jahrestagung von DGPF, DGfK, GfGI und GiN, 26. – 28. März 2014, Hamburg

Unter dem Motto „Geoinformationen öffnen das Tor zur Welt“ fanden der 62. Deutsche Kartographentag der DGfK, die 34. Wissenschaftlich-Technische Jahrestagung der DGPF, die Geoinformatik 2014 der GfGI und des GiN an der Hafen City Universität Hamburg (HCU) vom 26. bis zum 28. März 2014 statt.

Das wissenschaftliche Tagungsprogramm und eine Fachfirmenausstellung wurden durch Workshops, Tutorien und ein Rahmenprogramm abgerundet. Die Tagung war mit 540 Teilnehmern aus 12 Ländern sehr gut besucht. Insgesamt 25 ausstellende Fachfirmen und Fachbehörden zeigten ihre neuesten Entwicklungen im Foyer des Neubaus der HCU. Neben den Ausstellern unterstützten weitere fünf Organisationen die Tagung.

Die Tagung wurde vor Ort von Thomas Kersten und Jochen Schiewe in Zusammenarbeit mit der Geomatik Tagungs-GmbH unter der Leitung von Klaus Komp und einem kleinen Team der vier Gesellschaften mit Monika Sester, Christian Heipke, Bernhard Horst, Herbert Krauss und Eberhard Gülch organisiert.

Die gesamte Tagung war zweigeteilt. Sie bestand aus dem GI-Anwendertag am 26.3.2014 und der Gemeinsamen Jahrestagung am 27.3. und 28.3.2014.

### *GI-Anwendertag, Ausstellung und Workshops der Fachfirmen, Tutorien und Mitgliederversammlungen am 26.3.2014:*

Der *GI-Anwendertag* – mit Vorträgen zu „GI-Anwendungen in Wirtschaft und Verwaltung“ und Fachfirmen-Ausstellung wurde von Manfred Ehlers, Präsident des GiN, am Morgen des 26.3. vor fast 200 Teilnehmern eröffnet. Als eingeladener Vortragender informierte Wernher Hoffmann, Präsident des BEV – Bundesamt für Eich- und Vermessungswesen, Österreich, über Preise und Lizenzen für Geodaten am Beispiel Österreichs.

Anschließend konnten die Teilnehmer vier GI-Sitzungen mit insgesamt 12 Fachvorträgen sowie eine Postersession besuchen. Parallel dazu wurde ein DGfK-Workshop für Nachwuchswissenschaftler unter Leitung von Jochen Schiewe und ein DGPF-Tutorium mit dem Thema *Der Weg zum detaillierten 3D-Gebäudemodell* unter Leitung von Thomas Kersten angeboten.

Während des gesamten Tages war das Foyer mit den Ständen der Fachfirmen- und Fachbehörden zu besuchen, wobei parallel dazu eine große Anzahl der Aussteller ihre Entwicklungen in insgesamt 25 Workshops präsentieren konnten. Die drei angebotenen Exkursionen (s.u.) waren sehr gut besucht und fanden ebenfalls am Mittwochnachmittag statt.

Für die DGfK, die DGPF und den GiN wurden anschließend die ordentlichen Mitgliederversammlungen durchgeführt.

### *Gemeinsame Jahrestagung und Fachfirmenausstellung vom 27. bis zum 28.3.2014:*

Der Präsident der DGfK, Manfred Weisensee, begrüßte vor über 250 Teilnehmern Ehrengäste, Ehrenmitglieder und Teilnehmer und eröffnete die Gemeinsame Tagung 2014 der DGfK, der DGPF, der GfGI und des GiN.

Senatorin Dorothee Stapelfeld, die Zweite Bürgermeisterin und Senatorin für Wissenschaft und Forschung der Freien und Hansestadt Hamburg, überbrachte Grußworte und betonte die große Bedeutung dieser ersten Veranstaltung im gerade bezogenen Neubau der HCU Hamburg. Walter Pelka, Präsident der HafenCity University Hamburg, hob die enormen Anstrengungen des lokalen Organisationsteams und der gesamten HCU hervor, damit die Veranstaltung wie geplant im Neubau der HCU stattfinden konnte.

Im Rahmen der Eröffnungsveranstaltung fand auch die feierliche Verleihung des Hansa-Luftbild-Preises statt, die von Paul Hartfiel, Vorstandsmitglied der Hansa Luftbild AG,


DOI: 10.1127/1432-8364/2014/0237 1432-8364/14/0237 $ 6.50

vorgenommen wurde. Der Preis wurde an Richard Steffen für seine Arbeit *A Robust Iterative Kalman Filter Based On Implicit Measurement Equations* verliehen. Der Beitrag erschien in Heft 4/2013 der PFG. Die Auszeichnung ist mit 1500 EUR dotiert und wurde in diesem Jahr zum 40. Mal verliehen.

Der Plenarvortrag von Sebastian Saxe, Hamburg Port Authority (HPA) mit dem Titel *Hamburger Hafen – Jeden Tag intelligenter – Geodaten öffnen das Tor zur Welt* widmete sich der faszinierenden Welt des Hafens mit seinen enormen logistischen Herausforderungen und der herausragenden Bedeutung für die Hansestadt.

Im Anschluss an die Eröffnungsveranstaltung eröffneten Frau Senatorin Dorothee Stapelfeldt, begleitet von Walter Pelka und den Präsidenten der vier Gesellschaften, Manfred Weisensee, Thomas H. Kolbe, Manfred Ehlers und Klaus Greve, offiziell die Ausstellung mit einem Rundgang.

Am 27.3. und 28.3.2014 wurden Schwerpunkte des Tagungsprogramms in drei Plenarsitzungen durch Keynote-Vorträge von Stefan Hinz, KIT Karlsruhe (Thema: *Bildbasierte Egomotion-Bestimmung für Augmented Reality in dynamischen Szenen*), Georg Gartner, TU Wien und Präsident der International Cartographic Association (Thema: *Über die Rolle der modernen Kartographie*) und Jan-Henrik Haunert, Universität Osnabrück (Thema: *Graphen als gemeinsame Grundlage der Vektor- und Rasteranalyse*) vorgestellt.

An beiden Tagen sah das Programm in 19 Sitzungen insgesamt 76 Fachvorträge zu einem breiten Spektrum von Themen der drei Gesellschaften vor. Die Postersession der gemeinsamen Tagung wurde durch einen eigenen Sitzungsblock deutlich hervorgehoben und war sehr gut besucht. Über 40 Poster wurden präsentiert. Zehn Poster waren für die Endausscheidung des Karl-Kraus-Nachwuchsförderpreises vorgesehen, der dann am Abend des 28.3. verliehen wurde.

In der Closing Session wurde ein positives Fazit der ersten Veranstaltung in dieser Konstellation durch die Präsidenten der vier Gesellschaften gezogen. Nach dem Dank an das lokale Organisationsteam unter Leitung von Thomas Kersten und Jochen Schiewe wurden auch die Herren Uwe Breitkopf, Leibniz Uni-

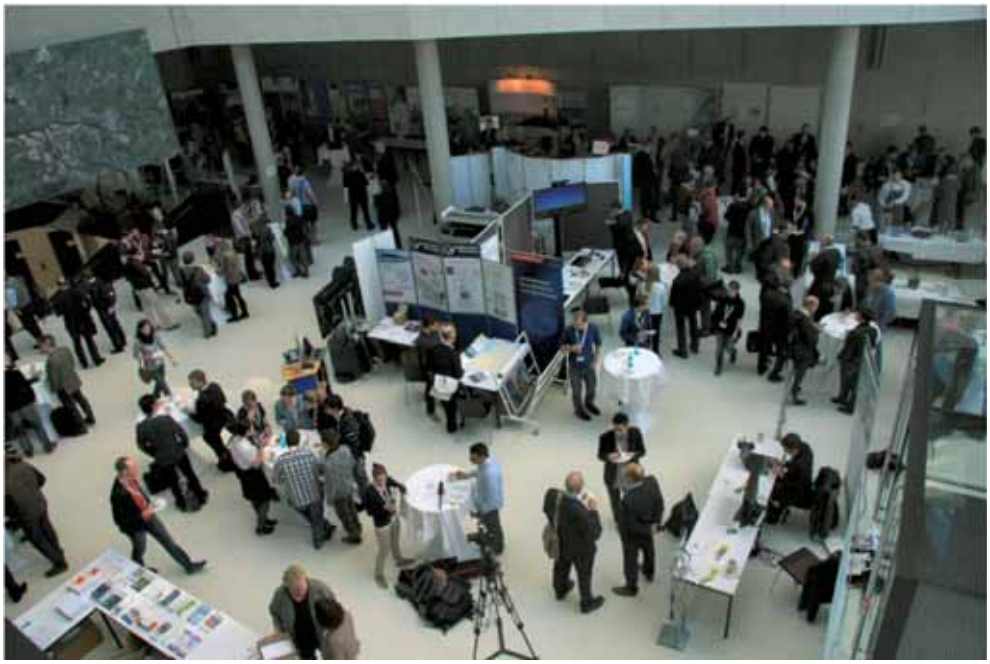

Das gut besuchte Foyer mit der Ausstellung (© Klaus Komp).

versität Hannover, und Tobias Schwarz aus Berlin für die herausragende Unterstützung in der Erstellung der On-Line-Proceedings bzw. für die tatkräftige Mithilfe während der Tagung mit einem kleinen Geschenk bedacht.

### *Exkursionen und Rahmenprogramm mit Preisverleihung*

Bereits am Abend des 25.3.2014 trafen sich über 70 Teilnehmer zu einem gemütlichen Beisammensein in der Gröninger Privatbrauerei in der Innenstadt. Am 26.3.2014 fanden eine gut besuchte Exkursion zum Landesbetrieb Geoinformation und Vermessung Hamburg und zwei Exkursionen zur Vorstellung der Hamburg Port Authority (HPA) mit Besichtigung des Multi-Sensor-Schiffes der HPA im Magdeburger Hafen statt. Beim anschließenden zwanglosen Abendtreff im Block Bräu an den Landungsbrücken pflegten über 230 Teilnehmer in entspannter Atmosphäre den fachlichen Austausch.

Bei der Abendveranstaltung am 27. März im Emporio setzten die über 200 Teilnehmer im festlichen Rahmen das (Social-)Networking bis in die späten Nachtstunden fort. Als Neuheit wurden bei dieser Veranstaltung zunächst alle zehn Kandidaten und dann die Preisträger des Karl-Kraus-Nachwuchsförderpreises 2014 für Photogrammetrie, Fernerkundung und Geoinformation in Anwesenheit von Frau Kraus geehrt. Der Preis wird gemeinsam von DGPF, OVG und SGPF verliehen. Ebenso wurden zwei GfGI-Preise verliehen. Den gelungenen Abschluss bildete nach der Closing Session am Freitag ein Farewell-Umtrunk im Foyer der HCU.

Allen Autoren, Gutachtern und Sitzungsleitern sei gedankt für die Gestaltung des Vortragsprogramms und allen Fachfirmen und Fachbehörden für das breite Spektrum an Entwicklungen, das auf der Tagung präsentiert wurde. Den vielen helfenden Händen, die bei Auf- und Abbau, bei Ausstellung, im Tagungsbüro und den Sitzungen geholfen haben, sei großer Dank geschuldet. Zuletzt ein besonderer Dank an alle Organisationen, die mit ihrer großzügigen finanziellen Unterstützung die Tagung erst möglich gemacht haben.

Für das Organisationsteam
Eberhard Gülch, Jochen Schiewe &
Herbert Krauss

Die zehn Finalisten für den Karl-Kraus-Nachwuchsförderpreis mit Frau Kraus, Vertretern der Jury und der Vorstände (© Klaus Komp).

## 10. GIS Ausbildungstagung, 12. – 13. Juni 2014, Potsdam

Am 12. und 13. Juni 2014 fand in Potsdam die zehnte Veranstaltung zur GIS-Aus- und Weiterbildung mit über 50 Teilnehmern statt. Jochen Schiewe ließ in seiner Eröffnung der Veranstaltung die zehn Jahre nochmals Revue passieren. Die Teilnehmerzahl hat sich in den letzten Jahren bei 50 bis 60 eingependelt. Die Themenbereiche haben über die Jahre immer wieder variiert. Am konstantesten waren die Themen Hochschulausbildung und GIS an Schulen. E-Learning erlebte einen Boom in den Jahren 2005 bis 2010, also gegen Ende einer intensiven Förderphase besonders durch das BMBF. Seit der Verabschiedung der neuen Ausbildungsberufe im Geoinformationswesen, speziell des Geomatikers, spielen Vorträge zur Berufsausbildung eine zunehmende Rolle. Schiewe gedachte in seiner Rede auch des im letzten Jahr verstorbenen Bernhard Harzer, der sich als Mitinitiator der Veranstaltung alle Jahre intensiv in die Organisation, Durchführung und Diskussion eingebracht hat. Er begrüßte zudem Christoph Harzer als Nachfolger in der Geschäftsführung des Harzer Verlags, der sich nun in die Ausbildungstagung einbringen wird. Auch in diesem Jahr fand zuvor ein Esri-Workshop statt.

Wie schon in den Vorjahren dominierte die Hochschullehrergruppe mit fast 60%. Die zweitstärkste Teilnehmergruppe kam aus der öffentlichen Verwaltung. Auffallend viele junge Teilnehmer unterstrichen das Interesse des wissenschaftlichen Nachwuchses an Ausbildungsthemen.

Im Keynote-Vortrag stellte der Geschäftsführer Landesvermessung und Geobasisinformation Brandenburg Christian Killiches den Zusammenhang zwischen einerseits dem Aufbau der Geodateninfrastruktur Brandenburg und andererseits der Rolle der neuen


Organisatoren der 10. GIS-Ausbildungstagung: Von links nach rechts Gerd König (TU Berlin), Ralf Bill (Uni Rostock), Matthias Möller (Beuth Hochschule Berlin), Christoph Harzer (Harzer Verlag Karlsruhe), Joachim Wächter (GFZ Potsdam) und Jochen Schiewe (HCU Hamburg).

Geomatiker beim GDI-Aufbau her. Gleichzeitig wies er darauf hin, dass intensive Bemühungen notwendig sind, um dem sich abzeichnenden Fachkräftemangel auf allen Ebenen in der Verwaltung zu begegnen.

In dieser Veranstaltung wurden wie auch schon in den vergangenen Jahren Aus- und Weiterbildungsthemen im Umfeld der Geoinformatik fächerübergreifend diskutiert und Erfahrungen ausgetauscht, wobei sich die gut 15 Vorträge um die Schwerpunkte *Schulen* und *Hochschulen* gruppierten. Als neues Thema wurde *Forschungsdateninfrastrukturen* in zwei Beiträgen durch Ralf Bill und Joachim Wächter vorgestellt. Beide wiesen darauf hin, dass dies neue Anforderungen in der Ausbildung bedeutet und der Geoinformatik hier eine prominente Rolle zukommen kann, da viele der Daten einen Raumbezug haben.

- GIS an Schulen: Vorgestellt wurden verschiedene Schulprojekte und neue Ansätze, z.B. ArcGIS-online für den Schuleinsatz. Die heutige digital groß gewordene Schülergeneration ist z.B. über Smartphones leicht in der Lage, Geodaten zu generieren, und damit auch motiviert, sich dem Thema GIS zu nähern.
- GIS in der Hochschulausbildung: Präsentiert wurden erste Ansätze zum mobilen Mikrolernen an der Universität Salzburg, indem kleine vorgefertigte „Wissenshäppchen" quizartig dem Studierenden auf seinem Smartphone zu jeder beliebigen Gelegenheit angeboten werden. Ein Beitrag der ETH Zürich zeigte, wie in Exkursionen ebenfalls eingebunden durch kleine Aufgaben, die mittels Smartphone gelöst werden können, Erfahrungen mit raumbezogenen Daten und Fragestellungen praktisch so nebenbei gewonnen werden können. Ralf Bill stellte eine Übersicht und Auswertung der GIS-Studiensituation im deutschsprachigen Bereich vor (Vgl. hierzu den Beitrag in Heft 4 gis.SCIENCE). de Lange referierte über erste Ideen aus einem Diskussionsprozess der Gesellschaft für Geoinformatik zu einem Kerncurriculum für das Nebenfach Geoinformatik.

Das GFZ-Team sorgte mit einer perfekten Organisation wie schon in den vergangenen Jahren für ein angenehmes Ambiente auf dem Telegrafenberg, zu dem auch das gute Wetter und das abendliche Buffet beitrugen. Viel Zeit blieb wie immer für Diskussionen, welches ebenfalls ein Kennzeichen dieser Veranstaltung ist.

Die Beiträge standen, wie auch schon in den Vorjahren auf einer CD gesammelt, zur Konferenz bereit. Weitere Informationen sind unter http://gis.gfz-potsdam.de/ zu finden.

Die Veranstalter setzen die Reihe mit alten und neuen Schwerpunkten im nächsten Jahr am 18. und 19. Juni fort, erneut begleitet durch einen Esri-Workshop sowie vermutlich auch angebunden an einen internationalen ISPRS-Workshop.

Ralf Bill, Rostock

# Berichte der Arbeitskreise der DGPF

## Arbeitskreis Aus- und Weiterbildung

### Arbeitsgebiete – Terms of Reference

- Beobachtung von Aus- und Weiterbildungsangeboten
- Beobachtung und Bewertung neuer Lehr- und Lernmethoden
- Förderung des wissenschaftlichen Nachwuchs
- Nationale und internationale Kooperationen
- Beobachtung von Maßnahmen zur Schülerberufsinformation im Umfeld der Gesellschaft

### Bericht von der Jahrestagung

Während der 34. Wissenschaftlich-Technischen Jahrestagung der DGPF fand eine Session des Arbeitskreises „Aus- und Weiterbildung" mit vier Vorträgen statt. Die Vortragenden beschäftigten sich zum einen mit der um-

fassenden Darstellung, was Geoinformatik grundsätzlich ausmacht, und zum anderen mit drei unterschiedlichen Ebenen der Vermittlung von Wissen über Geoinformatik, Fernerkundung und Kartographie:

Wolfgang Reinhardt (UniBw München) berichtete über aktuelle Arbeiten zur Bedeutung und inhaltlichen Gestaltung eines „Body-of-Knowledge“ (BoK) für die Geoinformatik. Roland Goetzke (Universität Bonn) stellte das Lernportal „Fernerkundung in Schulen“ (FIS, www.fis.uni-bonn.de) vor. Diese Internetplattform soll einen leichten Zugang für Lehrer und Schüler zu Themen der Fernerkundung ermöglichen. Erik Theile (Landesvermessung und Geobasisinformation Brandenburg) analysierte die Situation der Geomatikerausbildung in Brandenburg unter dem Aspekt der Umstellung der Ausbildungsordnung hin zur Trennung von Vermessungstechniker- und Geomatikerausbildung. Abschließend berichtete Gertrud Schrab (Hochschule Karlsruhe – Technik und Wirtschaft) über den Wandel in der Kartographie-Ausbildung an der Hochschule Karlsruhe.

Die große Zahl der Besucher und die rege Diskussion nach den Vorträgen fielen in diesem Jahr besonders auf. In Anbetracht des demographischen Wandels und der ständigen Veränderungen in den Schulsystemen der Länder rückt die Frage der strukturellen wie auch inhaltlichen Gestaltung von Ausbildung und auch die Bewerbung unserer Berufsfelder wieder stärker in den Vordergrund.

Als Novum fand in diesem Jahr eine Postersession zur Verleihung des Karl-Kraus-Nachwuchsförderpreises statt. Entsprechend der neuen Regularien wurden zehn Bewerber eingeladen, Poster zu ihren Abschlussarbeiten einzureichen. Diese wurden von einer Bewertungskommission, die durch Vertreter aller drei Gesellschaften besetzt wurde, besucht. Als Preisträger wurden in diesem Jahr ausgewählt und auf der Abendveranstaltung des Kongresses prämiert:

1. Preis: Corinna Harmening (Universität Hannover – Betreuer: Prof. Dr. Brenner) Thema: „Raumzeitliche Segmentierung von natürlichen Objekten in stark verdeckten Szenen“ (1.500 EUR)

2. Preis: Fabian Schneider (Universität Zürich – Betreuer Prof. Dr. Schaepmann) Thema: „Simulating imaging spectrometer data: 3D forest modeling based on LiDAR and in situ data“ (1.000 EUR)

3. Preis: Niklas Conen (Hochschule Oldenburg – Betreuer: Prof. Dr. Luhmann) Thema: „Entwicklung einer modellbasierten Eigenbewegungsschätzung eines Kraftfahrzeugs aus Fahrzeugbewegungsdaten und optischen Flussvektoren“ (500 EUR)

An anderer Stelle in der PFG erhalten die Preisträger die Gelegenheit, ihre Arbeiten vorzustellen (Seite 484–488).

Während der Session des Arbeitskreises wurde der erste Vorsitz des Arbeitskreises Aus- und Weiterbildung von Görres Grenzdörfer an Ansgar Brunn übergeben. Ansgar Brunn bedankte sich bei Görres Grenzdörfer für die langjährige erfolgreiche Leitung des Arbeitskreises.

## Weitere und geplante Aktivitäten

Die in 2013/2014 festgelegten neuen Regularien haben sich weitgehend bewährt. Dennoch werden kleinere Anpassungen der Ausschreibung diskutiert. Einzelheiten werden mit der neuen Ausschreibung im Herbst 2014 bekannt gegeben.

Der Arbeitskreis will sich zukünftig noch mehr an Aus- und Weiterbildungen im Bereich der Themen der DGPF beteiligen. Dies soll durch eine verstärkte Zusammenarbeit mit inhaltlich verbundenen Berufsverbänden erfolgen. Neu ist die Beteiligung des Arbeitskreises am 7. Anwenderforum „Laserscanning: Projektbezogene Auswertestrategien beim Terrestrischen Laserscanning – Software, Methoden, Lösungen“ am 7.11.2014 in Würzburg.

Neben der DGPF-Jahrestagung ist die mittlerweile 11. GIS-Ausbildungstagung am 18./19.6.2015 in Potsdam ein weiteres Highlight, bei dem sich viele Mitglieder des Arbeitskreises treffen und austauschen werden.

Görres Grenzdörfer, Rostock
Ansgar Brunn, Würzburg

## Arbeitskreis Optische 3D-Messtechnik

### Arbeitsgebiete – Terms of Reference

- Nahbereichsphotogrammetrie
- Terrestrisches Laserscanning
- Sensorintegration und Systemkalibrierung
- Aufnahme- und Auswertestrategien
- Prozessorientierte Auswertung und Automation
- 3D-Modellierung

### Bericht von der Jahrestagung

An der 34. wissenschaftlich-technischen DGPF-Tagung an der HafenCity Universität Hamburg konnte sich der Arbeitskreis durch zwei Sitzungen am 26. und 27. März präsentieren. Da in diesem Jahr die Tagung durch die drei Gesellschaften DGfK, DGPF und GfGI ausgerichtet wurde, wurden aktuelle Schwerpunktthemen festgelegt, die die Arbeitsgebiete der drei Fachgesellschaften gut abdecken. Acht Beiträge wurden in den beiden Sitzungen mit den Schwerpunktthemen *Punktwolken aus Laserscanning und Bilddaten und Neue Sensoren* vorgestellt. Ca. 70 Teilnehmer nahmen an der 1. Sitzung über Punktwolken teil, während sich ca. 50 Interessierte in der zweiten Sitzung am Freitag über die neuen Sensoren informierten.

Die erste Sitzung wurde mit einem Beitrag von Alexander Schlichting und Claus Brenner (Leibniz Universität Hannover) eröffnet. In diesem Beitrag wurde in Untersuchungen gezeigt, dass Automotive-Laserscanner für eine Fahrzeuglokalisierung durch stangenförmige Objekte und durch Ebenen, die vorher durch Mobile-Mapping-Systeme als Grundlage erfasst wurden, in Stadtgebieten geeignet sind. In dem zweiten Beitrag stellten Danilo Schneider, Maria Leonhardt und Volker Frevert (TU Dresden) ihre Untersuchungen zur simultanen GNSS-gestützten Positionsbestimmung (Registrierung) der Scanner-Standpunkte während des Scanvorganges vor. Anhand von signalisierten Kontrollpunkten konnte gezeigt werden, dass die GNSS-gestützte Scan-Registrierung mit einer Genauigkeit von 1–2 cm eine sehr einfache und effiziente Möglichkeit der globalen Registrierung von Punktwolken darstellt. Die stabile Orientierung von Stereokamerasystemen stellt bei der photogrammetrischen Crash-Test-Vermessung immer noch eine große Herausforderung dar, weil durch die auftretenden Kräfte während eines Crash-Tests Deformationen am Objekt und am Aufnahmesystem auftreten. Folkmar Bethmann (Co-Autoren Christian Jepping, und Thomas Luhmann, Jade Hochschule Oldenburg) präsentierten anhand von synthetischen und realen Datensätzen eine Methode, mit der nach Analyse der Oberflächendeformationen mithilfe eines RANSAC-basiertes Verfahren stabile Bereiche (Kongruenzanalyse) detektiert werden, die für eine stabile Orientierung des Stereo-Aufnahmesystems verwendet werden können. Das Autorenteam Sebastian Tuttas, Alexander Braun, André Borrmann und Uwe Stilla (TU München) stellten ein Konzept zur automatischen Baufortschrittskontrolle für eine mögliche Optimierung von Bauprozessen bei einem mehrstöckigen Haus im innerstädtischen Raum von München vor, bei dem durch Zuordnung eines Building Information Models und photogrammetrisch erzeugter temporaler Punktwolken der Baufortschritt dokumentiert und kontrolliert werden kann. Die Georeferenzierung erfolgte über Passpunkte und über Ebenen von bereits erstellten Bauteilen.

Am Freitag, dem 28.3., fand die zweite Sitzung des Arbeitskreises unter der Überschrift „Neue Sensoren“ statt. Nachdem in den letzten Jahren unter anderem Time-of-Flight-Kameras als neue Aufnahmesensoren eine große Rolle gespielt haben, rückten in diesem Jahr plenoptische Kameras, auch als Lichtfeldkameras bezeichnet, stärker in den Fokus. So wurden gleich zwei Beiträge präsentiert, die sich mit der Kalibrierung und dem Genauigkeitspotenzial dieser Sensoren beschäftigen: Im Beitrag von Niclas Zeller, Franz Quint und Uwe Stilla (TU München) wurden drei unterschiedliche Ansätze zur Kalibrierung von Lichtfeldkameras vorgestellt und miteinander verglichen. Im weiteren Beitrag von Thomas Luhmann, Christian Jepping und Benjamin Herd (Jade Hochschule Oldenburg) wurde die messtechnischen Leistungsfähigkeit der Lichtfeldkameras diskutiert.

Weiterhin präsentierte Christian Mulsow (TU Dresden) ein optisches Verfahren zur Erfassung von bewegten Wasseroberflächen, welches eine Erweiterung des klassischen

Verfahrens der optischen Triangulation darstellt. Dabei wird ausgenutzt, dass die Laserlichtschicht nach Reflexion an der eigentlichen Objektoberfläche auf zwei weitere Ebenen projiziert wird. Abgerundet wurde die Sitzung mit einem Vortrag von Franz Kurz vom DLR über ein echtzeitfähiges optisches Sensorsystem auf einem Hubschrauber für Einsätze bei Katastrophen, Großereignissen und anderen Überwachungsaufgaben. Dieses System basiert auf handelsüblichen High-End-Kleinbildkameras, die je nach Anwendung unterschiedlich konfiguriert werden können, zusätzlich auch nIR-Strahlung erfassen und 4K-Videos aufnehmen kann. Insgesamt wurde die zweite Sitzung ihrem Titel mehr als gerecht, weil die messtechnische Nutzung neuer Sensorik, die Weiterentwicklung klassischer Verfahren und die Kombination konventioneller Kameras zu einem neuartigen Echtzeitsystem vorgestellt worden ist.

Somit war das Vortragsprogramm des Arbeitskreises wieder sehr abwechslungsreich. Die Sitzungen waren gut besucht und die Beiträge wurden sehr intensiv diskutiert.

### Weitere und geplante Aktivitäten

- Das ISPRS-Symposium der technischen Kommission V *Close-Range Imaging, Analysis and Applications* fand am Gardasee in Riva del Garda (Italien) vom 23. bis zum 25. Juni 2014 statt (http://isprs-commission5.fbk.eu/).
- Am 2. und 3. Dezember 2014 wird die Fachtagung *LowCost3D - Sensors, Algorithms, Applications* an der Technische Universität Berlin veranstaltet (http://www.lc3d.net).
- Am 4. und 5. Februar 2015 werden die *14. Oldenburger 3D-Tage* stattfinden, bei denen der Arbeitskreis Optische 3D-Messtechnik als Mitveranstalter mitwirken wird (www.jade-hs.de/3dtage).
- Weitere Infos über relevante Veranstaltungen sind auf der Webseite des Arbeitskreises zu finden: www.dgpf.de/neu/dgpf/nahbereich.htm

Thomas Kersten, Hamburg und Danilo Schneider, Dresden

## Arbeitskreis Bildanalyse und Bildverstehen

### Arbeitsgebiete – Terms of Reference

- Geometrische Bildverarbeitung
- Merkmalsextraktion und –nutzung
- Semantische Modellierung

### Bericht von der Jahrestagung

Während der 34. wissenschaftlich-technischen DGPF-Tagung an der HafenCity Universität Hamburg, die vom 26. bis zum 28. März 2014 zusammen mit dem 62. Deutschen Kartographentag der DGfK, der Geoinformatik 2014 der GfGI und des GIN stattfand, wurden o.g. Arbeitsgebiete des Arbeitskreises in drei Sitzungen behandelt.

Die erste Sitzung zum Thema *Objektrekonstruktion aus Bilddaten und Punktwolken* wurde durch einen Beitrag von Wolfgang Förstner, in dem er sich mit der *Gruppierung unsicherer geometrischer Primitive* beschäftigte, eröffnet. Paul Rawiel stellte Arbeiten zur *Entwicklung und Implementierung von Algorithmen zur Merkmalsdetektion in 3D-Laserscanpunktwolken nach der Multiskalenstrategie* am Beispiel von Nahbereichsanwendungen / terrestrischem Laserscanning vor. Die *Automatisierte 3D Rekonstruktion von Gebäudeszenen aus 3D Punktwolken* war das Thema des Beitrages von Henry Meissner. Die genutzten Punktwolken wurden auf der Basis von Daten schrägaufnehmender Luftbildkameras abgeleitet. Den Abschluss dieser Sitzung bildete ein Vergleich von Softwarepaketen mit dem Titel *3D-Rekonstruktion von Objekten mittels Structure-from-Motion aus einer photogrammetrischen Aufnahme mit den Programmen VisualSFM und CMPMVS* von Marius Ziegler.

Die zweite Sitzung widmete sich dem Thema *Dense Image Matching*. Stephan Nebiker beschäftigte sich in seinem Beitrag mit *Untersuchungen zur Generierung historischer Oberflächenmodelle mittels Dense Image Matching und zu deren Nutzung für objektbasierte Veränderungsanalysen*. Dieses Thema wurde durch den Beitrag von Stefan Cavegn mit dem Titel *Dense Image Matching mit Oblique Luftbildaufnahmen – Ein systematischer Vergleich verschiedener Lösungen mit Auf-*

*nahmen der Leica RCD30 Oblique Penta* fortgeführt und die Thematik der Auswertung von Schrägluftbildern aus der ersten Sitzung wieder aufgenommen. Zum Programm dieser Sitzung gehörte ebenfalls der Beitrag *Integration von objektspezifischem Modellwissen in die dichte Bildzuordnung* von Moritz Menze. Den Abschluss bildete der Vortrag von Alessandro Cefalu zur *Multivariaten Kerndichteschätzung zur Filterung automatischer Punktzuordnungen*.

Die dritte Sitzung fasste Arbeiten zum Thema *Lernen und Zufallsfelder* zusammen. Sebastian Wuttke beschäftigte sich in seinem Beitrag mit der *Bewertung von Strategien des aktiven Lernens am Beispiel der Landbedeckungsklassifikation* mit dem Ziel der Selektion von Trainingsdaten. Die Nutzung von Conditional Random Fields stand dann im Mittelpunkt der nächsten beiden Vorträge von Tessio Novack mit dem Titel *Discriminative learning of Conditional Random Fields applied for the classification of urban settlement types* und von Lena Albert zur *Klassifikation der Bodenbedeckung in urbanen Gebieten mittels Conditional Randem Fields*. Zum Abschluss der Sitzung wurde von Anne Bienert eine anwendungsorientierte Arbeit zur *Segmentierung von Entfernungsbildern zur Registrierung von Laserscannerpunktwolken in Waldbeständen* vorgestellt.

Zusammenfassend ist festzuhalten, dass das Vortragsprogramm des Arbeitskreises wieder sehr abwechslungsreich war und ein breiter Themenfächer aufgespannt wurde. Es ist zu begrüßen, dass viele jüngere Kollegen das Forum des Arbeitskreises nutzen. Die gut besuchten Sitzungen überzeugten durch intensive Diskussionen. Bleibt zum Abschluss noch zu vermerken, dass Corinna Harmening von der Universität Hannover mit ihrer Arbeit zum Thema *Raumzeitliche Segmentierung von natürlichen Objekten in stark verdeckten Szenen* die Gutachter des Karl-Kraus-Nachwuchsförderpreises überzeugen konnte.

Uwe Weidner, Karlsruhe

## Arbeitskreis Hyperspektrale Fernerkundung

### Arbeitsgebiete – Terms of Reference

- Innovative Methoden und Verfahren in der hyperspektralen Fernerkundung
- Qualitative und quantitative Probleme der Datenerhebung
- Abbildende und nicht-abbildende Spektrometer
- Multimediale Wissenskommunikation und Visualisierung von Forschungsergebnissen

### Bericht von der Jahrestagung

Der Arbeitskreis Hyperspektrale Fernerkundung hatte bei der diesjährigen Jahrestagung der DGPF in Hamburg eine Sitzung unter dem Namen „Fernerkundung für Planung und Umweltmonitoring“. Die Vielfältigkeit der Anwendungs- und Forschungsgebiete der eingereichten Beiträge hat die Neustrukturierung und Umbenennung der Sitzung begründet. Die diesjährigen Beiträge zeigten Forschungsergebnisse aus den Bereichen der Bodenspektroskopie, Stadtfernerkundung, Raumplanung sowie Naturgefahren durch Erdrutschungen. Leider musste die Sitzung wegen mehreren Absagen gekürzt werden. Im Folgenden wird ein kurzer Überblick über die gehaltenen Vorträge gegeben.

Der erste Vortrag der Sitzung war ein Beitrag von András Jung (Universität Leipzig), der über die bodenkundliche Anwendung einer hyperspektralen „snapshot“-Kamera berichtet hat. Benjamin Bechtel (Universität Hamburg) hat seine Ergebnisse im Bereich der satellitengestützten Lufttemperaturbestimmung im städtischen Raum vorgestellt und deren anwendungsorientierten Möglichkeiten diskutiert. Michael Nolde (Christian-Albrechts-Universität) präsentierte ein räumliches Entscheidungsunterstützungssystem für Raumplanung im geologischen Untergrund, das bei der Ausweisung von Vorrangflächen für die Errichtung von unterirdischen Energiespeichern helfen soll. Frau Darya Golovko (Geoforschungszentrum Potsdam) schloss die Sitzung schließlich mit den Aspekten der Erdrutschung und deren fernerkundliche und GIS-basierte Kartierung in Kirgistan.

Wir bedanken uns bei allen Teilnehmern für ihre Beiträge, ihr Interesse an den Aktivitäten des Arbeitskreises sowie die lebhaften Diskussionen.

András Jung, Leipzig
Jonas Franke, München

## Arbeitskreis Radarfernerkundung und Flugzeuglaserscanning

### Arbeitsgebiete – Terms of Reference

- Synthetic Aperture Radar (SAR)
- SAR-Interferometrie und -Polarimetrie
- 3D-Objekterkennung aus Laserscannerdaten
- Vegetationsanalyse aus Laserscannerdaten

### Bericht von der Jahrestagung

In diesem Jahr wurden die Sitzungen der Jahrestagung nicht nach Arbeitskreisen sondern thematisch gegliedert. Infolgedessen verteilten sich die 11 Beiträge, welche sich mit Radarbildern und Flugzeuglaserscannerdaten befassten, auf vier Vortrags- und die gemeinsame Postersitzung.

Im Bereich der Radarfernerkundung fiel auf, dass sich immerhin 3 Beiträge der Auswertung von Daten flugzeuggestützter Sensoren widmeten. Stephan Palm (Fraunhofer FHR) stellte ein Verfahren zur Echtzeitprozessierung von videoartigen SAR-Bildern vor, das für die Erfassung großer Flächen in kurzer Zeit gedacht ist. Das Potential von Millimeterwellenradar zur Erkennung von Bäumen wurde von Oliver Maksymiuk (TU München) diskutiert. Mittels sogenannter morphologischer Attributfilter gelingt es, Baumgruppen in einzelne Bäume zu zerlegen. Julia Stockamp (DLR) nutzt neben Satellitendaten auch multi-frequente Flugzeug-SAR-Daten, um Schneeflächen zu analysieren. Rein auf satellitengestützten SAR-Daten fußten weitere 5 Beiträge, wovon 4 Zeitreihen von Bildern zu verschiedenen Zwecken auswerteten. So deckte Julia Jaenicke (LMU) anhand von Bildern des TerraSAR-X sowie ersten Höhenmodellen der laufenden Mission TanDEM-X Veränderungen an Vulkanen in Island auf. Ebenfalls auf TerraSAR-X griff Li Fang (TU München) zurück, der ein Verfahren zur Erkennung der Bewegungsmuster von Gletschern vorstellte. Sigrid Roessner (GFZ) schließlich überwachte mittels SAR-Bildern unterschiedlicher Sensoren Hangrutschungen in Kirgisien. Die Berücksichtigung von Einflüssen der Atmosphäre ist wichtig, um hohe geometrische Genauigkeiten zu erzielen, wie der Beitrag von Christoph Gisinger (TU München) zeigt, der GNSS-Daten zur Korrektur verwendet.

Im Bereich des Flugzeuglaserscannings widmeten sich 2 Beiträge der Küste, die beide von Mitarbeitern der Leibniz Universität Hannover präsentiert wurden. Alena Schmidt stellte eine Methode zur Änderungserkennung im Wattenmeer aus Zeitreihen von Höhenmodellen vor. Über ein Projekt zur Laserbathymetrie in der Ostsee berichtete Joachim Niemeyer. Es zeigt sich, dass mit dieser Technik gerade in Flachwasserbereichen sehr gute Ergebnisse erzielt werden können.

Zwei weitere Beiträge befassten sich mit Wäldern. Przemysław Polewski (Hochschule München) stellte ein Verfahren zur Erkennung von liegendem Totholz vor, das sowohl punktbasierte Merkmale als auch solche mit höherer Abstraktionsstufe nutzt. Fabian Schneider (Universität Zürich) schließlich nutzt Laserdaten, um den Strahlungstransfer eines natürlichen Mischwaldes zu simulieren.

### Weitere und geplante Aktivitäten

Die Datenerfassung für die Mission TanDEM-X geht ihrem Ende entgegen. Gegenwärtig erfolgen letzte ergänzende Messungen, die auf schwierige Flächen wie Gebirgslagen fokussieren. Parallel ist die Prozessierung des globalen DOM angelaufen, die zunächst auf jene Flächen beschränkt ist, für die keine zusätzlichen Aufnahmen erforderlich sind. Nach und nach kommen die restlichen Gebiete hinzu. Für den kommenden Herbst plant das DLR der wissenschaftlichen Gemeinschaft erste Daten des DOM zur Verfügung zu stellen. Deren Untersuchung wird mit Sicherheit eine große Rolle in den Arbeiten des Arbeitskreises spielen.

Die UAV-basierte Geodatenerfassung – eines der Hauptthemen dieser gelungenen Tagung – wird zukünftig auch durch miniaturisierte Laserscanner unterstützt. Damit eröff-

nen sich dieser Technik noch weitere Anwendungsmöglichkeiten, insbesondere im Vegetationsbereich.

Uwe Sörgel, Hannover
Peter Krzystek, München

## Arbeitskreis Sensoren und Plattformen

### Arbeitsgebiete – Terms of Reference

- Sensorkonzepte für Anwendungen in der Photogrammetrie und Fernerkundung auf unterschiedlichen Plattformen vom Satelliten bis hin zum Nahbereich
- Kooperation mit den Anwendern/Datennutzern zur anwendungsbezogenen Optimierung der Sensorsysteme und Sensorkomponenten sowie zur Ableitung/Definition neuer Aufgabenstellungen für Sensorsysteme
- Modellierung/Simulation der Sensoren und Aufnahmesysteme auch unter Berücksichtigung der Auswertealgorithmen zur Objekt- und Dateninterpretation
- Kalibrierung und Validierung von Sensorsystemen und erfassten Daten einschließlich der Dokumentation der jeweiligen Charakteristiken im Hinblick auf die vorgesehenen Anwendungen

### Bericht von der Jahrestagung

Unbemannte Fluggeräte (UAV, Unmanned Aerial Vehicle, UAS, Unmanned Aerial System oder RPAS, Remotely Piloted Aircraft System) etablieren sich derzeit neben den klassischen fahrzeuggebundenen, satellitengestützten und flugzeuggetragenen Plattformen als zusätzliche Option für die geodätisch-photogrammetrische Datenerfassung. Eine Reihe geowissenschaftlicher Forschungseinrichtungen nutzen und entwickeln entsprechende Soft- und Hardware. Das große Interesse an diesen Systemen zeigte sich auch anlässlich der zwei Sitzungen des Arbeitskreises Sensoren und Plattformen, die diesem Thema anlässlich der 34. Wissenschaftlich-Technischen Jahrestagung der DGPF gewidmet waren. Die Sitzung *UAV Sensoren* eröffnete Stephan Palm vom Fraunhofer Institut für Hochfrequenzphysik und Radartechnik mit einem Vortrag zum Monitoring weitreichender Gebiete durch SAR-Video Echtzeitprozessierung (siehe auch AK Radarfernerkundung und Laserscanning). Dabei wurde deutlich, dass kompakte und leichte Radarsensoren zur Verfügung stehen, die mittlerweile auch für den Einsatz auf Kleinflugzeugen bis hin zu UAV geeignet sind. Sehr häufig kommen auf UAV-Plattformen jedoch Mittel- und Kleinformat-Kameras zum Einsatz. Zudem weicht die Blickrichtung oft von der Vertikalen ab. Verfahren zur Kalibrierung solcher Oblique und UAV Kameras wurden im Beitrag von Balazs Melykuti und Erwin Kruck vorgestellt. UAV-Photogrammetrie als Alternative für die terrestrische Geodatenerfassung ist insbesondere in schwierig zugänglichen Bereichen von Interesse. Dies wurde im Vortrag von Thomas Kraft und Matthias Gessner, Institut für Optische Sensorsysteme des DLR, am Beispiel der Dokumentation eines Gleisbereichs unter laufendem Betrieb deutlich. Die große Anzahl von UAV-Plattformen und deren zunehmenden Nutzung für die Geodatenerfassung legt eine Evaluation dieser Systeme im Rahmen eines Vergleichstest nahe. Eine solche Evaluation im Rahmen eines europäischen „Fly-In“ wurde zum Abschluss dieser ersten Sitzung von Görres Grenzdörffer Universität Rostock vorgeschlagen.

Die zweite Sitzung *UAV Anwendungen* eröffnete Michael Cramer von der Universität Stuttgart mit einem Vortrag zur 3D-Dokumentation von Hangrutschungen als Beispiel für operationelle Einsatzmöglichkeiten von UAV-Systemen. Dieses Projekt wurde in Kooperation mit dem Landesamt für Geoinformation und Landentwicklung Baden-Württemberg durchgeführt. Die Einsatzmöglichkeiten von UAV für landwirtschaftliche Anwendungen – unter anderem durch die Nutzung hyperspektraler Kamerasysteme – demonstrierte der Beitrag von Georg Bareth, Universität zu Köln, ebenso wie der Vortrag von Görres Grenzdörffer zur Bestandshöhenermittlung landwirtschaftlicher Kulturen aus UAS-Punktwolken. Abschließend diskutierte Werner Mayr, GerMAP GmbH, die Einsatzmöglichkeiten von UAV aus Sicht eines kommerziellen Anwenders. Insgesamt zeigten die Beiträge das breite Spektrum von UAV-Plattformen und Anwendungen, dem zu

Recht in den beiden sehr gut besuchten Sitzungen des Arbeitskreises Sensoren und Plattformen große Aufmerksamkeit entgegengenbracht wurde.

### Weitere und geplante Aktivitäten

Der AK Sensoren und Plattformen beteiligt sich derzeit an der ISPRS/EuroSDR Initiative Benchmark on High Density Image Matching. Diese untersucht das Potential der dichten Bildzuordnung für die großflächige und effiziente Erfassung hochgenauer Höhenmodelle im urbanen und ländlichen Raum für Aufnahmen klassischer digitaler Luftbildkameras sowie für Oblique-Systeme.

NORBERT HAALA, Stuttgart

## Arbeitskreis Standardisierung und Qualitätssicherung

### Bericht von der Jahrestagung

Auf der Jahrestagung 2014 fand eine Session des Arbeitskreises Standardisierung und Qualitätssicherung statt.

Zunächst referierte WOLFGANG KRESSE über den aktuellen Status der ISO-Normen für Photogrammetrie und Fernerkundung. In den letzten Jahren sind im Rahmen des ISO/TC 211 „Geographic information / Geomatics“ eine Reihe von Normen für Photogrammetrie und Fernerkundung entstanden, die sich vor allem auf die Teilgebiete Georeferenzierung, Metadaten und Sensorkalibrierung beziehen. Die meisten dieser Normen sind bereits veröffentlicht. Aktuell ist noch die Norm zur Kalibrierung von Lidar-Sensoren in Arbeit. Für einige der ISO-Normen ist derzeit die Entwicklung eines Implementierungsinterfaces in XML in Arbeit.

Im zweiten Thema durchleuchte SVEN BALTRUSCH die Effektivität und Effizienz von Bildflügen aus der Sichtweise des amtlichen Vermessungswesens. Mittlerweile werden auf Basis von amtlichen Befliegungen nicht mehr lediglich Digitale Orthophotos abgeleitet, sondern auch Oberflächenmodelle, 3D-Gebäudemodelle. Hinzu tritt die bildbasierte Klassifizierung. Das Ergebnis eines Befliegungsvorhabens ist von einer Vielzahl von Faktoren abhängig. Bedingt durch den technologischen Fortschritt sind den Bildflugparametern kaum noch Grenzen gesetzt. Geometrische Vorgaben, wie z.B. Bodenauflösung, Längs- und Querüberdeckung, können frei definiert und erreicht werden. Im Rahmen der Arbeit der AdV-Projektgruppe „ATKIS®-DOP“ hat sich die Gruppe mit den Stellschrauben befasst, welche für das Erreichen eines definierten Zielproduktes erforderlich sind. Mit Fokus auf das zu erreichende Produkt werden die Eingangsgrößen differenziert, um ein effizientes Ergebnis zu erreichen, da von dem Mengengerüst der Eingangsbilder letztendlich der Folgeprozess und somit neben der Produktionszeit auch die Bereitstellung einer effektiven Hard- und Softwarelandschaft abhängig ist.

Im Vortrag „*Spezifikationen von Prüfplänen und Prüfergebnissen von 3D-Stadtmodellen*“ ging DETLEV WAGNER auf die Datenqualität von 3D-Stadtmodellen ein, welche mit der wachsenden Vielfalt der Anwendungszenarien zunehmend an Bedeutung gewinnt. Automatisierte Prüftools sind vorhanden, z.B. CityDoctor oder val3dity, jedoch bestehen noch keine allgemein anerkannten Grundsätze, wie Prüfanforderungen und Validierungsergebnisse dokumentiert werden. Sie sollen sowohl menschenlesbar als auch maschineninterpretierbar sein, damit komplexe Objekte referenziert und in einem späteren Bearbeitungsschritt automatisch korrigiert oder zur Analyse in geeigneter Weise visualisiert werden können. In seinem Vortrag beschreibt WAGNER den Aufbau und die Spezifikation eines Prüfplans, der anwendungsspezifische Erfordernisse, wie etwa Geschlossenheit von Volumenkörpern (Wasserdichtigkeit) oder die Verwendung bestimmter Geometriearten berücksichtigt. Ein Modell zur standardisierten Dokumentation und Speicherung von Prüfergebnissen wurde vorgestellt. Damit kann die Eignung des Datensatzes für die vorgesehene Anwendung bewertet werden. Schließlich wurde ein Verfahren beschrieben, das mittels eines Hashcodes sicherstellt, dass der validierte Datensatz und das Prüfergebnis zusammengehören und konsistent sind. Damit ist eine eindeutige und sichere Zuordnung von geprüftem Datensatz und Prüfergebnis auch zu einem späteren Zeitpunkt gewährleistet.

CityGML ist als internationaler Standard zur Repräsentation und den Austausch virtueller, geometrisch semantischer 3D-Stadtmodelle akzeptiert. In seinem Beitrag „*Aktuelle Trends in der Entwicklung von CityGML 3.0*“ wurden durch Marc O. Löwner die erheblichen Änderungen für die Version CityGML 3.0, die sich an 19 Arbeitspaketen der CityGML Special Working Group manifestieren, herausgearbeitet. Ziel des Beitrages war es, die Akzeptanz des Standards weiter zu erhöhen und Diskussionen über vorgeschlagene Änderungen zu ermöglichen. Die wichtigsten aktuellen Diskussionen betreffen eine Neudefinition des Level of Detail Konzeptes (LoD), die Anpassungen alter und Einführung neuer Module sowie eine Harmonisierung mit den benachbarten Standards der Industry Foundation Classes (IFC) und INSPIRE. Die nächste Version wird konform zu den Normen des ISO/TC 211 sein. Die CityGML XML-Schemata werden automatisch aus dem konzeptionellen UML-Modell abgeleitet werden können.

Sven Baltrusch, Schwerin

## Arbeitskreis 3D-Stadtmodelle

### Arbeitsgebiete – Terms of Reference

- Aufbau von 3D-Stadtmodellen
- Anwendungen von 3D-Stadtmodellen
- Neuerungen und Forschungen auf diesem Gebiet
- Regelmäßiger Erfahrungsaustausch (Organisation von Workshops, AK-Treffen)

### Bericht von der Jahrestagung

Der gemeinsame Arbeitskreis von DGfK und DGPF war bei der 34. Wissenschaftlich-Technischen Jahrestagung der DGPF vom 26. – 28. März 2014 in Hamburg mit einer Session mit dem Titel „3D-Geoinformationen – Anwendungen“ vertreten. In den neueren Entwicklungen im Bereich der Forschung spielt das Thema „Zeit“ demnach eine immer größere Rolle. Gleichzeitig ist ein deutlicher Trend zu verzeichnen, sich immer intensiver mit den Bauwerkseigenschaften zu befassen. Herauszuheben ist der Beitrag von Maximilian Sindram, der sich mit der semantischen Modellierung von Maßnahmen unter Nutzung von 3D-Stadtmodellen befasste. Die Umsetzung ist bereits in Schritten erfolgt, die Ergebnisse werden sicherlich mit großem Interesse beobachtet werden.

### Weitere und geplante Aktivitäten

Im Rahmen der Nachwuchsförderung prämierte der Arbeitskreis herausragende studentische Abschlussarbeiten, um junge Menschen anzuspornen, sich mit dem Themenkomplex der 3D-Stadtmodelle zu beschäftigen. Den drei Preisträgern wurde die Teilnahme an der 26. „International Cartographic Conference“ im August 2013 in Dresden ermöglicht. Die prämierten Arbeiten wurden dort mindestens mit einem Poster publiziert, die Ehrungen wurden im feierlichen Rahmen ausgesprochen.

Gemeinsam mit dem InGeoForum hat der Arbeitskreis die Broschüre „3D-Stadtmodelle – Projekte im Raum“ herausgegeben, die anhand von kurzen Beschreibungen Anwendungsbeispiele für 3D-Stadtmodelle in Form von Steckbriefen zeigt und Voraussetzungen und Nutzen darstellt.

Mitte April trafen sich die AK-Mitglieder zu einer weiteren Sitzung in Darmstadt. Die Sitzung diente wie immer auch dem Erfahrungsaustausch der Mitglieder und fand in den Räumen des Fraunhofer-Instituts für Graphische Datenverarbeitung (IGD) in Darmstadt statt. Auf der Tagesordnung stand daher auch die Vorstellung von aktuellen Projekten des IGD, die alle die Visualisierung von 3D-Modellen betrafen. So wurden die Möglichkeiten vorgestellt, sich in einem virtuellen Modell frei bewegen zu können, das insbesondere für Museen einsetzbar ist und im konkreten Fall historische Räume nachstellte. Ebenso wurde die Kombination von virtuellen mit reellen Modellen vorgeführt, hier am Beispiel von Instandhaltungsarbeiten. Schließlich diskutierten die AK-Mitglieder den aktuellen Stand eines Projektes zur Unterstützung in Planungs- und Beteiligungsprozessen sowie zur Entscheidungsfindung. Am Beispiel der Trassen- und Standortplanung wurde der Einsatz eines Kommunikationsinstruments vorgeführt, das die Transparenz aller Grundlagen für das erforderliche Abstimmungs- und Ge-

nehmigungsverfahren bietet und gleichzeitig eine interaktive Plattform für die Diskussion der alternativen Planungsszenarien bietet.

Ein weiterer wichtiger Tagesordnungspunkt der Sitzung war die Vorbereitung des diesjährigen Workshops „3D-Stadtmodelle“ am 4. und 5.11.2014 in Bonn. Dazu wurden die Wünsche und Anregungen aus den Feedback-Bögen des letzten Jahres ausgewertet, Themenschwerpunkte diskutiert und der grobe Rahmen des Programms festgelegt.

Die Vorbereitungen für diesen Workshop laufen auch nach der Sitzung auf Hochtouren. Beiträge zur Fortführung von 3D-Stadtmodellen stehen ebenso auf dem Programm wie Berichte zu Qualitätsprüfungen und Visualisierungen. Von Anfang an guter Brauch beim mittlerweile sechsten Workshop des Arbeitskreises: Es wird wieder Vorträge zu Arbeiten im benachbarten Ausland geben.

Bettina Petzold, Wiesbaden

## Arbeitskreis Geoinformatik

### Arbeitsgebiete – Terms of Reference

- Geodatenaggregation, -abstraktion, -interpretation und -integration
- Automation der GIS-Analyse
- Neue Visualisierungstechniken
- Integration von GIS und Bilddaten

### Bericht von der Jahrestagung

Die gemeinsame Jahrestagung von DGPF, DGfK, GFGi und GiN e.V. stellte für den DGPF-Arbeitskreis Geoinformatik eine besondere Gelegenheit dar, sich als Bindeglied zwischen Geoinformatik, Kartographie und Photogrammetrie präsentieren zu können. Dieses geschah u.a. in den einzelnen Sessions mit Fachvorträgen über die Visualisierung von 3D-Geodaten, Anwendungen von nutzergenerierten Daten, Geodateninfrastrukturen und die Automation in der Kartographie. In vielen Fällen wäre eine eindeutige Zuordnung des Vortragsthemas zu einer der vier beteiligten Gesellschaften schwierig, wenn nicht unmöglich gewesen. Die Notwendigkeit eines Austausches zwischen den Fachdisziplinen, etwa durch zukünftige gemeinsame Seminare und Tagungen, ergibt sich daraus fast zwangsläufig. Gemeinsame Grundlagen sollten verstärkt in der Lehre vertreten und in der Forschung weiterentwickelt werden. Als Trend ist zum Beispiel eine zunehmende Bedeutung der Graphentheorie zu beobachten, was sowohl in Beiträgen aus der Geoinformatik als auch in Vorträgen zur Bildanalyse zum Ausdruck kam. So präsentierte Marc-Oliver Löwner (TU Braunschweig) einen graphentheoretischen Ansatz zur Repräsentation raumzeitlicher Entwicklungen von Landformen, während Lena Albert (Universität Hannover) die Verwendung eines graphischen Modells für die Luftbildklassifikation vorstellte. Jan-Henrik Haunert (Universität Osnabrück) ging in der Plenarsitzung Geoinformatik auf Graphen als disziplinübergreifende Grundlage ein.

### Weitere und geplante Aktivitäten

Der Arbeitskreis Geoinformatik wird seit Oktober 2013 von Jan-Henrik Haunert (Universität Osnabrück) geleitet, der Jürgen Döllner (Universität Potsdam) in dieser Funktion ablöste. Neuer stellvertretender Leiter ist Bernhard Höfle (Universität Heidelberg). Der Arbeitskreis befindet sich momentan in einer Erneuerungsphase, in der Anregungen zur zukünftigen thematischen Ausrichtung des Arbeitskreises und Ideen zu Kooperationen mit anderen Arbeitskreisen besonders willkommen sind. Grundsätzlich strebt der Arbeitskreis an, methodische Ansätze für die Verarbeitung strukturierter Daten und die Analyse von Sensordaten zu entwickeln und zu untersuchen. Ansätze, die sich auf beide Bereiche anwenden lassen oder beide Bereiche vereinen, sind dabei von besonderem Interesse.

Jan-Henrik Haunert, Osnabrück

## Gemeinsame Kommission von DGPF, DGfK, und DVW „Geodaten und Recht“

### Arbeitsgebiete – Terms of Reference

- Urheberrecht
- Recht des Datenbankherstellers
- Datenschutzrecht
- Geodateninfrastrukturrecht
- Informationsweiterverwendungsrecht.

### Bericht zu aktuellen Fragen

Der Landesbeauftragte für den Datenschutz Baden-Württemberg hat in einer Beanstandung 2011 die Auffassung vertreten, dass Luftbildaufnahmen und Orthophotos mit einer Bodenauflösung genauer 25 Zentimetern personenbezogene Daten seien. Das Innenministerium Baden-Württemberg hat den Standpunkt des Landesbeauftragten für den Datenschutz nicht akzeptiert. Das Landesamt für Geoinformation und Landentwicklung Baden-Württemberg lässt weiterhin Luftbildaufnahmen und Orthophotos mit einer Bodenauflösung von 10 Zentimetern erstellen und stellt sie den Nutzern zur Verfügung. Seither hat es in dieser Angelegenheit keine weitere Entwicklung mehr gegeben. Die Verantwortung für die Einhaltung datenschutzrechtlicher Bestimmungen liegt beim Nutzer. Die Kommissionsmitglieder sprechen sich mehrheitlich gegen eine gesetzliche Festlegung einer datenschutzrechtlich noch unbedenklichen Bodenauflösung aus.

Der Europäische Gerichtshof hat mit Urteil entschieden, dass bei Urheberrechtsverletzungen über das Internet das angerufene nationale Gericht nur für die Entscheidung über den Schaden zuständig ist, der im Hoheitsgebiet des Mitgliedsstaats verursacht worden ist, zu dem es gehört.

Nachdem das Landgericht München I die Frage, ob eine topographische Karte eine Datenbank sei, bejahte und das Oberlandesgericht München diese Frage verneint hat, ist derzeit das Revisionsverfahren beim Bundesgerichtshof anhängig.

Der Bundestag hat das Gesetz gegen unseriöse Geschäftspraktiken verabschiedet. Dieses will Verbraucher und Kleingewerbetreibende vor unseriösen Geschäftsmethoden schützen. So wurden auch die Abmahngebühren für Anwälte bei Urheberrechtsverletzungen durch einen privaten Nutzer durch Festlegung des Gegenstandswerts auf 1.000 EUR für die erste Abmahnung begrenzt. Dadurch wird die Abmahngebühr im Regelfall 155,30 EUR betragen.

### Weitere und geplante Aktivitäten

Die gemeinsame Kommission, hat den Leitfaden „Urheberrecht leicht gemacht“ zusammengestellt. Er soll im beruflichen und privaten Umfeld den Umgang mit urheberrechtlichen Fragen im Alltag erleichtern. Er wendet sich insbesondere auch an Hochschullehrer, Studenten, Lehrer und Schüler, die bei ihrer täglichen Arbeit Geodaten und Karten nutzen.

Martina Braune, Potsdam

# Hochschulnachrichten

## Leibniz Universität Hannover

### *Dissertation von Alexander Schunert*

Herr Dipl.-Ing. Alexander schunert wurde am 27.1.2014 an der Fakultät für Bauingenieurwesen und Geodäsie der Leibniz Universität Hannover mit der Arbeit *Assignment of Persistent Scatterers to Buildings* zum Dr.-Ing. promoviert.

1. Referent: Prof. Dr.-Ing. habil. Christian Heipke, Leibniz Universität Hannover,
2. Referent: Prof. Dr.-Ing. Steffen Schön, Leibniz Universität Hannover,
3. Referent: Prof. Dr.-Ing. Uwe Sörgel, Technische Universität Darmstadt.

*Kurzfassung:*

Persistent Scatterer Interferometrie (PSI) ist eine Methode zur Erfassung von Deformationen der Erdoberfläche im Millimeterbereich mithilfe eines Stapels von SAR-Bildern. Die Technik beruht auf der Erkennung von Punktzielen mit zeitlich konstanten Reflexionseigenschaften. Diese Punktziele werden als Persistent Scatterer (PS) bezeichnet. Da PS überwiegend an künstlichen Objekten zu finden sind, ist die Technik vor allem für die Überwachung von Städten geeignet. Die Anzahl von PS pro Gebäude ist üblicherweise recht groß, wenn hochauflösende SAR-Daten, z.B. TerraSAR-X oder COSMO-Skymed Spot-

light-Daten, verwendet werden, so dass eine Überwachung einzelner Gebäude auf Basis von PSI möglich erscheint. Die PS zeigen oft regelmäßige Muster an Fassaden, was durch die rechtwinklige Anordnung der Strukturen bedingt ist, die diese PS erzeugen. Diese Regelmäßigkeiten enthalten Information, die für die PS-Auswertung nützlich sind.

Der Schwerpunkt dieser Arbeit ist die Zuordnung von PS zu Gebäuden unter Zuhilfenahme eines dreidimensionalen Stadtmodells. Es wird eine Methode entwickelt, um die PS den Gebäudegrenzflächen dieses Stadtmodells zuzuordnen. Das Ziel der durchgeführten Experimente ist vor allem die Erkennung von Effekten, die diese Zuordnung stören. Es zeigt sich, dass PS und Kartendaten an Fassaden weitestgehend übereinstimmen, während an Dächern stärkere Unterschiede auftreten. Das liegt größtenteils an Generalisierungseffekten, die an Dachstrukturen deutlich stärker ausgeprägt sind. Eine wesentliche Feststellung ist, dass sich einige PS innerhalb von Gebäuden befinden können. Die Ursachen, die zur Entstehung solcher PS führen, konnten nicht abschließend geklärt werden. Allerdings könnten diese PS wesentliche Probleme bei der Interpretation von Deformationsergebnissen verursachen.

Um eine Zuordnung der PS zu den Grenzflächen des Stadtmodells zu ermöglichen, wird ein Verfahren zur geometrischen Registrierung beider Datensätze entwickelt. Die Grundlage der Methode bildet ein Iterative Closest Plane Algorithmus, der auf die speziellen Charakteristika der PS-Punktwolke angepasst wird. Die Plausibilität der erhaltenen Ergebnisse wird in Fallbeispielen und anhand des Konvergenzverhaltens der iterativen Prozedur gezeigt.

Anzahl und Verteilung der PS hängen von der Szene ab und können der Überwachungsaufgabe nicht angepasst werden. Das stellt eines der größten Nachteile von PSI dar, da auftretende Bodenbewegungen unter Umständen nicht erkannt werden. Um dieses Problem zu mildern, wird eine Karte, die die PS-Dichte für jede Grenzfläche des dreidimensionalen Stadtmodells zeigt, aus der bereits bekannten Zuordnung zwischen PS und Gebäuden erzeugt, was zumindest die Erkennung unterabgetasteter Gebiete ermöglicht. Die Dichte-Karte wird zur Erkennung einiger Faktoren genutzt, die die PS-Dichte wesentlich beeinflussen. Letztere werden anhand von Fallbeispielen diskutiert.

Um die regelmäßige Anordnung der PS an Gebäudefassaden auszunutzen, wird ein Produktionssystem zur Erkennung regelmäßiger horizontaler Muster entwickelt. Die erhaltenen Ergebnisse sind heterogen. Manche Fassaden enthalten eine Vielzahl von Gruppen, während an anderen Fassaden kaum Muster erkannt werden. Das kann zu großen Teilen auf Layover-Effekte zurückgeführt werden, die Muster erheblich stören können. Die gewonnene Gruppierungsinformation kann zur Verbesserung der Höhenschätzung des kompletten Musters genutzt werden. Für die Bestimmung der vertikalen Position jeder Gruppe wird das gewichtete Mittel der Höhen der einzelnen PS diskutiert. Der erwartete Genauigkeitsgewinn wird theoretisch auf Basis des Cramer-Rao lower bound (CRLB) einer einzelnen Höhenschätzung durch Fehlerfortpflanzung bestimmt.

Schließlich werden die vertikalen Distanzen zwischen PS-Gruppen und horizontalen Strukturen in light detection and ranging (Lidar) Daten ausgewertet. Ziel dieser Untersuchung ist die Zuordnung der PS zu real existierenden Strukturen, die durch die Lidar-Daten repräsentiert werden. Die Untersuchung beschränkt sich auf die Fassaden zweier Gebäude mit sehr einfachem Aufbau.

Die Dissertation ist in der Schriftenreihe „Wissenschaftliche Arbeiten der Fachrichtung Geodäsie und Geoinformatik der Leibniz Universität Hannover“ (ISSN 0174-1454) als Heft Nr. 311 erschienen. Gleichzeitig ist die Arbeit in der Reihe C der Deutschen Geodätischen Kommission bei der Bayerischen Akademie der Wissenschaften (ISSN 0065-5325) unter der Nr. 728 online veröffentlicht (www.dgk.badw.de).

## *Dissertation von Marcel Ziems*

Herr Dipl.-Ing. Marcel Ziems wurde am 27.2.2014 an der Fakultät für Bauingenieurwesen und Geodäsie der Leibniz Universität Hannover mit der Arbeit *Automatic verification of road databases using multiple road models* zum Dr.-Ing. promoviert.

1. Referent: Prof. Dr.-Ing. habil. Christian Heipke, Leibniz Universität Hannover,
2. Referent: PD Dr.-Ing. habil. Franz Rottensteiner, Leibniz Universität Hannover,
3. Referent: Prof. Dr.-Ing. habil. Monika Sester, Leibniz Universität Hannover,
4. Referent: Prof. Dr.-Ing. Jörn Ostermann, Leibniz Universität Hannover.

*Kurzfassung:*
Die Arbeit stellt einen neuen Ansatz zur automatischen Verifikation von Straßendatenbanken auf Grundlage von aktuellen Luft- und Satellitenbildern vor. Im Gegensatz zu bereits vorliegenden Forschungsarbeiten ist der neue Ansatz nicht auf spezifische Straßentypen, Kontextbereiche oder geographische Regionen beschränkt. Dies wird primär durch eine Kombination mehrerer unterschiedlicher Forschungsarbeiten, welche als unabhängige Verifikationsmodule im Gesamtsystem integriert sind, erreicht. Jedes dieser Module basiert auf einem spezifischen Straßenmodell, dessen Anwendbarkeit auf bestimmte Straßentypen, Kontextbereiche oder geographische Regionen beschränkt bleibt, die in Kombination jedoch nahezu Allgemeingültigkeit erreichen. Die verbleibenden nicht modellierten Straßenobjekte werden automatisch erkannt und können somit manuell verifiziert werden.

Die Kombination selbst basiert auf einer statistischen Auswertung der Ergebnisse aller Module. Hierfür liefert jedes Modul zu jedem Straßenobjekt der zu verifizierenden Datenbank ein aus zwei Teilen bestehendes Ergebnis. Der erste Teil ist eine Wahrscheinlichkeitsverteilung, welche den Zustand eines Straßenobjektes (*richtig*, *falsch*) beschreibt. Der zweite Teil ist eine Wahrscheinlichkeitsverteilung, welche den Zustand eines Modells (*anwendbar*, *nicht anwendbar*) beschreibt. Die prinzipielle Definition dieses Ergebnisteils ist ein wichtiger Beitrag der vorliegenden Arbeit. Die grundlegende Idee dabei ist, dass ein Modell nur genau dann *anwendbar* ist, wenn alle Modellannahmen bezüglich eines Straßenobjektes im Bild *erfüllt* sind. Ausgehend von den ursprünglichen Forschungsarbeiten beziehen sich Modellannahmen auf die Präsenz bestimmter Straßentypen, Kontextbereiche oder geographische Regionen, aber auch auf die Sichtbarkeit von Merkmalen oder, bei statistischen Ansätzen, auf die Verfügbarkeit von repräsentativen Trainingsdaten. Somit liefern die Module Wahrscheinlichkeiten bezüglich zweier Zustandsräume. Diese werden auf Grundlage der Dempster-Shafer Theorie auf einen neuen Zustandsraum abgebildet, welcher die Zustände *richtig*, *falsch*, und *unbekannt* beinhaltet.

Experimente mit drei realen Straßendatenbanken, welche insgesamt 7742 richtige und 669 fehlerhafte Straßen enthalten, zeigen das Potential des neuen Ansatzes. Dabei stellt sich heraus, dass eine Datenbankqualität von 97,5% – 100% erreicht wird, wenn alle Straßenobjekte, die als *falsch* oder *unbekannt* klassifiziert sind, von einem menschlicher Operateur betrachtet und gegebenenfalls berichtigt werden. Hierbei müssen nur 25% – 33% aller Straßenobjekte vom Operateur betrachtet werden. Reduziert man den manuellen Aufwand weiter und berücksichtigt nur die maximal 9% der als *falsch* klassifizierten Straßenobjekte, vermindert sich die Datenbankqualität im Durchschnitt um ca. 5%. Weitere Experimente auf Grundlage von Benchmark-Datensätzen ordnen den neuen Ansatz wissenschaftlich ein. Die Ergebnisse zeigen, dass der neue Ansatz in allen Testszenen mindestens gleich gute Ergebnisse wie der jeweils beste Ansatz des entsprechenden Benchmark Tests liefert. In zwei der sechs Szenen sind die Ergebnisse mit ca. 25% höherer Vollständigkeit sogar deutlich besser.

Die Dissertation ist in der Schriftenreihe „Wissenschaftliche Arbeiten der Fachrichtung Geodäsie und Geoinformatik der Leibniz Universität Hannover“ (ISSN 0174-1454) als Heft Nr. 313 erschienen. Gleichzeitig ist die Arbeit in der Reihe C der Deutschen Geodätischen Kommission bei der Bayerischen Akademie der Wissenschaften (ISSN ISSN 0065-5325) unter der Nr. 724 online veröffentlicht (www.dgk.badw.de).

## *Apl. Professur für PD Franz Rottensteiner*

Am 19. Mai 2014 wurde PD Dr. techn. Franz Rottensteiner, Privatdozent am Institut für Photogrammetrie und GeoInformation (IPI) der Leibniz Universität Hannover, zum außerplanmäßigen Professor ernannt. Franz Rotten-

steiner hat an der TU Wien Vermessungswesen studiert und wurde dort auch promoviert und habilitiert. Nach Stationen im Australien kam er 2008 nach Hannover und leitet seitdem am IPI die Forschungsgruppe „Photogrammetrische Bildanalyse“, für die er mehrere DFG-Projekte einwarb. Seine Aktivitäten in der Lehre konzentrieren sich auf die Photogrammetrie und Bildanalyse.

## TU Clausthal

### *Dissertation von Nazemeh Ashrafianfar*

Frau Nazemeh Ashrafianfar (M.Sc.) promovierte am 1.11.2013 an der Fakultät für Energie- und Wirtschaftswissenschaften der Technischen Universität Clausthal mit der Arbeit *The Application of Satellite Radar Interferometry in the Development of a Dynamic Neural Model of Land Subsidence Induced by Overexploitation of Groundwater* zum Dr.-Ing.

1. Referent: Prof. Dr.-Ing. Wolfgang Busch, TU Clausthal,
2. Referent: Prof. Dr.-Ing. habil. Hossein Tudeshki, TU Clausthal,
3. Referent: Prof. Dr.-Ing. Daniel Goldmann, TU Clausthal.

*Abstract:*
This research undertakes to substantiate the feasibility of a dynamic neural model of land subsidence due to groundwater over-exploitation in an inverse problem approach. The inverse problem approach refers to a field of applied science that investigates and simulates unknown causes from observed effects. The methodology of artificial neural networks (ANN) is iterative learning of cause and effect data, in order to extract and generalize their nonlinear relationships. This methodology was applied here as an inverse problem approach for spatio-temporal simulation of subsidence. The learning algorithm of the nonlinear multilayer ANNs is the core of this inverse problem approach. The neural models enable the extraction of the nonlinear relations between subsidence (effect) and aquifer system parameters (causes).

Interferometric synthetic aperture radar (InSAR) as well as differential InSAR (dInSAR) based on ENVISAT ASAR and ALOS PALSAR data have been applied to measure subsidence and to monitor variations of it over time. This data was used as input for the solution patterns of the neural models.

The dInSAR time series results were applied in a linear regression analysis to estimate the degree of the linear relationships and interdependence between subsidence and aquifer parameters. Furthermore, a model of time-independent nonlinear feed-forward neural network model was developed and applied to generalize the nonlinear relations between the Hashtgerd land subsidence and the aquifer parameters. This time-independent (static) neural model simulated subsidence using aquifer parameters. Finally, an appropriate structure of recurrent neural networks was applied to develop the time-dependent (dynamic) model of subsidence. This dynamic model simulated subsidence by using monthly groundwater data in the defined simulation time steps.

The recurrent neural model was optimized by a pattern search algorithm in an unconstrained optimization approach. The optimized model demonstrated a method of subsidence simulation/prediction, which uses the potential of dInSAR technique and the following features of the dynamic neural model: Topology, supervised learning paradigm, regularization algorithm and validation method. This dynamic model of subsidence is applicable in the simulation and prediction of subsidence in other overexploited aquifer systems, considering hydro-geological parameters of aquifers. This is helpful in the reduction of future hazards, which provoke the quantitative and qualitative depletion of aquifers.

## TU München

### *Dissertation von Sebastian Türmer*

Herr Dipl.-Ing. Sebastian Türmer promovierte am 6. Mai 2014 an der Ingenieurfakultät Bau Geo Umwelt (Fachgebiet Photogrammetrie und Fernerkundung) der Technischen Universität München mit der Arbeit *Car detection in low frame-rate aerial imagery of dense urban areas* zum Dr.-Ing.

1. Gutachter: Prof. Dr.-Ing. Uwe Stilla, Technische Universität München,

2. Gutachter: Prof. Dr. rer. nat. Ralf Reulke, Humboldt-Universität zu Berlin,
3. Gutachter: Prof. Dr.-Ing. Peter Reinartz, Universität Osnabrück

*Zusammenfassung:*
Das Wissen von Anzahl und Position bewegter und stehender Fahrzeuge ist wichtig für Verkehrsmanagement und -planung. Aufgrund dieser Informationen können beispielsweise die Sicherheit von Massenveranstaltungen erhöht oder Rettungskräfte im Katastrophenfall unterstützt werden. Zur Gewinnung dieser Information sind die interessierenden Gebiete aktuell und flächig aufzunehmen. Hierfür eignen sich besonders flugzeuggestützte, optische Kamerasysteme. Allerdings ist zur automatischen Auswertung dieser Luftbilder ein zuverlässiges Verfahren notwendig, um die Fahrzeuge zu detektieren.

In der vorliegenden Arbeit wird ein Verfahren zur automatischen Extraktion von Fahrzeugen in städtischem Gebiet vorgestellt. Das Verfahren kombiniert eine objektbasierte mit einer gradientenbasierten Strategie und ist in drei Hauptbereiche unterteilt. Der erste Bereich behandelt die Extraktion von Bodenflächen. Unter der Annahme, dass für Fahrzeuge befahrbare Flächen in dicht besiedelten Städten meistens Bodenflächen sind, werden Höhenbilder mit dem Semi-global Matching Algorithmus (SGM) berechnet. Danach wird automatisch ein Grenzwert bestimmt, um Bodenflächen von Nicht-Bodenflächen zu trennen (Minimum Error Thresholding). Im zweiten Bereich wird ein objektbasiertes Verfahren eingeführt, um Fahrzeugkandidaten zu bestimmen. Hier wird zunächst die zeitliche Veränderung des Bildes aufgrund des Krümmungsflusses genutzt, um das Eingabebild zu glätten. Im nächsten Schritt wird ein Regionenwachstumsverfahren angewendet. Die erhaltenen Regionen werden als selbständige Objekte betrachtet und nach ihren geometrischen Eigenschaften mehrfach gefiltert. Der dritte Bereich beschreibt die Untersuchung der verbleibenden Fahrzeugkandidaten mit einem gradientenbasierten Klassifikator (HOG-Merkmale), welcher mit einem maschinellen Lernverfahren (AdaBoost) trainiert ist. Dieser Klassifikator ist jedoch nur mit wenigen Beispielen und Iterationsschritten trainiert.

Das Verfahren wird mit fünf innerstädtischen Luftbildern des 3K+ Kamerasystems (13 cm Bodenpixelgröße) und des UltraCam Eagle Kamerasystems (20 cm Bodenpixelgröße) getestet. Aufgrund der Verwendung von Disparitätsbildern kann die Qualität der Fahrzeugerkennung in dicht besiedelten innerstädtischen Gebieten erhöht werden. Objekte auf dem Dach von Gebäuden werden nun vom Detektionsprozess ausgeschlossen. Weiterhin ist das Verfahren fähig, ohne die Anpassung der Parameter Fahrzeuge in unterschiedlichem Datenmaterial (verschiedene Sensoren mit unterschiedlicher Auflösung) zu erkennen. Die Ergebnisse der Detektion zeigen, dass bei einer Vollständigkeit von 80% eine Korrektheit zwischen 65% und 95% erreicht wird.

Die Dissertation ist verfügbar unter: http://www.pf.bv.tum.de/pub/2014/tuermer_phd14_dis.pdf

## *Dissertation von Ludwig Hoegner*

Herr Dipl.-Inf. Ludwig Hoegner promovierte am 28. Mai 2014 an der Ingenieurfakultät Bau Geo Umwelt (Fachgebiet Photogrammetrie und Fernerkundung) der Technischen Universität München mit der Arbeit *Automatische Texturierung von Gebäudemodellen aus terrestrischen IR-Bildfolgen* zum Dr.-Ing.

1. Gutachter: Prof. Dr.-Ing. Uwe Stilla, Technische Universität München,
2. Gutachter: Prof. Dr.-Ing. Helmut Mayer, Universität der Bundeswehr München

*Zusammenfassung:*
Thermische Inspektionen von Gebäuden mit Infrarot(IR)-Kameras erfolgen traditionell in der Bildgeometrie. Eine 3D Georeferenzierung oder objektbezogene Speicherung der abgebildeten Objektoberflächen erfolgt nicht. Die Arbeit beschäftigt sich mit der Herstellung des dreidimensionalen Raumbezugs und der objektbezogenen Speicherung der abgebildeten Fassadenflächen unter Verwendung von 3D Gebäudemodellen. Gebäudemodelle werden heutzutage sowohl für die Erfassung des Bestands in standardisierter Form (CityGML) in Geoinformationssystemen als auch für Planung, Bau und Betrieb in Bauwerksinformationssystemen (BIM) verwendet. Durch die

Herstellung eines 3D Raumbezugs wird es möglich, komplexe Gebäude thermographisch zu untersuchen, die in einzelnen Aufnahmen nicht vollständig erfasst werden können. Ebenso lassen sich dann Daten verschiedener Aufnahmezeitpunkte und Sensoren vergleichen und kombinieren. Weiterhin ergibt sich auch die Möglichkeit, Objekte in den Infrarottexturen zu detektieren und in die 3D Struktur des Gebäudemodells zu integrieren.

Als Eingangsdaten dienen neben den Modellen Bildsequenzen von Fassaden, die von einem Fahrzeug mit einer IR-Kamera aufgenommen werden. Ungünstige Sichtbedingungen und Verdeckungen in innerstädtischen Bereichen erlauben in Einzelbildern keine direkte Zuordnung von Fassadenflächen zu korrespondierenden Bildbereichen mit ausreichender Genauigkeit. Daher werden in dieser Arbeit Verfahren beschrieben und untersucht, die durch eine gemeinsame Auswertung von Bildern einer Folge eine genauere Zuordnung ermöglichen. Die einzelnen Verarbeitungsschritte von der Aufnahme der Sequenz bis zur Auswertung der Textur werden behandelt und bewertet.

Die Vorgehensweise zur geometrischen Kalibrierung der IR-Kamera wird vorgestellt und die Qualität der Kalibrierung bestimmt. Um eine möglichst gute Verknüpfung der IR-Bilder durch homologe Punkte zu erreichen, werden Verfahren zur Extraktion von markanten Punkten (Förstner-Punkte und SIFT-Features) verglichen. Da die Anzahl und Qualität der markanten Punkte abhängig von der verwendeten Szene ist, werden für gleiche Szenenausschnitte die Ergebnisse der Bilder einer IR-Kamera mit denen einer Videokamera verglichen.

Anschließend werden zwei Verfahren zur Orientierung der Bildsequenzen und Koregistrierung mit dem 3D Gebäudemodell vorgestellt. Beim ersten Verfahren wird zunächst ein Szenenmodell auf Basis der relativen Orientierung rekonstruiert und anschließend mit dem Gebäudemodell koregistriert. Beim zweiten Verfahren wird das Vorwissen des Gebäudemodells in die Orientierung der Bildsequenz integriert, um so die Orientierungen der Bilder der Sequenz an das Gebäudemodell anzupassen. Dieses Verfahren zeigt gegenüber dem ersten Verfahren für die meisten Szenen eine höhere Genauigkeit der Orientierungsparameter.

Zur Texturierung der Fassaden wird ein Verfahren vorgestellt, das aus der IR-Bildfolge ein entzerrtes Bildmosaik erstellt. Schließlich werden Ansätze zur Analyse der Fassadentexturen vorgestellt, wie z.B. die Bestimmung der Temperaturdifferenz zwischen zwei Aufnahmezeitpunkten und die Detektion von Leckagen und Heizungsrohren.

Die experimentellen Ergebnisse zeigen, dass sich die für Bilder aus dem sichtbaren Spektrum entwickelten Verfahren auch auf Bilder im thermischen Infrarotspektrum übertragen lassen, wenn auch mit geringerer Genauigkeit der Koregistrierung.

Die Dissertation ist verfügbar unter: http://www.pf.bgu.tum.de/pub/2014/hoegner_phd14_dis.pdf

## Preisträger des Karl-Kraus-Nachwuchsförderpreises

Mit dem Karl-Kraus-Nachwuchsförderpreis sollen herausragende Diplom-, Bachelor- und Masterarbeiten gewürdigt werden. Der Preis wird seit 2007 gemeinsam von der DGPF, der SGPF (Schweiz) und der OVG (Österreich) verliehen und erinnert an Karl Kraus, den bekannten Hochschullehrer und Lehrbuchautor der TU Wien, der 2006 verstarb.

Erstmals werden in diesem Jahr die Preisträger in einem zweistufigen Verfahren ermittelt. Im ersten Schritt werden aus den eingesandten Beiträgen die zehn besten ausgewählt. Die drei Preisträger gehen dann aus der Posterpräsentation während der Jahrestagung hervor. Alle eingeladenen Kandidatinnen und Kandidaten erhalten einen Reisekostenzuschuss zur Teilnahme an der Jahrestagung.

**1. Preis:** Corinna Harmening, Universität Hannover

# Raumzeitliche Segmentierung von natürlichen Objekten in stark verdeckten Szenen

## Introduction

Phenotyping becomes an increasingly important issue in crop research. Understanding the effects of external factors on the plant phenotype will ultimately lead to a higher yield of crop plants. In order to improve existing methods for phenotyping, Paffenholz & Harmening (2014) propose an automatic and contact free data acquisition by means of a laser scanner based robotic multi-sensor system which provides time series of 3D point clouds. An automatic analysis of the data requires a spatio-temporal segmentation of the point cloud, which is the main focus of this contribution.

## Spatial Segmentation

A spatial pre-segmentation is obtained by means of the graph based image segmentation algorithm proposed by Felzenszwalb & Huttenlocher (2004), whose strength lies in the automatic adaption to different noise levels. In order to apply this image segmentation algorithm to a 3D point cloud, a graph is constructed on the basis of point proximity, and local surface normals are computed. The similarity of regions is then defined as the angle between their normal vectors. Since the change of the normal vector within a leaf may be larger than the change of the normal vector between two contacting leaves, this usually leads to an over-segmented result (Fig. 1). In a statistically based post-processing step, these segments are merged if they describe the same surface or if their border edges follow the same curve in space. Both of these decisions are made by means of a statistical hypothesis test (Harmening 2013). The overall result of the spatial segmentation is shown in Fig. 2: Nearly all over-segmented regions are merged, while contacting leaves remain separated.

**Fig. 1:** Pre-segmentation.

## Temporal Segmentation

In order to determine the evolution of the plant's characteristics, it is necessary to obtain a consistent segmentation of the time series of point clouds. As a segment may split between time intervals, a tracking is realized by means of a shape matching, which judges the similarity of two segments by comparing their shapes. This comparison is based on dynamic

**Fig. 2:** Region-merging.

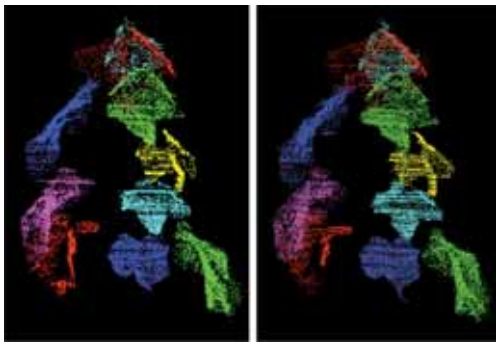

**Fig. 3:** Final result of the temporal segmentation.

time warping (Müller 2007). In order to eliminate the remaining over-segmented regions, combined segments are also included in the forward and backward tracking process. The overall result is shown in Fig. 3: All segments are tracked successfully. In addition, tracking results were used to merge over-segmented regions from individual spatial segmentations.

### References


Felzenszwalb, P.F. & Huttenlocher, D.P., 2004: Efficient Graph-Based Image Segmentation. – International Journal of Computer Vision **59** (2): 167–181.

Harmening, C., 2013: Raum-zeitliche Segmentierung von natürlichen Objekten in stark verdeckten Szenen. – Master thesis (unpublished), Leibniz Universität Hannover, Hannover, Institut für Kartographie und Geoinformatik.

Müller, M., 2007: Information Retrieval for Music and Motion. – 1st Edition, Springer, Berlin und Heidelberg.

Paffenholz, J.-A. & Harmening, C., 2014: Spatiotemporal monitoring of natural objects in occluded scenes by means of a robotic multi-sensor system. – 4th International Conference on Machine Control & Guidance: 63 – 74, Braunschweig.


## 2. Preis: Fabian Schneider, Universität Zürich, Schweiz

## Simulation von Bildspektrometerdaten: 3D Waldmodellierung basierend auf LiDAR and in situ Daten

Fernerkundung bietet einzigartige Möglichkeiten um Waldökosysteme über Raum und Zeit zu untersuchen. Die Ableitung von biochemischen Blatteigenschaften aus Fernerkundungsdaten ist von großem Interesse, da diese Eigenschaften Aufschluss über Photosynthese, Gesundheit, Funktionstyp und Art der Pflanzen geben können. Aufgrund der strukturellen Komplexität des Waldes ist die Skalierung von Messungen auf der Blattebene auf die Bestandesebene jedoch nicht trivial. Deshalb werden vorzugsweise physikalisch basierte Strahlungstransfermodelle verwendet, um spektrale Information zu skalieren.

Meine Masterarbeit im Fach Geographie – Spezialisierung Fernerkundung – hatte zum Ziel, das Strahlungstransfermodell DART (Gastellu-Etchegorry et al. 2012) mit Hilfe von in situ und flugzeuggestützten Daten zu parametrisieren und simulierte Radianzwerte mit Messungen eines flugzeuggestützten Bildspektrometers zu vergleichen. Die Arbeit wurde an der Universität Zürich in Zusammenarbeit mit dem Centre d'Études Spatiales de la Biosphère (CESBIO, Toulouse) verfasst (Schneider et al. 2014). Das Untersuchungsgebiet befindet sich auf den Lägern (Baden,

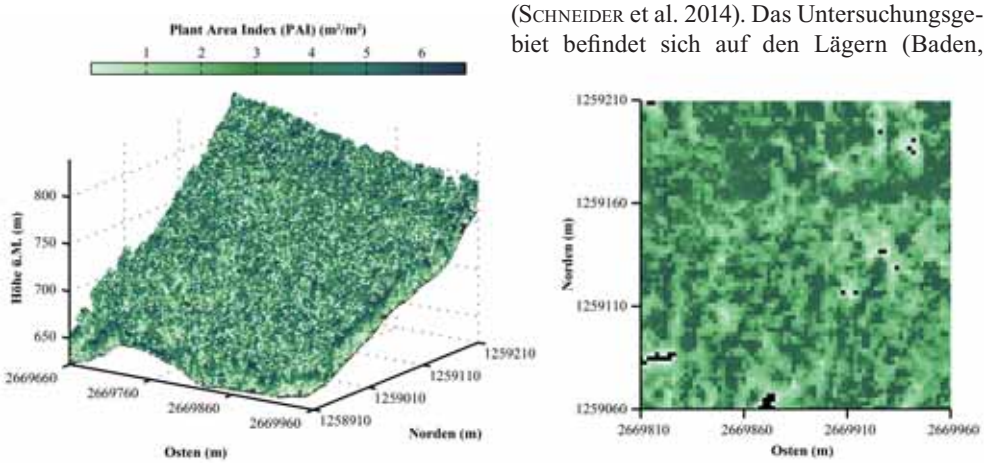


**Abb. 1:** Waldrekonstruktion mit dem Voxelgitter-Ansatz in 3D (links) und 2D (rechts). Der Ausschnitt rechts in 2D zeigt den nordwestlichen Teil der Szene (modifiziert nach Schneider et al. 2014).

Schweiz), in einem temperierten Mischwald, der sich durch steile Hänge, heterogenen Untergrund und hohe Artenvielfalt auszeichnet. Um die komplexe Architektur des Waldes abzubilden, wurden zwei Modelle zur Waldrekonstruktion verglichen: 1) basierend auf einem Voxelgitter und 2) basierend auf einer Einzelbaumdetektion. Beide Methoden basieren auf flugzeuggestütztem Laserscanning (Lidar) und lassen sich auf unterschiedliche Waldökosysteme und Skalenebenen anwenden. Das Resultat der Waldrekonstruktion mit dem Voxelgitter-Ansatz ist in Abb. 1 dargestellt. Der Voxelgitter-Ansatz ist der Parametrisierung basierend auf Einzelbäumen vorzuziehen, da die Waldstruktur wesentlich realistischer abgebildet wird. Dies zeigt sich auch im direkten Vergleich der simulierten Radianzwerte mit Bildspektrometerdaten. Räumliche Muster sind vergleichbar, wobei absolute Werte je nach Wellenlänge stark abweichen können. Unter mehreren Faktoren konnten zwei identifiziert werden, die einen besonders starken Einfluss auf die Simulation hatten: einerseits die hohe spektrale Variabilität der blattoptischen Eigenschaften, die als Input für das Strahlungstransfermodell diente, und andererseits kleinskalige Struktureffekte, die zum Beispiel durch die Anordnung von Nadeln innerhalb eines Zweiges hervorgerufen werden. Folglich sind weitere Studien nötig, um die spektrale Variabilität der Blätter besser zu verstehen beziehungsweise das Verständnis über den Einfluss der Blattoberfläche, des Blattinnern sowie der direkten und diffusen Streuung auf die blattoptischen Eigenschaften zu verbessern. Außerdem sollte ein Schwerpunkt auf die Modellierung und bessere Parametrisierung von kleinskaligen Struktureffekten gelegt werden.

### Literaturverzeichnis

Gastellu-Etchegorry, J.-P., Grau, E. & Lauret, N., 2012: DART: a 3D model for remote sensing images and radiative budget of earth surfaces. – Alexandru, C. (Hrsg.): Modeling and Simulation in Engineering. – InTech, Rijeka, Kroatien.

Schneider, F.D., Leiterer, R., Morsdorf, F., Gastellu-Etchegorry, J.-P., Lauret, N., Pfeifer, N. & Schaepman, M.E., 2014: Simulating imaging spectrometer data: 3D forest modeling based on LiDAR and in situ data. – Remote Sensing of Environment, überarbeitete Fassung eingereicht.

## 3. Preis: Niklas Conen, Hochschule Oldenburg

# Entwicklung einer modellbasierten Eigenbewegungsschätzung eines Kraftfahrzeugs aus Fahrzeugbewegungsdaten und optischen Flussvektoren

### Motivation

Ein gewöhnliches Rückfahrkamerasystem mit nur einer Kamera bietet nicht die Möglichkeit, das Fahrzeug an Straßenmarkierungen auszurichten. Beim Rückwärtseinparken sind diese Markierungen gerade zum Ende des Manövers nicht mehr sichtbar. In diesem Kurzbeitrag wird eine Funktion vorgestellt, die dem Fahrer trotzdem eine Art Rundumsicht von oben auf das Fahrzeug bietet und eine bessere Ausrichtung ermöglicht. Insbesondere werden die Effekte einer nicht ebenen Fahrzeugbewegung, z. B. verursacht durch Fahrschwellen, untersucht und kompensiert.

### Erzeugung der erweiterten Rückfahransicht

Um nur aus den Bildern der Rückfahrkamera eine Rundumsicht von oben zu erzeugen, muss das Fahrzeug rückwärts fahren und die zuvor aufgenommenen Bilder kontinuierlich wie folgt verarbeiten:

- Fisheye-Verzeichnung entfernen gemäß Mei & Rives (2007),
- Normalbilder in Straßenebene nach Hartley & Zisserman (2003, S. 196) umbilden, wobei äußere Orientierung bekannt und fest,
- die so entstandenen Orthobilder entsprechend eines ebenen Fahrzeugbewegungsmodells (Schramm et al. 2010, S. 244ff) mit den aktuellen Sensordaten wie Lenkwinkel und Geschwindigkeit (Eigenbewegungsschätzung) relativ zueinander orientieren.

Während der Rückwärtsfahrt entsteht schließlich ein Bildverband, der sich unter bzw. neben das Fahrzeug schiebt.

Sobald jedoch ein Hindernis überfahren wird, verändern sich die bislang als fest angenommenen äußeren Kameraparameter und es

treten Verzerrungen im Bildverband auf. Deshalb werden aus den Vektorfeldern von einem Optischen Fluss (Ist) und dem Bewegungsmodell (Soll) Differenzvektoren berechnet, die bei Höhenänderungen einen Lageversatz beschreiben. Aus diesem Lageversatz wird laut Luhmann (2010, S. 261) eine Höhenkorrektur rekonstruiert und an die Kameraorientierung angebracht.

## Fazit und Ausblick

Mithilfe der höhenkorrigierten Übersichtskarte kann sich der Fahrer auch bei der Überfahrt von Fahrschwellen an Parklinien oder Hindernissen neben dem Fahrzeug orientieren und sogar auf die Fahrbahn unter dem Auto blicken.

Wenn die Spezifikationen es zulassen, könnten selbst die bisherigen Rückfahrkamerasysteme um diese Funktion erweitert werden, da lediglich ein Softwareupdate notwendig wäre.

## Literaturverzeichnis

Conen, N., 2013: Entwicklung einer modellbasierten Eigenbewegungsschätzung eines Kraftfahrzeugs aus Fahrzeugbewegungsdaten und optischen Flussvektoren. – Masterarbeit, Jade Hochschule Oldenburg.

Hartley, R. & Zisserman, A., 2003: Multiple View Geometry in Computer Vision. – 2. Auflage, Cambridge University Press, Cambridge, UK.

Luhmann, T., 2010: Nahbereichsphotogrammetrie. – 3. Auflage, Wichmann, Berlin.

Mei, C. & Rives, P., 2007: Single View Point Omnidirectional Camera Calibration from Planar Grids. – IEEE International Conference on Robotics and Automation: 3945–3950, Roma, Italy.

Schramm, D., Hiller, M. & Bardini, R., 2010: Modellbildung und Simulation der Dynamik von Kraftfahrzeugen. – Springer, Berlin, Heidelberg.

Adressen der Preisträger und Betreuer:
Corinna Harmening, TU Wien, Tel.: +43-1-58801-12839, e-mail:corinna.harmening@geo.tuwien.ac.at, Betreuer: Claus Brenner, Hannover

Fabian Daniel Schneider, Universität Zürich, Tel.: +41-44-6355130, e-mail: fabian-daniel.schneider@geo.uzh.ch, Betreuer: Michael Schaepmann, Zürich, Schweiz

M.Sc. Niklas Conen, Jade Hochschule Oldenburg, Tel.: +49-441-7708-3346, e-mail: niklas.conen@jade-hs.de, Betreuer: Thomas Luhmann, Oldenburg

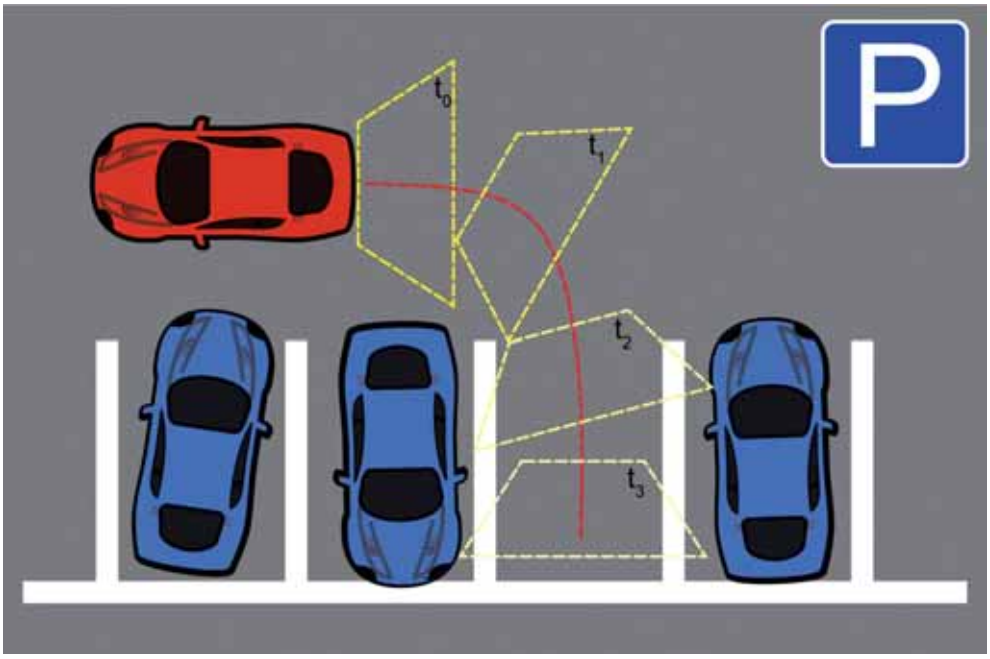


**Abb. 1:** Schema des Bildverbandes beim Einparkvorgang.

# Veranstaltungskalender

## 2014

6.–8. Oktober: **ISPRS Technical Commission II Symposium 2014** in **Toronto,** Kanada. www2.isprs.org/2014GeoTPMA/home.html

7.–9. Oktober: **INTERGEO 2014** in **Berlin**. Intergeo.de

22.–24. Oktober: **International Conference on Image Analysis and Recognition (ICIAR) 2014** in **Vilamoura,** Portugal. aimi-conf.org/iciar14

27.–30. Oktober: **International Conference on Image Processing (ICIP) 2014** in **Paris,** Frankreich. icip2014.com

3.–8. November: **EUROMED 2014 – Progress in Cultural Heritage e-Documentation, Preservation and Protection** in **Limassol,** Zypern. culturalheritage2014.eu

11.–13. November: **3d GeoInfo 2014** in **Dubai,** Vereinigte Arabische Emirate. 3dgeoinfo2014.org

15.–17. November: **GI Research2014** in **Teheran,** Iran. giresearch.ut.ac.ir

17.–20. November: **ISPRS Technical Commission I Symposium 2014** in **Denver,** USA. isprs.org/2014tc1symposium

26.–27. November: **MoLaS 2014 – Mobile Laserscanning Technology Workshop** in **Freiburg**. ipm.fraunhofer.de/en/tradefairs-events/molas-workshop-2014.html

26.–28. November: **11th Symposium on Location-Based Services** in **Wien,** Österreich. lbs2014.org

2.–3. Dezember: **LowCost3D 2014** in **Berlin**. lc3d.net

4.–5. Dezember: **3D-NordOst 2014** in **Berlin**. 3d-NordOst.de

9.–12. Dezember: **ISPRS Technical Commission VIII Symposium 2014** in **Hyderabad,** Indien. nrsc.gov.in/technicalcommission8.html

14.–17. Dezember: **ICDM - IEEE Conference on Data Mining 2014** in **Shenzhen,** China. icdm2014.sfu.ca/

Weitere Konferenzen und Workshops finden sich beispielsweise unter:
isprs.org/calendar
conferences.visionbib.com

# Korporative Mitglieder

**Firmen**

AEROWEST GmbH
AICON 3D Systems GmbH
aphos Leipzig AG
Bernhard Harzer Verlag GmbH
Black Bridge AG
Blom Deutschland GmbH
Brockmann Consult GmbH
bsf swissphoto GmbH
Büro Immekus
CGI Systems GmbH
DB Netz AG
DELPHI IMM GmbH
Deutsches Bergbau-Museum
EFTAS Fernerkundung Technologietransfer GmbH
ESG Elektroniksystem- und Logistik-GmbH
Esri Deutschland GmbH
EUROPEAN SPACE IMAGING
Eurosense GmbH
Exelis Visual Information Solution GmbH
fokus GmbH
g.on experience gmbh
GAF GmbH
GeoCart Herten GmbH
Geoinform. & Photogr. Engin. Dr. Kruck & Co. GbR
geoplana Ingenieurgesellschaft mbH
GEOSYSTEMS GmbH
GGS - Büro für Geotechnik, Geoinformatik, Service
Hansa Luftbild AG
Herbert Wichmann, VDE Verlag GmbH
IAGB mbH
IGI - Ingenieur-Gesellschaft für Interfaces mbH
ILV Ingenieurbüro für Luftbildauswertung und Vermessung
Infoterra GmbH
INVERS - Industrievermessung & Systeme
J. Linsinger ZT-GmbH
Leica Geosystems GmbH
Luftbilddatenbank-Würzburg
Messbildstelle GmbH
Microsoft Photogrammetry
MILAN Geoservice GmbH
M.O.S.S. Computer Grafik Systeme GmbH
PHOENICS GmbH
PMS - Photo Mess Systeme AG
RIEGL Laser Measurement Systems GmbH
RWE Power AG, Geobasisdaten/Markscheidewesen
technet GmbH
Terra-Messflug GmbH
topometric GmbH
TRIGIS Vermessung + Geoinformatik GmbH
Trimble Germany GmbH
trimetric 3D Service GmbH
Z/I Imaging Ltd.

**Behörden**

Amt für Geoinformationswesen der Bundeswehr
Bayerische Landesanstalt für Wald und Forstwirtschaft
Bundesamt für Kartographie und Geodäsie
Bundesmininisterium für Ernährung, Landwirtschaft und Verbraucherschutz
Hessisches LA für Bodenmanagement und Geoinformation
Innenministerium NRW, Gruppe Vermessungswesen
Institut für Umwelt- und Zukunftsforschung
LA für Geoinformation und Landentwicklung, BW
LA für Vermessung und Geoinformation, Bayern
LB Geoinformation und Vermessung, Hamburg
LB für Küstenschutz, Nationalpark und Meeresschutz, SH
Landeshauptstadt Düsseldorf, Vermessungs- und Liegenschaftsamt
Landesvermessung und Geobasisinformation Niedersachsen
Märkischer Kreis, Vermessungs- und Katasteramt
Regierungspräsident Tübingen, Abt. 8 Forstdirektion
Regionalverband Ruhr
Staatsbetrieb Sachsenforst
Stadt Bocholt, Fachbereich 31
Stadt Köln, Amt für Liegenschaften, Vermessung und Kataster
Stadt Wuppertal, Vermessung, Katasteramt und Geodaten
Thüringer LA für Vermessung und Geoinformation

**Hochschulen**

BTU Cottbus, Lehrstuhl für Vermessungskunde
FH Frankfurt a.M., FB 1, Studiengang Geoinformation
FH Mainz, Institut für Raumbezogene Informations- und Messtechnik
Jade Hochschule, Institut für Angewandte Photogrammetrie und Geoinformatik
HCU HafenCity Universität Hamburg, Geomatik
HfT Stuttgart, Vermessung und Geoinformatik
HS Bochum, FB Vermessung und Geoinformatik
HS Karlsruhe, Fakultät für Geomatik
HTW Dresden, FB Vermessungswesen/Kartographie
LUH Hannover, Institut für Kartographie und Geoinformatik
LUH Hannover, Institut für Photogrammetrie und Geoinformation
MLU Halle, FG Geofernerkundung
Ruhr-Uni Bochum, Geographisches Institut
RWTH Aachen, Geodätisches Institut
TU Bergak. Freiberg, Institut für Markscheidewesen und Geodäsie
TU Berlin, Computer Vision & Remote Sensing
TU Berlin, Institut für Geodäsie und Geoinformationstechnik
TU Braunschweig, Institut für Geodäsie und Photogr.
TU Clausthal, Institut für Geotechnik und Markscheidewesen
TU Darmstadt, Institut für Photogrammetrie und Kartographie
TU Dresden, Institut für Photogrammetrie und Fernerkundung
TU München, FG Photogrammetrie und Fernerkundung
TU Wien, Institut für Photogrammetrie und Fernerkundung
Uni Bonn, Institut für Photogrammetrie
Uni Göttingen, Institut für Waldinventur und Waldwachstum
Uni Heidelberg, IWR Interdisziplinäres Zentrum für Wissenschaftliches Rechnen
Uni Kassel, FB Ökologische Agrarwissenschaften
Uni Kiel, Geographisches Institut
Uni Stuttgart, Institut für Photogrammetrie
Uni Trier, Institut für Umweltfernerkundung und Geoinformatik
Uni Würzburg, Geographisches Institut
Uni zu Köln, Geographisches Institut

## Korrigendum zu PFG 4/2014

Sehr geehrte Leser der PFG,

versehentlich wurde im Manuskript Gianpaolo Conte auf Seite 295 die Beschreibung für die obere Abbildung der Fig. 7 nicht abgedruckt.

Korrigierte vollständige Version:

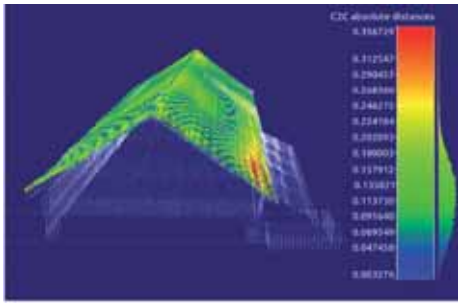

(a) Airborne lidar

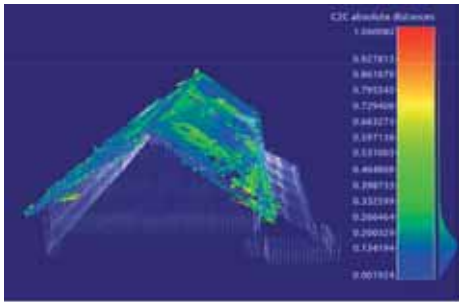

(b) Photogrammetry

**Fig. 7:** Deviation between the reference model and reconstruction based on the two methods examined. The values of on the colour bars are in meters.

Die Daten wurden bei Ingenta und auf unserer Homepage korrigiert.
Bitte entschuldigen Sie das Versehen.

Schweizerbart Science Publishers

## Corrigendum in PFG 4/2014

Dear readers of PFG,

in the paper of Gianpaolo Conte, page 295, the description for the upper part of Fig. 7 has not been printed

Corrected complete version:

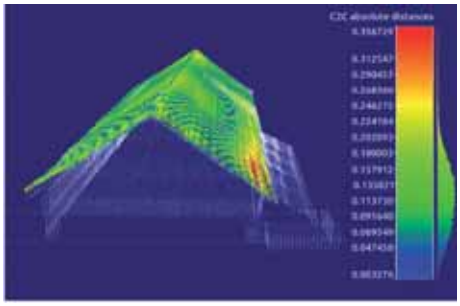

(a) Airborne lidar

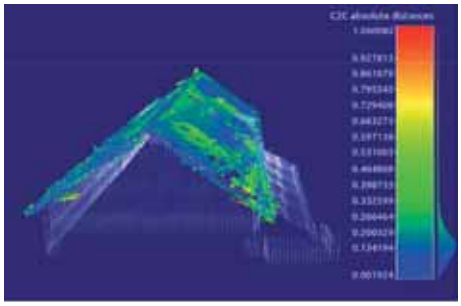

(b) Photogrammetry

**Fig. 7:** Deviation between the reference model and reconstruction based on the two methods examined. The values of on the colour bars are in meters.

Data were corrected at Ingenta and on our website.
Please excuse the mistake.

Schweizerbart Science Publishers

universitätbonn

landwirtschaftliche fakultät

igg

An der **Rheinischen Friedrich-Wilhelms-Universität** ist an der **Landwirtschaftlichen Fakultät** im **Institut für Geodäsie und Geoinformation (IGG)** zum 01.August 2016 eine

# W3-Professur für Geoinformation

**(Nachfolge Prof. Dr. L. Plümer)**

zu besetzen.

Der/Die zukünftige Stelleninhaber/-in soll in der Forschung auf dem Gebiet der Geoinformation international ausgewiesen sein, wobei Schwerpunkte im gesamten Spektrum der Geoinformation liegen können. Kooperationsbereitschaft mit den Bereichen des IGG, der Landwirtschaftlichen Fakultät und anderen Fakultäten wird im Hinblick auf zukünftige Forschungsverbünde begrüßt. In der Lehre ist das Fach Geoinformation im Studiengang Geodäsie und Geoinformation (Bachelor und Master) sowie als Nebenfach in weiteren Studiengängen zu vertreten.

Die Bewerberinnen/Bewerber müssen die allgemeinen Einstellungsvoraussetzungen nach § 36 des Hochschulgesetzes für das Land Nordrhein-Westfalen erfüllen.

Chancengleichheit ist Bestandteil unserer Personalpolitik.

Bewerbungen mit den üblichen Unterlagen (Lebenslauf, Zeugnisse, Schriftenverzeichnis, Darstellung der Lehraktivitäten, Drittmitteleinwerbung und Forschungsperspektiven) sind bis zum **10. November 2014** zu richten an den **Dekan der Landwirtschaftlichen Fakultät, Rheinische Friedrich-Wilhelms-Universität, Meckenheimer Allee 174, 53115 Bonn.**